To the Graduate Council:

I am submitting herewith a dissertation written by Sumeet Salaniwal entitled "Self-Assembly of Di-Chain Surfactant in Carbon Dioxide". I have examined the final copy of this dissertation for form and content and recommend that it be accepted in partial fulfillment of the requirements for the degree of Doctor of Philosophy, with a major in Chemical Engineering.

Peter T. Cummings, Major Professor

We have read this dissertation
and recommend its acceptance:

Accepted for the Council:

Associate Vice Chancellor and
Dean of The Graduate School

SELF-ASSEMBLY OF DI-CHAIN SURFACTANT IN CARBON DIOXIDE

A Dissertation
Presented for the
Doctor of Philosophy
Degree
The University of Tennessee, Knoxville

Sumeet Salaniwal
May 2000

DEDICATION

To my family
for their loving support and encouragement

ACKNOWLEDGEMENTS

I take this opportunity to express my gratitude and thanks to my advisor, Peter T. Cummings, whose guidance and support has been very helpful during this research. His technical expertise along with his enthusiasm and humor have made this a rewarding and enjoyable experience. I would like to express my thanks to the members of my thesis committee: Hank Cochran, John Prados, and Mark Dadmun for providing their valuable insight and suggestions. Many thanks are due to our office secretary and a good friend, Teresa Finchum, who has always been very helpful. I am grateful to my friends and colleagues: Jonathan Moore, Sunil Gupta, Clare McCabe, Jose Rivera-Rojas, Mohammed Houssa, and Milan Predota, for helpful conversations and making my stay at UT an enjoyable one. Special thanks are due to Ariel Chialvo and Shengting Cui for their valuable suggestions during this research work.

Most of all, I would like thanks my parents and brother, Puneet, who have always encouraged me to pursue my dreams. This thesis would not have seen daylight without their love and the motivation they provided. Finally, this acknowledgement will not be complete without mentioning my wife, Ruchi, who has filled my life with joy and love.

ABSTRACT

Carbon dioxide holds considerable potential as an environmentally and chemically benign alternative to the potentially hazardous conventional industrial solvents. In spite of its promise, one of the reasons that CO_2 has so far failed to achieve its full potential is that few "CO_2-philic" surfactant molecules are known at present that form stable reversed micelles in carbon dioxide. The aqueous or polymeric cores of these surfactant aggregates provide a medium for solubilizing substances (hydrophiles, polar molecule, proteins) that are otherwise insoluble in CO_2.

As a step in this direction, molecular dynamics simulation of a dichain (or hybrid) surfactant + water + carbon dioxide (solvent) ternary system is presented in this work to gain valuable insight into the aggregation behavior of these surfactant molecules. Two different system sizes were investigated using detailed and quite realistic molecular models for all the three chemical species involved. One of the system sizes investigated mimicked the overall composition studied in a recent experimental (SANS) work, while the other provided valuable insight into the effect of surfactant chemistry and architecture on surfactant aggregation. The simulations for the two system sizes used different solvent conditions (supercritical CO_2 and high temperature liquid CO_2) to provide information into the effect of solvent condition on surfactant aggregation.

The surfactant system showed a rapid and spontaneous propensity for aggregation of surfactant and water molecules into aggregates that resemble reversed micellar aggregates i.e. the aggregates consisted of an aqueous core surrounded by a layer of surfactant molecules with their head groups immersed in the core and the tails forming a corona. The aggregation mechanism observed in these simulations was a two-step mechanism involving rapid ion-hydration followed by gradual surfactant

aggregation via hydrogen bond formation. The aggregation process was found to be diffusion-controlled i.e. dependent on the size of aggregates and the solvent density. Another factor influencing the aggregation process was the steric resistances offered by the surfactant tails. The structural properties of the aggregates were dependent on the water-to-surfactant molar ratio of the system. The size and shape of the aggregates predicted by these simulations were in reasonably good agreement with prior experimental results.

Contents

1 Introduction 1

2 Literature Review 12

2.1 Experiments 13

2.2 Simulations 19

2.2.1 Oil-in-water micelles 19

2.2.2 Water-in-oil micelles 27

3 Molecular Models 30

3.1 Alkane tail 31

3.2 Perfluoroalkane tail 32

3.3 Sulfate head group and sodium counter-ion 34

3.4 Carbon dioxide 40

3.5 Water 42

4 Methodology 44

4.1 System composition 45

4.1.1 Small System 46

4.1.2 Large System 47

4.2 Starting configurations 48

4.3 Rattle Algorithm 51

4.4 Replicated Data Algorithm 53

5 Results and Discussion 60

5.1 Aggregation mechanism 61

5.2 Aggregation dynamics 82
5.3 Aggregate structure 92
5.4 Aggregate Microstructure 97
5.5 Tail conformation 101
5.6 Structure of aqueous core 104
5.7 Effect of tail chemistry 118
5.8 Effect of tail length 122

6 Conclusions and Recommendations **129**
6.1 Conclusions 129
6.2 Recommendations for Future work 134

Bibliography **136**

Appendix **143**

A Site-site reaction field method **144**

B Iterative procedure for Rattle algorithm **146**

C SANS studies on polymers in supercritical carbon dioxide **150**

Vita **217**

List of Tables

2.1 Structural properties of RMs of dichain surfactant observed by Eastoe et al. [54] in a SANS investigation ($T = 298K$). The uncertainties for R_{core} are $\pm$ 1 Å 17

3.1 Potential parameters for the intra-molecular and inter-molecular interactions for the alkane tail and perfluoroalkane tail 36
3.2 Potential parameters for the sulfur and oxygen atoms of the head group and the sodium ion 38
3.3 Potential parameters for the carbon dioxide potential model 41
3.4 Potential parameters for the SPC/E potential model for water 43

4.1 Composition and the state condition of the two system sizes studied . 48

5.1 Structural properties of the largest aggregate formed in the large simulation system (aggregated starting configuration) 93
5.2 Structural properties of surfactant aggregates formed in the small simulation system (aggrega ted starting configuration) 95

List of Figures

1.1 Amphiphiles can self-associate into a variety of aggregates with distinct structural characteristics. These structures can transform from one into another by changing the solution conditions, such as electrolyte concentration, pH, or temperature [Source: J. N. Israelachvilli, *Physics of Amphiphiles: Micelle, Vesicles and Microemulsions*, 1985]. 2

1.2 Typical structure of a reversed micellar (RM) aggregate. The aggregate has a polar core that is quite often aqueous. The surfactant molecules form a coating over the core with their head groups lying at the surface and the tails forming the corona. 5

1.3 Molecular structure of the hybrid (dichain) surfactant molecule used in this simulation study. The surfactant has two distinct seven-member long tails, an alkane tail and a perfluoroalkane tail. Sulfate forms the anionic head group and sodium is the counter-ion. 10

3.1 Lennard-Jones (LJ) potential for the non-bonded intra-molecular and intermolecular interactions. 33

3.2 Torsional potential for the alkane and the perfluoroalkane tail of the dichain surfactant molecule. 35

3.3 Molecular geometry of the sulfate head group. 37

3.4 Molecular model for the dichain surfactant molecule used in this study. 39

3.5 Molecular model for the carbon dioxide molecule. 40

3.6 Molecular geometry of the water molecule. 42

4.1 Snapshots of the starting configurations for the small system used in this study. (a) aggregated starting configuration (b) scattered starting configuration. 49
4.2 Snapshots of the starting configurations for the large system used in this study. (a) aggregated starting configuration (b) scattered starting configuration. 50
4.3 Replicated data parallelization strategy. 54
4.4 Sequence of events for the replicated data parallelization of the simulation code. 56
4.5 Performance curve for the simulation code used in this study. 59

5.1 Snapshots of the simulation taken at (a) 5.5 ps, (b) 44.6 ps, (c) 148.3 ps, and (d) 1036.0 ps showing the mechanism of surfactant aggregation for the small system with aggregated starting configuration. The color scheme of the various species is as follows: light blue for perfluoroalkane tail, dark blue for alkane tail, yellow for sulfur, red for oxygen, white for hydrogen, and grey for sodium. CO_2 molecule are not shown for visual clarity. 63
5.2 Time evolution of the surfactant-surfactnt (U_{ss}) and surfactant-water (U_{sw}) interaction energies in the small system with aggregated starting configuration. Arrows indicate the times corresponding to the snapshots in Figure 5.1. 65
5.3 Time evolution of the fraction of water molecules present in the small system (aggregated starting configuration) that are associated with the surfactant molecules. Arrows indicate the times corresponding to the snapshots in Figure 5.1. 68
5.4 Time evolution of the surfactant-surfactnt (U_{ss}) and surfactant-water (U_{sw}) interaction energies in the small system with scattered starting configuration. 69

5.5 Time evolution of the fraction of water molecules present in the small system (scattered starting configuration) that are associated with the surfactant molecules. 70

5.6 Snapshots of the simulation taken at (a) 5 ps, (b) 20 ps, (c) 100 p s, and (d) 1000 ps showing the mechanism of surfactant aggregation for the large system with aggregated starting configuration. The color scheme of the various species is as follows: light blue for perfluoroalkane tail, dark blue for alkane tail, yellow for sulfur, red for oxygen, white for hydrogen, and grey for sodium. CO_2 molecule are not shown for visual clarity. 72

5.7 Snapshots of the simulation taken at (a) 100 ps, (b) 200 ps, (c) 500 p s, and (d) 2000 ps showing the mechanism of surfactant aggregation for the large system with scattered starting configuration. The color scheme of the various species is as follows: light blue for perfluoroalkane tail, dark blue for alkane tail, yellow for sulfur, red for oxygen, white for hydrogen, and grey for sodium. CO_2 molecule are not shown for visual clarity. 73

5.8 Time evolution of the fraction of water molecules present in the large systems (for both starting configuration) that are associated with the surfactant molecules. 75

5.9 Time evolution of the surfactant-surfactnt (U_{ss}) and surfactant-water (U_{sw}) interaction energies in the large system with aggregated starting configuration. Arrows indicate the times corresponding to the snapshots in Figure 5.7. 76

5.10 Mean-squared displacement (MSD) of the C_7-tailed hybrid surfactant during the first 80 ps of the aggregation process for the small system (aggregated starting configuration) and the large system (scattered starting configuration). 79

5.11 Mean-squared displacement (MSD) of the C_7-tailed hybrid surfactant during two different time periods of the aggregation process for the small system with aggregated starting configuration. 81

5.12 Time evolution of the number of aggregates during the simulation for the C_7-tailed dichain surfactant in the large system. The definition of an aggregate is based on the cluster counting algorithm of Sevick and co-workers [81]. 83
5.13 Variation of the diffusivity of surfactant aggregates with $m^{\frac{1}{3}}$ for the large system. 87
5.14 Time evolution of a) number of collision aggregates and (b) number of surfactant aggregates during the simulation for the C_7-tailed hybrid surfactant in the large system (scattered starting configuration). The definition of an aggregate is based on the cluster counting algorithm of Sevick and co-workers [81]. 89
5.15 Time evolution of the number of aggregates during the simulation for the C_7-tailed hybrid surfactant in the large system (scattered starting configuration) with and without surfactant molecules. The definition of an aggregate is based on the cluster counting algorithm of Sevick and co-workers [81]. 90
5.16 Time evolution of the number of aggregates during the simulation for the C_7-tailed hybrid surfactant in the small system (aggregated starting configuration). The definition of an aggregate is based on the cluster counting algorithm of Sevick and co-workers [81]. 91
5.17 Time evolution of the shape properties of the three aggregates formed in the small system with aggregated starting configuration, (a) I_{max}/I_{min} (b) η. 96
5.18 Structural properties of the aggregate formed in the large system with aggregated starting configuration, (a) water and carbon dioxide (b) microstructure of surfactant molecule. 98
5.19 Radial density profiles of the water molecules, sodium ions, sulfate head group, perfluoroalkane tail, and alkane tail from center of mass of the aggregate for the small system with aggregated starting configuration. 100

5.20 Time evolution of the % trans bonds (extent of fully extended tails) for the perfluoroalkane tail and the alkane tail of the C_7-tailed hybrid surfactant for the small system with aggregated starting configuration. 102
5.21 Radial distribution of the functional groups of the perfluoroalkane tail and the alkane tail for the C_7-tailed hybrid surfactant for the small system with aggregated starting configuration. 103
5.22 Radial distribution function (rdf) and running co-ordination number (rcn) for (a) Na-Na pair (b) Na-head group pair. 105
5.23 Radial distribution function (rdf) and running co-ordination number (rcn) for (a) Na-water pair (b) head group-water pair. 107
5.24 Schematic representation of the definition of the hydrogen bond adopted in this study. 109
5.25 Interparticle-dipole vector angle angular distribution function (adf) for water molecules lying within the primary hydration shell of the ions. . 110
5.26 Interparticle-bond angle vector angular distribution function (adf) for water molecules lying within the primary hydration shell of the ions. . 111
5.27 Interparticle-dipole vector angular distribution function (adf) for water molecules at varying distances from the sodium ion. 112
5.28 Interparticle-dipole vector angular distribution function (adf) for water molecules at varying distances from the anionic head group. 114
5.29 Dipole-dipole vector angle angular distribution function (adf) for water molecules within the bulk-like region of the aqueous core. 115
5.30 Interparticle-dipole vector angle angular distribution function (adf) for water molecules within the bulk-like region of the aqueous core. . . . 116
5.31 Interparticle-bond vector angle angular distribution function (adf) for water molecules within the bulk-like region of the aqueous core. . . . 117
5.32 Mean-squared displacement (MSD) of the C_7-tailed fully-fluorinated and C_7-tailed fully-hydrogenated surfactants during the first 80 ps of the aggregation process. 120

5.33 Time evolution of the number of aggregates during the simulation for the C_7-tailed fully-fluorinated and C_7-tailed fully-hydrogenated surfactant. The definition of an aggregate is based on the cluster counting algorithm of Sevick and co-workers [81]. 121
5.34 Snapshots of the system configuration for (a) C_7-tailed fully-fluorianted surfactant, and (b) C_7-tailed fully-hydrogenated surfactant. The snapshots are at $\sim$ 1.2 ns. 123
5.35 Mean squared displacement (MSD) of the C_5-tailed dichain surfactant and C_9-tailed dichain surfactant during the first 80 ps of the aggregation process. 125
5.36 Time evolution of the number of aggregates during the simulation for the C_5-tailed dichain surfactant and C_9-tailed dichain surfactant. The definition of an aggregate is based on the cluster counting algorithm of Sevick and co-workers [81]. 126
5.37 Snapshots of the system configuration for (a) C_5-tailed dichain surfactant, and (b) C_9-tailed hybrid surfactant. The snapshots are at $\sim$ 1.1 ns. 127

Chapter 1

Introduction

A well known and fundamentally important property of surfactant molecules (also known as surface-active agents) is their ability to undergo, under certain conditions, spontaneous self-association into a variety of molecular aggregates when dissolved in various polar (or non-polar) solvents. This phenomenon of self-association is often characterized (especially in polar/aqueous solvents) by drastic changes in the various bulk physical properties (e.g. surface tension, turbidity, electrical conductance, osmotic pressure etc.) of the surfactant solution [1]. In fact, it is the sudden changes in these properties that characterizes the critical concentration (called critical micelle concentration) of the surfactant molecules that marks the onset of surfactant aggregation. Although surfactant aggregates of various morphologies (globular, rod-like, or disc-like micelles, monolayers and bilayers, vesicles) have been experimentally observed, as shown in Figure 1.1, these aggregates are commonly referred to as micelles and the phenomenon of surfactant aggregation is called micellization. Properties such as size, shape, and polydispersity of these aggregates are found to be quite sensitive not only to the molecular architecture of the surfactant molecule but to factors such as solvent temperature and pH, presence of co-solvents [2, 3]. A detailed understanding of the various aspects of surfactant self-aggregation and the morphology of surfactant aggregates is of fundamental importance as they find numerous applications in a wide

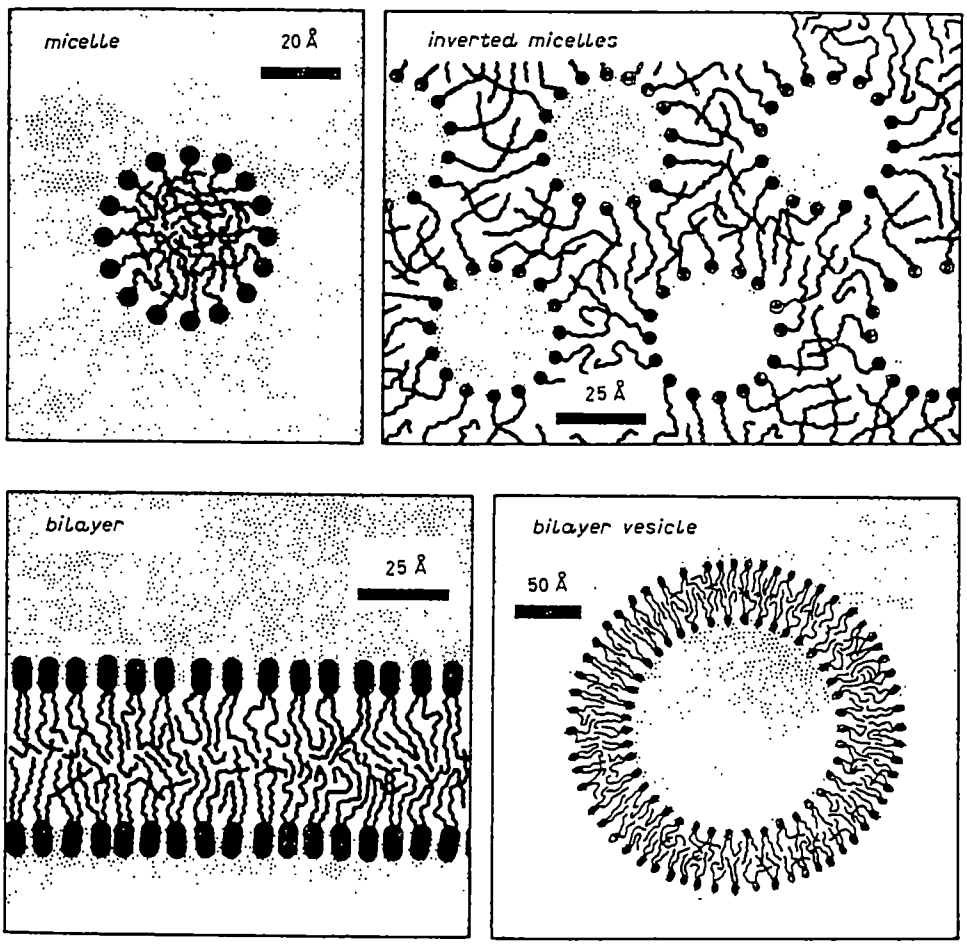


Figure 1.1: Amphiphiles can self-associate into a variety of aggregates with distinct structural characteristics. These structures can transform from one into another by changing the solution conditions, such as electrolyte concentration, pH, or temperature [Source: J. N. Israelachvilli, *Physics of Amphiphiles: Micelle, Vesicles and Microemulsions*, 1985].

variety of fields, such as detergency, emulsification, lubrication, catalysis, and tertiary oil recovery, to name a few.

The characteristic structural feature of the surfactant molecules responsible for their surface activity and micellization is the presence of two different moieties within the same molecule. One of these has a strong affinity for the solvent (known as lyophilic), while the other has little or no affinity for the solvent and hence called lyophobic. This dualistic character of the surfactant molecules is called amphipathy, and hence surfactant molecules are also referred to as amphiphilic molecules or simply amphiphiles. It should be pointed out that quite often terms like hydrophilic and hydrophobic are used to denote solvent affinity and phobicity respectively, because the term micelle is most commonly used in context of aqueous surfactant solutions. The chemical structure of the groupings suitable as the lyophilic and lyophobic portions of the surfactant molecule varies with the nature of the solvent medium and the conditions of use. Thus, for surface activity in a particular solvent the chemical structure of the surfactant molecule must be amphiphilic in that solvent under the desired operating conditions.

The classification of surfactant molecules is based on the nature of their hydrophilic part (commonly known as the head group) that is either ionic (anionic, cationic, or zwitterionic) or polar (polyxyethylene chain, amine oxide etc). The hydrophobic part (known as the tail or chain) is usually composed of long-chain hydrocarbons, often one or two linear (or branched) chains that sometimes contain unsaturated portions or aromatic moieties. The different (often opposite) solvation characteristics of the head group and the tail are responsible for the formation of a micellar phase in the surfactant solution. For instance, in aqueous solvents the hydrophobic tails behave as if they want to avoid contact with the solvent while the hydrophilic head groups behave as if they like the aqueous environment surround-

ing them. As a result of this contrasting behavior, the tails of surfactant molecules aggregate to form a hydrophobic core with the head groups lying at the surface of the aggregate thereby effectively shielding the hydrophobic core from the aqueous solvent. By achieving this arrangement the surfactant molecules can exist as a soluble entity in an aqueous solvent at fairly high concentrations. Since the cores of these aggregates are hydrophobic, surfactant aggregates in aqueous solutions are also known as oil-in-water (o/w) micelles. On the other hand, the roles of the hydrophilic and hydrophobic parts of the amphiphile are reversed in the presence of a non-polar solvent medium i.e. the hydrophilic head groups form the core of the aggregate while the hydrophobic tails extend into the solvent forming a corona around the core. Since this arrangement of surfactant molecules simply involves a reversal in their orientation compared to that in aqueous/polar solvents, these aggregates are called water-in-oil (w/o) or inverted or reversed micelles (RMs). Figure 1.2 shows the typical structure of a reversed micellar aggregate. Quite often the formation of RMs in non-polar solvents requires the addition of small quantities of water to the surfactant solution that acts to facilitate aggregation of the head groups of various surfactant molecules together. Thus, these aggregates often contain well-defined aqueous cores that provide a unique environment for the solubilization, often in significant quantities, of substances (such as hydrophiles, polar solutes, and proteins) that are otherwise insoluble in the non-polar solvent. Because of this unique property of solubilization, RMs find numerous applications such as lubricants, catalytic environments for chemical reactions, and capsules for drug delivery.

Following the pioneering work of Hartley [4] in the early part of this century on o/w micelles and aqueous surfactant solutions in general, such systems have been an area of active research because of their widespread applications in diverse fields. These applications range from the simple household cleaning to complex phenomenon,

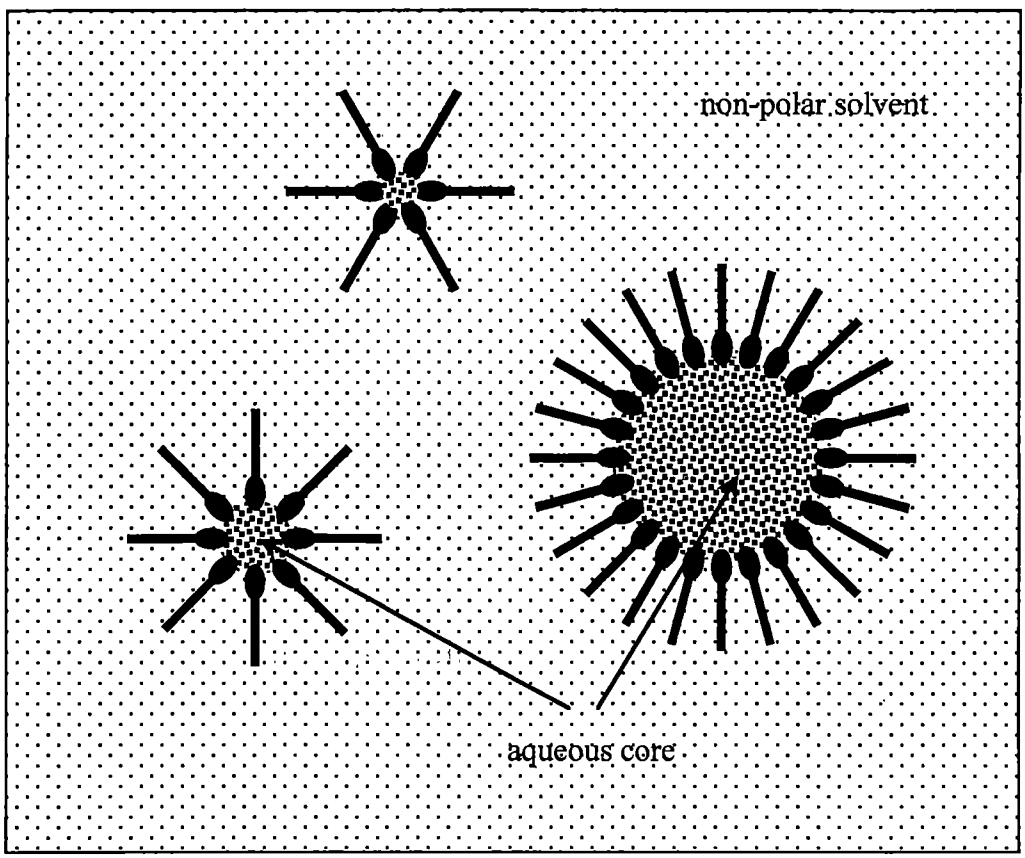


Figure 1.2: Typical structure of a reversed micellar (RM) aggregate. The aggregate has a polar core that is quite often aqueous. The surfactant molecules form a coating over the core with their head groups lying at the surface and the tails forming the corona.

such as molecular transport through a cell membrane. Theoretical/structural models [5, 6, 7, 8], experimental investigations [9, 10, 11, 12, 13] and lately molecular simulation studies [14, 15, 16, 17, 18, 19, 20, 21, 22, 23, 24, 25, 26, 27, 28, 29, 30] have investigated and analyzed numerous aspects of micellization in aqueous solvents, such as thermodynamics and kinetics of surfactant self-aggregation, critical micelle concentration (CMC), structural properties of the hydrophobic core, and extent of solvent penetration into the hydrophobic core. These studies have often complemented each other and together have been quite successful in generating a wealth of information that can now be used to enhance the effectiveness of presently used surfactant molecules or to design new ones tailored for specific applications.

In contrast, as pointed out by Eicke and others [31, 32] little attention has been devoted to understand the various physico-chemical properties of RMs and surfactant aggregation in non-polar solvents. Earliest attempts [31, 32, 34] to understand the phenomenon of micellization in non-polar solvents were based on the reasoning that these aggregates have properties very similar to those observed for o/w micelles, since the structure of RMs is simply a "reversed version" of their aqueous counterparts. Moreover, it was argued that since the building blocks (hydrophilic and hydrophobic moieties within the same molecule) of the two types of aggregates are quite similar, their thermodynamic properties should be quite similar. However, in reality RMs exhibit strikingly different physico-chemical properties than their aqueous surfactant aggregates. For instance, the driving force for aggregation in non-polar solvents and the forces responsible for holding surfactant molecules together in a RM are due to electrostatic interactions between the polar head groups, dipole-dipole interaction, or hydrogen bonding interactions. The unrestricted growth of the aggregate is prevented by the dominance of steric repulsion between surfactant molecules, particularly surfactant tails. In contrast, the hydrophobic effect [35] is responsible for providing the

driving force for aggregation in aqueous surfactant solutions. Another remarkable feature of RMs is their low to moderate aggregation numbers. The aggregation number of most of the surfactants that form RMs are $\sim$ 5 - 50 amphiphiles per aggregate [31], while for o/w micelles the aggregation numbers are normally $\sim$ 200 - 1000 amphiphiles per aggregate [36]. A direct consequence of the low aggregation number in RMs is that the CMC (surfactant concentration that marks the onset of micellization) in such systems is quite low. The CMC for most surfactant molecules in non-polar solvents varies from 10^{-3} - 10^{-4} M to as low as 10^{-7} M in some systems [31], whereas for surfactant aggregation in aqueous systems CMCs are normally in the range of 10^{-3} - 10^{-2} M [36, 37]. As a result, experimental data on the CMC of surfactants in non-polar solvents have often been found conflicting and sources of considerable confusion. Moreover, most of the experimental methodologies used to study aqueous surfactant systems depend on the electrical conductivity of the solvent medium and hence are unsuitable for studying aggregation in non-polar solvents. In light of this, molecular simulation techniques can play an important role in understanding the behavior of these less known yet highly important surfactant systems.

Traditionally, the various non-polar solvents commonly used as a medium for supporting RMs have been linear aliphatic, cycloaliphatic and aromatic hydrocarbons such as benzene, toulene, cyclohexane, carbon tetrachloride etc. However, these solvents not only offer limited flexibility in controlling the dynamics of self-aggregation and morphology of aggregates, they are less than desirable solvents because of their high costs, difficult processibility, and environmental risks. Recently, numerous experimental studies [38, 39, 40, 41] have shown the formation of RMs in supercritical alkanes and inert gases that offer numerous interesting advantages over the conventional industrial solvents. Supercritical solvents i.e. solvents above their critical temperature and pressure are unique in the sense that their properties, such as vis-

cosity, density, solvating power etc., can be easily varied from gas-like to the near liquid-like phase limits by simply changing the system pressure and/or temperature [42, 43]. This ability to control solvent properties offers novel control on surfactant aggregation in such systems.

In an effort to cut down toxic emissions and wastes and reduce processing costs, the chemical industry over the last few years has been aggressively seeking environmentally benign and low cost alternatives to conventional industrial solvents. Amongst the likely candidates, carbon dioxide (CO_2) is has received considerable attention because of its numerous attractive properties. Carbon dioxide is a non-polar compound that is a chemically inert (non-toxic, non-flammable) and environmentally safe alternative to potentially hazardous industrial solvents currently used. Also, its easy availability and low cost make it a cheap raw material. In addition, its relatively low critical constants ($T_c = 31\ ^oC$, $P_c = 73.8$ bar) allows its use as a supercritical solvent at reasonable industrial operating conditions. Formation of surfactant aggregates in CO_2 offers numerous possibilities of carrying out a wide range of industrial operations, such as emulsion polymerization, micro-particle and fiber formation, spray painting etc. in a medium with minimum emissions. Unfortunately, as shown by Consani and Smith [44], most of the industrially available surfactants are incapable of forming RMs in CO_2 because of their negligible solubility. This is attributed to the fact that most of these surfactants are suited for aqueous solvents while CO_2 is relatively non-polar (CO_2 has a weak quadrapole) because of its low polarizibility and dielectric constant. This has motivated numerous research efforts [45, 46, 47, 48, 49, 50, 51, 52, 53], over the last decade or so, to discover and/or design suitable surfactants. These surfactants are termed as "CO_2-philic" surfactants because they should exhibit favorable interactions with CO_2 to enable dispersion of the aggregates.

As mentioned earlier, molecular simulation techniques have significantly con-

tributed towards understanding the structure, dynamics, and rheology of aqueous surfactant systems and how these properties relate to surfactant self-assembly, micelles, amphiphilic monolayers and bilayers, and oil solubilization. Based on precisely defined molecular models of amphiphilic aggregates, these techniques provide a detailed quantitative description of the size, shape, surface roughness, and internal structure of these aggregates. These descriptions can help clarify interpretation of experimental results and establish the significance of assumptions made in theories devised for predicting those structures. In certain conditions where experiments are impractical or impossible (e.g. high temperatures and pressures), molecular simulation techniques can be successfully applied to obtain the much-needed information. The unique advantage of molecular simulation techniques lies in the fact that they provide a direct route from the microscopic details of the system (mass of atoms, intermolecular interaction potential, molecular geometry etc.) to the macroscopic properties of experimental and fundamental interest. With efficient algorithms and increased computational resources, the scope and capability of these techniques have increased significantly over the last few years and are projected to increase in future.

In this work, we have chosen to study the self-aggregation behavior of a dichain (or hybrid) surfactant [$(C_7F_{15})(C_7H_{15})CHSO_4^-Na^+$] and water in the presence of carbon dioxide as a non-polar solvent. As shown in Figure 1.3, the dichain surfactant molecule is characterized by the presence of two seven-carbon tails attached to an (anionic) sulfate head group. One of the tails is a *n*-perfluoroalkane tail, while the other is a *n*-alkane tail. The *n*-perfluoroalkane provides the necessary CO_2-philic behavior. This particular surfactant molecule was chosen for two main reasons. Firstly, in terms of the molecular complexity this is a relatively small molecule compared to other known CO_2-philic surfactant molecules. Thus, from a computational perspective, it is relatively easy to model this surfactant to a sufficient degree of detail and study

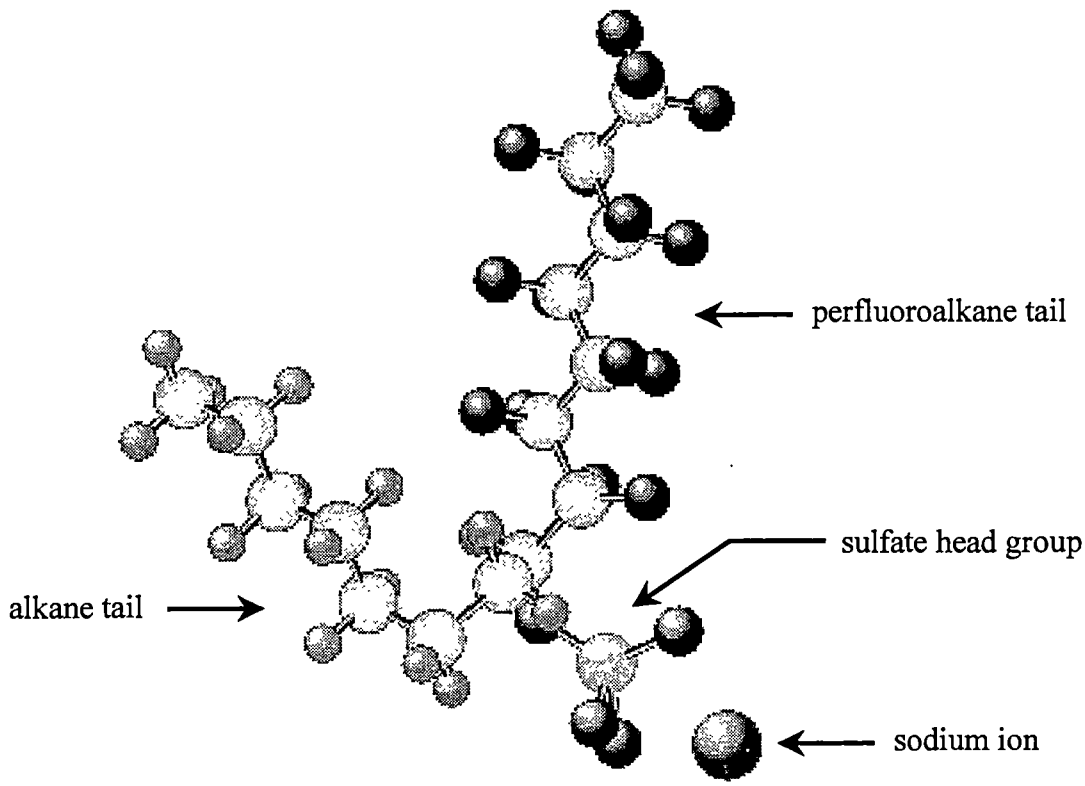


Figure 1.3: Molecular structure of the hybrid (dichain) surfactant molecule used in this simulation study. The surfactant has two distinct seven-member long tails, an alkane tail and a perfluoroalkane tail. Sulfate forms the anionic head group and sodium is the counter-ion.

the aggregation behavior for a relatively large system size. Secondly, the structural features of RMs formed in dichain surfactant + water + carbon dioxide ternary system were recently reported by Eastoe and co-workers [54] using small-angle neutron scattering (SANS). Thus, quantitative comparisons with their results can be made. It is expected that the results of this work will motivate further experimental or simulation investigations of surfactant aggregation in CO_2. The objectives of this work are to obtain a molecular level insight into the dynamics of aggregation in this system and to obtain structural properties of the aggregates formed. Effects of surfactant architecture, surfactant chemistry, and solvent properties on aggregation are studied. The ultimate objective would be to develop a much-needed knowledge base that will be helpful in designing new and improved CO_2-philic surfactants viable for industrial applications.

Chapter 2

Literature Review

As mentioned in the previous chapter, supercritical fluids (SCFs) are a desired solvent medium for the formation and stable existence of reversed micellar aggregates because of their many advantages (variable solvating power, high diffusivity, low density etc.) as a process fluid. Use of low molecular weight supercritical alkanes, such as ethane and propane as a solvent medium for supporting surfactant aggregates is quite well studied and extensively reported in literature [38, 39, 40]. These studies have not only demonstrated the feasibility of using supercritical solvents in surfactant solutions but also explained the thermodynamic behavior of such systems. For example, Smith and co-workers [39, 40] performed solubility, conductivity, and density measurements to characterize the effects of temperature and pressure on the phase behavior of AOT/water/supercritical ethane or propane ternary mixtures. AOT is a common commercially available surfactant that is quite similar to the dichain surfactant investigated in this work. The results of these studies indicated the formation of surfactant aggregates that have structural properties quite similar to those of a typical RM (Figure 1.2). Subsequent dynamic light scattering and spectroscopic probe studies [55] showed the effect of solvent density on the size and solubilization capacity of surfactant aggregates formed in the system.

2.1 Experiments

Over the last few years, supercritical carbon dioxide has received considerable attention for various industrial applications, including use as a non-polar solvent medium for solubilizing various polar or polymeric solutes. The early excitement concerning CO_2 as a viable solvent medium was due to its solubility parameter at pressures above 200 bar, which resembles those of normal alkanes. This implied that many of the conventional organic solvents could simply be replaced by CO_2. Consani and Smith [44] performed solubility studies of $\sim$ 130 industrially available surfactants in CO_2 and observed that most of the surfactant molecules tested were either completely insoluble or only very slightly soluble at temperatures and pressures up to 50 ^{o}C and 100 - 500 bar, respectively. Also, the partially soluble surfactants did not solubilize appreciable amounts of water. This clearly indicated the need to identify new surfactant molecules suitable for CO_2 applications. This was later explained by Johnston and co-workers [47] on the basis of the quadrupole moment of CO_2, which tends to inflate its solubility parameter by as much as 20 %, thereby making CO_2 an analogous solvent to normal alkanes. Interestingly, Consani and Smith [44] also observed that partially fluorinated and silicon-based surfactants showed higher solubility in CO_2 than other surfactants. Also, surfactants containing fluorine-carbon bonds invariably dissolved at much lower temperatures and pressures than their hydrogenated counterparts. These results clearly indicated the apparent compatibility between fluorinated hydrocarbons and CO_2 (known as CO_2-philicity). These solubility results attributed to the low polarizibility or electron donor capability of these compounds, since CO_2 also has a low polarizibility and is a weak Lewis acid.

Hoefling and co-workers [45] reported some of the first direct evidence of the formation of RMs in near-critical and supercritical CO_2 using surfactants such as flu-

orinated AOT analogues, fluoroalkyl and fluoroether carboxylate salts, and hydroxyaluminum surfactants. These surfactant molecules were designed on the premise that the hydrophobic tails of a CO_2-philic surfactant molecule should possess functional groups with low solubility parameters (silicones and fluoroethers) and low polarizibility (fluorinated alkanes) or which act as Lewis bases (tertiary amines). In essence, these model surfactants should exhibit favorable thermodynamic interactions with CO_2 to allow for the formation of CO_2 solutions with high surfactant concentrations at moderate temperatures and pressures. As expected, the phase behavior of these surfactant systems showed a considerably high solubility of all these surfactants in CO_2. Also, the surfactant systems showed the capability to solubilize thymol blue, a hydrophilic dye that is completely insoluble in pure CO_2 at pressures up to 10000 psi at 40 ^oC, thereby successfully demonstrating the feasibility of the formation of RMs in CO_2.

DeSimone et al. [50] observed that high molecular weight homopolymers of various fluorinated acrylic monomers are soluble in CO_2, up to $\sim$ 25 % (w/v) depending on the solution temperature and pressure. These exceedingly high solubilities facilitated the homopolymerization studies of 1,1 -dihydroperfluorooctyl acrylate (FOA) in CO_2 and synthesis of block copolymers of FOA with ethylene, styrene, butyl acrylate, and methyl methacrylate that are essentially insoluble in CO_2. The reaction kinetics revealed a high degree ($\sim$ 83 %) of initiator efficiency (homopolymerization of FOA is a free radical polymerization reaction with the overall rate of polymerization and the molecular weight of the resulting polymer depending strongly on the initiator efficiency) indicating the effectiveness of the polymerization reaction. Gel permeation chromatography (GPC) on the polymer made in CO_2 indicated a reasonably high molecular weight polymer product ($M_w \approx$ 270000 g/mol). FTIR and NMR spectroscopic analysis on the resulting polymer showed that the polymer synthesized in CO_2

had identical properties as that formed in CFC's, which is the conventional reaction medium for homopolymerization of FOA.

Johnston and co-workers [49] used low molecular weight perfluoropolyether (PFPE) carboxylate surfactant (M_w = 740 g/mol) to form RMs and microemulsions in CO_2. The PFPE surfactant molecule was chosen because of its reasonably high solubility in CO_2 at pressures below 300 bar. Moreover, the biological inertness of PFPE surfactant complements the non-toxic nature of CO_2. The cloud point data at 116 bar and 35 ^oC, indicated the presence of aggregated water domains in the system. The authors argued that this indicated the presence of surfactant aggregates (with the molar water to surfactant ratio of $\sim$ 10) in the system, since a single surfactant molecule would not be hydrated by so many water molecules. The FTIR spectroscopy, ultra-violet visible absorbence, fluorescence, and EPR experiments demonstrated the existence of an aqueous domain in CO_2 with a polarity approaching that of bulk-water. The solubilization study of a model protein (acrylodan-labeled BSA) indicated that the BSA-Ac present in these aqueous domains was quite similar to that observed in native BSA-Ac at a pH of 7. This implied that the conformation of BSA-Ac protein is unaltered when solubilized in the aqueous core of surfactant aggregates. Later, Heitz et al. [53] investigated the structural properties of PFPE based microemulsions using X-band EPR studies and time resolved anisotropy measurements. They observed that at a fixed temperature, increasing the CO_2 pressure increases the capacity for water intake, i.e. increases the size of the aggregates. To obtain information regarding micellar motion and polarity in the aqueous core, an EPR-active probe, 4-hydroxy-TEMPO (a nitroxide that is soluble in water but only sparingly soluble in CO_2) was used with PFPE ammonium carboxylate and $Mn(PFPE)_2$ surfactant. These studies showed the formation of non-spherical aggregates in the system.

McFann et al. [47] studied the feasibility of using non-ionic surfactants for the

formation of RMs in supercritical CO_2, since non-ionic surfactants are generally more soluble than ionic surfactants in non-polar solvents. They chose penta-ethylene-glycol *n*-octyl ether (C_8E_5), a polyethylene glycol, as the surfactant molecule because the partition coefficients of polyethylene glycols (PEG) in supercritical CO_2 indicated appreciable solubility of low molecular weight PEGs in CO_2. Also, the presence of five ethylene oxide groups in the surfactant molecule should be capable of solubilizing significant amounts of water. The results of the study showed that although C_8E_5 was quite soluble in CO_2 at normal experimental conditions, the tendency for self-aggregation was quite low. The observed aggregation number of surfactants was about four surfactants per aggregate. Further addition of water resulted in a phase separation, which was attributed to micelle-micelle interactions and subsequent coalescence. Addition of *n*-pentanol (co-surfactant) increased the water intake by about 2 - 5 fold but required a high concentration of co-surfactant in the system, thereby significantly altering the system composition. The FTIR spectra indicated that some of the water is associated with surfactant and co-surfactant, which is distinguishable from water in bulk CO_2. Dye solubilization and solvatochromic probe data showed significant changes near the phase boundary as the size and structure of the aggregates changes with system pressure.

In an effort to identify new CO_2-philic surfactants, Johnston et al. [51] studied the phase behavior of the dichain surfactant mixture (which is the subject of this simulation study) in CO_2 and water. They observed that this surfactant does not exhibit any aggregation in the absence of water, thereby implying that "dry" RMs are not formed in this system. The surfactant was found to be insoluble in CO_2 over a temperature range of 20 - 60 ^oC and pressure up to 345 bar for a concentration of $\sim$ 1.9 wt%. However, addition of a small amount of water ($\sim$ 0.48 wt%) caused the surfactant to be dissolve in CO_2, thereby indicating the formation of surfactant aggregates

Table 2.1: Structural properties of RMs of dichain surfactant observed by Eastoe et al. [54] in a SANS investigation ($T = 298K$). The uncertainties for R_{core} are $\pm$ 1 Å

P (bar)	$\rho_{solvent}$ (g/cc)	R_{core} (Å)
500	1.03	25.0
400	1.01	24.6
260	0.95	23.0
120	0.85	20.5

in the system. Thus, the driving force for aggregation was attributed to the hydrogen bonding property of the water. It was suggested that the water molecules formed hydrogen bonds with the sulfate head group of the surfactant molecule thereby resulting in surfactant aggregation. They observed up to $\sim$ 1.98 wt% water was soluble in the surfactant solution. This indicated the formation of micellar aggregates with significantly high water-to-surfactant molar ratio ($W_o \sim 32$). Subsequently, Eastoe et al. [54] performed small angle neutron scattering (SANS) studies on this ternary system to study the structural properties (size, shape, and size distribution) of the surfactant aggregates formed. The SANS results revealed the formation of spherical aggregates with a narrow size distribution. However, in contrast to the findings of Smith et al. [39, 40] for RMs in supercritical alkanes, Eastoe et al. [54] observed an increase in the size of aggregates with increase in pressure. Table 2.1 lists the experimental observations of Eastoe et al. [54] showing the pressure dependence of the aggregate size. They also observed a significantly higher ($\sim$ 140 Å^2) interfacial area per surfactant molecule, which is about a factor of two greater than that observed for AOT surfactants. Thus, the dichain surfactant does indeed show the formation of micellar aggregates in CO_2, with water being the necessary component for aggregation.

McClain et al. [48] performed a small angle neutron scattering (SANS) investigation of the self-assembly of polystyrene-b-poly(1,1-dihydroperfluorooctyl acrylate) (PS-b-PFOA) copolymers in supercritical CO_2 to study the morphology of surfactant aggregates formed and the ability of these aggregates in solubilizing CO_2-insoluble hydrocarbons in CO_2. The scattering data was fitted to a spherical "core plus shell" structural model based on a solid PS core surrounded by a uniform thickness shell containing PFOA chains swollen by solvent molecules. Based on this analysis, the aggregates formed had near spherical geometry. Increasing the solvent density resulted in the formation of smaller surfactant aggregates with low aggregation numbers. This was attributed to increased solvation of both segments (PS and PFOA) of the copolymer with the surrounding solvent. The solubilization capability of PS-b-PFOA micellar solution was demonstrated by addition of model hydrocarbon oligomers into the system. SANS characterization of the resulting solution showed stabilization of more than 99 % of added oligomers into the cores of the aggregates.

Fulton et al. [52] used small angle X-ray scattering (SAXS) measurements to characterize the aggregation of three different surfactants in CO_2. The three surfactant molecules included, a high M_w graft copolymer consisting PFOA backbone with PEO grafts, a semi-fluorinated nonionic surfactant [$F(CF_2)_{6-10}CH_2CH_2O(CH_2CH_2O)_{3-8}H$], and a semi-fluorinated alkane di-block molecule [$F(CF_2)_{10}(CH_2)_{10}H$]. The general strategy adopted for the synthesis of these compounds was to incorporate CO_2-philic segments in the desired surfactant molecules to enhance their solubility in CO_2. The PFOA-g-PEO surfactants formed RMs with a PEO rich core domain and were able to solubilize small amounts of water. A small decrease in pressure resulted in a small increase in the aggregate size due to an increase in the interfacial tension at lower pressures. The non-ionic surfactant completely dissolved in CO_2 at relatively high pressures at 65 ^oC. The system yielded a roughly bi-nodal distribution of larger mi-

celles in equilibrium with small oligomers including monomers, dimers, and trimer species. The semi-fluorinated di-block surfactant formed only small aggregates with no larger than about four monomers per aggregate.

2.2 Simulations

As mentioned earlier, over the last decade or so, molecular simulation techniques have played an increasingly important role in understanding the structural properties, dynamics and rheology of surfactant aggregates. Although most of these studies apply these techniques on aqueous micellar aggregates, these techniques can be equally useful in studying reversed micellar aggregates because the simulation strategy involved in these two types of surfactant aggregates are quite similar. Thus, a review of the various simulation studies of aqueous micellar aggregates is relevant to the present work.

2.2.1 Oil-in-water micelles

Haan and Pratt [14] reported the first molecular simulation study of micelle structure using a highly simplified molecular model for the surfactant molecule. Using the Monte Carlo (MC) technique on a simple lattice-based representation of a micelle with 20, 30, or 50 chain (surfactant) molecules, the authors attempted to study the microscopic structural characteristics of the surfactant aggregate. In their simplified model, each surfactant molecule consisted of a chain of atoms strung on a 3-d lattice. For each chain, one of the end groups was designated as the head group, while the remaining constituted the tail. All the remaining vacant lattice sites represented solvent molecules. The potential energy (U) of the system was simply estimated as a sum of the various interactions energies and given by the expression

$$U = \epsilon_{tt} n_{tt} + \epsilon_{hh} n_{hh} + \epsilon_{th} n_{th} + v_g g \tag{2.1}$$

where, $\epsilon_{\alpha\beta}$ and $v_g g$ are energy parameters, and $n_{\alpha\beta}$ denotes the total number of $\alpha - \beta$ group pairs which are nearest neighbors on the lattice. The parameters α, β can be h (head) or t (tails) while g is the total number of gauche bonds in the aggregate. The values of the energy parameters were fixed ($\epsilon_{tt} = -3k_bT$ for tail-tail attraction, $\epsilon_{hh} = 2k_bT$ for head-head repulsion, $\epsilon_{th} = 0$, and $v_g = -1.5k_bT$) to enable the formation of stable surfactant aggregates. Based on these parameters, the results indicated the formation of a rather loose and highly non-spherical aggregate with a non-zero probability of head groups at the center of the aggregate. Also, approximately half of the micellar surface was exposed to the surrounding solvent. Thus, the simplified surfactant model (Equation 2.1) does predict the formation of micellar aggregates but with properties quite different than those observed experimentally. However, the study showed that the relative mean-square length of the surfactant molecules in the aggregates is $\sim$ 3 % larger than those in an isolated surfactant molecule. This is in general agreement with prior experimental findings. Subsequently, Owenson and Pratt [15] extended this work further to investigate the effect of ϵ_{th} (head-tail interaction) on the morphology of the aggregate, and made comparisons between the structural properties of the surfactant aggregate and a liquid hydrocarbon droplet. The simulations revealed that the magnitude of ϵ_{th} had a negligible effect on the structural properties of the surfactant aggregates. This was attributed to the fact that strong tail-tail attraction forces essentially squeezed out the head groups to the outer surface of the micelle, and thus these head groups rarely encounter any interactions with the tail groups. Comparisons with the simulation of a liquid hydrocarbon droplet revealed a much sharper interface for the hydrocarbon droplet. This was attributed to two possible causes. Firstly, the micelle had head groups sticking out on the surface giving rise to fluctuations and thereby resulting in a less sharper interface. Secondly, the restoring force for surface fluctuations were expected to be much smaller for the

micelle, since the chains are more ordered near the surface of the micelle than near the surface of the liquid droplet.

Haile and O'Connell [16] reported the first MD simulation study of a model micelle to investigate the internal structure of surfactant aggregates. Their model micelle consisted of skeletal alkane chains, each composed of 13 soft spheres mimicking a dodecyl surfactant. The intermolecular forces were accounted by the 6-9 Lennard-Jones (LJ) pair potential, while the intra-molecular interactions included harmonic potentials for bond vibration and bond bending. The model micelle was a constrained aggregate in the sense that the surfactants were enclosed within a spherical shell with their head groups fixed at points within segments of equal areas distributed over the spherical surface. The aqueous solvent medium around the aggregate was modeled as a continuum by a r^{-12} repulsive spherical potential surrounding the aggregate. Thus, the methylene functional groups of the surfactant molecules experience strong solvaphobic repulsion thereby forcing them to lie within the aggregate. Since the head groups were fixed, no explicit head-head and head-solvent interactions were used. The results of the simulation indicated that only a very small fraction ($\sim$ 2 %) of chains were in an all-trans (fully extended) conformation, and even those were not aligned along the radial direction, in disagreement with some prior experimental studies. Also, the tail conformation revealed an average of $\sim$ 29 % gauche conformation at equilibrium which was slightly lower than in *vacuovalue* ($\sim$ 34 %) indicating straightening of chains in surfactant aggregates. In the following paper, O'Connell and co-workers [17] modified the model of the micelle by relaxing the fixed constraint on the head groups and including explicit head-head and head-solvent interactions. Thus, the head groups were free to skate on a spherical shell representing the micelle surface. The head-solvent interaction was modeled by a harmonic potential acting normal to the surface of the shell to which the head groups were attached while the head-head

interactions were modeled by a purely repulsive potential that included contribution from dipole-like repulsion and excluded volume effects. The head-head repulsion was given by the expression

$$U_{hh} = \epsilon_{hh}(r^{-3} + r^{-12}) \tag{2.2}$$

where r is the distance (in reduced units) between the head group and the surrounding spherical shell. The results of this simulation showed that relaxing the constraint of fixed head groups does not significantly alter the overall structural characteristics of the model micelle. Although the micelle with unconstrained head groups promotes the de-localization of two or three tail groups nearest to the head group, other characteristics such as the distribution of other tail groups, the overall density, and the gauche bond distribution were only marginally affected. Also, no preferential locations of the gauche bonds on the surfactant tails were observed. In a further extension of this study, Karaborni and O'Connell [18, 19, 20] performed a series of MD simulations of the model micelle described earlier [17], to study the effect of tail length, head group size, and micelle-solvent interactions on the micelle shape, core density, and tail conformation within the aggregate. In their first paper [18] they studied two different model octyl surfactants, viz. surfactants with "polar methyl" heads, and surfactants with nonionic sulfate head groups, to investigate the effect of head group size on micellar structure. Two different potential models for chain-solvent (cs) interactions used in this study were given by

$$U_{cs} = \begin{cases} (r_{cs} - r)^{-12} & r \leq r_{cs} \\ \infty & r > r_{cs} \end{cases} \tag{2.3}$$

$$U_{cs} = \frac{\kappa}{[1 + \rho\,(r/r_{cs})^{\tau}]} \tag{2.4}$$

where κ is the height of the energy barrier on the hydrocarbon chains and is of the same value as the energy of solubilization of the hydrocarbon segment in water.

Equation 2.3 represents the solvent as an impenetrable continuum while Equation 2.4 models the solvent more realistically as a penetrable continuum, in which the tail groups can dissolve once they overcome a finite energy barrier. Similarly, for the head-solvent (hs) interaction also both harmonic and finite energy potentials were used

$$U_{hs} = \gamma(r_{hs} - r)^2 \tag{2.5}$$

$$U_{hs} = \begin{cases} \frac{\beta}{[1+\rho(2-r/r_{hs})^\tau]} & r < 2r_{hs} \\ 0 & r \geq 2r_{hs} \end{cases} \tag{2.6}$$

where γ controls the interfacial thickness by constraining the head groups, and β represents the height of the finite energy barrier for the dissolution of head groups in the hydrophobic core. The authors also performed a hydrocarbon droplet simulation for comparison of the hydrocarbon core density. The results showed that the hydrocarbon distribution within the micelle core was essentially the same as that in the hydrocarbon droplet. The hydrocarbon distribution for the case of finite barrier potential for chain-solvent interaction (Equation 2.4) and for the head-solvent interactions (Equation 2.6) were found to be in excellent agreement with other simulation studies. The average position of the segments in the micelle was found to be independent of the head group size and the chain length. The overall shape of the micelle was found to be slightly non-spherical. In their subsequent papers [19, 20], the authors investigated the effect of tail length on aggregate structure. The results showed that the microscopic structure of the micelle is largely unaffected by the tail length. However, considerable influence on the micellar shape was observed.

Smit et al. [21, 22] performed a series of MD simulation studies of oil + water + surfactant system to study the structural characteristics of the surfactant system. The authors modeled all the three components present in the system by two kinds of particles viz. o (oil) and w (water). Each oil molecule was represented by a single

o particle, while a single w particle represented each water molecule. The surfactant molecule was a chain of two w particles (hydrophilic part) followed by five o particles (hydrophobic part), each bound to its neighbor by a harmonic potential. The intermolecular potential between all the particles was represented via a 12-6 LJ interaction potential. The $o - w$ interaction was truncated at $2^{1/6}\sigma$ and shifted to make these interactions completely repulsive. The simulation results showed that the many surfactant molecules were preferentially adsorbed at the oil-water interface as a monolayer. In the water-rich phase, formation of o/w micelles was observed, while some aggregation was noticeable in the oil-rich phase also. However, no discernable reversed micellar aggregates were observed. An interesting result of these simulations was the prediction of a surfactant depletion layer in the water-rich phase next to the monolayer. As the name suggests, this depletion layer was characterized by the absence of surfactant molecules in this layer. This was attributed to the solvation forces that resulted in the short-ranged repulsion between the micelles and the surfactant monolayer in the water-rich phase. In another study [23] with the same molecular model for the surfactant molecule, Smit and co-workers studied the dynamics of surfactant self-assembly. The equilibrium micellar size distribution of the surfactant system was in excellent agreement with prior experimental predictions. The authors also successfully quantified various dynamic processes such as, monomer assimilation into a micelle, fusion of small micelles to form larger micelles, and break-up of large unstable aggregates. Using a similar model for the surfactant molecule, Karaborni et al. [24] studied the solubilization of oil in aqueous surfactant solutions. The authors observed spontaneous transfer of oil molecules from an oil-rich phase to the micelle-rich phase. The results also indicated that molecules with smaller molecular volumes were preferentially solubilized by micellar aggregates, given identical flexibility and polarity of molecules.

Karaborni and co-workers [25] also studied the self-assembly of gemini (dimeric) surfactant molecules in aqueous solvent using a surfactant model quite similar to the one used earlier by Smit et al. [23]. A gemini surfactant molecule essentially consists of two surfactant molecules connected via a hydrophobic spacer between the head groups. The length of the spacer can be as long as the tails of the surfactant molecules. The simulation results revealed that at low surfactant concentrations, gemini surfactants with single spacer formed linear thread-like micelles, while surfactants with two or more spacers formed a mixture of spheroids and tree-like micelles. The formation of a specific aggregate shape for a certain gemini surfactant depended on the equilibrium separation between head groups due to repulsion, the degree of hydrophobicity of the spacer, and the flexibility of the spacer.

Some recent molecular simulation studies of oil-in-water micelles have used realistic, detailed models for the surfactant molecule. To study the effect of specific tail chemistry, Jonsson et al. [27] performed MD simulation of a model sodium octanoate micelle in aqueous solution using explicit representation of the solvent molecules. The intermolecular interactions included the 12-6 Lennard-Jones potential for non-bonded interactions and Coulombic interactions between partial charges for electrostatic interactions. Intra-molecular interactions included bond stretching, bond angle vibration, and torsional angle potentials. Water (solvent) molecules were modeled using the Simple Point Charge (SPC) model [56]. Two different sets of interaction potentials, a full charge (FC) model and a reduced charge (RC) model for the surfactant molecule were investigated, since it was believed that SPC water model was inadequate in screening the ionic interactions between the surfactant molecules. Interestingly, the simulation results were found to be quite sensitive to the choice of the interaction potential. The FC model resulted in a loosely organized, highly non-spherical micelle with considerable water penetration into the core, while the RC model resulted in a

more compact and nearly spherical aggregate. However, both FC and RC models gave relatively broad radial distribution for the carboxyl carbon (head group) indicating a rough micellar surface (large surface fluctuations). Also, the dynamics of the water molecules close to the micellar surface revealed a water structure quite similar to bulk water. Using the similar potential model for the surfactant molecules, Watanabe and co-workers [26] also performed MD simulation of a sodium octanoate micelle using explicit water molecules. The differences between this work and that of Jonsson et al. [27], was a different torsional potential for the surfactant tail, and use of Ewald summation for evaluation of long-range electrostatic interactions (Jonsson et al. used simple truncation of Coulombic interactions after a distance of 10 Å). The results of this study also showed a highly diffuse and non-spherical micellar structure. However, the simulations revealed the formation of an ionic micelle with a net charge of $-8.7e$, in close agreement with previous neutron scattering studies.

Shelley and co-workers [28] also performed MD simulation study of aqueous sodium octanoate micelle, but with a polarizable model (POL) for the surfactant molecule. This particular surfactant model was based on a scheme initially developed to study water and ionic solutions using an extended Lagrangian technique. In this approach, additional charge sites are added to the desired molecule and the magnitudes of these charges are treated as classical dynamical variables, which evolve in response to the local electric field. Thus, the value of polarization at any given instant is determined from regular second order equations of motion derived from the extended Lagrangian. In essence, in the POL model the basic structure of the octanoate anion was not changed except that each atom (or pseudoatom) was provided with a polarizable center. The SPC/E potential model [57] was used to represent the water molecules. Other potentials were similar to the simulation studies of Watanabe et al. [26]. The results of this study showed that switching from a non-polarizable surfactant model

to the POL model resulted in the dissociation of all contact ion pairs between the Na^+ counter-ion and the head group, in agreement with experimental data. However, the overall character of the micellar aggregate, its geometry, and the dynamics of the monomers was relatively unaffected by the inclusion of the induction sites.

2.2.2 Water-in-oil micelles

Brown and Clarke [58] reported the first MD simulation of a water-containing model reversed micelle in a non-polar solvent (mimicking *n*-octane). The system consisted of 36 surfactant, 792 water and 1079 solvent molecules contained in a spherical cavity. The environment outside the spherical cavity represented the solvent continuum. The surfactant molecule consisted of two LJ interaction sites attached to each other via a harmonic bond, one representing the cationic head group and the other representing the hydrophobic tail. The SPC model [56] was used to represent the water molecules, and single site LJ interaction centers were used to model the non-polar solvent molecules. Since no periodic boundary conditions were used, the mean field potential representing the interactions of different molecules with static solvent molecules outside the spherical cavity, was given by

$$\Phi = \frac{3^{\frac{3}{2}}}{2}\epsilon_{iw}\left[\left(\frac{\sigma_{iw}}{r_{iw}+\Delta r_{iw}}\right)^9 - \left(\frac{\sigma_{iw}}{r_{iw}+\Delta r_{iw}}\right)^3\right] \tag{2.7}$$

where r_{iw} is the distance of a particular molecule of species from the wall of radius . The results of the simulation showed that although the solvent showed liquid-like behavior, the micelle components showed very little diffusion. Not only did the whole micelle exhibited very low diffusion as a whole, there was little mobility within the micelle itself. The energetics of the system showed that the dominant contribution to the binding energy of micelle assembly was due to ion-ion interactions. Anion hydration provided the remaining substantial contribution. The structural properties of the RM showed an extensive overlap between the water and tail distributions,

implying considerable penetration of water molecules into the hydrophobic region of the micelle. The similar profiles of the anions and head group imply a high degree of ion pairing. The mean shape and fluctuations showed a non-spherical aggregate with substantial surface roughness. However, despite surface roughness the surfactant molecules in the interface had a high degree of orientation along the aggregate radius. The authors also observed specific orientation of the water molecules in the "hydrophobic region" of the aggregate (region near the solvent continuum). This was due to the characteristic bonding structure of the water molecules at the extremities of the micelle with the water directly hydrogen bonded to the ionic species.

Linse [59] performed a molecular dynamics study of the aqueous core of a reversed ionic micelle to investigate the nature of the aqueous core. The system consisted of sodium ions and water molecules, spherically enclosed by a hydrophobic interface carrying carboxylate head groups. The interactions among water molecules, sodium ions, and carboxylate oxygens were evaluated explicitly assuming pairwise additivity. The radial distribution functions for sodium ions showed a high degree of counter-ion association close to the charged surface of the system, quite similar to the surface charge densities shown by experiments. The radial distribution of water molecules showed rather uniform distribution of water, with slight oscillations near the charged surface. The water dipoles were strongly ordered by the presence of ions and the hydrogen-bonded network was partially broken.

In the only prior study of RM using realistic and detailed models, Tobias and Klein [60] performed a MD simulation of calcium carbonate/calcium sulfonate reversed micelle in non-polar solvents (carbon tetrachloride, octane, and vacuum). The potential model of the surfactant consisted of intra- and intermolecular van der Waals and Coulombic interaction. Harmonic bond stretching, bond angle bending, and dihedral angle potentials were used for intra-molecular interactions. The parameter

values used in the simulation were from the CHARMM PARAM19 parameter set. Water molecules were modeled via SPC/E model of Berendsen et al. [57]. The average structure of the reverse micelle was nearly spherical with a large degree of ionic core exposed to the solvent, except for case with vacuum. In vacuum, the surfactant hydrocarbon chains had collapsed onto the surface of the core, greatly reducing its exposure. The radial density profiles of water revealed that the structure of water in the core is largely unaffected by the non-polar solvent. The structure of the solvent shows significant ordering, especially close to the surface of the reverse micelle.

Chapter 3

Molecular Models

The general approach used in most of the prior simulation studies [16, 17, 18, 19, 20, 21, 22, 23] of micellar aggregates is to use a highly simplified and coarse-grained bead-spring model for the surfactant molecule. In the bead-spring model, the surfactant molecule essentially consists of oil-like and water-like particles attached via harmonic springs. Depending on the nature of intermolecular interactions, the interactions were mimicked by simply truncating the potential at varying distances. For instance, Smit and co-workers [21, 22, 23] used Lennard-Jones (LJ) interaction potential with $R_c = 2.5\sigma$ for attractive interactions, while $R_c = 2^{1/6}\sigma$ for purely repulsive interactions. Further simplifications of the simulation system involved lattice based simulations [29, 30] or a constrained aggregate [16, 17, 18, 19, 20] where the solvent is not modeled explicitly but instead represented by a spherical potential around the aggregate. Since the dominant interactions in o/w micellar aggregates are short-ranged hydrophobic interactions, the bead-spring model described above may be suitable to adequately represent these interactions. In contrast, the interactions responsible for holding the surfactant molecules together in a non-polar solvent are primarily long-ranged electrostatic interactions. Although these interactions can be represented by adding partial charges to the bead-spring model, some degree of detail and realism is desirable in the surfactant model for such systems to accurately represent all the

intermolecular interactions of an actual surfactant molecule. Since the objective of the present work is to make quantitative comparisons with the experimental work of Eastoe et al. [54], an attempt has been made to use a detailed molecular model for the dichain surfactant molecule. The simulations presented in this work involve detailed and realistic molecular models for all the three chemical species (dichain surfactant, water, and carbon dioxide) present in the system. Although, this makes the system computationally complex and demanding, it minimizes any artificiality that might be included in the system and affect the dynamics of surfactant aggregation and/or the morphology of the aggregates formed. With these factors in consideration, the potential model for the hybrid surfactant molecule used in this simulation study was constructed by assembling existing potential models for each of the four functionally distinct parts of the molecule i.e. the alkane tail, perfluoroalkane tail, sulfate head group, and the sodium counter-ion. This allows the surfactant model to capture most of the essential characteristics of the real dichain surfactant molecule (Figure 1.3).

3.1 Alkane tail

The potential model for the alkane tail of the surfactant molecule is the united atom model for alkanes proposed by Siepmann and co-workers [61] (SKS model). This model accurately predicts the vapor-liquid phase envelope of n-alkanes that agrees well with the experimentally reported values. More importantly, the SKS model predicts the solubility of n-alkanes in CO_2 that is also consistent with experimentally determined values [62]. In this potential model, each of the methylene (CH_2) and methyl (CH_3) functional group is represented as a single spherical interaction site (united atom) with its interaction center located at the center of the carbon atom. The interaction sites are connected via rigid bonds of length 1.54 Å. Interaction sites

on different surfactant molecules and those on the same molecule separated by more than three bonds interact via the well known 12-6 Lennard-Jones (LJ) potential given by

$$U_{LJ}(r_{ij}) = 4\epsilon_{ij}\left[\left(\frac{\sigma_{ij}}{r_{ij}}\right)^{12} - \left(\frac{\sigma_{ij}}{r_{ij}}\right)^{6}\right] \tag{3.1}$$

where ϵ_{ij} is the well depth and σ_{ij} is the zero point of the potential between site i and site j, as shown in Figure 3.1. The LJ size parameters for the methyl and methylene functional groups are same ($\sigma_{CH_3} = \sigma_{CH_2} = 3.93$ Å) while the well-depth energy parameters are $\epsilon_{CH_3}/k = 114K$ and $\epsilon_{CH_2}/k = 47K$, respectively. The intramolecular interactions include the bond-angle bending potential to account for the bond vibrational motion, and torsional angle potential to account for the spatial orientation of the tails. The bond angle bending potential is described by a harmonic function of the form

$$U_{bending}(\theta_i) = \frac{1}{2}k_\theta(\theta_i - \theta_{eq})^2 \tag{3.2}$$

where θ_{eq} is the equilibrium angle between successive bonds and k_θ is the force constant and is a measure of the rigidity of the bond angle. The torsional angle potential for the alkane tail is given by [63]

$$U_{torsion}(\phi) = \sum_{i=0}^{3} a_i cos(i\phi) \tag{3.3}$$

where ϕ is the torsional angle that is defined as the angle between the normal to the two planes, each of which is formed by three successive interaction sites.

3.2 Perfluoroalkane tail

The potential model for the perfluoroalkane tail used in this study is that proposed by Cui et al. [64] and is quite similar to that of the alkane tail described above.

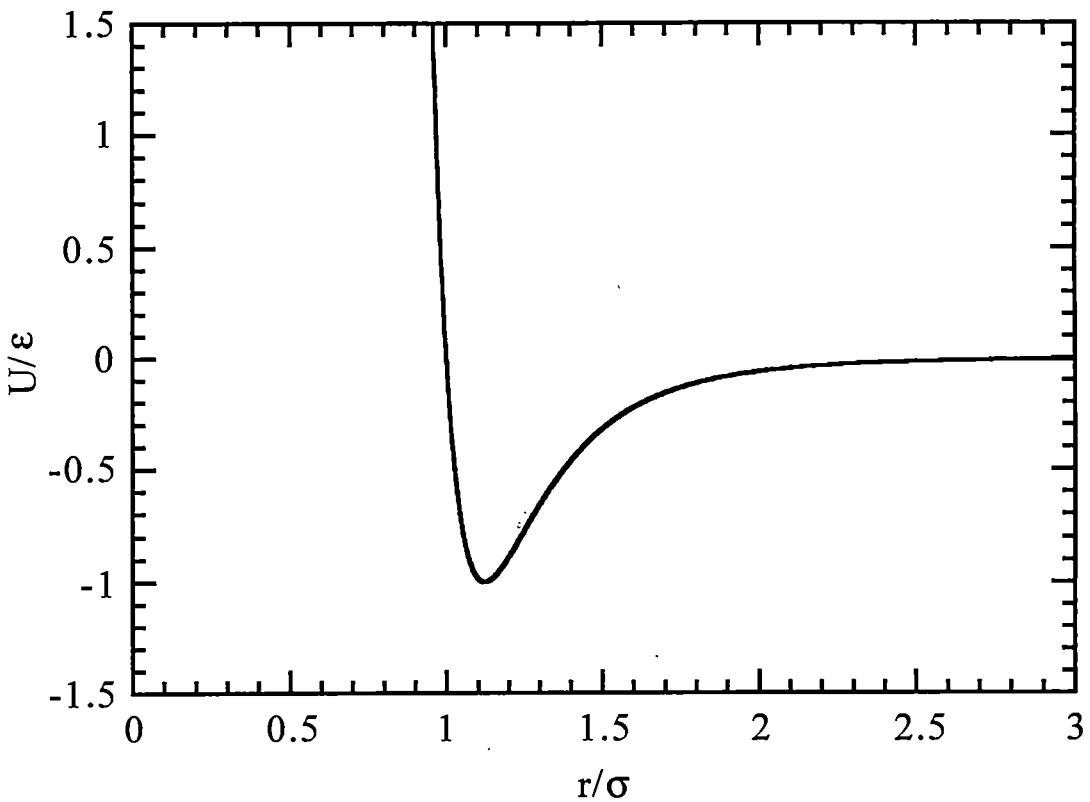


Figure 3.1: Lennard-Jones (LJ) potential for the non-bonded intra-molecular and intermolecular interactions.

This model was chosen because it is fitted to the vapor-liquid phase envelope of *n*-perfluroralkanes and also does good *de novo* prediction of pefluoroalkane/CO_2 phase equilibrium [62]. United atoms with effective LJ well-depth and size parameters are used to represent the CF_2 and CF_3 functional groups of the tail ($\sigma_{CF_3} = \sigma_{CF_2} = 4.6$ Å, $\epsilon_{CF_3}/k = 79K$, $\epsilon_{CF_2}/k = 30K$). The bond length between the united atoms is assumed fixed at 1.54 Å. The non-bonded interactions are described via a 12-6 LJ potential (Equation 3.1) while the bond-angle bending and torsional angle potential account for the intra-molecular interactions. The bond angle potential is similar to that of the alkane tail (Equation 3.2) with the only difference being the slightly larger (114.6^o) equilibrium bond angle. The torsional angle potential for the perfluoroalkane tail is given by

$$U_{torsion}(\phi) = a_0 + \sum_{i=1}^{7} a_i (cos\phi)^i \tag{3.4}$$

where ϕ is the dihedral angle. The important features of the torsional potential for perfluoroalkane are that it has a twisted trans minimum at an approximate dihedral angle of 17^o, a gauche minimum at $\sim$ 125^o and a second gauche minimum at around at around $\sim$ 83^o. Figure 3.2 shows the torsional potentials for the two tail groups. The important differences between the potentials for the two tails is the presence of trans conformation at non-zero dihedral angle for the perfluoroalkane tail. Also, there are two gauche minima for perfluoroalkane tail compared to just one for the alkane tail. Table 3.1 summarizes the potential parameters for the two tails groups.

3.3 Sulfate head group and sodium counter-ion

The potential model for the sulfate head group of the surfactant molecule is a fully atomistic (each interaction site represents an individual atom) model proposed by Cannon and co-workers [65]. Figure 3.3 shows the geometry of model of the sulfate

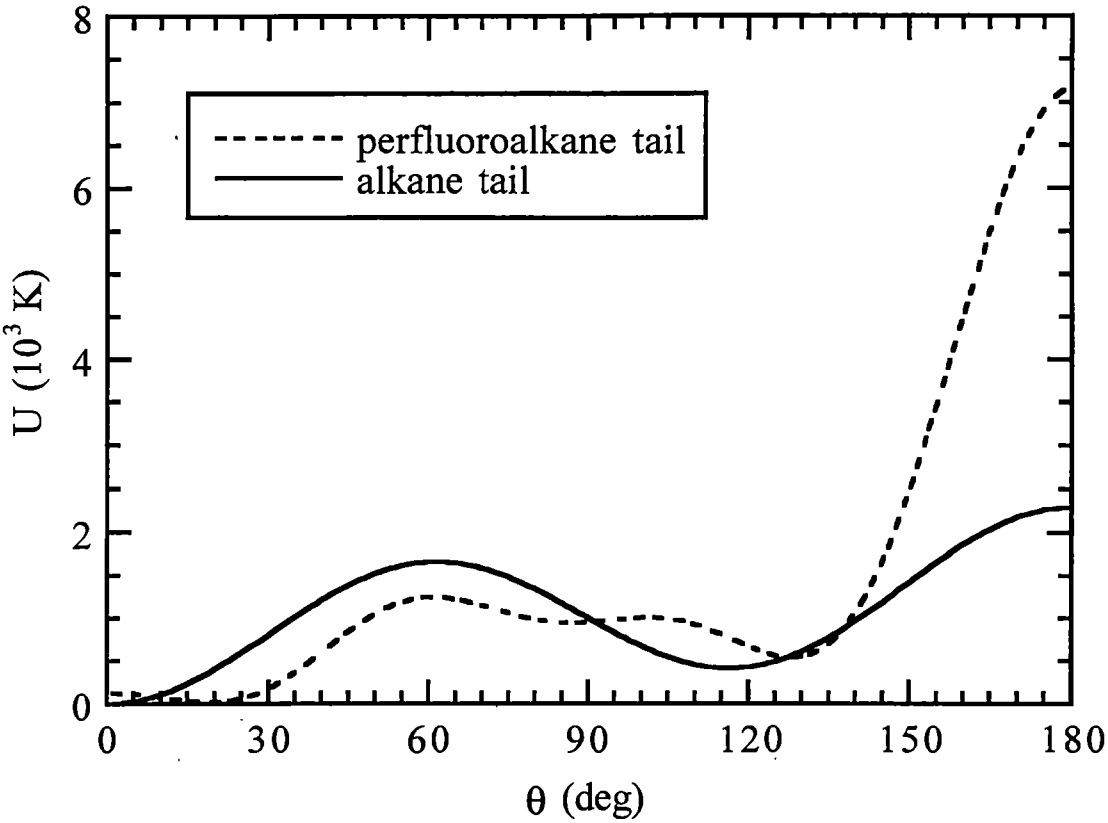


Figure 3.2: Torsional potential for the alkane and the perfluoroalkane tail of the dichain surfactant molecule.

Table 3.1: Potential parameters for the intra-molecular and inter-molecular interactions for the alkane tail and perfluoroalkane tail

Type of interaction	Alkane tail	Perfluoroalkane tail
LJ interaction	$\sigma_{CH_3} = \sigma_{CH_2} = 3.93$ Å	$\sigma_{CF_3} = \sigma_{CF_2} = 4.6$ Å
	$\epsilon_{CH_3}/k = 114K$	$\epsilon_{CF_3}/k = 79K$
	$\epsilon_{CH_2}/k = 47K$	$\epsilon_{CH_2}/k = 30K$
Bond bending	$k_b = 62500K/rad^2$	$k_b = 62500K/rad^2$
	$\theta_{eq} = 114.0^o$	$\theta_{eq} = 114.6^o$
Torsional	$a_0 = 1078.16K$	$a_0 = 959.4K$
	$a_1 = 355.03K$	$a_1 = -282.7K$
	$a_2 = -68.19K$	$a_2 = 1355.2K$
	$a_3 = 791.32K$	$a_3 = 6800.0K$
		$a_3 = -7875.3K$
		$a_3 = -14168.0K$
		$a_3 = 9213.7K$
		$a_3 = 4123.7K$

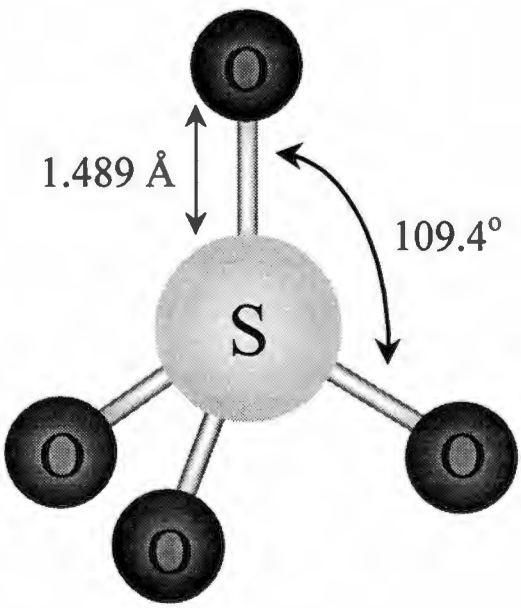


Figure 3.3: Molecular geometry of the sulfate head group.

Table 3.2: Potential parameters for the sulfur and oxygen atoms of the head group and the sodium ion

Atom type	σ (Å)	ϵ/k (K)	q (e)
sulfur	3.55	126	+2
oxygen	3.15	126	-1
sodium	2.667	37.65	+1

head group used in this study. It has a rigid tetrahedral structure (O-S-O bond angle of 109.4°) with the sulfur atom at the axis and the oxygen atoms at the four apexes. The bond between sulfur and oxygen atoms is fixed at 1.489 Å. To account for electrostatic interactions, the sulfur atom carries a charge of $+2e$ while three oxygen atoms carry a charge of $-1e$. The fourth oxygen atom does not carry any negative charge as it is attached to the CH group, which in turn is attached to the two tails. A sum of Coulombic (for electrostatic interactions) and LJ terms describes the intermolecular interactions

$$U(r_{ij}) = \sum_i \sum_j \frac{q_i q_j}{r_{ij}} + 4\epsilon_{ij}\left[\left(\frac{\sigma_{ij}}{r_{ij}}\right)^{12} - \left(\frac{\sigma_{ij}}{r_{ij}}\right)^{6}\right] \tag{3.5}$$

where q represents the Coulombic charge on the atoms, A_{ij} and C_{ij} are the constants for the LJ interaction and are functions of ϵ_{ij} and σ_{ij}. A single LJ sphere with a unit positive charge represents each sodium ion. Table 3.2 lists the potential parameters for sulfur and oxygen atoms and sodium ion used in this study. Figure 3.4 shows the schematic of the complete molecular model for the dichain surfactant molecule assembled by combining all the potential models described above. According to this molecular model, each surfactant molecule consists of 21 interaction sites including one for the Na^+ ion.

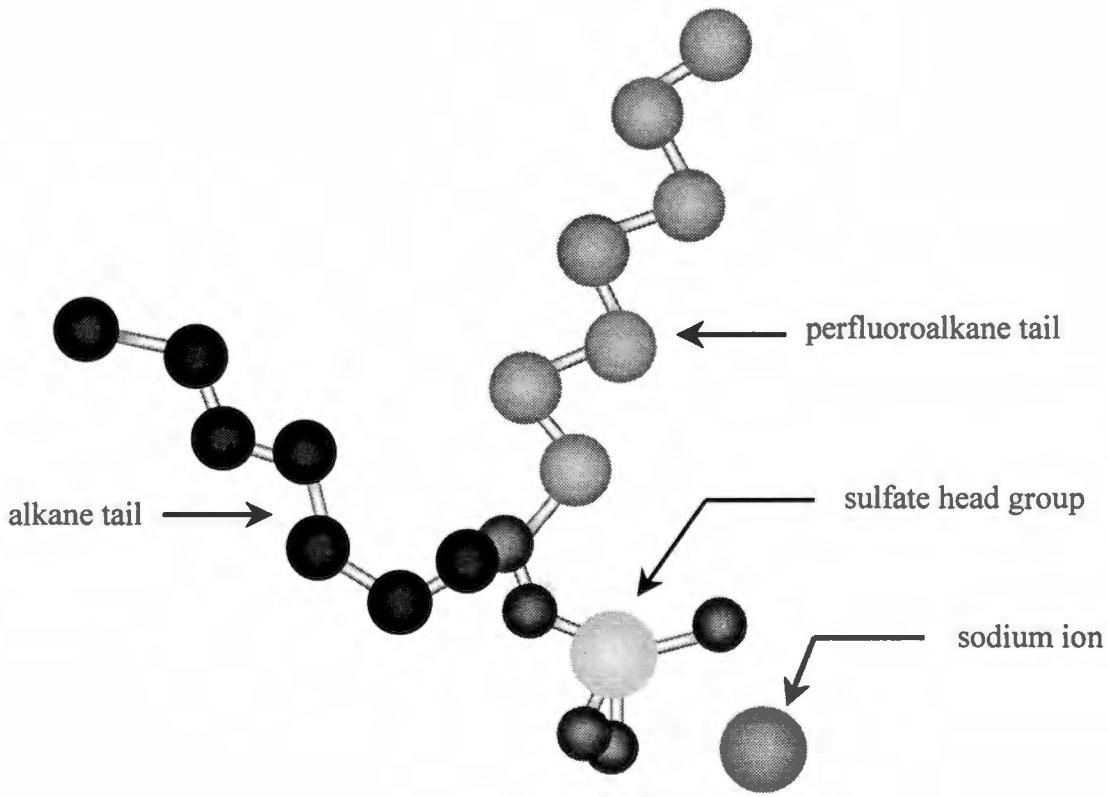


Figure 3.4: Molecular model for the dichain surfactant molecule used in this study.

3.4 Carbon dioxide

The carbon dioxide (solvent) molecules are represented by a simple site-based potential model proposed by Harris and Yung [66], that has been shown to accurately reproduce the experimental vapor-liquid co-existence curve and critical point of pure CO_2. As shown in Figure 3.5, the model consists of three LJ interaction sites with a Coulombic charge centered on each atom. The molecule has a rigid linear (O-C-O bond angle = 180°) geometry with the C-O bond length of 1.149 Å. The carbon atom carries a charge of $+0.6512e$ while the two oxygen atoms carry a charge of $-0.3256e$ each to make the molecule electrically neutral. Table 3.3 lists the potential parameters of the potential model.

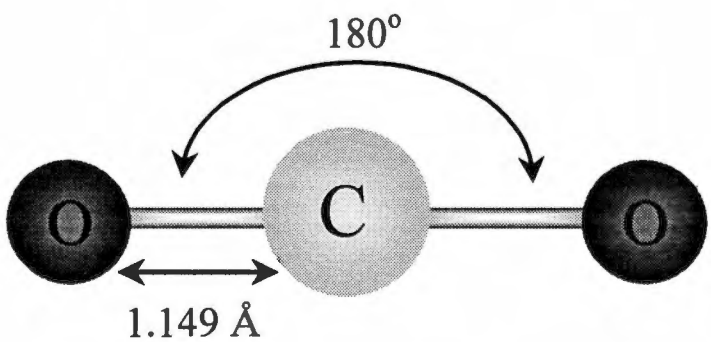


Figure 3.5: Molecular model for the carbon dioxide molecule.

Table 3.3: Potential parameters for the carbon dioxide potential model

Atom type	σ (Å)	ϵ/k (K)	q (e)
carbon	2.757	28.129	+0.6512
oxygen	3.033	80.507	-0.3256

3.5 Water

For water molecules, the extended simple point charge (SPC/E) potential model of Berendsen et al. [57] is used in this study. The model has a single LJ site for the oxygen atom that also carries a charge of $-0.8476e$. The two hydrogen atoms are simply represented by point charges, each carrying a charge of $-0.4238e$. Rigid molecular geometry is assumed with the O-H bond length of unity and H-O-H bond angle equal to the tetrahedral angle (109.4^o). Figure 3.6 shows the schematic of the SPC/E model. Table 3.4 lists the potential parameters for this model.

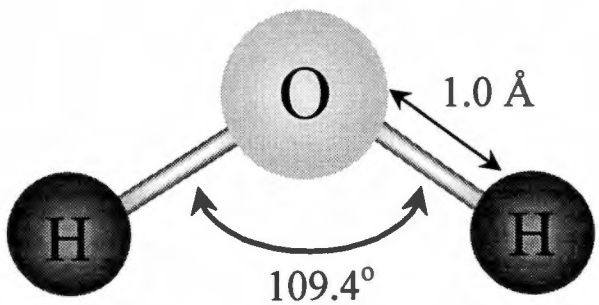


Figure 3.6: Molecular geometry of the water molecule.

Table 3.4: Potential parameters for the SPC/E potential model for water

Atom type	σ (Å)	ϵ/k (K)	q (e)
hydrogen	0.0	0.0	+0.4238
oxygen	3.166	78.23	-0.8476

Chapter 4

Methodology

The two simulation techniques that have been used for investigating surfactant systems are Molecular Dynamics (MD) and Monte Carlo (MC). Although both of these techniques take the intermolecular potentials as the input and provide structural and thermodynamic properties as output, the MD technique also allows one to investigate the dynamic behavior as well. Thus, the MD technique has been chosen for this work. As the name suggests, the MD simulation technique is based on tracking the system trajectory through the phase space from a single initial starting phase point. The method involves numerical solution of Newtonian equations of motion for all the particles (interaction sites) present in the system. The results are then estimated by sampling equilibrium (or non-equilibrium) averages that are tied to the natural time evolution of the interacting particles.

Based on the molecular models of the surfactant molecule used in this study, complete interactions between various sites require calculation of LJ and Coulombic interactions. The LJ interactions can be calculated in a straightforward manner, since they are short-ranged and thus the interactions can be simply truncated at a distance of few angstroms from the reference interaction site. However, Coulombic interactions are long-ranged and thus require special treatment for accurate estimation. In this study, the site-site reaction field method [67, 68] is used to account for

Coulombic interactions. This method was chosen for its relative simplicity in implementation and low computational requirement. The method essentially involves splitting the electrostatic interactions experienced by a reference particle into a direct and an indirect contribution. The direct contribution is due to other particles within a spherical cavity centered at the reference particle, while the indirect contribution is due to the surrounding continuum that is polarized by the spherical cavity and in turn produces an addition electric field in the cavity. This additional electric field is called the reaction field. Thus, the total electrostatic energy (U_E) acting on a particle is given by

$$U_E = U_D + U_R \tag{4.1}$$

where, U_D is the direct contribution and U_R is the contribution due to the reaction field. The details of this method are provided in Appendix A.

4.1 System composition

The simulations performed in this work can be broadly divided into two main categories based on the size of the system studied:

- Small system
- Large system

The small system, as the name suggests, is a reasonably small system ($\sim$ 8300 total interaction sites) and was initially chosen for exploratory calculations. The molar ratio of surfactant to water molecules used in the small system was essentially governed by computational simplicity. On the other hand, the large system ($\sim$ 42000 total interaction sites) corresponds to the size of a single "average-sized" reversed micellar aggregate at the overall composition studied by Eastoe et al. [54] via neutron

scattering. The difference in the composition of the two systems, as described in the following sub-sections, reflects the effect of factors such as, surfactant concentration, water-to-surfactant molar ratio, and solvent properties on surfactant aggregation.

4.1.1 Small System

The small system consists of 30 dichain surfactant, 132 water, and 2452 carbon dioxide molecules within a cubic simulation box of length 71.8 Å. Thus based on the molecular models of the three chemical species present described in the previous chapter, this system consists of 8382 interaction sites. As mentioned before, the concentration of the dichain surfactant (0.135 mol/liter) and water (0.594 mol/liter) molecules used in this system do not correspond to any particular experimental system but were chosen simply to limit the size of the simulations for exploratory calculations. Since the critical micelle concentration of most surfactants that form RMs lies in the range of 10^{-3} to 10^{-5} mol/liter [31], the few orders of magnitude higher concentration of surfactants in this simulation study apparently manifests itself primarily in the increased rate of aggregation, as discussed in Section 5.2. The structural properties of the aggregates and their aggregation number are predominantly determined by the architecture of surfactant molecule and water-to-surfactant ratio, and thus should be largely unaffected by high surfactant concentration in this system. Also, the relatively high concentration of surfactant and water molecules in this system could result in bulk-phase separation instead of forming micellar aggregates. This aspect is addressed in Section 5.1 of the following chapter. To limit the system size as small as possible, a relatively low water-to-surfactant molar ratio ($W_o \sim 4$) is used in this system. Thus, the results pertaining to the structural characteristics of aggregates cannot be assumed to be valid for values of W_o greater than the low W_o value used in this system. The solvent conditions used in this system correspond to $T = 310\ K$

and $\rho_{solvent} = 0.484$ g/cc. At these state conditions CO_2 is in the near supercritical state which should also enhances the surfactant aggregation process. These solvent conditions were chosen to facilitate the study of self-aggregation within a reasonable computer time.

4.1.2 Large System

The large system has a composition of 33 dichain surfactant, 1175 water, and 12800 carbon dioxide molecules within a simulation box of length 103.5 Å. This corresponds to 42618 total interaction sites, which represents one of the largest system sizes used to study surfactant self-assembly via molecular simulation [69]. The concentration of the surfactant (0.05 mol/liter) and water (1.75 mol/liter) in this system exactly mimics the concentrations used by Eastoe et al. [54] in their SANS study of this ternary system. As mentioned before, the number of surfactant and water molecules used in this simulation study corresponds to one "average-sized" surfactant aggregate observed in the experimental work. Besides the low concentration of the dichain surfactant molecules in this system, an important difference between this system and the small system is the relatively high water-to-surfactant ratio ($W_o \sim 35$) in this system. As mentioned earlier, the high value of W_o in this system might manifest itself as some discernable difference in the dynamics and/or morphology of the aggregates formed in this system compared to those formed in the small system. The solvent conditions used in this system correspond to $T = 298\ K$ and $\rho_{solvent} = 0.848$ g/cc. At these conditions, CO_2 is in a high temperature liquid state, which should also affect the diffusion-limited aggregation process (as described later), observed in this three component system. Table 4.1 summarizes the composition and state conditions for the two systems described above.

Table 4.1: Composition and the state condition of the two system sizes studied

	Small system	Large system
Surfactant	30	33
Water	132	1175
Carbon dioxide (solvent)	2452	12800
W_o	4.4	35.6
Temperature (K)	310	298
Solvent density (g/cc)	0.482	0.848

4.2 Starting configurations

The simulations were performed with two independent starting configurations, viz. the aggregated starting configuration and the scattered starting configuration, for the two different system sizes. Figures 4.1(a)-(b) and 4.2(a)-(b) show both the starting configurations for the small system and the large system, respectively. The two starting configurations were chosen to test if different starting configurations had any effect on the dynamics of aggregation and/or morphology of the aggregates. It should be pointed out that these initial configurations are just two of the infinite possible configurations that can be used and were chosen solely because they were simple and less time consuming to generate. As shown in Figures 4.1(a) and 4.2(a), in the aggregated starting configuration, all the water molecules were placed within a spherical core at the center of the simulation box. The surfactant molecules with fully extended tails were placed on the surface of the core with their head groups pointing towards the center. Structurally, this configuration resembles a reversed micellar aggregate and hence the name aggregated starting configuration. In the scattered starting configu-

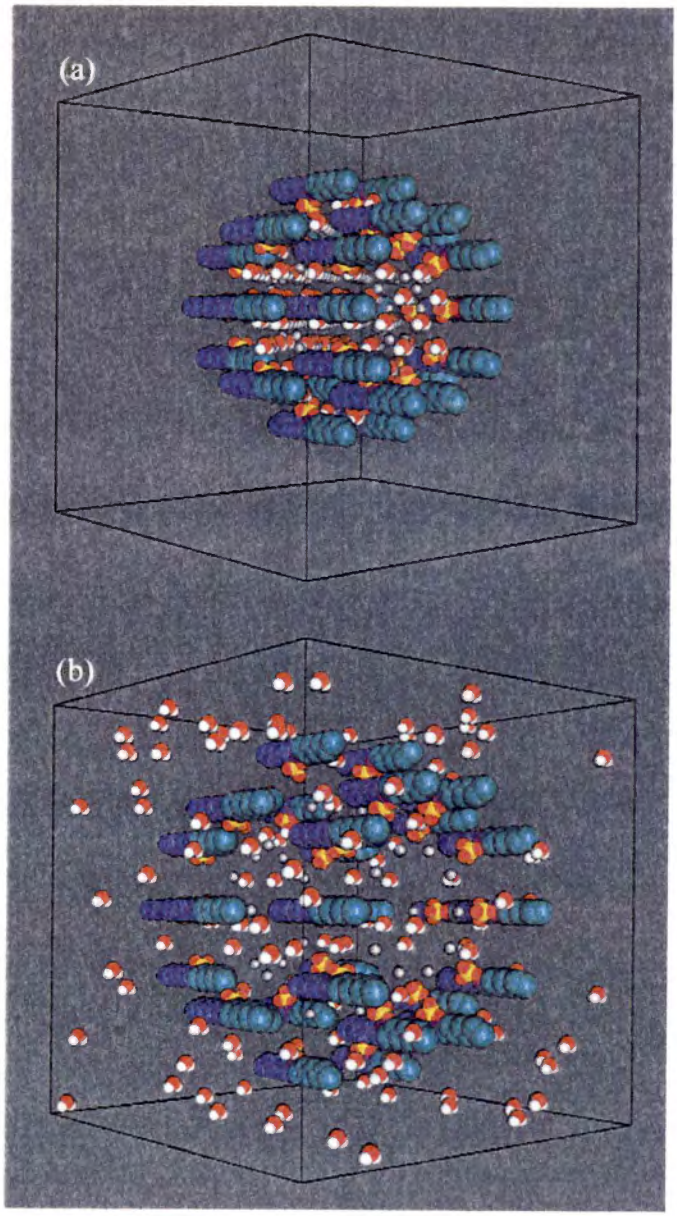


Figure 4.1: Snapshots of the starting configurations for the small system used in this study. (a) aggregated starting configuration (b) scattered starting configuration.

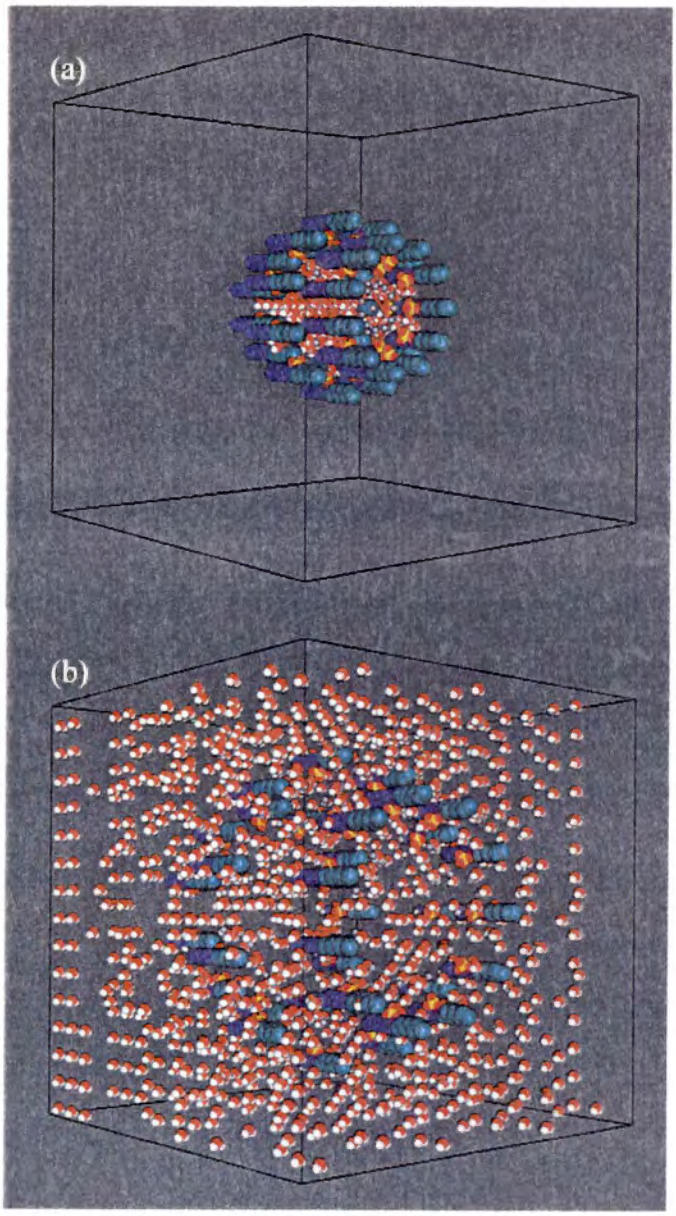


Figure 4.2: Snapshots of the starting configurations for the large system used in this study. (a) aggregated starting configuration (b) scattered starting configuration.

ration (Figures 4.1(b) and 4.2(b)) all the water molecules were scattered within the simulation box and the distance between the surfactant molecules was also increased. In a sense, the two starting configurations represent the two extremes of the system configurations. The scattered starting configuration is a more realistic starting state, while the aggregated starting configuration (especially for the large system) is closer to the desired final state characterized by the presence of a single surfactant aggregate. It is important to mention that the similar starting configurations for the two system sizes are somewhat different (due to different water-to-surfactant ratio) and their effect on the aggregation dynamics and aggregate morphology will be discussed in the following chapter.

4.3 Rattle Algorithm

As described in the previous section, the molecular models for all the three chemical species present in the system involve fixed bond lengths between atoms or pseudo-atoms. Clearly, a special technique is needed to handle the dynamics of this molecular system where certain selected degrees of freedom (bond lengths) are constrained while others (bond angles, torsional angles) remain free to evolve under the influence of inter-molecular and intra-molecular forces. The constrained MD is an approach that in effect uses a set of undetermined multipliers to represent the forces directed along the rigid bonds (called constraint forces) required to maintain the bond lengths constant. The general technique is to solve the equations of motion for one time step in the absence of the constraint forces, and subsequently determine their magnitude and correct the atomic positions accordingly.

Amongst the various techniques proposed in literature [70, 71] to perform constrained MD, this study used the Rattle algorithm [72] because it guarantees that

the constraints are satisfied at each time step. This implies that the constraint forces themselves are only correct to the same order of accuracy as the integration algorithm, resulting in computational stability. The Rattle algorithm is based on the Verlet algorithm [71] for integrating the equations of motion and retains the simplicity of using Cartesian co-ordinates for each of the atoms to describe the configuration of molecule with internal constraints. It calculates the atomic positions and velocities at the next time step from the atomic positions and velocities at the present time step without requiring information about the past trajectory of the molecule.

For a constrained molecular system, the equation of constrained dynamics for an atom is given by

$$m_i \ddot{\mathbf{r}}_i = \mathbf{F}_i + \mathbf{G}_i \tag{4.2}$$

where $\mathbf{F}_i$ are the physical forces of inter-molecular and intra-molecular interactions not associated with constraints, $\mathbf{G}_i$ represents the constraint forces, $\ddot{\mathbf{r}}_i$ is the acceleration (second derivative of position) and m_i is the mass of atom i. The functional form of $\mathbf{G}_i$ is given by

$$\mathbf{G}_i = -\sum_j \lambda_{ij}(t) \nabla_i \sigma_{ij} \tag{4.3}$$

where λ_{ij} are the time-dependent Lagrange multipliers associated with the intra-molecular forces of the constraints, are the constraints (Note that $\sigma_{ij} = \sigma_{ji}$ and $\lambda_{ij} = \lambda_{ji}$) and the summation is over only those atoms j that are connected to atom i by a constraint. For fixed bond lengths, the constraint equation is given by

$$\sigma_{ij}\left(\{\mathbf{r}(t)\}\right) = |\mathbf{r}_i(t) - \mathbf{r}_j(t)|^2 - {d_{ij}}^2 = 0 \tag{4.4}$$

where $\mathbf{r}$ is the position vector of atom i, and d_{ij} is the fixed distance between atoms i and j. The time derivative of the constraint equation gives the constraint on the

velocities, namely

$$|\dot{\mathbf{r}}_i(t) - \dot{\mathbf{r}}_j(t)| \,.\, |\mathbf{r}_i(t) - \mathbf{r}_j(t)| = 0 \tag{4.5}$$

The Rattle algorithm involves making approximation for the Lagrange multipliers. Since the Rattle algorithm is based on the velocity version of the Verlet algorithm, the formulation of the equations of motion for the constrained dynamics would be of the form

$$\begin{aligned}\mathbf{r}_i(t+h) &= \mathbf{r}_i(t) + h\dot{\mathbf{r}}_i(t) + \left(\frac{h^2}{2m_i}\right)[\mathbf{F}_i(t) + \mathbf{G}_i(t)] \\ &= \mathbf{r}_i(t) + h\dot{\mathbf{r}}_i(t) + \left(\frac{h^2}{2m_i}\right)\left[\mathbf{F}_i(t) - 2\sum_j \lambda_{RR_{ij}}(t)\mathbf{r}_{ij}(t)\right]\end{aligned} \tag{4.6}$$

and

$$\begin{aligned}\dot{\mathbf{r}}_i(t+h) = \dot{\mathbf{r}}_i(t) + \left(\frac{h^2}{2m_i}\right)\Bigg[&\mathbf{F}_i(t) - 2\sum_j \lambda_{RR_{ij}}(t)\mathbf{r}_{ij}(t) \\ &+ \mathbf{F}_i(t+h) - 2\sum_j \lambda_{RV_{ij}}(t+h)\mathbf{r}_{ij}(t+h)\Bigg]\end{aligned} \tag{4.7}$$

where $\mathbf{r}_{ij}(t) = \mathbf{r}_i(t) - \mathbf{r}_j(t)$. The quantity $\lambda_{RR_{ij}}(t)$ is chosen so that the constraint equation (Equation 4.4) are satisfied at time $t+h$, and $\lambda_{RV_{ij}}(t+h)$ is chosen to satisfy the time derivative of the constraint equation (Equation 4.5) at time $t+h$. Equations 4.6 and 4.7 are solved for $\lambda_{RR_{ij}}(t)$ and $\lambda_{RV_{ij}}(t+h)$ using the iterative method proposed by Ryckaert et al. [73]. Appendix B gives the details of the iterative procedure for Rattle algorithm.

4.4 Replicated Data Algorithm

Considering the fact that the simulations performed in this study are computationally intensive, parallelization of the simulation code is employed to speed up the integration of the equations of motion. The parallelization strategy used in this study, shown

in Figure 4.3, is called the replicated data technique. As the name suggests, this technique involves replication of all the position variables for every atom or site at every processor, even though each processor performs integration on only a specified set of atoms or sites. Since all the processors have information for all the atoms or sites, the number of communications between the processors is greatly reduced compared to domain decomposition. This technique was chosen for its simplicity and effectiveness in parallelization of an existing serial code that has been tested previously for accuracy. This technique is essentially the "atomic decomposition" method described by Plimpton [74].

Figure 4.4 shows the flowsheet of the parallel version of the simulation code used in this study. As shown in the figure, there are basically two force calculations in this system viz. inter-molecular interactions and intra-molecular interactions. Since, the forces due to intra-molecular interactions are calculated prior to the calculation of forces due to inter-molecular interactions and only require information regarding the particle position of a single molecule, these calculations are done for all sites at all processors. Thus, in essence, no parallelization is used for the calculation of forces due to intra-molecular interactions. One can use parallelization for calculation of intra-molecular forces, especially for large molecules, but a balance has to be established between the cost of force calculation and the communication between the processors. In this study, the surfactant molecule is relatively small (only 21 interaction sites) and thus it is more beneficial to avoid parallelization for calculation of intra-molecular forces. On the other hand, the forces due to inter-molecular interactions are evaluated within a double loop that compares uniquely every interaction within a cut-off distance from the given atom or site. This is the most computationally intensive part of the simulation and the speed with which these forces can be calculated determines the overall performance of the simulation code. According to the simple

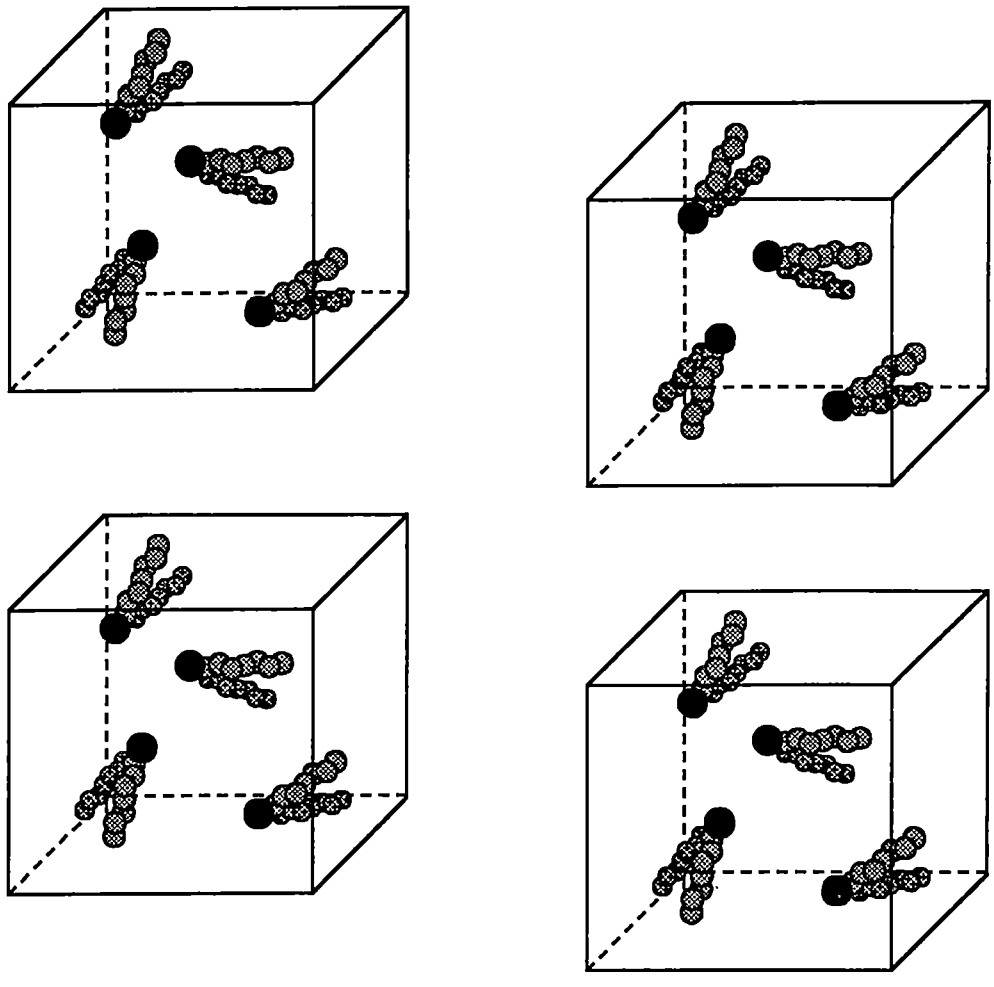


Figure 4.3: Replicated data parallelization strategy.

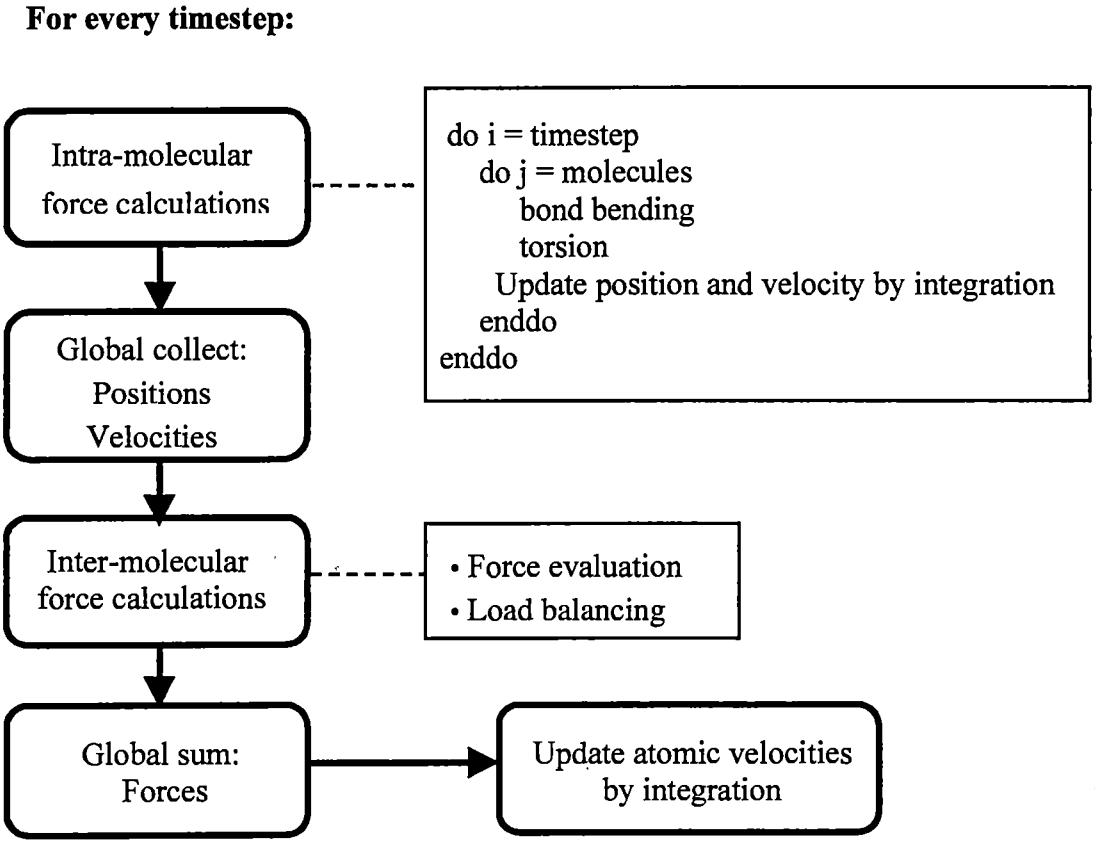


Figure 4.4: Sequence of events for the replicated data parallelization of the simulation code.

parallelization scheme described above, the computational work is divided (as equally as possible) amongst processors by assigning a range of outer loop iterations to each processor. These processors can then work in parallel, thereby significantly increasing the computational speed..

At least some form of load balancing is still required because of the fact that the quantity of computational work in the double loop structure is not uniformly distributed by simply dividing the outer loop iterations equally into the total number of processors. This is due to the structure of the double loop which when represented as a matrix, is a triangular matrix. Thus, simply dividing the outer loop iterations result in the earlier processors performing much more computational work than the later ones. To effectively counter this imbalance, a simple approach is adopted in this study i.e. to divide the computational work for a set of N processors, in such a way as if $2N$ processors are available. Then iterations from opposite end of the outer loop are assigned to each processor, thereby giving each processor a large and a small chunk to work with. This method has the obvious advantage that it is fairly easy to implement and permits quite effective parallelization. Further parallelization can be realized if the computational work of the inner loop is divided as well, but this is not quite advantageous for the simulation code used in this study.

Hence in the parallelization strategy implement in this study, two communications between processors are required to ensure an accurate calculation of inter-molecular and intra-molecular forces (Figure 4.4). One of these communications is done after the integration step following the calculation of intra-molecular forces, while the other follows the estimation of inter-molecular forces. Both of these communications involve a so-called "global sum" which basically gathers relevant data from each processor and then distributes the data for all atoms or sites to all processors. The first communication step collects and distributes (scatters) the position vectors for

all the particles to all the processors, for the calculation of inter-molecular forces using the parallelization technique. The inter-molecular forces are then calculated and the atomic forces are then "globally summed", so that all the processors have sufficient information to update the system, and subsequently commence the next step of integration.

Figure 4.5 shows results pertaining to the scaling of the simulation code, with respect to the number of processors (N_p), used in this study. The figure plots the simulation time required to perform a single iteration step versus the inverse of the number of processor ($1/N_p$). In an ideal case, this dependence should be inversely proportional, as shown by the dotted line in the figure. However, the figure shows that simulation code does not scale linearly with the number of processors. As the number of processors increases, the simulation time does not reduce proportionally. This is because as the number of processors increases ($1/N_p$ decreases), the actual time for integration decreases (inversely proportional to N_p), while the time for communication between processors increases (proportional to N_p). It is the increase in the communication time that results in the deviation from the ideal curve, thereby resulting in the behavior shown in Figure 4.5. Most of the simulations reported in this work were performed on 8 processors ($N_p = 8$) on the Cray T3E at NERSC. This particular value of N_p provided the optimum utilization of the allocated computational time for the real time needed to needed to perform these simulations.

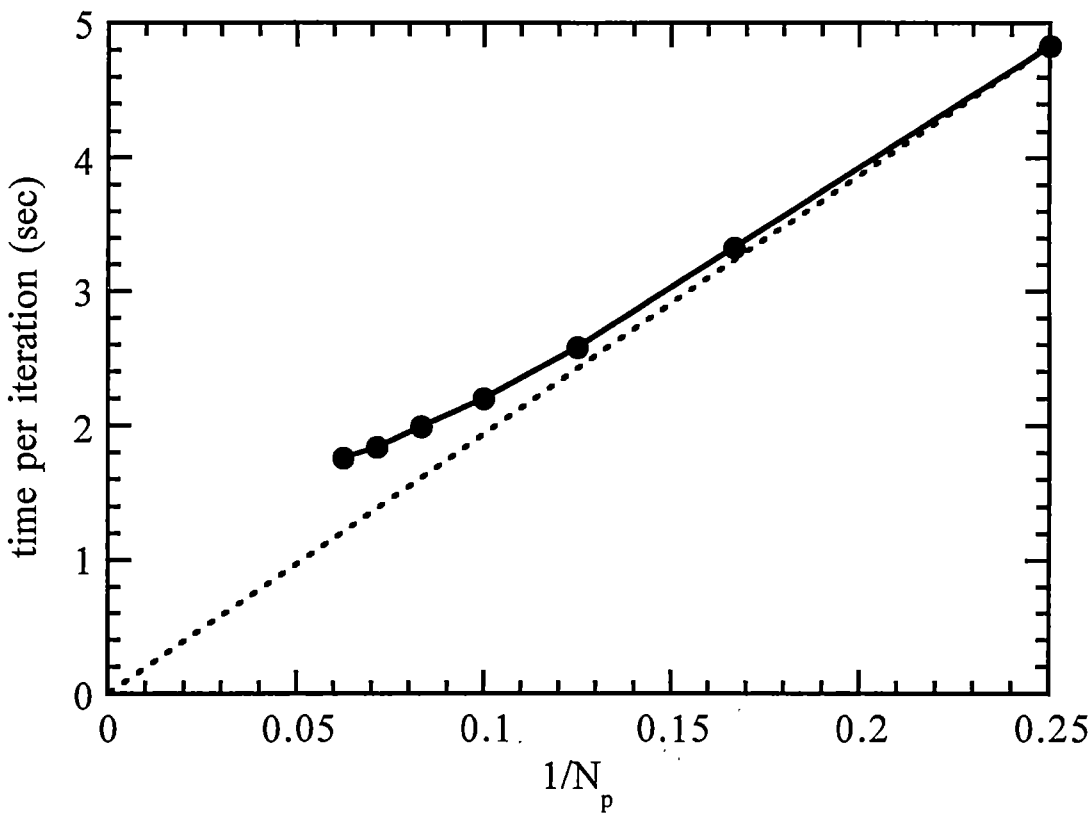


Figure 4.5: Performance curve for the simulation code used in this study.

Chapter 5

Results and Discussion

As mentioned earlier, most of the prior simulation studies [58, 59, 60] of surfactant systems that form reversed micellar aggregates or w/o microemulsions have primarily focussed on understanding the general structural properties of these aggregates. Areas of investigation have mainly included aggregate shape and fluctuations, tail conformation and packing, solvent penetration into the core, extent of counter-ion coupling with the head group, and behavior of solutes. Although these studies took explicit account of all the forces between component molecules, only Tobias and Klein [60] attempted to reproduce the detailed characteristics of a specific surfactant system. As suggested by DeGennes and Taupin [75], steric packing effects that are very specific to a particular surfactant molecule play an essential role in determining the stability and size distribution of surfactant aggregates in non-polar solvents. Thus, detailed and surfactant-specific studies of RMs are needed to fully understand the reasons for their spontaneous formation in non-polar solvents, especially solvents like supercritical carbon dioxide.

As an initial step in this direction, the focus of this research work is to obtain a comprehensive molecular level description of self-aggregation in a dichain surfactant + water + carbon dioxide (solvent) ternary system. Besides investigating the various structural properties mentioned previously and making direct comparisons with the

SANS results of Eastoe et al. [54], one of the main objectives of this work is to obtain a molecular level insight into the dynamic processes involved in the aggregation of dichain surfactant molecules in supercritical CO_2. Thus, for this purpose a detailed and realistic molecular model of the dichain surfactant molecule as well as explicit representation of solvent molecules is used in this simulation study. In this work, numerous simulations were performed to study the effect of surfactant tail length and chemistry, water-to-surfactant molar ratio (W_o), solvent conditions etc. on the dynamics of aggregation and the morphology of the aggregates formed. The results were analyzed mainly to explain the suitability and effectiveness of the dichain surfactant molecule as a CO_2-philic surfactant.

The results presented in this chapter are organized as follows: Sections 5.1 and 5.2 describe results pertaining to the dynamics of aggregation (mechanism and time-scales of self-aggregation, rate of aggregation etc.). This is followed by the discussion of the general structural properties (size, shape, tail conformation etc.) of the surfactant aggregates formed, in Sections 5.3 and 5.4. The details of the microstructure of the surfactant molecules are discussed in Sections 5.5 and 5.6. Finally, results pertaining to the effect of surfactant chemistry and architecture on aggregation are presented in Section 5.7 and 5.8.

5.1 Aggregation mechanism

An important aspect of the dynamics of surfactant self-aggregation is the mechanism through which randomly dispersed surfactant molecules spontaneously form stable and highly organized molecular aggregates or micelles. Understanding the mechanism of surfactant aggregation is also important in identifying the interactions between component molecules that are responsible for holding the surfactant molecules

together in an aggregate. The mechanism of the formation of o/w micelles is quite well understood (both theoretically and experimentally) and has been used to develop mathematical models that provide an estimate of the CMC of these systems [36, 37]. On the other hand, even standard experimental methods such as temperature and pressure jump and stopped flow techniques that have been quite successful for aqueous surfactant systems, are not useful for surfactant aggregates in non-polar solvents because these techniques are strongly dependent on the electrical conductivity of the solvent medium. The MD simulation technique is able to follow the molecular trajectory directly and thus can be quite useful in understanding the mechanism of surfactant aggregation in non-polar solvents.

Figures 5.1(a)-(d) show the snapshots of the small system (with aggregated starting configuration) at the various important stages of the aggregation process highlighting the mechanism of surfactant self-assembly. Although these snapshots correspond to the system evolution from the aggregated starting configuration (Figure 4.1(a)), as shown later, a similar mechanism was observed for the system evolution from the scattered starting configuration of this system as well. In all these snapshots the solvent molecules are intentionally not shown for reasons of visual clarity. Figure 5.1(a) shows the system configuration at 5.5 ps, which is quite early in the aggregation process. All the dichain surfactant and water molecules appear somewhat randomly dispersed within the simulation box with no evidence of surfactant aggregation. The only noticeable fact is that the Na^+ ions and the anionic surfactant molecules exist as contact ion-pairs. As shown by Shelley and co-workers [28] for an aqueous surfactant system, it is possible that the contact ion-pairs shown in Figure 5.1(a) could exhibit dissociation of some (or all) ion-pairs between the Na^+ ions and sulfate head group. Further simulations with a polarizable surfactant model are needed to address this issue. Also, the system configuration at this instant appears to have little correlation

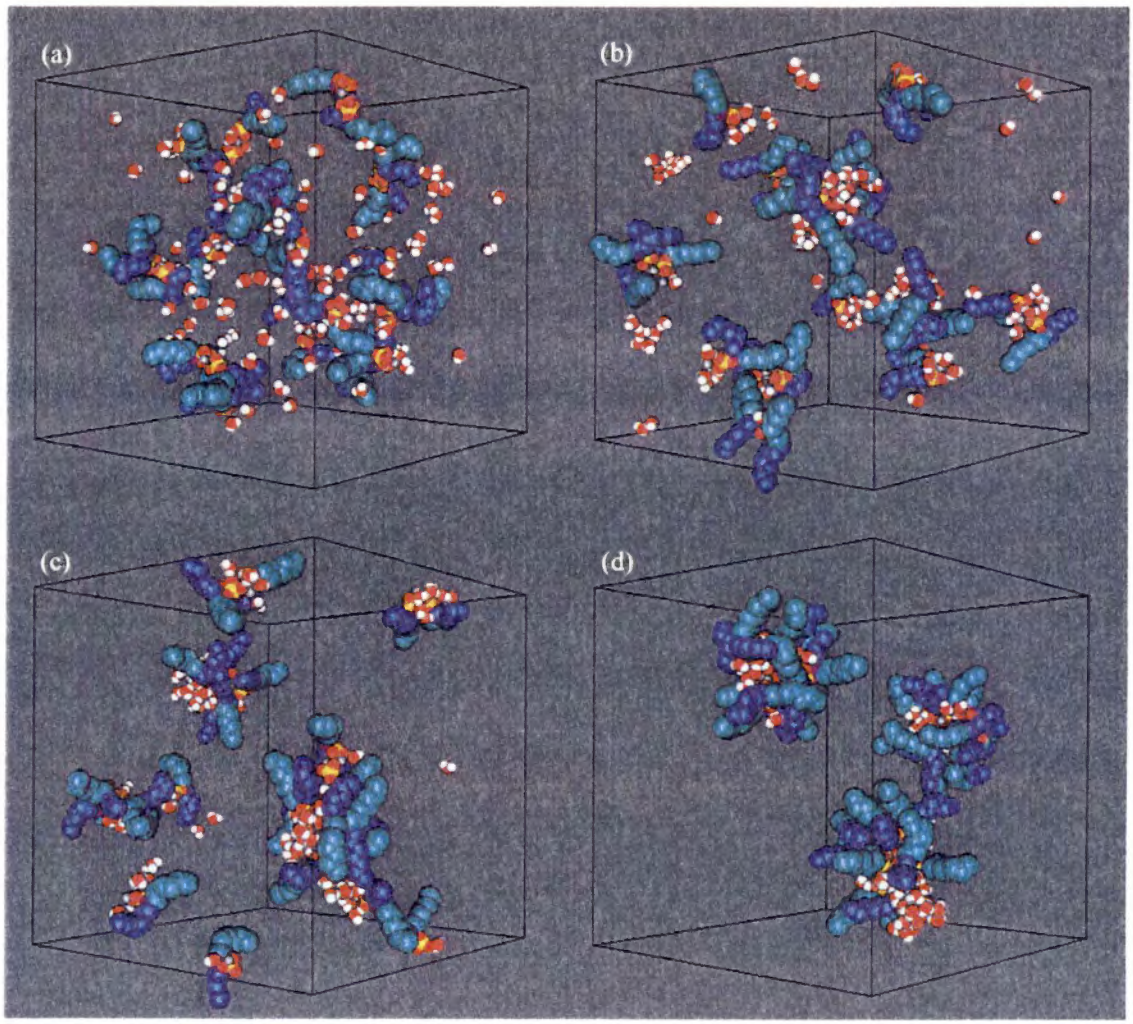


Figure 5.1: Snapshots of the simulation taken at (a) 5.5 ps, (b) 44.6 ps, (c) 148.3 ps, and (d) 1036.0 ps showing the mechanism of surfactant aggregation for the small system with aggregated starting configuration. The color scheme of the various species is as follows: light blue for perfluoroalkane tail, dark blue for alkane tail, yellow for sulfur, red for oxygen, white for hydrogen, and grey for sodium. CO_2 molecule are not shown for visual clarity.

with the aggregated starting configuration, suggesting that perhaps the starting configuration has little effect on the long-time dynamics of this system. Figure 5.1(b) shows the system configuration at 44.6 ps. At this stage a significant number of water molecules have associated themselves with the ionic species present in the system, i.e. the water molecules tend to hydrate the anionic head group and Na^+ counter-ion of the surfactant molecules. Although preliminary evidence of surfactant aggregation is noticeable by the presence of small clusters of hydrated surfactant molecules, still no appreciable aggregation is evident in the system. The system configuration in Figure 5.1(c) corresponds to 148.3 ps and shows that nearly all the water molecules have directly or indirectly associated with the surfactant molecules. Also, small surfactant aggregates have developed in the system indicating the beginning of surfactant aggregation. However, no reversed micelle-like (an aqueous core surrounded by surfactant molecules with their head groups immersed in the aqueous core and the tails forming a corona) aggregates are noticeable in the system. However, after a sufficiently long time (1036.0 ps) the system consists of three roughly similar-sized surfactant aggregates that have the appearance of RMs, as shown in Figure 5.1(d). The water molecules in these aggregates appear to form an aqueous core that is well shielded from the surrounding solvent by a layer of surfactant molecules with their head groups pointing towards the aqueous core and tails extending into the solvent. This morphology of the aggregates formed closely resembles that of RMs (as shown in Figure 1.2) thereby indicating the formation of reversed micelle-like aggregates in this system.

The aggregation process described above can be further clarified by following the energetics of the system. Figure 5.2 shows the time evolution of surfactant-surfactant (U_{ss}) and surfactant-water (U_{sw}) interaction energies observed in the small system. The term surfactant here denotes contributions from the anionic surfactant molecule as well as the sodium counter-ion (cation). The figure shows two distinct steps in

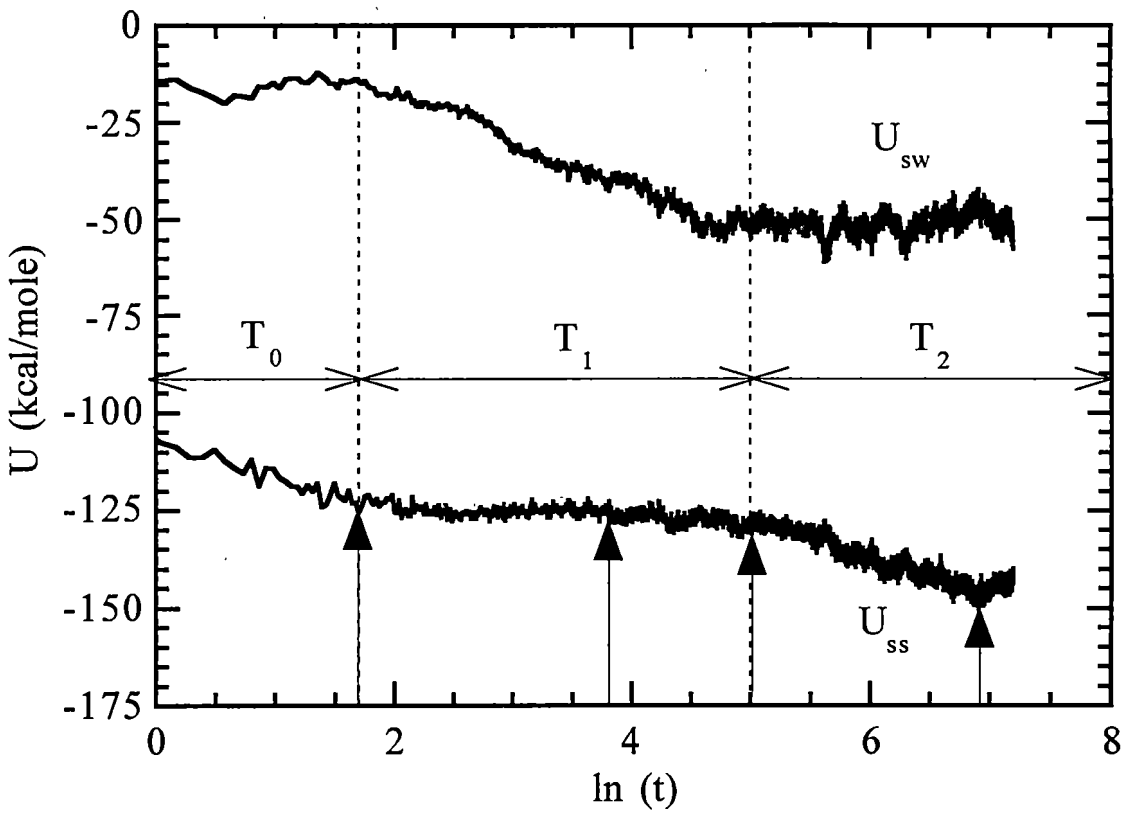


Figure 5.2: Time evolution of the surfactant-surfactnt (U_{ss}) and surfactant-water (U_{sw}) interaction energies in the small system with aggregated starting configuration. Arrows indicate the times corresponding to the snapshots in Figure 5.1.

the evolution of U_{ss} and U_{sw}. The first step, which corresponds to the time interval $T_1 \equiv 1.7 < ln(t) \leq 5.0$ ($5.5 < t \leq 148.3$ ps), shows a decrease in U_{sw} from a value of -20 kcal/mole to about -50 kcal/mole while U_{ss} remains nearly constant. This decrease in U_{sw} is attributed to hydration of anionic surfactant - Na^+ ion-pair by the water molecules present in the system, as shown in Figures 5.1(b)-(c). The U_{ss} remains constant because there is no appreciable surfactant aggregation during this step. The time interval preceding T_1 ($T_0 \equiv ln(t) \leq 1.7 \Rightarrow t \leq 5.5$ ps) simply involves the formation of ion-pair (Figure 5.1(a)) from the starting configuration and does not contribute to the aggregation process. During the second step of the aggregation process ($T_2 \equiv ln(t) > 5.0 \Rightarrow t > 148.3$ ps), the trends in the evolution of U_{ss} and U_{sw} change with the U_{ss} showing a gradual decrease (considering the fact that the horizontal axis in Figure 5.2 is logarithmic time) while U_{sw} remains nearly constant. The gradual decrease in U_{ss} is due to the inter-molecular interaction of hydrated surfactant molecules resulting in the formation of surfactant aggregates. As the hydrated surfactant molecules assemble to form RM-like aggregates with their head groups forming the core, their tail groups experience strong steric packing effects. As a result the surfactant molecules within the aggregate re-arrange to achieve steric stabilization. Thus U_{ss} decreases gradually until it reaches a minimum where the interaction energy simply oscillates around a constant value. The interaction between water and surfactant molecules remains unchanged during this step of the aggregation process since there is negligible change in the hydration characteristics due to the low W_o in this system.

Thus, the aggregation process in the small system (with aggregated starting configuration) described above appears to follow a two-step aggregation mechanism. The first step (T_1) involves a rapid (within the first 150 ps) of hydration of anionic head groups and the sodium counter-ions that exist as ion-pairs prior to hydration. There

is no appreciable surfactant aggregation during this step. Figure 5.3, which shows a plot of the fraction of total water molecules associated with surfactant molecules versus time for this system, clearly depicts that the first step primarily involved ion-hydration. The figure shows that almost all the water molecules present in the system become associated with the sodium ion - anionic surfactant ion-pair during the first step and remain associated subsequently. In contrast, the second step (T_2) of the aggregation process is a much slower step involving gradual aggregation of the hydrated surfactant molecules via hydrogen bond formation (shown later) into stable RM-like aggregates.

For the small system with scattered starting configuration, Figure 5.4 shows the energy profiles of U_{ss} and U_{sw}. The figure clearly shows two distinct steps (T_1 and T_2) in the aggregation process quite similar to those observed for the small system with aggregated starting configuration. The first step (T_1) involves a decrease in U_{sw} while U_{ss} remains nearly constant, while the second step (T_2) involves a gradual decrease in U_{ss} while U_{sw} remains nearly constant. Thus, as stated earlier, this system also exhibits the two-step aggregation mechanism (ion-hydration followed by surfactant aggregation) described earlier. Figure 5.5 shows the plot of the fraction of total water molecules associated with surfactant molecules versus time for this system (small system with scattered starting configuration). The figure shows that the fraction of water molecules associated with surfactant molecules approaches unity within a time step of $\sim$ 150 ps. Again, this is similar to that observed for the small system with aggregated starting configuration (Figure 5.3). Thus, it can be concluded that both the starting configurations for the small system exhibit similar aggregation mechanism leading to the formation of RM-like aggregates.

As shown in Table 4.1, the composition of the large system is significantly different from that of the small system, such as low surfactant concentration, high water-to-

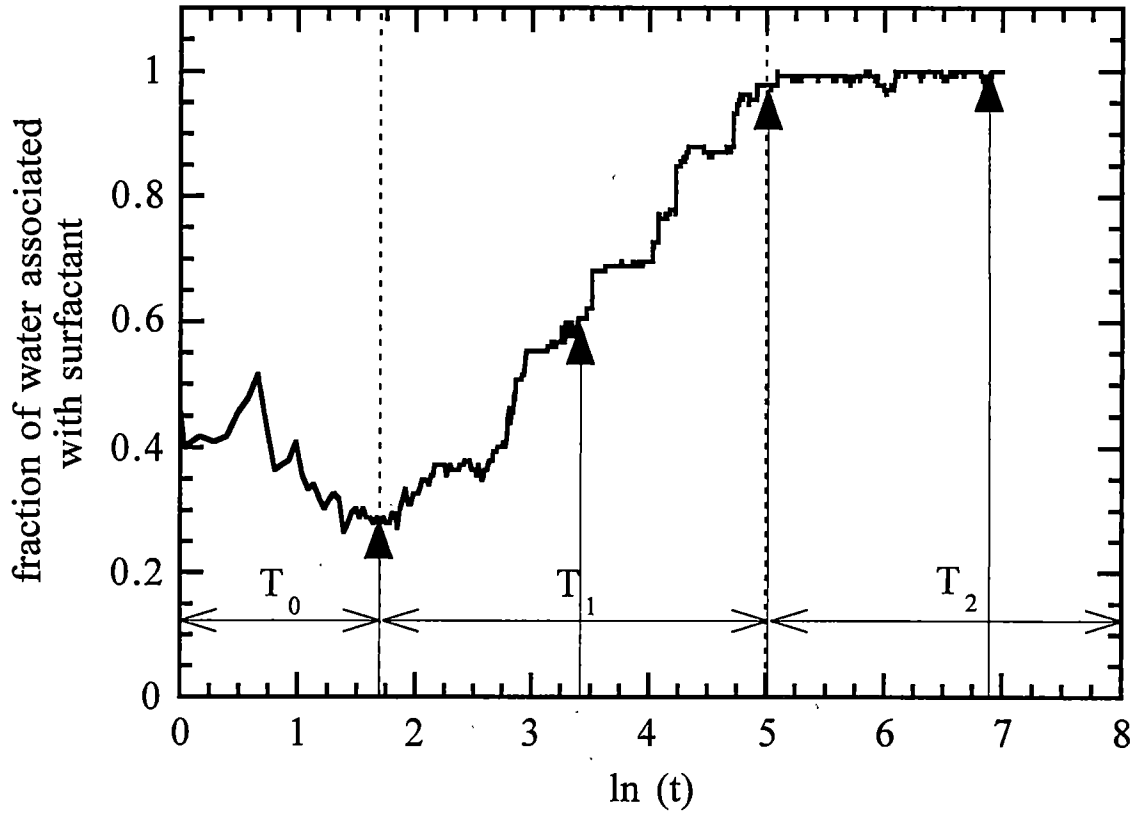


Figure 5.3: Time evolution of the fraction of water molecules present in the small system (aggregated starting configuration) that are associated with the surfactant molecules. Arrows indicate the times corresponding to the snapshots in Figure 5.1.

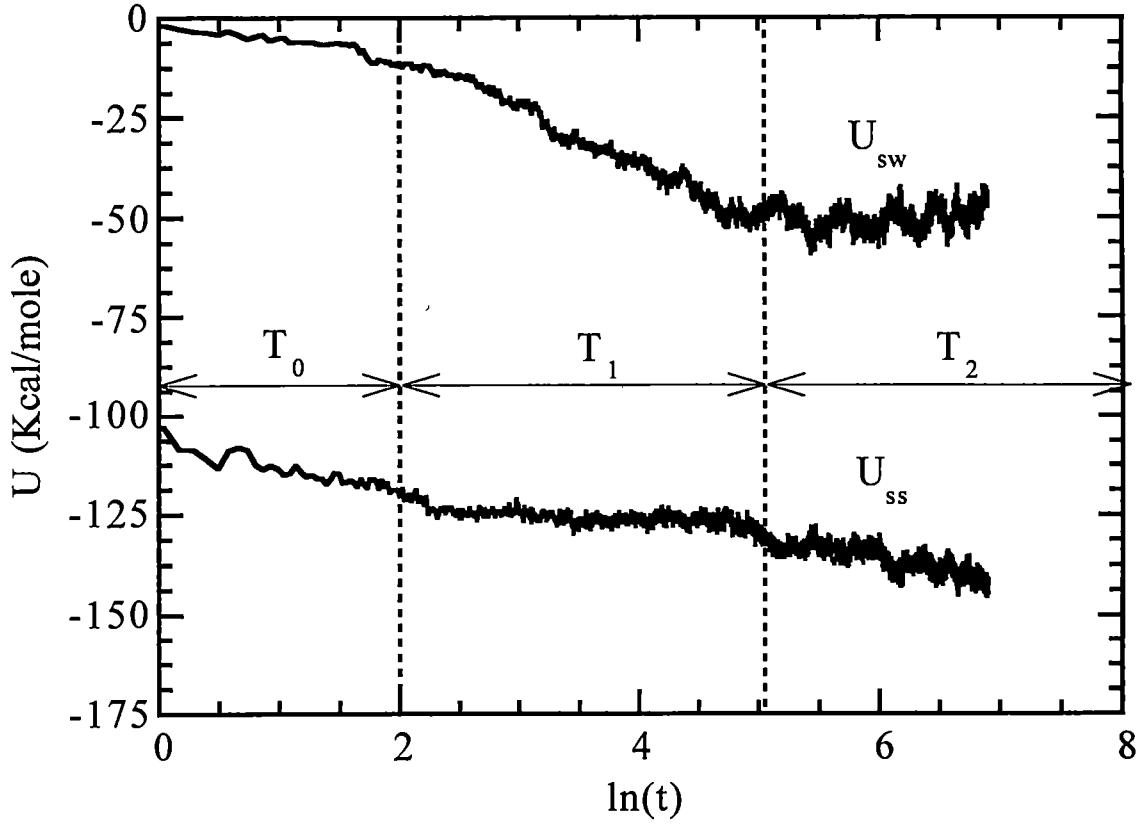


Figure 5.4: Time evolution of the surfactant-surfactnt (U_{ss}) and surfactant-water (U_{sw}) interaction energies in the small system with scattered starting configuration.

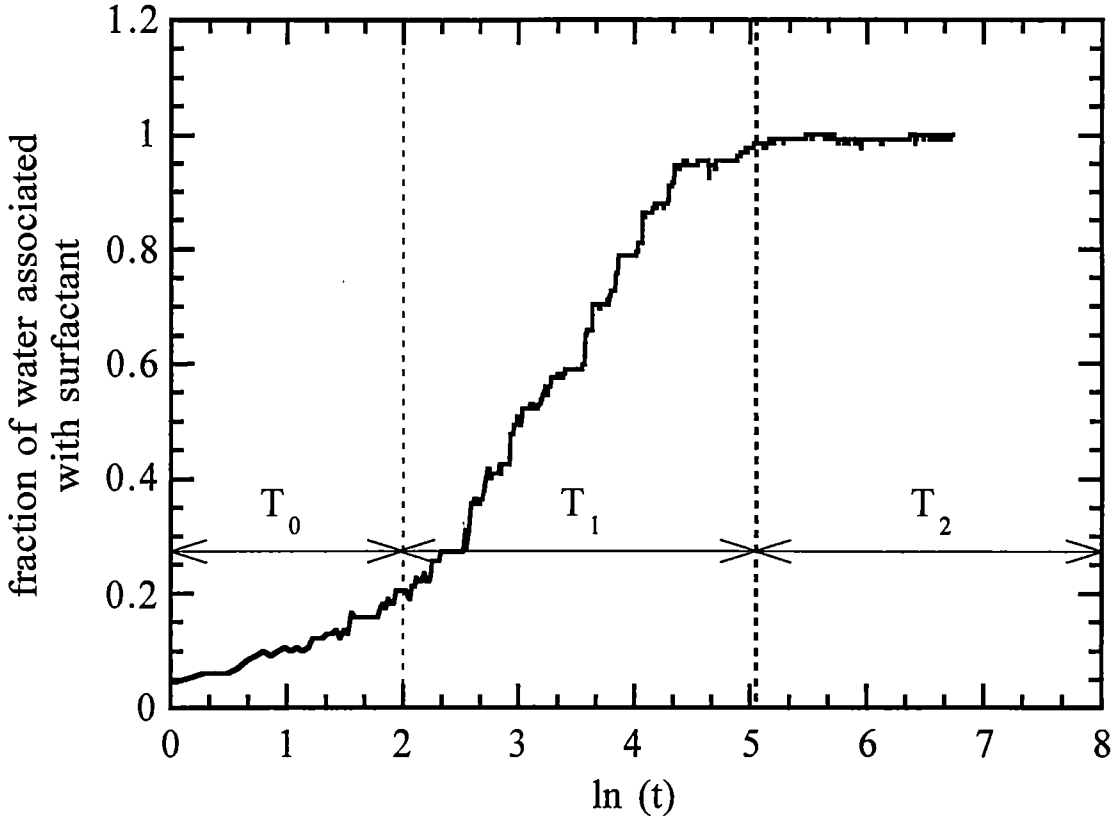


Figure 5.5: Time evolution of the fraction of water molecules present in the small system (scattered starting configuration) that are associated with the surfactant molecules.

surfactant molar ratio, and high solvent density. It should be insightful to investigate if these factors play any role in the aggregation process for this system. Figures 5.6(a)-(d) and 5.7(a)-(d) show the snapshots of the evolution of the large system with aggregated and scattered starting configurations, respectively. Figures 5.6(a)-(d) shows the aggregation process observed in the large system with aggregated starting configuration at 5, 20, 100, and 1000 ps, respectively. Figure 5.6(a) shows that the starting configuration expands almost instantaneously ($\sim$ 5 ps). However, in contrast to the small system (Figure 5.1(a)), the high water-to-surfactant molar ratio in this system ($W_o \sim 35$) prevents dispersion of surfactant and water molecules as monomers and dimers. Most of the surfactant molecules appear to be connected to each other via water bridges. The system then rapidly re-aggregates (within $\sim$ 100 ps) to form four surfactant aggregates (one large aggregate consisting of most of the surfactant and water molecules while the remaining surfactant and water molecules distributed between the remaining three aggregates) as shown in Figure 5.6(c). No further aggregation is observed in this system even up to $\sim$ 1.0 ns, as shown in Figure 5.6(d).

For the large system with scattered starting configuration, Figures 5.7(a)-(d) show the snapshots of the system at 100, 200, 500, and 2000 ps, respectively. During the first 200 ps (Figures 5.7(a)-(b)), most of the surfactant molecules appear to be randomly distributed with their anionic head groups (and Na^+ counter-ions) hydrated by the water molecules present in the system. Nearly, all the water molecules present in the system appear to be directly or indirectly associated with surfactant molecules within this time step. No appreciable surfactant aggregation is evident in the system at this stage. Figure 5.7(c) shows the presence of small surfactant aggregates (mostly consisting of 2 - 3 surfactant molecules per aggregate) indicating the propensity of the system for surfactant aggregation. Finally, Figure 5.7(d) shows the presence of

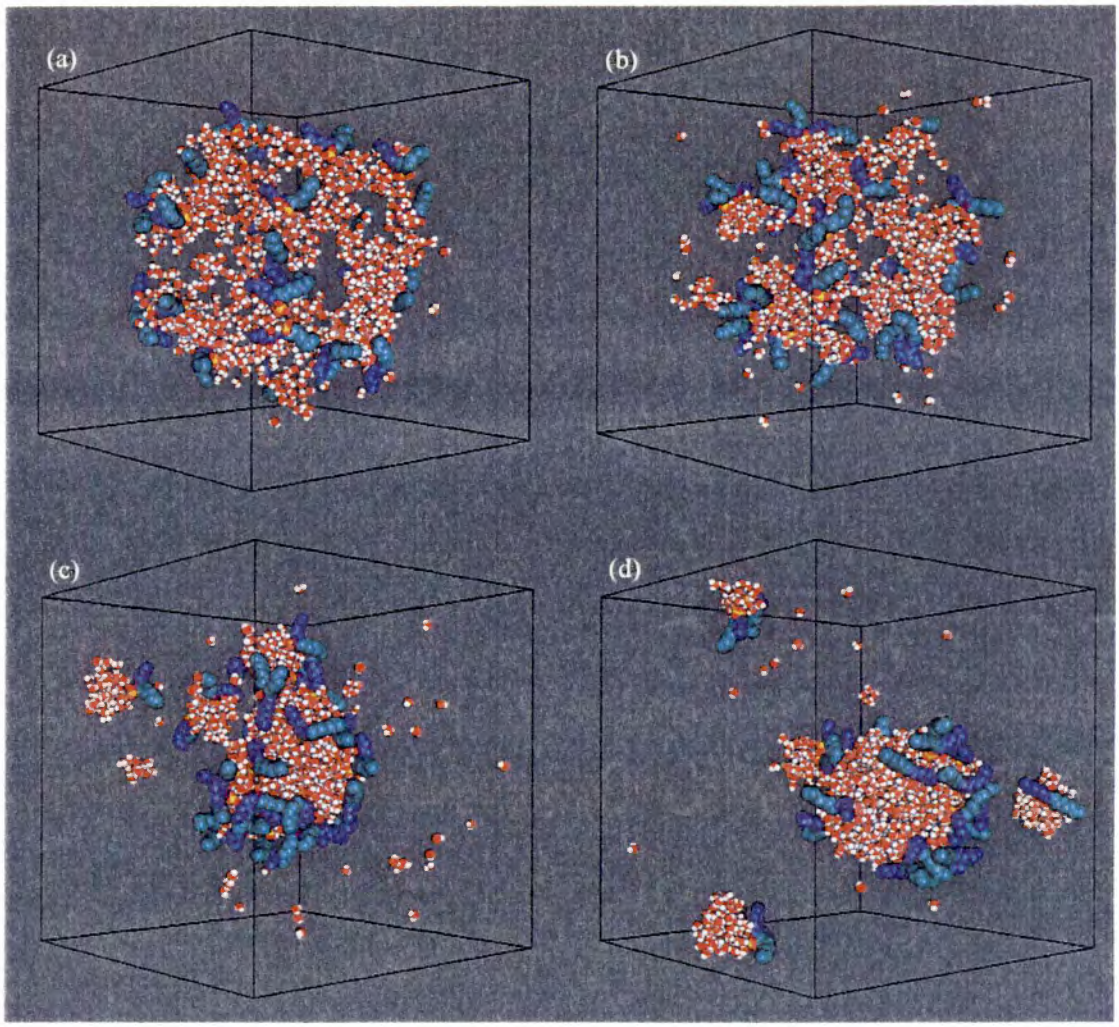


Figure 5.6: Snapshots of the simulation taken at (a) 5 ps, (b) 20 ps, (c) 100 p s, and (d) 1000 ps showing the mechanism of surfactant aggregation for the large system with aggregated starting configuration. The color scheme of the various species is as follows: light blue for perfluoroalkane tail, dark blue for alkane tail, yellow for sulfur, red for oxygen, white for hydrogen, and grey for sodium. CO_2 molecule are not shown for visual clarity.

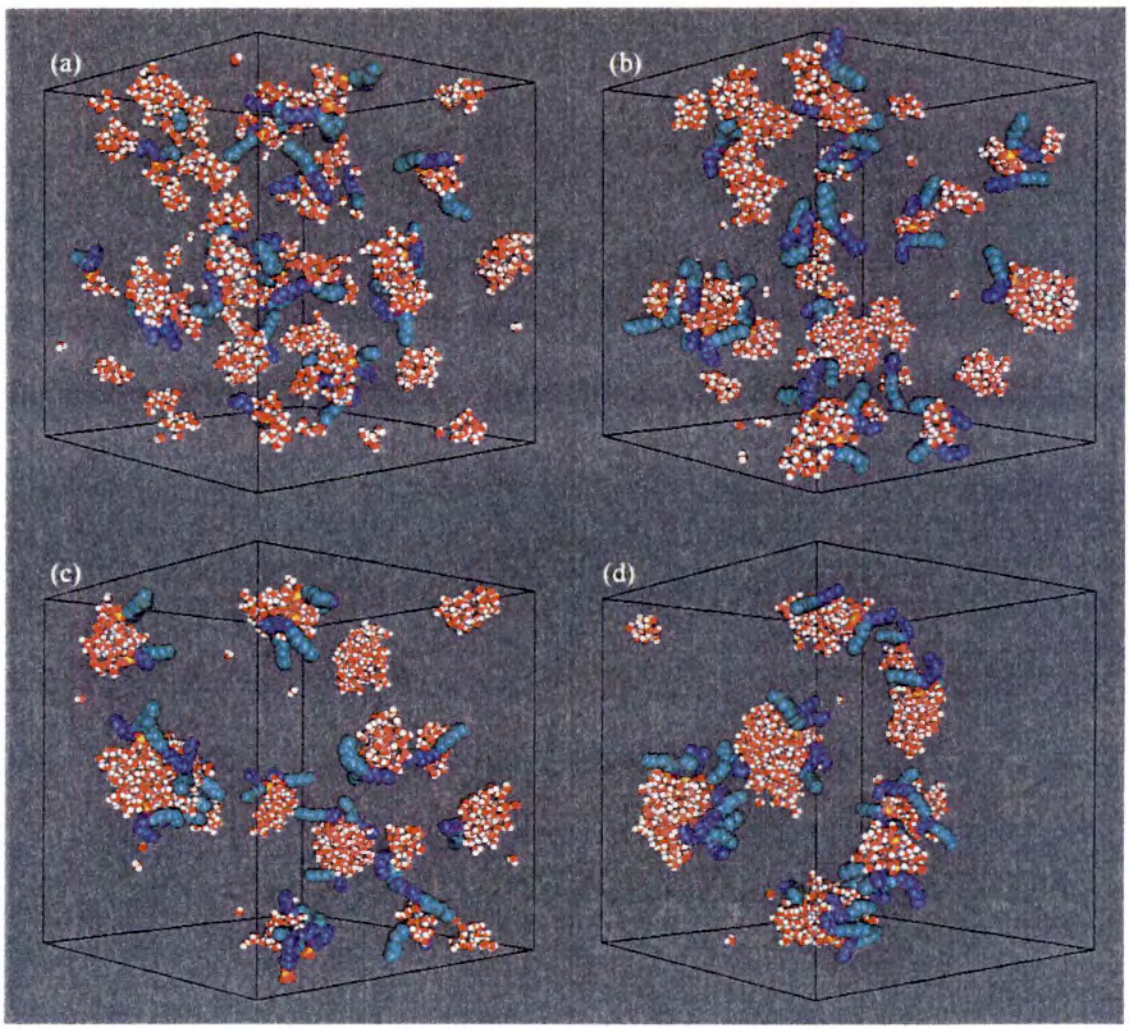


Figure 5.7: Snapshots of the simulation taken at (a) 100 ps, (b) 200 ps, (c) 500 p s, and (d) 2000 ps showing the mechanism of surfactant aggregation for the large system with scattered starting configuration. The color scheme of the various species is as follows: light blue for perfluoroalkane tail, dark blue for alkane tail, yellow for sulfur, red for oxygen, white for hydrogen, and grey for sodium. CO_2 molecule are not shown for visual clarity.

five surfactant aggregates in the system at 2000 ps.

Figure 5.8 shows the plot of fraction of water molecules associated with surfactant molecules for the large system with both the starting configurations. The curve for the large system with scattered starting configuration shows an almost linear increase in the fraction of water molecules associated during the interval $T_1 \equiv ln(t) \leq 6.0$ ($t \leq 403.4$ ps). This behavior is quite similar to those observed for the small system (Figures 5.3 and 5.5), implying that this system follows the two-step aggregation mechanism (ion-hydration followed by surfactant aggregation). A further evidence of this is shown in Figure 5.9, which shows the energetics of this system. As expected, the evolution of U_{ss} and U_{sw} shows two distinct steps indicating the two-step aggregation process.

In contrast, the large system with aggregated starting configuration shows that the fraction of water molecules associated initially decreases, reaches a minimum of ~ 0.8 at $ln(t) = 1.5$ ($t = 4.5$ ps), and finally increases gradually as time increases. This behavior is not only different from the large system with scattered starting configuration but also different from the small systems. Clearly, this system does not follow the two-step aggregation mechanism, instead the evolution of this system is influenced by the aggregated starting configuration. This can be explained as follows: in the large system, the aggregated starting configuration has a spherical core in the center of the simulation box (Figure 4.2(a)) with a water density of $\sim$ 0.97 g/cc compared to ~ 0.11 g/cc in the small system (Figure 4.1(a)). Thus, all the surfactant molecules in the large system are associated with the water molecules to begin with. As a result, the ion-hydration step of aggregation process is not observed in this system. The second aggregation step is also significantly absent due to the incomplete dispersion of surfactant and water molecules. As will be shown later, the structural properties of the aggregate formed in this system (Figure 5.6(d)) are

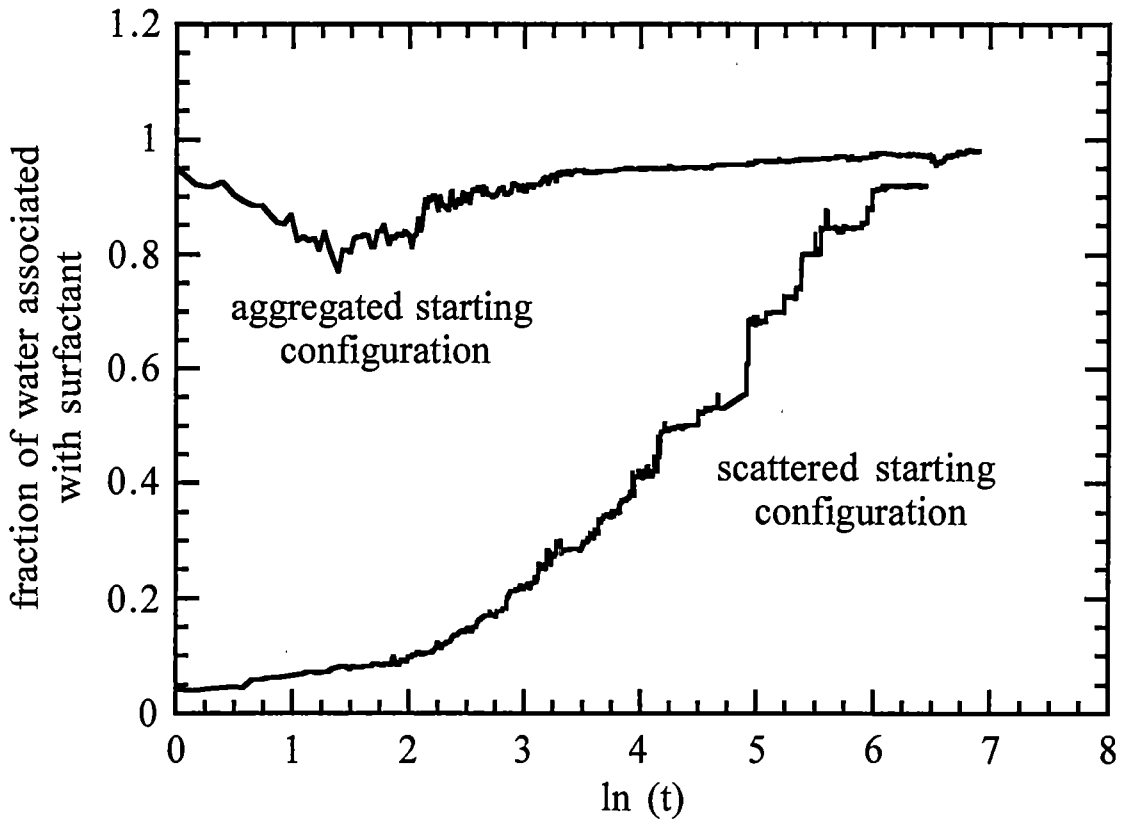


Figure 5.8: Time evolution of the fraction of water molecules present in the large systems (for both starting configuration) that are associated with the surfactant molecules.

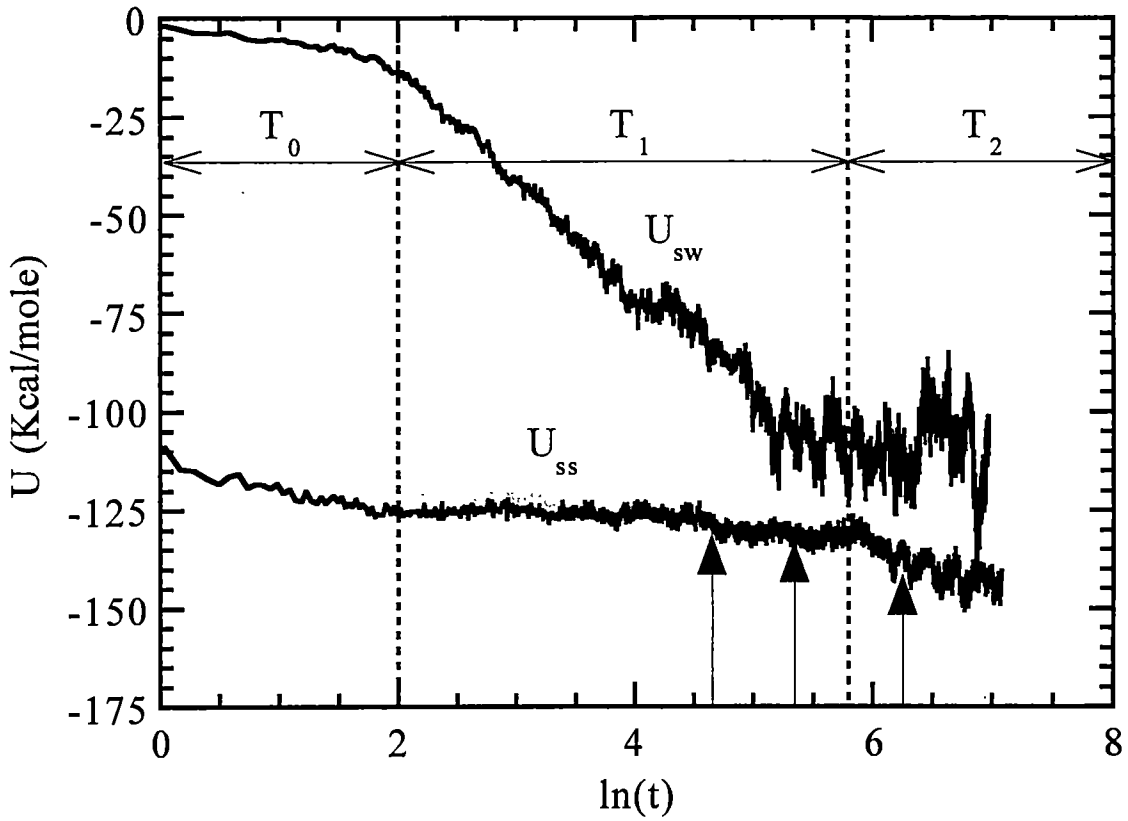


Figure 5.9: Time evolution of the surfactant-surfactnt (U_{ss}) and surfactant-water (U_{sw}) interaction energies in the large system with aggregated starting configuration. Arrows indicate the times corresponding to the snapshots in Figure 5.7.

in reasonably good agreement with the experimental results of Eastoe et al. [54]. This suggests that, although the system fails to exhibit the expected aggregation mechanism, the aggregate formed in this system is in agreement with the experimental results. Thus, it can be argued that aggregated starting configuration in the large system simply hastens the approach to the expected final state while the scattered starting configuration follows a more realistic trajectory.

Based on the above description, it can be concluded that the aggregation of dichain surfactant and water molecules in CO_2 essentially follows a two-step mechanism. The first step of this mechanism involves hydration of anionic surfactant and Na^+ counter-ions, while the second step involves aggregation of hydrated ions to form stable surfactant aggregates. This two-step mechanism (hydration interaction and subsequent hydrogen bond formation linking the surfactant molecules) of surfactant aggregation has been previously reported by Eicke and co-workers [76] based on the dielectric increment measurements for the system consisting of AOT surfactants in benzene. As mentioned earlier, AOT is an anionic surfactant molecule with two tails, which is structurally quite similar to the dichain surfactant molecule studied in this work. Thus, it can be concluded that aggregation of dichain surfactant in CO_2 is similar to that of other ionic surfactants (namely AOT) and is essentially governed by the electrostatic interactions between the surfactant head groups and water molecules.

Based on the description of the aggregation mechanism presented, an estimate of the time-scales of the two steps of surfactant aggregation can also be obtained. The first step which involves ion-hydration occurs over $\sim 10^{-10}$ sec while the aggregation of surfactant molecules into RM-like aggregates occurs over a time scale of $\sim 10^{-6}$ - 10^{-9} sec depending on the system size. As evident from Figures 5.3, 5.5, and 5.8, the ion-hydration step for the small system is $\sim$ 150 ps compared to $\sim$ 300 ps for

the large system. This may be attributed to the high concentration of the surfactant molecules (0.135 mol/liter) in the small system. Another factor that also appears to play a role, is the difference in the solvent condition of the two systems. Figure 5.10 shows the mean-squared displacement (MSD) of surfactant molecules during the first 80.0 ps (during which most of the surfactant molecules are in the dispersed state) for the small system (aggregated starting configuration) and the large system (scattered starting configuration). The slope of the MSD versus time curve is a measure of the diffusivity (mobility) of the surfactant molecules [71]. As expected, the curve for the small system has a higher slope than that for the large system, implying that the surfactant molecules in the small system have higher diffusivity than in the large system. This clearly suggests that solvent conditions also play an important role in the dynamics of surfactant aggregation in CO_2. The simulations also showed that for the second step of the aggregation process, the small system exhibits much shorter time scales (about an order of magnitude or more) compared to the large system. This can also be attributed to the supercritical state of the solvent in the small system (it will be shown in the next section that surfactant aggregation in this ternary system is diffusion-limited).

In general, these time scales are a few orders of magnitude smaller than those observed for surfactant aggregation in aqueous media which occurs over a time scale of $\sim 10^{-5} - 10^{-6}$ sec [77]. This may be attributed to the difference in the driving forces for aggregation in two solvent media. As mentioned earlier, the driving forces for aggregation in the non-polar solvents are electrostatic (ion-ion and ion-dipole) in nature, which are much stronger and long-ranged compared to the weak and short-ranged hydrophobic interactions responsible for aggregation in aqueous surfactant systems [35]. As a result, the surfactant and water molecules dispersed in a non-polar solvent experience more stronger aggregation forces, even at low concentrations.

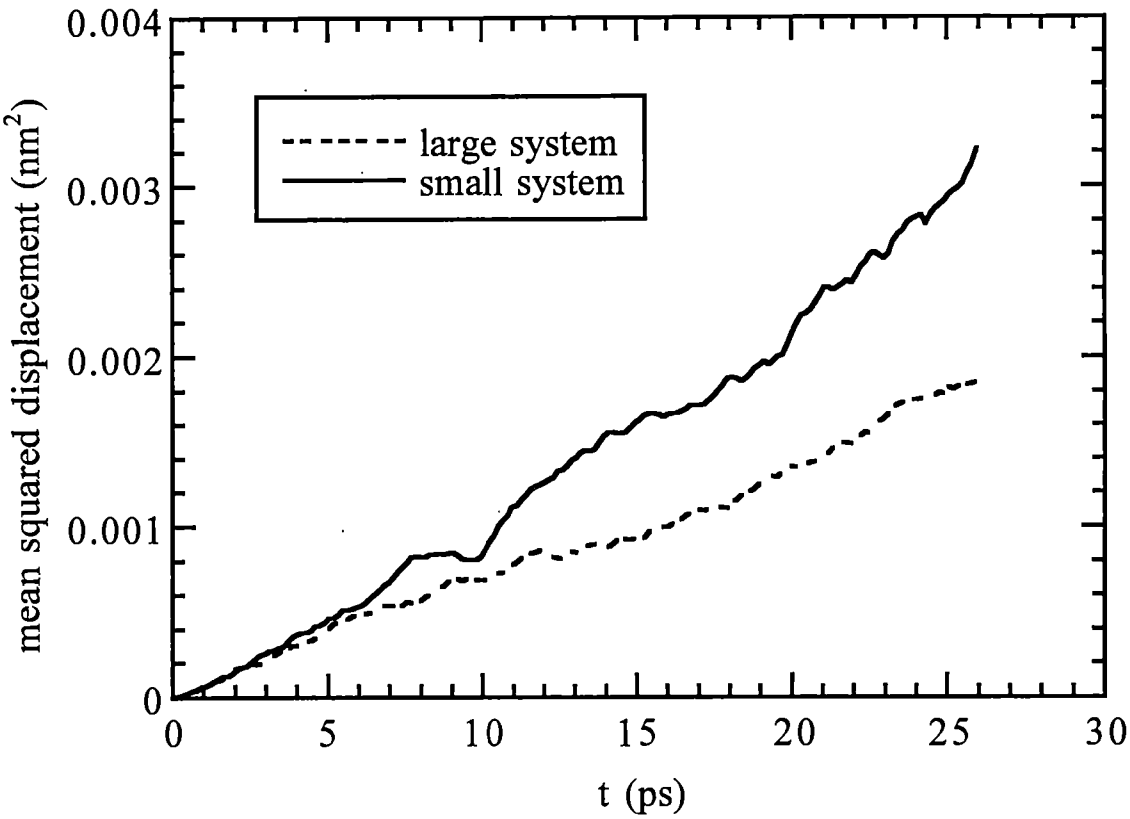


Figure 5.10: Mean-squared displacement (MSD) of the C_7-tailed hybrid surfactant during the first 80 ps of the aggregation process for the small system (aggregated starting configuration) and the large system (scattered starting configuration).

Therefore, surfactants in non-polar solvents exhibit much rapid aggregation dynamics compared to those observed in aqueous surfactant systems. Another consequence of stronger aggregation forces in non-polar solvents is the low CMC values observed in these systems compared to their aqueous counterparts.

An important question that arises from the simulations described above is whether the system will form RMs or will result in bulk-phase separation. This is especially important for the small system since this system has a high concentration of surfactant molecules, which might represent a supersaturated solution thereby precipitating the surfactant as a bulk phase. Since the surfactant concentration in the large system mimics the experimental values of Eastoe et al. [54], it is more likely that aggregates formed in this system are indeed RMs. Although the visualization of these simulations showed exchange of water molecules between surfactant aggregates, thereby suggesting some level of equilibration with respect to mass transfer, it is not sufficient to verify the formation of equilibrium micellar aggregates. Unfortunately, one of the limitations of the MD simulation technique is its inability to distinguish between micelle formation and phase separation. One of the approaches that can be used to investigate this aspect is to perform a Grand Canonical Monte Carlo (GCMC) simulation on this system [70]. This, however, is beyond the scope of the present study and will be a topic of future investigations.

A direct consequence of the aggregation process is the reduced mobility of the surfactant molecules as they form RM-like aggregates. Figure 5.11 shows the MSD of the surfactant molecules during the first 80.0 ps and after $\sim$ 1.0 ns (during which stable RM-like aggregates are present in the system) of the aggregation process for the small system. As expected, the MSD curve has a significantly higher slope in the dispersed state, as the molecules are free to move about randomly in the simulation box; however, their mobility reduces drastically (reduced slope) as these surfactant

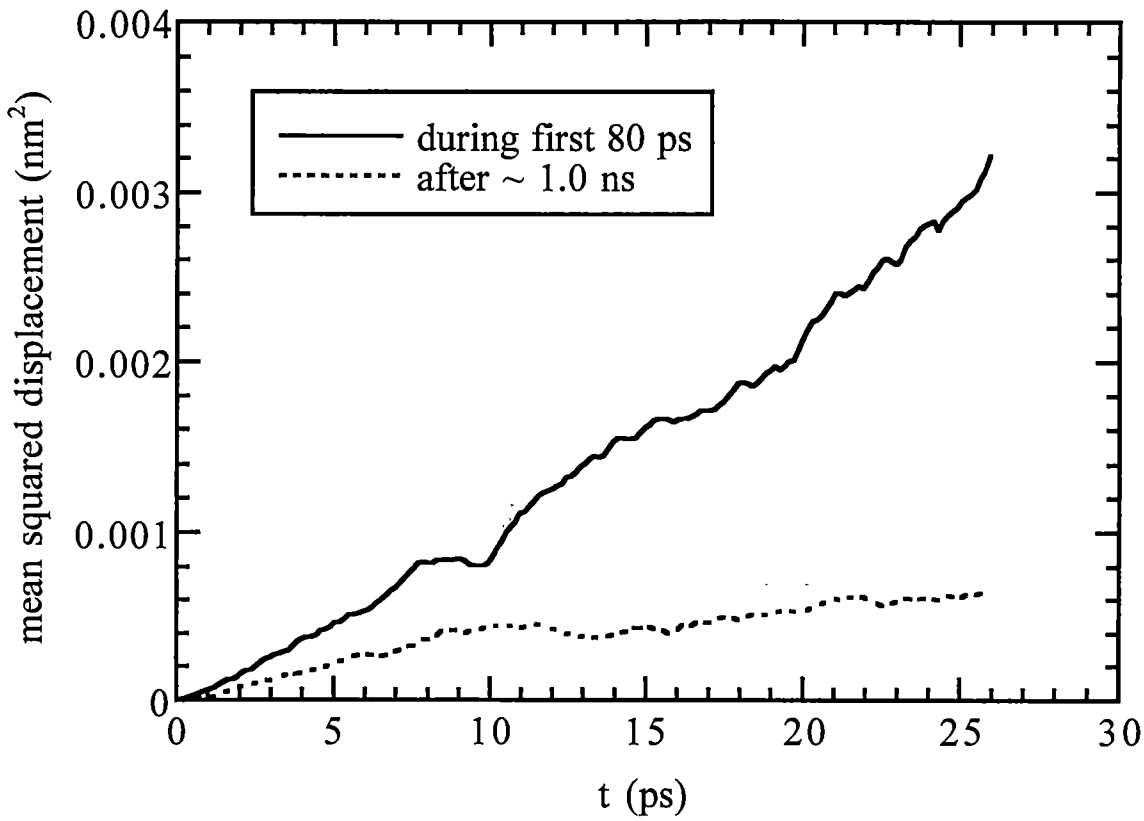


Figure 5.11: Mean-squared displacement (MSD) of the C_7-tailed hybrid surfactant during two different time periods of the aggregation process for the small system with aggregated starting configuration.

molecules are gradually incorporated into surfactant aggregates. Similar results have been observed by Brown et al. [58] for a model reversed micellar aggregate.

Another important feature observed in these simulations is the fact that the surfactant aggregates formed in the system scavenge almost all the water from the solvent into their cores, as shown in Figure 5.1(d), 5.6(d) and 5.7(d). Although the large system does show some water molecules dispersed in the non-polar solvent, this represents a very small fraction (less than 1%) of the total water molecules in the CO_2 phase. Similar observations regarding the scavenging of water by RMs, have been previously reported [78, 79] for AOT in decane and dinonylnaphthalene sulfonate in benzene systems. This has been attributed to the high ionic concentration within the aqueous cores that causes a substantial reduction in the chemical potential of the water in the core, thereby providing the driving force for the transfer of water molecules from the solvent to the core of the aggregate. In a separate simulation of only water in carbon dioxide (no surfactant present), water was found to have a solubility of about 0.3 ± 0.1 mol% in CO_2 for this model system, which is in good agreement with the saturation concentration of water in CO_2 measured by Jackson et al. [80]. Thus, it can be inferred that the addition of surfactant molecules to a water + carbon dioxide system not only disperses water in the form of micro-droplets but also scavenges all the water from the solvent into the cores of the surfactant aggregates.

5.2 Aggregation dynamics

To quantify the progress of self-aggregation in a surfactant system, the parameter most often used is the rate of aggregation. In the present study, a measure of this quantity is estimated by the slope of the plot of $ln[N(t)]$ versus $ln(t)$. Figure 5.12 shows the plot for the large system with both starting configurations. The quantity

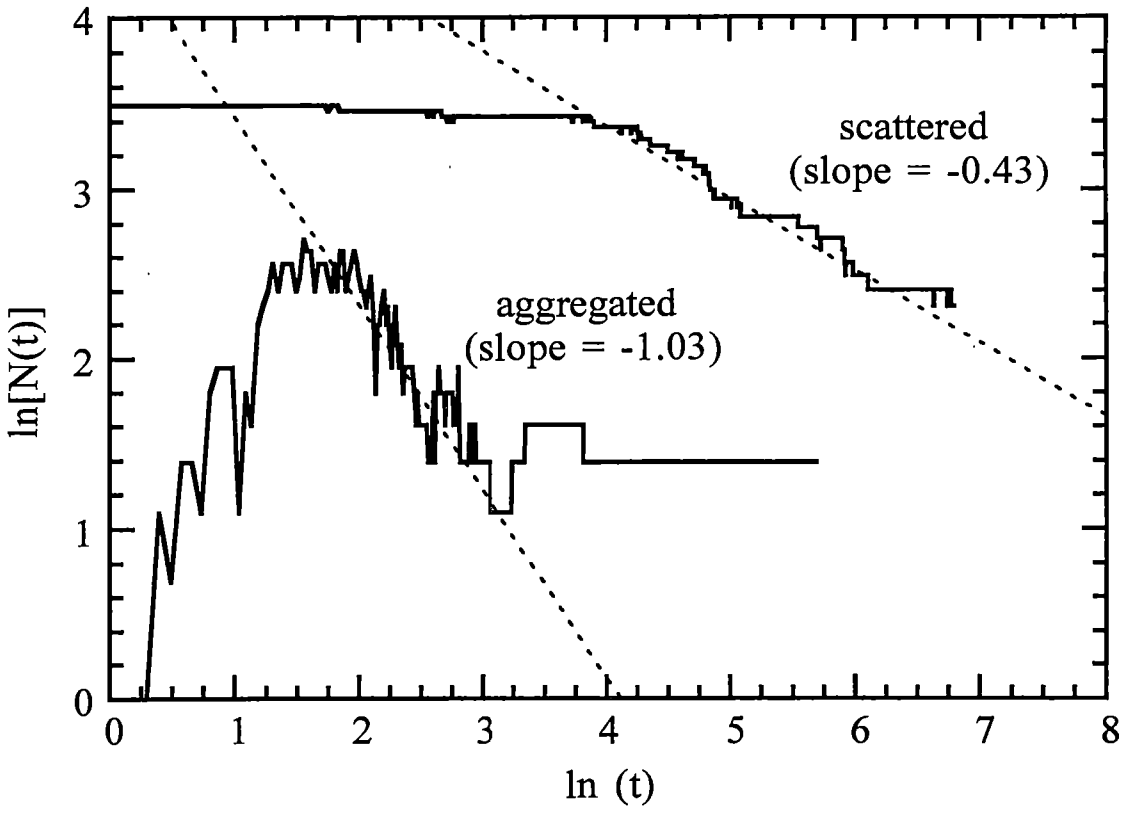


Figure 5.12: Time evolution of the number of aggregates during the simulation for the C_7-tailed dichain surfactant in the large system. The definition of an aggregate is based on the cluster counting algorithm of Sevick and co-workers [81].

$N(t)$ represents the total number of surfactant aggregates present in the system at any instant of time. In this work, $N(t)$ is calculated based on an efficient cluster-counting algorithm proposed by Sevick et al. [81] according to which any two particles are considered members of the same cluster if they lie within a particular distance of each other. In the present study, the atomic sites of the water molecules, surfactant head groups, and Na^+ (sites in the tail groups are not considered) are considered as part of the same cluster if their center-of-center distance is 3.3 Å. Also, according to the definition of a surfactant aggregate adopted in this study, a cluster of molecules classifies as an aggregate if it contains at least one surfactant molecule. Thus, clusters of only water molecules are not counted in $N(t)$. Strictly speaking, surfactant aggregates with only one or two surfactant molecules are not really micellar aggregates. Instead, they simply represent (pre-micellar) surfactant aggregates that may eventually aggregate to form stable RM-like aggregates in the system. It should be stated that this definition of an aggregate is somewhat arbitrary and was chosen solely for the sake of convenience. Figure 5.12 shows that $ln[N(t)]$ has an inverse linear dependence on $ln(t)$ with a slope of -0.43 for the scattered starting configuration. If it is assumed that the aggregation curve follows this slope for long times, then the figure suggests that aggregation process in this system should result in the formation of a single surfactant aggregate consistent with Eastoe et al. [54] in $\sim$ 200 ns. Unfortunately, the simulation time of $\sim$ 200 ns is beyond the practical limits of this simulation study.

For the aggregated starting configuration, the shape of the aggregation curve in Figure 5.12 shows a portion with positive slope followed by a portion with negative slope and finally a portion where $ln[N(t)]$ remains constant. By fitting a straight line through the portion of the aggregation curve with the negative slope, a value of $\sim$ -1.04 is obtained. The magnitude of this slope is significantly higher than that for the scattered starting configuration ($\sim$ -0.43) and is consistent with the fact that the

aggregated starting configuration is much closer to the expected final state (a single surfactant aggregate as observed by Eastoe et al. [54]) compared to the scattered starting configuration.

The inverse linear dependence over a limited range of time implies that the aggregation behavior can be well represented by a scaling relation of the form $N(t) \sim t^{-z}$ over this range, where z is the absolute value of the slope of the aggregation curve. This type of aggregation behavior is consistent with the Smolouchowski's theory of diffusion-limited aggregation [82] according to which the rate of aggregation in a system of interacting particles can be represented by a rate equation of the form

$$\text{Rate of aggregation} = K_{ij} n_i n_j \tag{5.1}$$

where n_i and n_j are the number of aggregates of size i and j respectively, and K_{ij} is called the rate kernel, which is a function of aggregate diffusivity. The basic assumption involved in this theory is that the probability of aggregation upon collisions between aggregates (or surfactants) is constant i.e.

$$\frac{[\text{collisions contributing to aggregation}]}{[\text{total collisions}]} = \text{constant}$$

As shown in Equation 5.1, according to this theory the rate of aggregation depends on two factors: the concentration of the aggregating particles and their diffusivity. In essence, this implies that the rate is essentially governed by the frequency of collisions between aggregating particles. The applicability of the Smolouchowski's theory of aggregation to the system under consideration can be explained as follows. During the early stages of aggregation most of the water and surfactant molecules are present mainly as monomers. Thus, the concentration (n_i) is high. The value of the rate kernel (K_{ij}) is also high because of higher diffusivity of dispersed surfactant molecules (Figure 5.11). As a result the frequency of collisions is quite high in the

early stages of the aggregation process resulting in high rate of aggregation. However, as aggregation proceeds n_i reduces since the concentration of aggregating particles reduces and simultaneously K_{ij} also reduces because the aggregating particles become larger. Thus, as time proceeds the frequency of collisions reduces resulting in reduced rates of aggregation. Figure 5.13 shows a plot of the diffusivity of aggregates (D) versus $m^{\frac{1}{3}}$, where m is the mass of the aggregate. The quantity $m^{\frac{1}{3}}$ is an approximate measure of the diameter of the aggregate. The figure shows that for the large system with both starting configurations the diffusivity versus $m^{\frac{1}{3}}$ shows a nearly linear dependence with a negative slope. Thus, it can be implied that the Stokes-Einstein relation ($D = \frac{kT}{3\pi\mu d}$, where T is the temperature, μ is the viscosity of the solvent, and d represents the diameter of the particle) is valid for the diffusivity of surfactant aggregates formed in the system under investigation i.e the diffusivity of the surfactant aggregates varies inversely with their size (diameter) under conditions of constant solvent viscosity and constant temperature.

An important aspect of the aggregation behavior observed in this system, is the effect of steric resistances on aggregation offered by the two tails of the dichain surfactant molecule. The steric resistances arise because of the typical structure of the aggregates formed in this system. As stated earlier, the RM-like aggregates formed in this system are characterized by the presence of an aqueous core, which consists of closely assembled surfactant head groups, while the tails surround this aqueous core forming a corona. Since the aqueous cores of two colliding aggregates should come in contact with each other to form a larger aggregate, successful aggregation involves overcoming the steric resistances offered by the respective coronas. As a result only a small fraction of aggregate collisions are expected to be successful in the formation

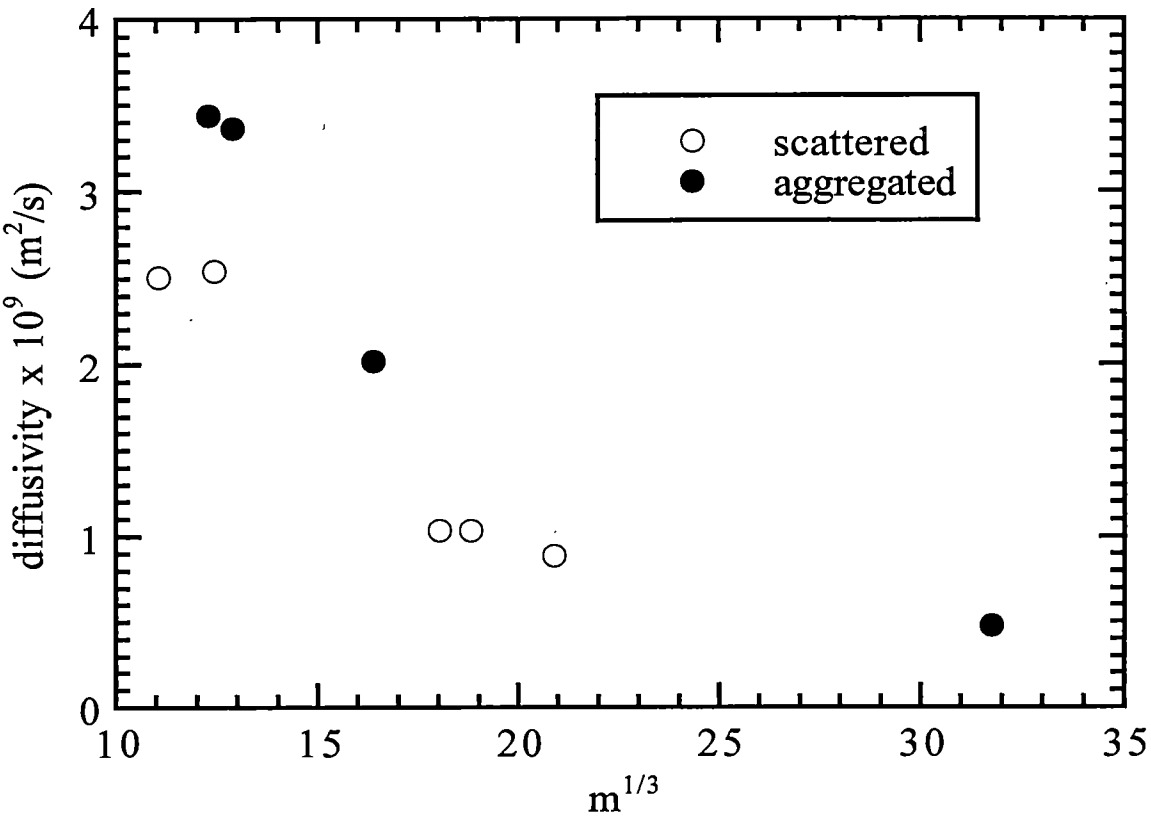


Figure 5.13: Variation of the diffusivity of surfactant aggregates with $m^{\frac{1}{3}}$ for the large system.

of larger aggregates i.e.

$$\frac{\text{[collisions contributing to aggregation]}}{\text{[total collisions]}} \ll 1$$

This is shown in Figures 5.14(a)-(b), which plots the time evolution of $N_{coll}(t)$ and $N(t)$, respectively, where $N_{coll}(t)$ represents the number of "collision aggregates" at any instant of time. As the name suggests, a "collision aggregate" is an aggregate formed when any two parts of surfactant molecules or aggregates (tail groups included) satisfy the distance criteria ($\leq$ 3.3 Å) mentioned earlier. The figures show that $N_{coll}(t)$ varies much more frequently with time than $N(t)$ showing many instances of $N_{coll}(t)$ decreasing by one or more units and then immediately returning to its previous value (a collision that did not result in aggregation), indicating that numerous collisions between surfactant molecules or aggregates are required before coalescence occurs. To further investigate the effect of steric resistances, a simulation of the large system (scattered starting configuration) without surfactant molecules (water in CO_2 only) was performed. Figure 5.15 shows the aggregation curve for this system along with that for the system with surfactants. The slope of the aggregation curve for the system without surfactants has a slope of $\sim$ -0.76, which is higher than that for the system with surfactants (slope $\sim$ -0.43). Clearly, the lack of steric resistances in the system without surfactants results in an enhanced rate of aggregation, compared to the system with surfactants.

Figure 5.16 shows the aggregation curve for the small system with aggregated starting configuration. As expected, the shape of the curve is similar to that for the large system with scattered starting configuration, however with a slope of -0.53. The higher slope for the small system is consistent with the fact that the rate of aggregation in the small system is enhanced due to high surfactant concentration and the supercritical state of the solvent. A caveat to this conclusion is that the difference

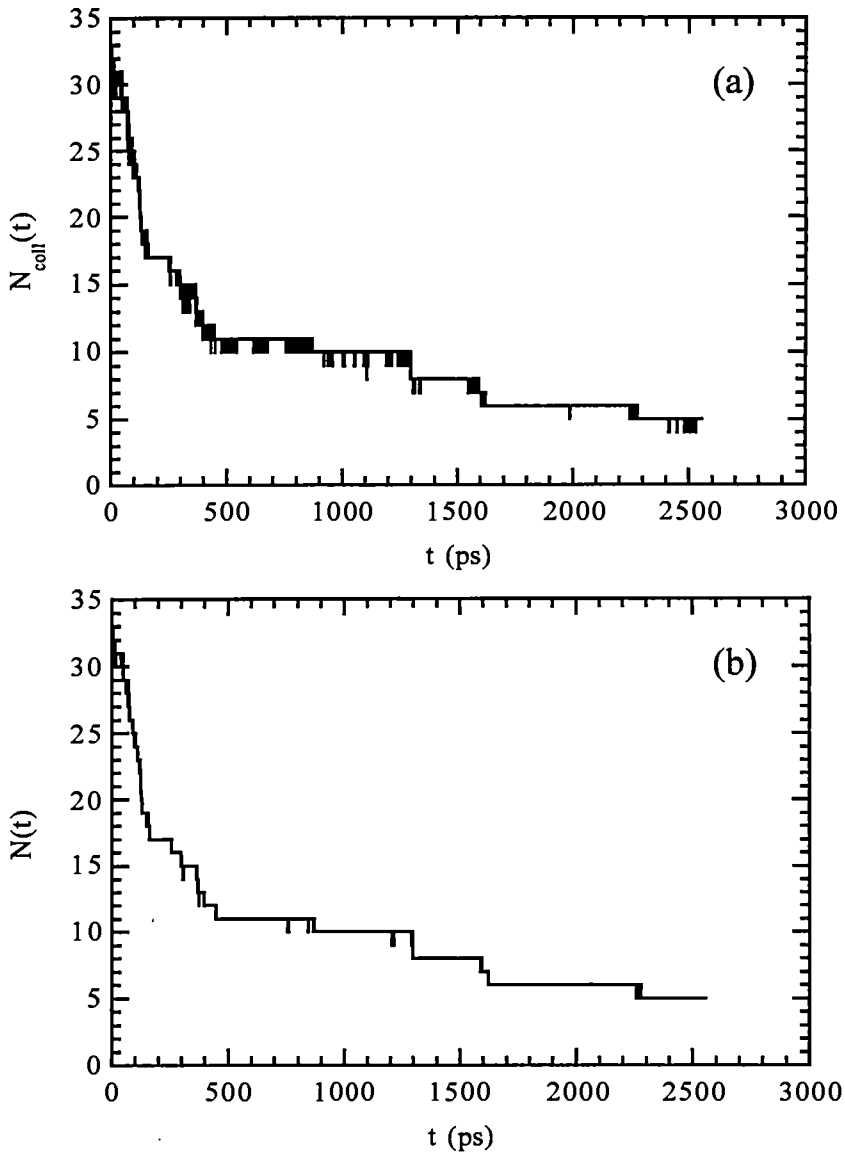


Figure 5.14: Time evolution of a) number of collision aggregates and (b) number of surfactant aggregates during the simulation for the C_7-tailed hybrid surfactant in the large system (scattered starting configuration). The definition of an aggregate is based on the cluster counting algorithm of Sevick and co-workers [81].

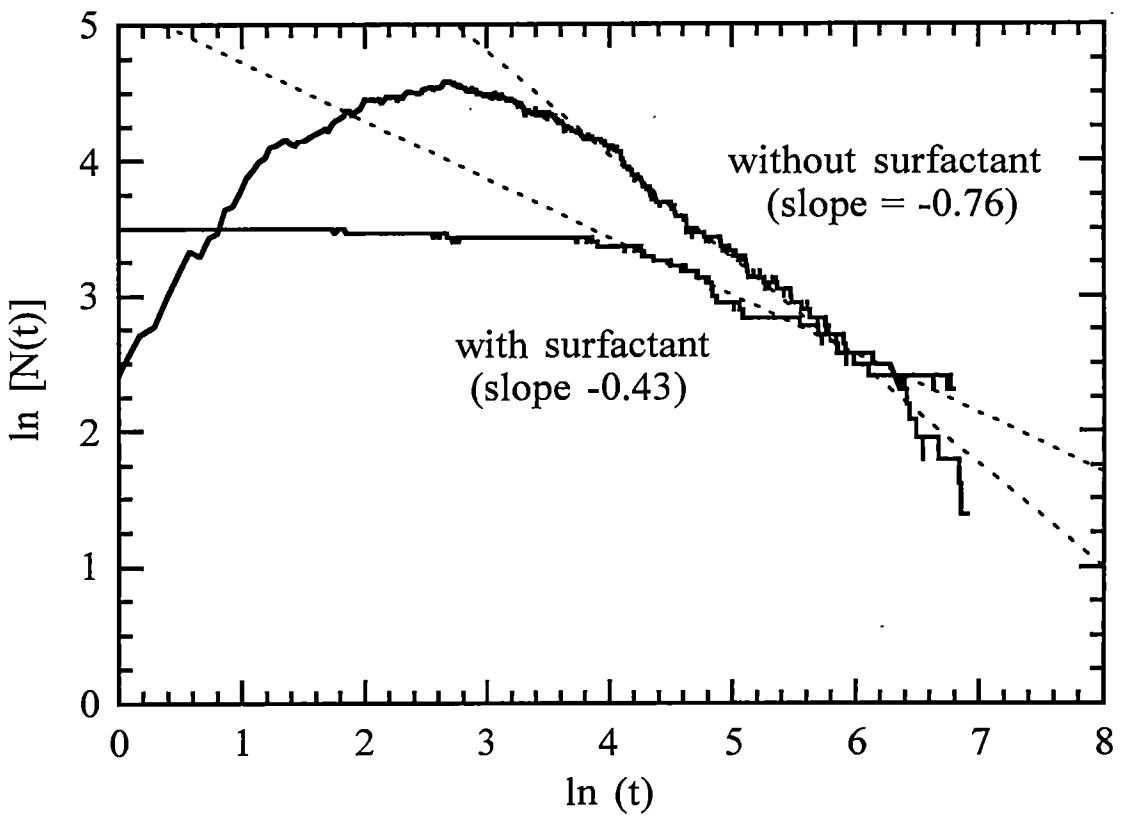


Figure 5.15: Time evolution of the number of aggregates during the simulation for the C_7-tailed hybrid surfactant in the large system (scattered starting configuration) with and without surfactant molecules. The definition of an aggregate is based on the cluster counting algorithm of Sevick and co-workers [81].

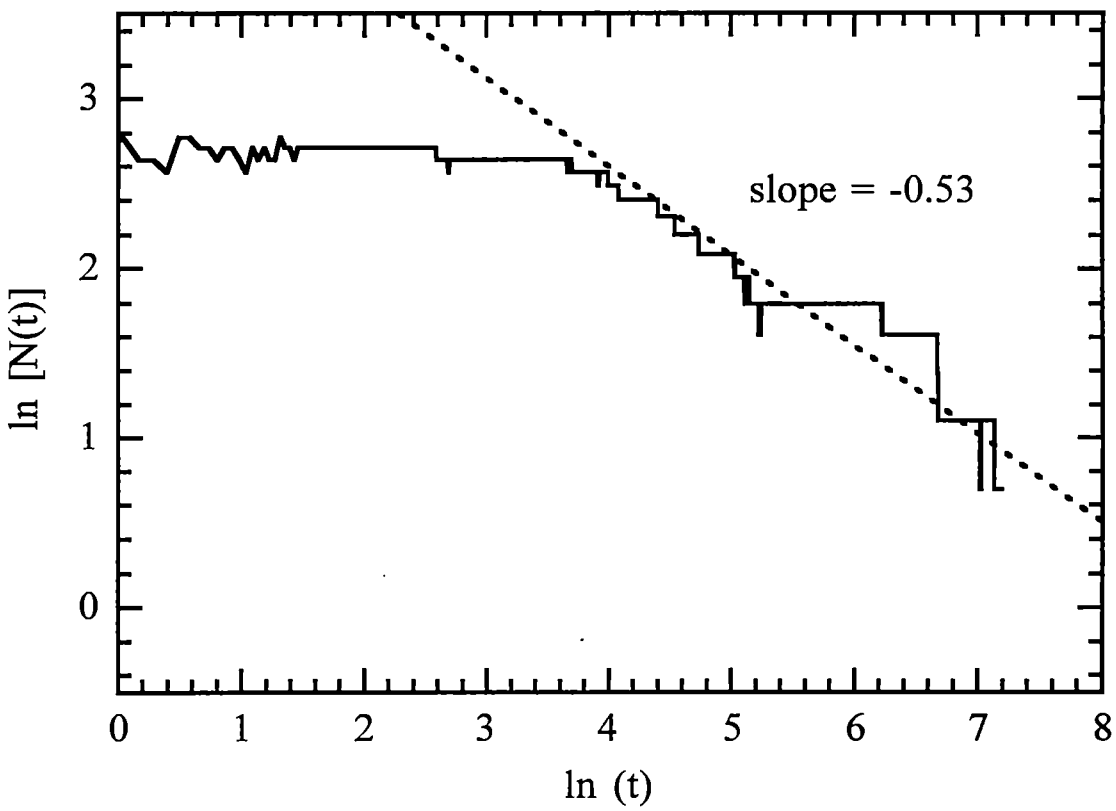


Figure 5.16: Time evolution of the number of aggregates during the simulation for the C_7-tailed hybrid surfactant in the small system (aggregated starting configuration). The definition of an aggregate is based on the cluster counting algorithm of Sevick and co-workers [81].

between the slopes is small and may be statistically insignificant. As shown by Ziff et al. [82] and Meakin et al. [83], the quantitative estimates of the slopes can be improved by carrying out numerous ($\sim 10^3$) independent simulations, but this would be impractical in a study like the present one.

5.3 Aggregate structure

The general structural properties of the RM-like aggregates formed in the simulations presented above, can be characterized by the shape and size of their aqueous cores. A good measure of the size is the radius of gyration (R_g), which is a measure of the distribution of the mass of atomic groups or molecules that constitute the aqueous core relative to its center of mass. Since the core is essentially made up of water molecules, sodium ions and anionic head groups, the mass of only these groups is considered in the estimation of R_g. Thus, the R_g of the aqueous core can be calculated by the equation

$$R_g^2 = \sum_i m_i (r_i - r_o)^2 \tag{5.2}$$

where m_i is the mass of atom i located at a radial distance r_i from the center of mass of the aggregate core (r_o). The shape of the aqueous core can be quantified using two different parameters, namely the ratio of the largest to the smallest principal moments of inertia (I_{max}/I_{min}) and the eccentricity (η). The eccentricity is calculated by the equation

$$\eta = 1 - \frac{I_{min}}{I_{avg}} \tag{5.3}$$

where I_{avg} is the average of all the three components of the principal moment of inertia. Both these parameters provide a measure of the deviation from a perfectly spherical object ($I_{max}/I_{min} = 1$, $\eta = 0$). The uncertainty in the values of these

Table 5.1: Structural properties of the largest aggregate formed in the large simulation system (aggregated starting configuration)

	This work	SANS experiments [54]
Water	916 ± 10	-
Surfactant	26	-
W_o	35.2	35.0
R_g	15.4 ± 0.2	20.5 ± 1.0
I_{max}/I_{min}	1.3 ± 0.1	-
η	0.12 ± 0.05	-
A_s (Å^2)	115 ± 3	140

parameters reflects the effect of the spatial or temporal fluctuations in the shape of the aqueous core. Together these two parameters can reveal details of the actual shape (spherical, cylindrical, or disc-like) of the aggregates.

Table 5.1 provides the structural properties of the largest aggregate formed in the large system with aggregated starting configuration (Figure 5.6(d)) along with the experimentally measured values measured by Eastoe et al. [54] via SANS experiments on the same surfactant system. As mentioned earlier, although the dynamics of the large system with aggregated starting configuration are strongly influenced by the starting configuration, the aggregates formed in this system may be close to equilibrium configurations and can be quantitatively compared to the experimental results. The radius of gyration (R_g) of the aggregate formed in this simulation study is 15.4 ± 0.3 Å. This is in a reasonable agreement with the experimentally reported value of 20.5 ± 1.0 Å [54], given that the time for which the simulation has been carried may be considerably shorter than that required to achieve an equilibrium

state. The shape parameters for the aggregate are I_{max}/I_{min} = 1.2 ± 0.1 and η = 0.1 ± 0.05 (no experimental data available), which indicates that the aggregate is nearly spherical with small fluctuations. This is expected because of the high water-to-surfactant ratio ($W_o \sim 35$) in this aggregate. The high value of W_o provides the aggregate with an aqueous core of considerably large volume (and surface area) which facilitates a reasonably low packing density of surfactant molecules around the aqueous core. To characterize the shape of the aggregates formed in the experimental investigation, Eastoe et al. [54] determined the surface area of the aqueous core per surfactant molecules (A_s), given by the equation

$$A_s = \frac{4\pi R_g^2}{N_s} \tag{5.4}$$

where N_s is the aggregation number (number of surfactant molecules in the aggregate). In essence, this quantity is a measure of the packing density of the surfactant molecules in the aggregate and thus, can be related to the shape of its aqueous core. The value of A_s for the aggregate estimated from the simulation is 115 Å^2, which is in approximate agreement with the experimentally reported value of 140 Å^2 [54].

For surfactant aggregates formed in the small system (Figure 5.1(d)), the structural properties are influenced by the low water-to-surfactant ratio ($W_o \sim 4$) in this system. Table 5.2 lists the R_g, I_{max}/I_{min}, and η values for all three aggregates shown in Figure 5.1(d). The R_g values for all the three aggregates lie within the range of 6.2 - 7.2 Å indicating nearly equal sized aggregates. The I_{max}/I_{min} values for all the three aggregates are significantly greater than unity and the values are significantly greater than zero. Thus, the aggregates formed are highly non-spherical compared to those formed in the large system. Clearly, the low W_o in this system results in aggregates with much smaller aqueous cores (smaller R_g), thereby resulting in significantly higher packing density of surfactant molecules. Another factor that may

Table 5.2: Structural properties of surfactant aggregates formed in the small simulation system (aggrega ted starting configuration)

	Aggregate #1	Aggregate #2	Aggregate #3
Water	26	57	49
Surfactant	10	9	11
W_o	2.6	6.3	4.4
R_g (Å)	6.2 ± 0.1	7.2 ± 0.2	6.9 ± 0.1
I_{max}/I_{min}	1.8 ± 0.1	1.7 ± 0.3	1.5 ± 0.1
η	0.28 ± 0.02	0.27 ± 0.08	0.13 ± 0.03

also contribute to the high non-sphericity in these aggregates is the ineffective dielectric screening of ionic head groups. The simulations showed that most of the water molecules ($\sim$ 94 %) in the small system lie within the hydration shell of anionic head groups and Na^+ ions (in contrast to $\sim$ 62 % for the large system) and thus very few water molecules were available to provide the dielectric screening of ionic charges. As a result the interactions between ionic charges leads to the distortion of the interface. Similar results were obtained by Brown and Clarke [58] for a model reversed micelle with a low water-to-surfactant ratio ($W_o = 2$). They also observed the formation of highly non-spherical aggregates due to the ineffective dielectric screening of the ionic head groups. Interestingly, the standard deviations in the values of I_{max}/I_{min} and for these aggregates, as shown in Table 5.2, are quite low. As mentioned earlier, the deviations are a measure of the fluctuations in the shape of the aggregates. The low value of these deviations suggests that the shape of these aggregates is quite constant. Figures 5.17(a)-(b) show the time evolution of the I_{max}/I_{min} and η for the three aggregates. The deviations are more prominent in aggregate number 2 than in

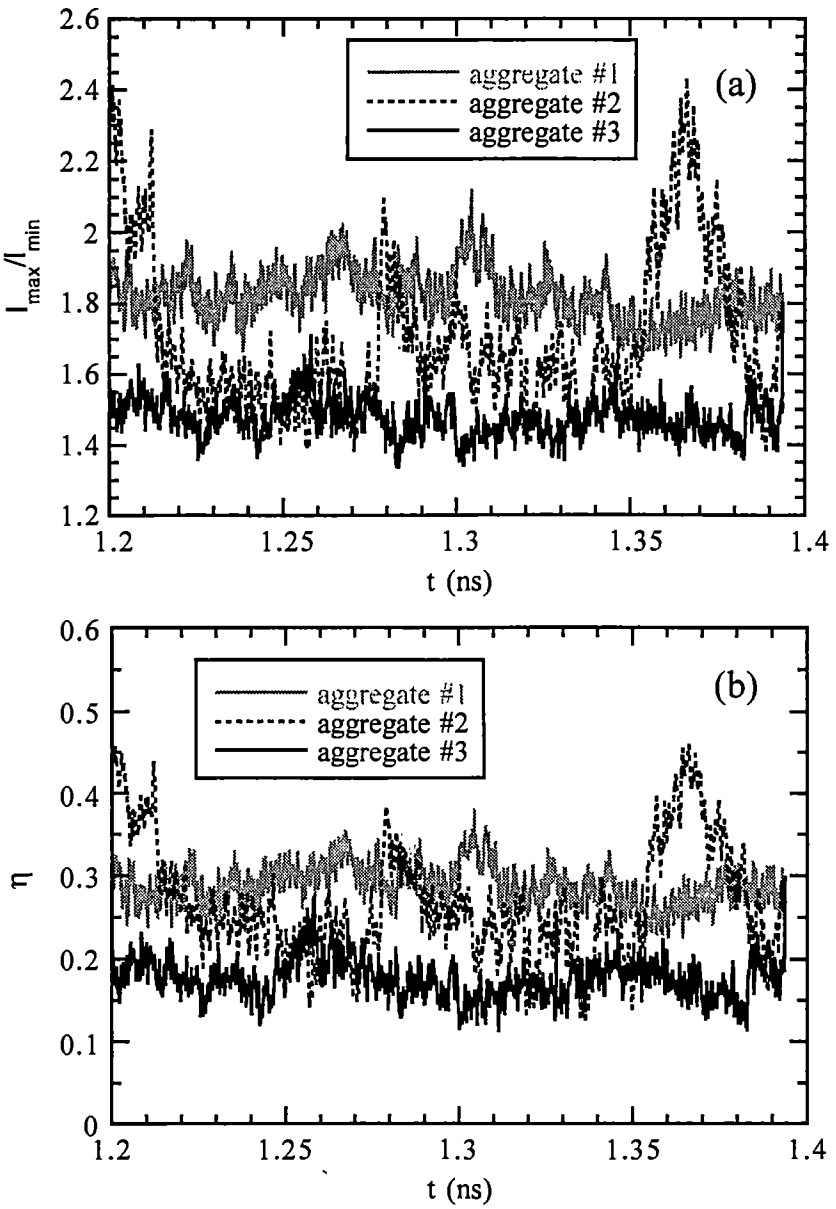


Figure 5.17: Time evolution of the shape properties of the three aggregates formed in the small system with aggregated starting configuration, (a) I_{max}/I_{min} (b) η.

the other aggregates. This can be attributed to a slightly higher water-to-surfactant ratio in this particular aggregate ($W_o \sim 6$) compared to the other two aggregates.

5.4 Aggregate Microstructure

Having established that the structure of the largest aggregate formed in the large system with aggregated starting configuration is in reasonable agreement with the experimental findings, it is logical to explore the microstructure of this aggregate. Molecular simulations provide an effective tool to obtain this information. A primary measure of the microscopic structure is the singlet distribution function (singlet radial density) profiles of the various atomic groups or molecules constituting the aggregate. As the name suggests, the singlet distribution function is a time-averaged measure of the distribution of an atom or molecule from a reference point. It is calculated by the equation

$$\rho(r) = \frac{\langle N(r) \rangle}{4\pi r^2 \Delta r} \tag{5.5}$$

where $\langle N(r) \rangle$ is the time-average of the number of an atom or molecule that is found in a shell of thickness Δr at a radial distance r from a reference point. The center of mass of the aqueous core represents a suitable reference point.

Figures 5.18(a)-(b) show the microscopic details of the largest aggregate formed in the large system with aggregated starting configuration. Figure 5.18(a) shows the density profile of water and CO_2 (solvent) molecules. The density of water in the aqueous core is $\sim$ 1.0 g/cc indicating the presence of bulk-like water. A considerably broad ($\sim$ 10 - 15 Å) interfacial region is observed, where the water density decreases while the CO_2 density increases as the distance from the center of mass of the increases. The solvent density approaches its bulk density of $\sim$ 0.85 g/cc outside the interfacial region. Negligible penetration of the solvent molecule into the aqueous core

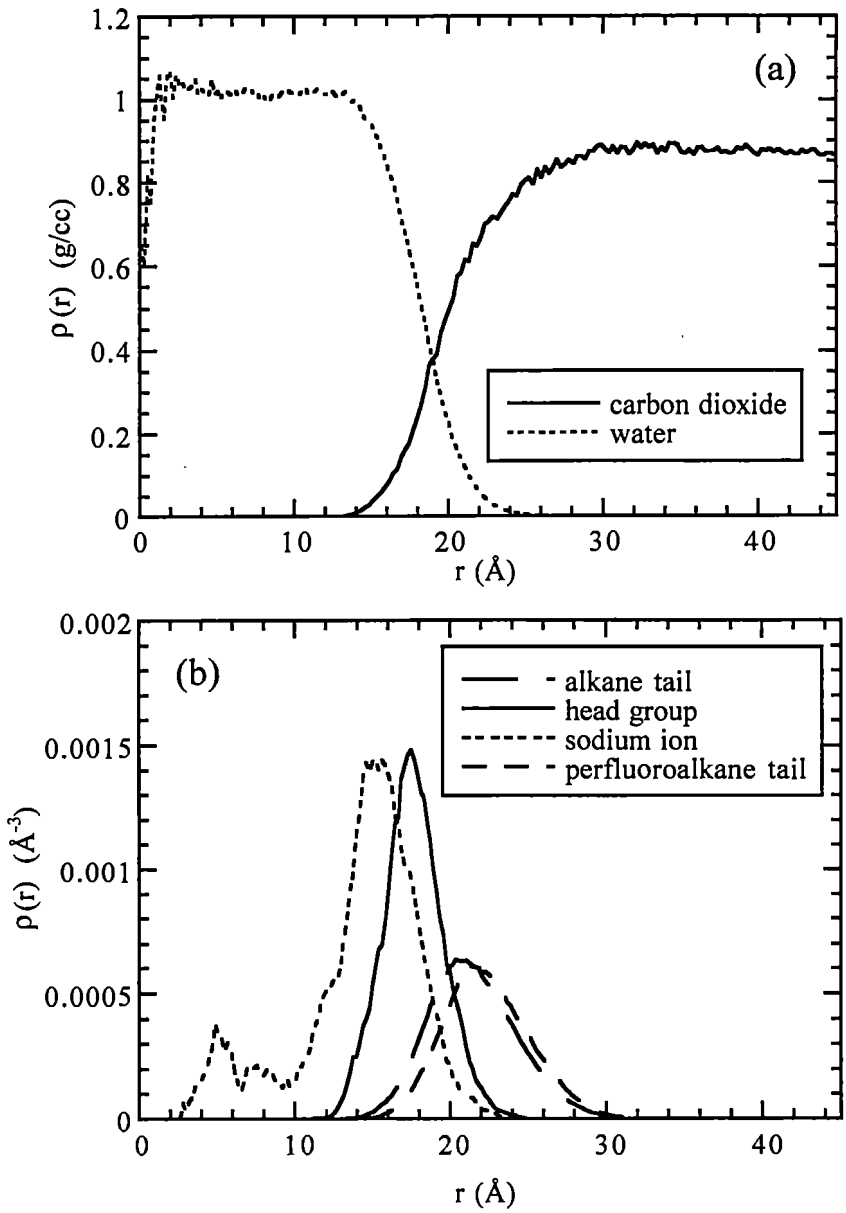


Figure 5.18: Structural properties of the aggregate formed in the large system with aggregated starting configuration, (a) water and carbon dioxide (b) microstructure of surfactant molecule.

of the aggregate is observed. Figure 5.18(b) plots as a function of the radial distance (r) for the various groups of the surfactant molecules. The distribution of the head groups show a peak at $\sim$ 17.2 Å indicating the presence of head groups at the surface of the aqueous core. The distribution for the Na^+ ions is quite similar to that for the head groups implying that the Na^+ ions also reside at the surface of the aqueous core and are ion-paired to the anionic head groups. The high degree of ion pairing in this aggregate will be more clearly evident in Section 5.6. The distribution of the two tails suggests that the tails form the corona of the aggregate. The distribution of the perfluoroalkane tail is shifted slightly away from the center of mass and is an indication of its CO_2-philic behavior.

Figure 5.19 shows the singlet radial density curves for water, sodium ion, anionic head group, and the two tails for the aggregates formed in the small system (Figure 5.1(d)). The figure shows that the core of the aggregates is essentially made up of water molecules and the sodium ions. The head groups lie at the surface of the aqueous cores while the tails form the corona surrounding the cores. The non-zero radial density of the head groups within the core ($r \leq 6.2$ Å) is not due to the penetration of the head groups but simply an artifact of the highly non-spherical shape of these aggregates (Table 5.2). Also, the presence of numerous peaks and troughs in the radial density distribution of the sodium ions and anionic head groups is a manifestation of the rigid structure of the aqueous core. The radial density distributions of the two tails are quite similar except a slight shift away from the center of mass observed for the perfluoroalkane tail. As mentioned earlier, this is due to the CO_2-philic nature of this tail.

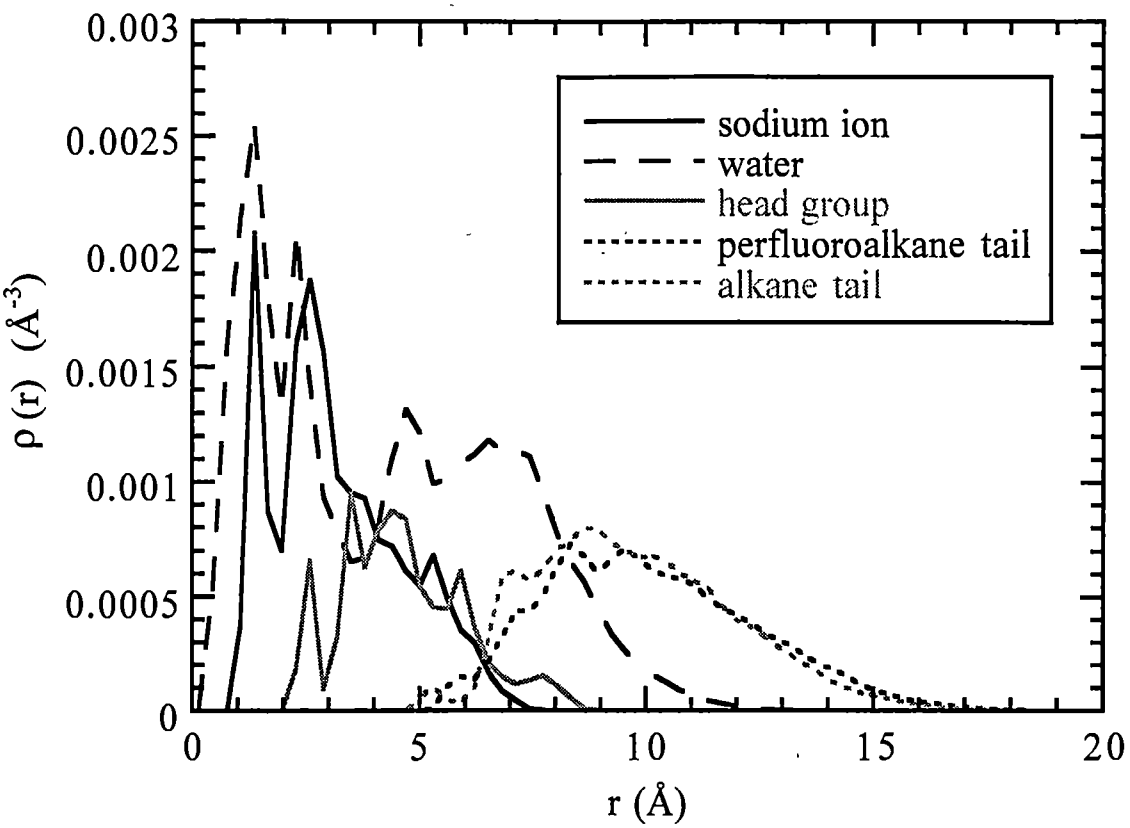


Figure 5.19: Radial density profiles of the water molecules, sodium ions, sulfate head group, perfluoroalkane tail, and alkane tail from center of mass of the aggregate for the small system with aggregated starting configuration.

5.5 Tail conformation

A good measure of the CO_2-philic behavior of the two different tail groups is the degree to which these tails are fully extended. Figure 5.20 plots the fraction of torsional angles in each tail that are in trans conformation (fully stretched) as a function of time for the small system with aggregated starting configuration. Similar results were obtained for the large system. The perfluoroalkane tails have an average of 90 $\pm$ 2 % trans conformation compared to 74 $\pm$ 5 % for the alkane tails. This implies that the perfluoroalkane tails are approximately 16 % more extended than the alkane tails. Interestingly, the behavior of the two tails is quite opposite in *vacuo*. The perfluoroalkane tail has a trans conformation of 80 % in *vacuo* compared to 89 % for the alkane tail. Thus, in presence of carbon dioxide as a solvent medium, the perfluoroalkane tails assumes more extended conformations, which is an indication of its CO_2-philic nature while the alkane tails are less extended indicating their CO_2-phobicity.

More detailed information on the spatial conformation of the two tails can be obtained by calculating the distribution of the radial position of each segment (functional group) of the tails from the CH group, as shown in Figure 5.21. The common feature of the two tails evident from the figure is the progressive broadening of the distribution for groups farther away from the head group. The broadening is relatively larger for the alkane tail compared to that for the perfluoroalkane tail because of the relative stiffness of the perfluoroalkane tail. Also, the distributions of the first two segments are the same for the two tails. The broadening is attributed to the fact that the farther away the segment is from the head group the more freedom it has to move. This mobility is due to the ability of torsional angles associated with these segments to switch back and forth between trans and gauche conformations.

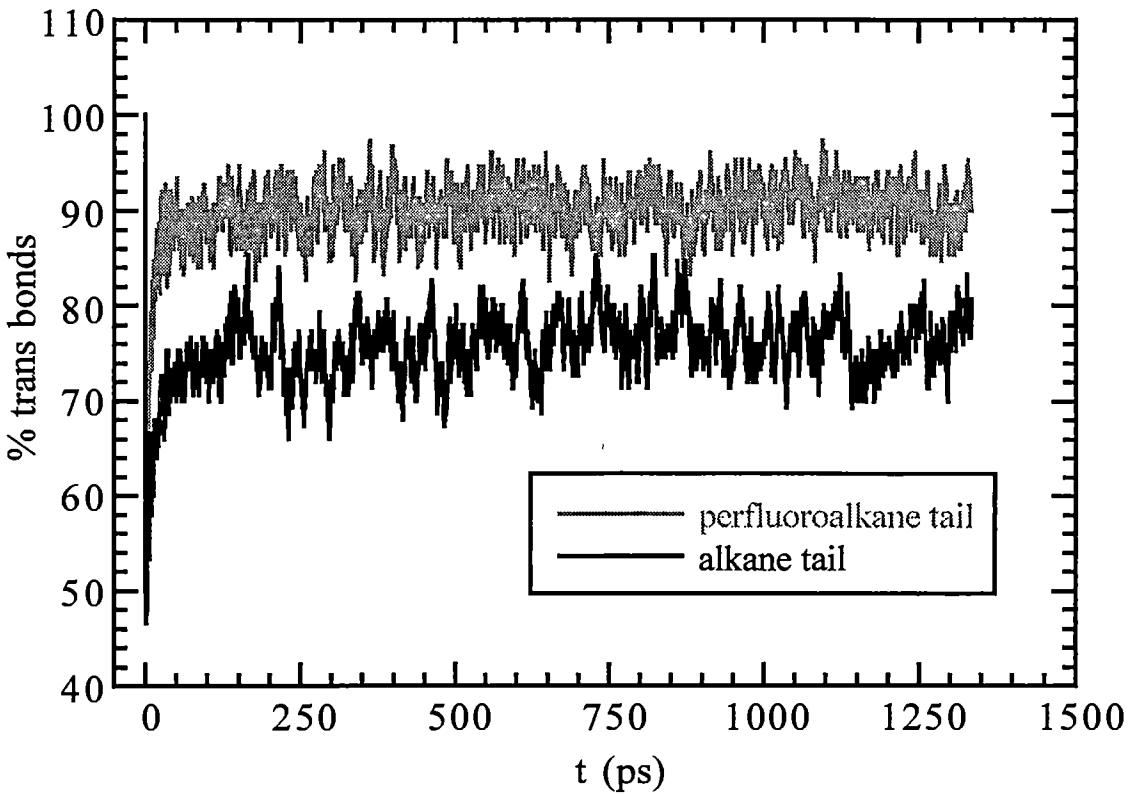


Figure 5.20: Time evolution of the % trans bonds (extent of fully extended tails) for the perfluoroalkane tail and the alkane tail of the C_7-tailed hybrid surfactant for the small system with aggregated starting configuration.

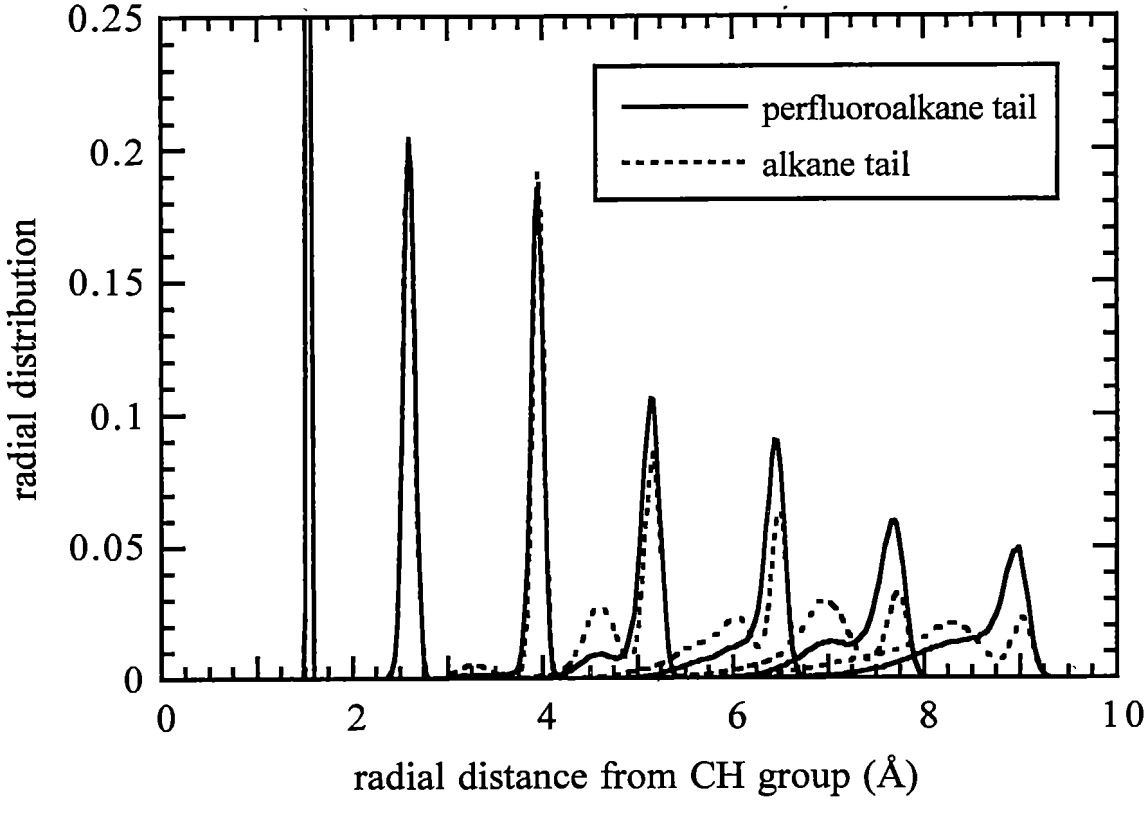


Figure 5.21: Radial distribution of the functional groups of the perfluoroalkane tail and the alkane tail for the C_7-tailed hybrid surfactant for the small system with aggregated starting configuration.

For the alkane tail the distribution of farther segments exhibit two distinct peaks indicating near equal probability of gauche and trans conformation of the torsional angles associated with these segments.

5.6 Structure of aqueous core

As shown earlier, the surfactant aggregates formed in this simulation study are characterized by the presence of an aqueous cores. These aqueous cores can provide a medium for solubilizing polar and/or polymeric substances in CO_2. Thus, understanding the detailed structure of water in these aqueous cores is of fundamental importance in understanding the solubilization characteristics and behavior of solutes. The aqueous environment in these cores is somewhat different from that encountered in typical electrolyte solution because of the high ionic concentration and its non-uniform distribution.

To get an insight into the detailed structural characteristics of the aqueous cores, Figures 5.22(a)-(b) plot the radial distribution function (rdf) and running coordination number (rcn) respectively, for Na-Na and Na-X pairs (X = anionic head group) in the large aggregate shown in Figure 5.6(d). As discussed earlier, the structural properties of this surfactant aggregate are closest to the RMs observed by Eastoe et al. [54] via SANS experiments. The usual interpretation of rdf is not applicable here, since the environment of the reference ion is anisotropic, even at small distances. As a result, the rdf decays to zero with increasing radial distance instead of approaching unity as observed for isotropic systems. However, the rcn has its normal interpretation i.e. it represents the number of neighbors in the radial direction. Figure 5.22(a) shows that Na-X rdf has a prominent first peak at 2.45 Å and a minimum at 3.2 Å. The second peak in the rdf is due to the remaining two negatively charged oxygen's

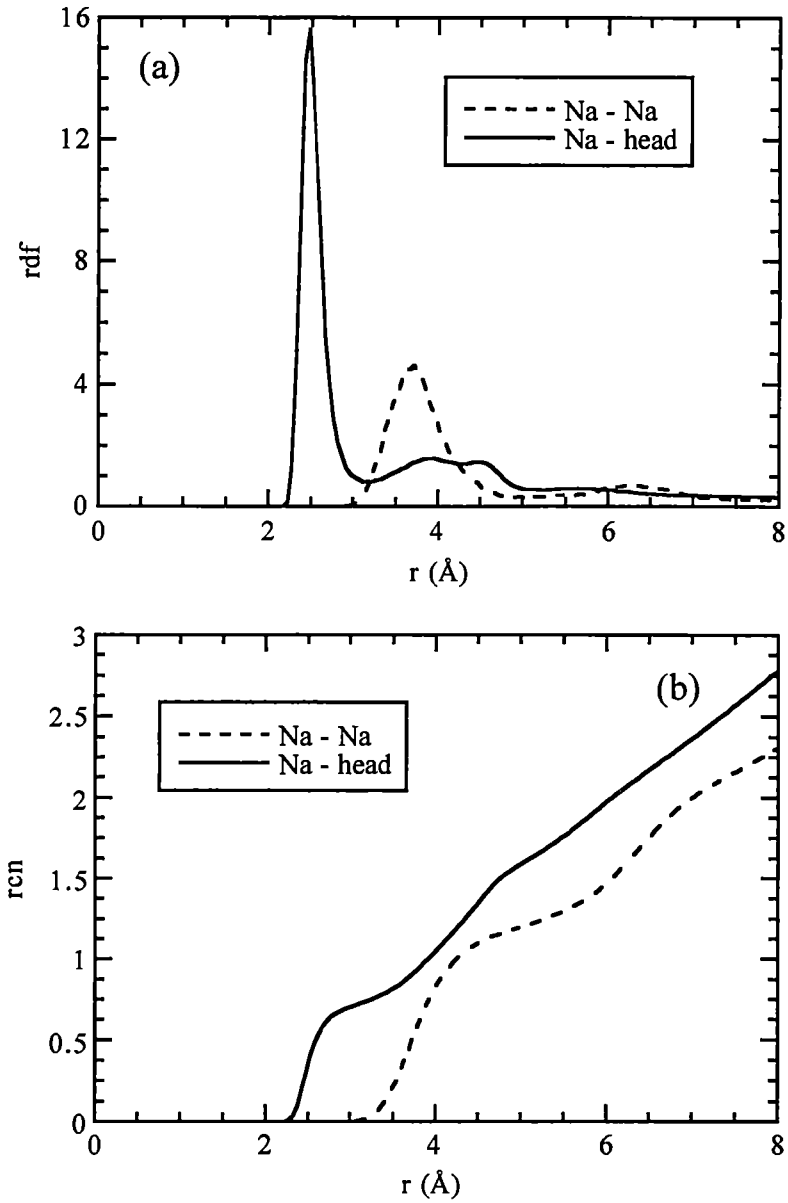


Figure 5.22: Radial distribution function (rdf) and running co-ordination number (rcn) for (a) Na-Na pair (b) Na-head group pair.

on the head group. As shown in Figure 5.22(b), the first maximum integrated up to 3.2 Å involves $\sim$ 0.75 head group. The Na-Na rdf shows a peak at 3.7 Å, a broad minimum at 5.0 Å, and a second peak at 6.3 Å, indicating a weaker ion-ion correlation, as expected. The presence of a prominent peak in Na-Na rdf is an indication of the fact that the environment of the aqueous cores is highly ionic. Figures 5.23(a)-(b) show the rdf and rcn for the Na-W (W = water) and X-W pairs. The rdf for the Na-W (Figure 5.23(a)) shows a distinct hydration shell with a maximum at 2.5 Å. A second hydration peak exists at 4.4 Å. Thus, there exist two distinct hydration shells for the Na^+ ion implying a stronger structuring of water molecules around the reference ion. As shown in Figure 5.23(b), the average number of water molecules in the first (primary) hydration ions is $\sim$ 4.1, while the average number of water in the secondary hydration shell is $\sim$ 5.0. The rdf for the X-W shows a less prominent first peak at 4.1 Å and weak second peak at 6.0 Å. The presence of a less prominent first peak in the X-W rdf may be attributed to the "correlation hole effect" [84] and is related to the particular geometry of the surfactant head groups. Since each head group has three negatively charged oxygen atoms at a fixed distance from each, a number of possibilities exist in which a particular water molecule can exist around the reference ion. As a result, the pair correlation function involves averaging over distances that involve the van der Waal diameter (σ) as well as the length scale corresponding to fixed inter-atomic distances. Thus, the peak in the X-W rdf is broader and lower. Clearly, additional simulations with different head geometry and charge distribution are needed for further clarification. The rcn for the first hydration shell of X-W shows an average number of water molecules to be $\sim$ 9.0, implying higher degree of hydration of the anionic head group compared to that of the Na^+ ion.

An important characteristic of the water molecules in the aqueous core is the extent of their hydrogen bonding. A hydrogen bond is defined to exist if any one of

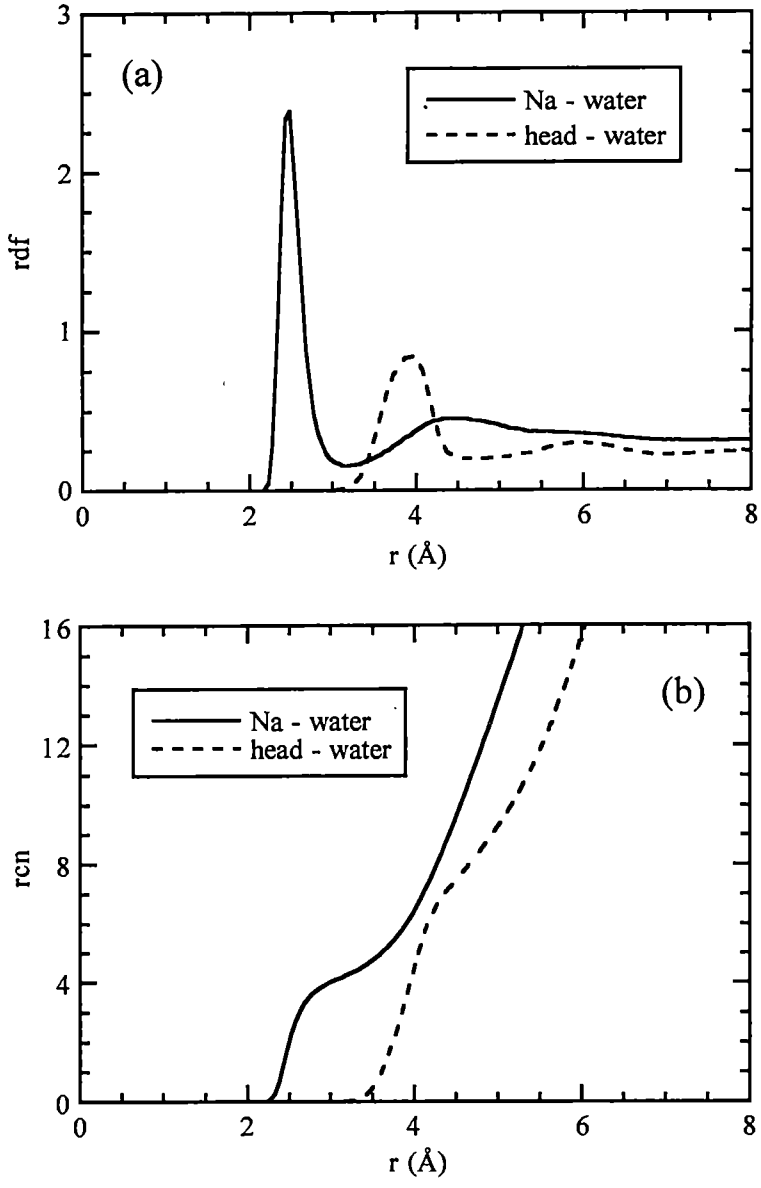


Figure 5.23: Radial distribution function (rdf) and running co-ordination number (rcn) for (a) Na-water pair (b) head group-water pair.

the O-H bonds of a particular water molecule is collinear with an oxygen atom of a neighboring water molecule. Figure 5.24 shows the typical representation of a hydrogen bond based on the geometric criteria defined above. To analyze the orientation of the water molecules, angular distribution functions (adf) are used. Figure 5.25 shows the adfs of the interparticle-dipole vector for water molecules belonging to the primary hydration shell of the Na^+ ion and sulfate head group. The adf for the Na^+ ion shows a monotonic decrease along the angular range indicating the alignment of water in such a way that the dipole of water molecules is collinear with the Na^+ ions. This is due to the strong electrostatic interaction between Na^+ ion and the negatively charged oxygen atoms of water molecules. The adf for the head group shows a peak at $\cos\phi \sim 0.6$ ($\phi \sim 53^o$) which is due to the fact that the anionic head group interacts with positively charged hydrogen atoms of the water molecules thereby aligning the water dipole at the angle of $\sim 53^o$. This clearly shows that the strong electric fields from the Na^+ ion and the anionic head group tend to orient the water dipole vectors in their primary hydration shells. As expected, the orientation effects are relatively stronger for the Na^+ ions than the head groups due to the delocalization of negative charges on the anionic head group. Figure 5.26 shows the adfs for the interparticle-bond vector angle for water molecules residing in the primary hydration, again exhibiting strong orientation effects of the two ionic species. The adf for the Na^+ ion shows a peak at $\cos\phi \sim$ -0.5 ($\phi \sim 120^o$) while the adf for the anionic head group shows a peak at $\cos\phi \sim 1.0$ ($\phi \sim 0^o$). This is another indication that the water molecules directly associated to the two ionic species are oriented in response to the strong electric fields of the ions.

For water molecules lying outside the primary hydration shell, decreases in the orientation effects are noted. Figure 5.27 shows the adf for the interparticle-dipole vector angle for water molecules residing at varying distances from the reference

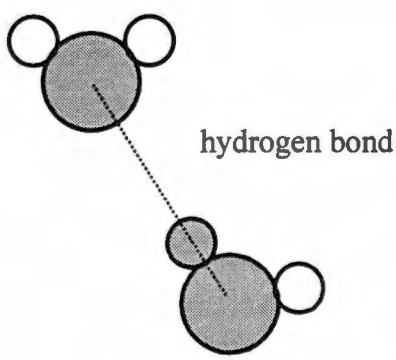


Figure 5.24: Schematic representation of the definition of the hydrogen bond adopted in this study.

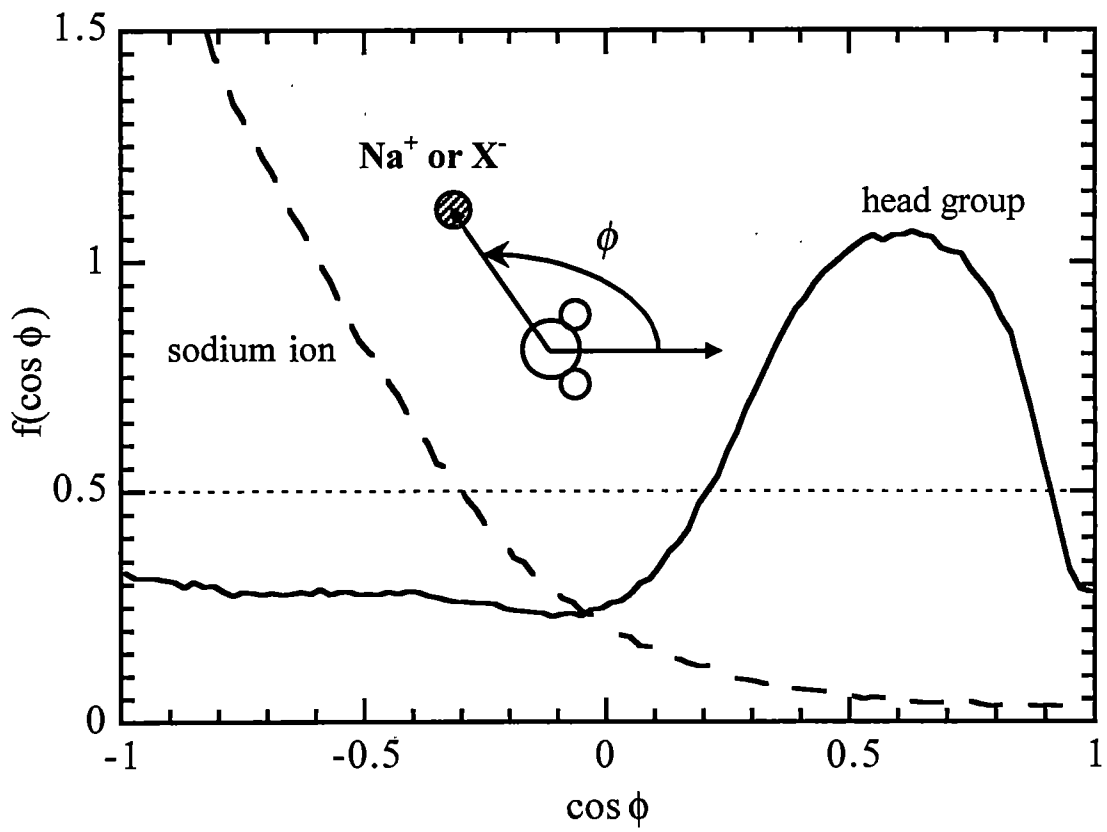


Figure 5.25: Interparticle-dipole vector angle angular distribution function (adf) for water molecules lying within the primary hydration shell of the ions.

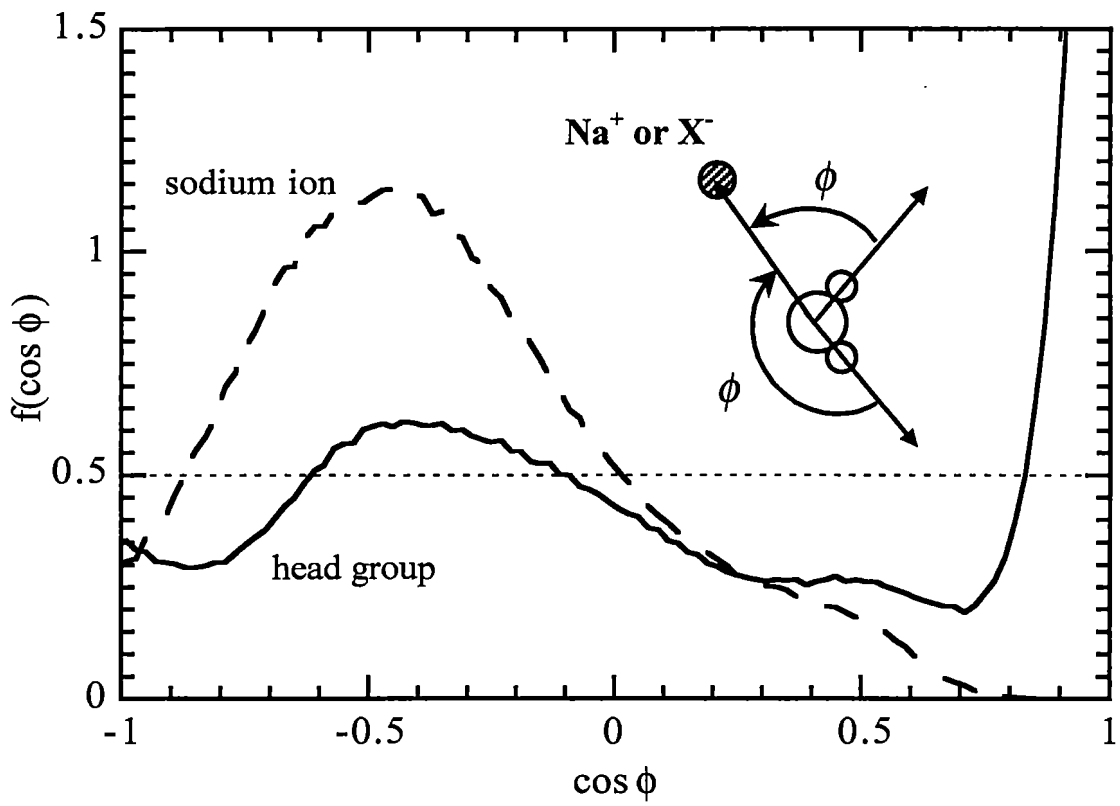


Figure 5.26: Interparticle-bond angle vector angular distribution function (adf) for water molecules lying within the primary hydration shell of the ions.

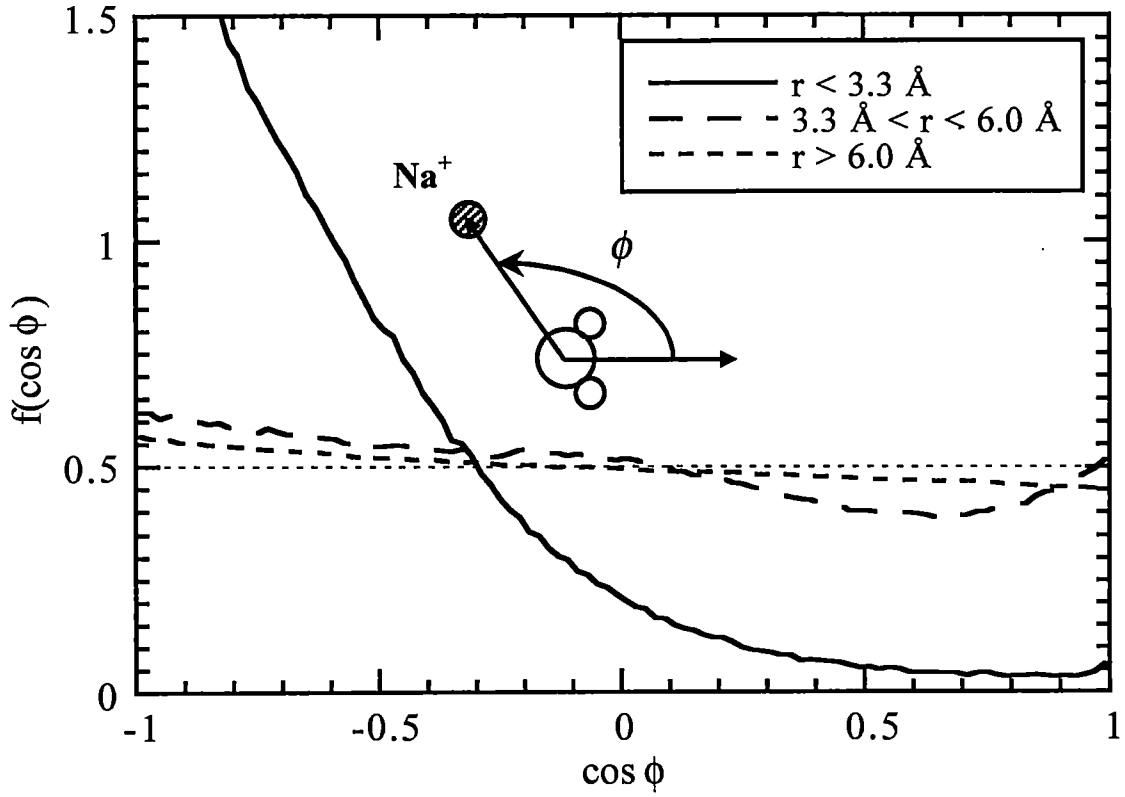


Figure 5.27: Interparticle-dipole vector angular distribution function (adf) for water molecules at varying distances from the sodium ion.

Na^+ ion. The figure clearly shows that, as the distance of water molecules from the ion increases, reduction in the orientation effects is observed. The water molecules lying within the distance of 3.3 - 6.0 Å (secondary hydration shell) show very little orientation effects compared to those in the primary hydration shell. The water molecules lying at distances larger than 6.0 Å show negligible orientation effects. Similar profiles are obtained for the adf of sulfate head group, as shown in Figure 5.28. Thus, based on this analysis the water molecules within the aggregate can be divided into two distinct classes based on their orientation to the ionic environment at the interface. The interfacial water which lies in the primary hydration shell show significant orientation effects, while the bulk-like water which lies outside the primary hydration shell are nearly unaffected. Figures 5.29-5.31 show the orientation of water molecules present in the bulk-like region of the aqueous core. Figure 5.29 shows the adf for the dipole-dipole vector angle for the water molecules. The figure shows most of the water pairs have a dipole-dipole vector angle alignment less than $\phi \sim 90^o$. Thus, water molecules exhibit a tendency to form hydrogen bonds (a hydrogen bond is defined if one of the OH bond of a water molecule is collinear with the oxygen atom of a neighboring water molecule) in the bulk-like region, as expected. Figure 5.30 shows the adf for the interparticle-dipole vector angle. The adf shows a distinct peak at $\cos\phi \sim 0.6$ ($\phi \sim 53^o$). Figure 5.31 shows the adf for the interparticle-bond vector angle and shows two peaks, one at $\cos\phi \sim$ -0.3 ($\phi \sim 107^o$) while the other at $\cos\phi \sim 1.0$ ($\phi \sim 0^o$). The two peaks correspond to the two bond vectors in a water molecule. The positions of the two peaks clearly indicate the collinearity of OH bond on the water molecules with the oxygen atom of the reference molecule.

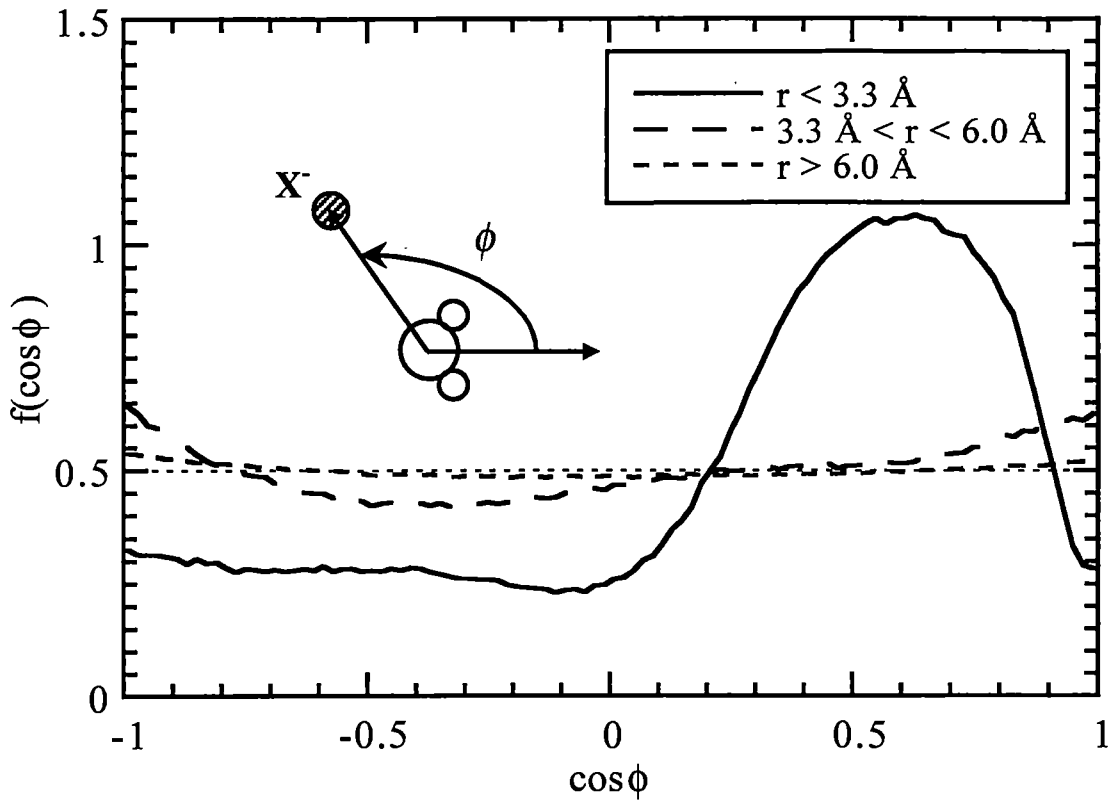


Figure 5.28: Interparticle-dipole vector angular distribution function (adf) for water molecules at varying distances from the anionic head group.

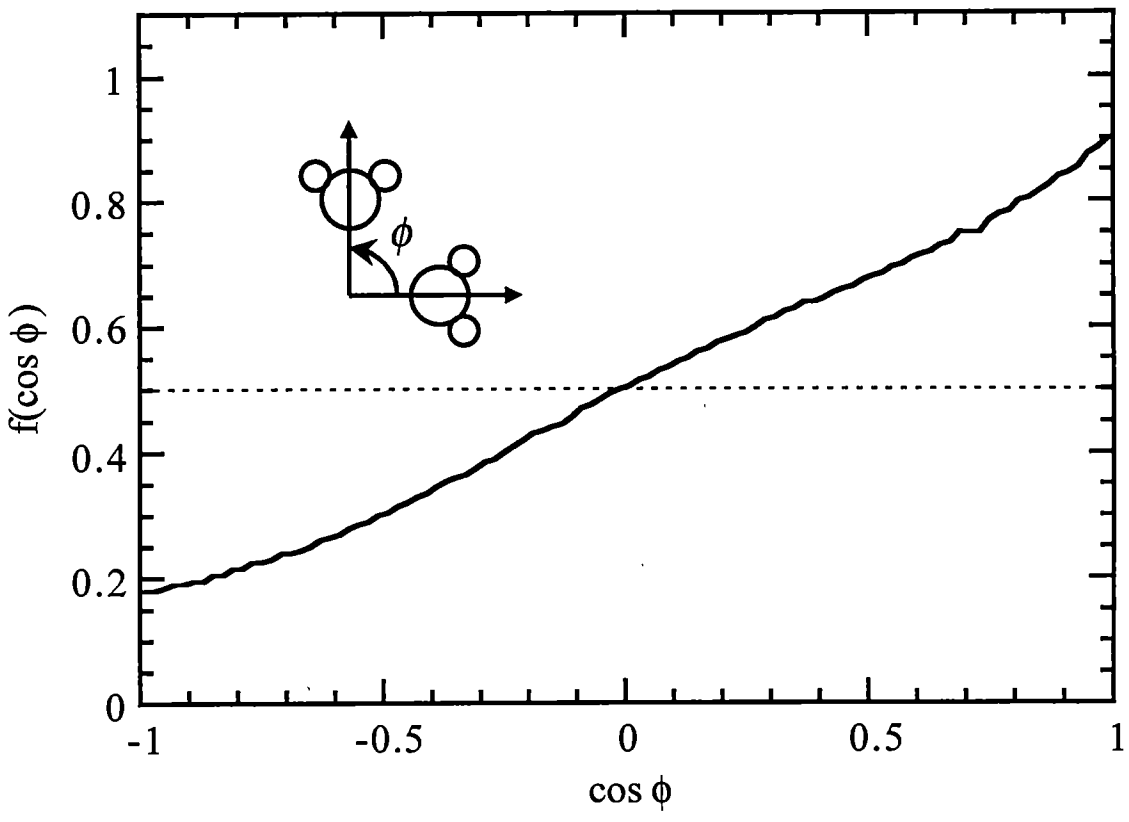


Figure 5.29: Dipole-dipole vector angle angular distribution function (adf) for water molecules within the bulk-like region of the aqueous core.

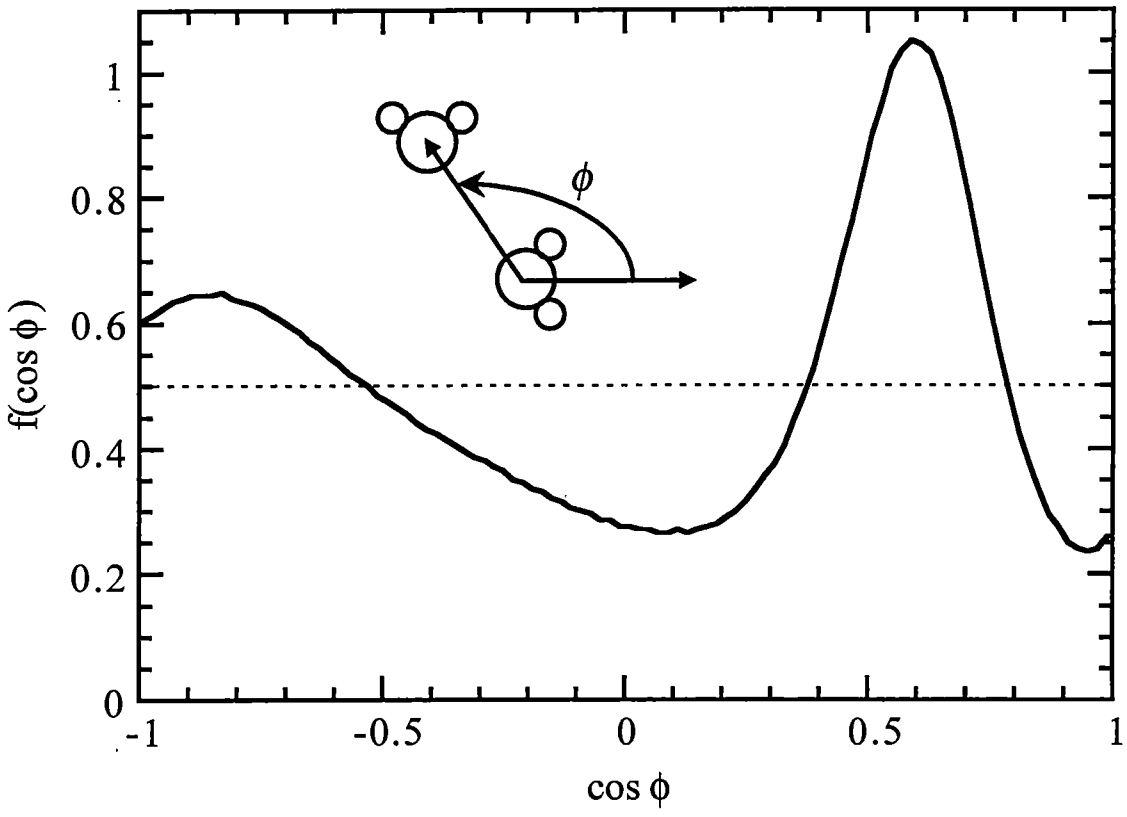


Figure 5.30: Interparticle-dipole vector angle angular distribution function (adf) for water molecules within the bulk-like region of the aqueous core.

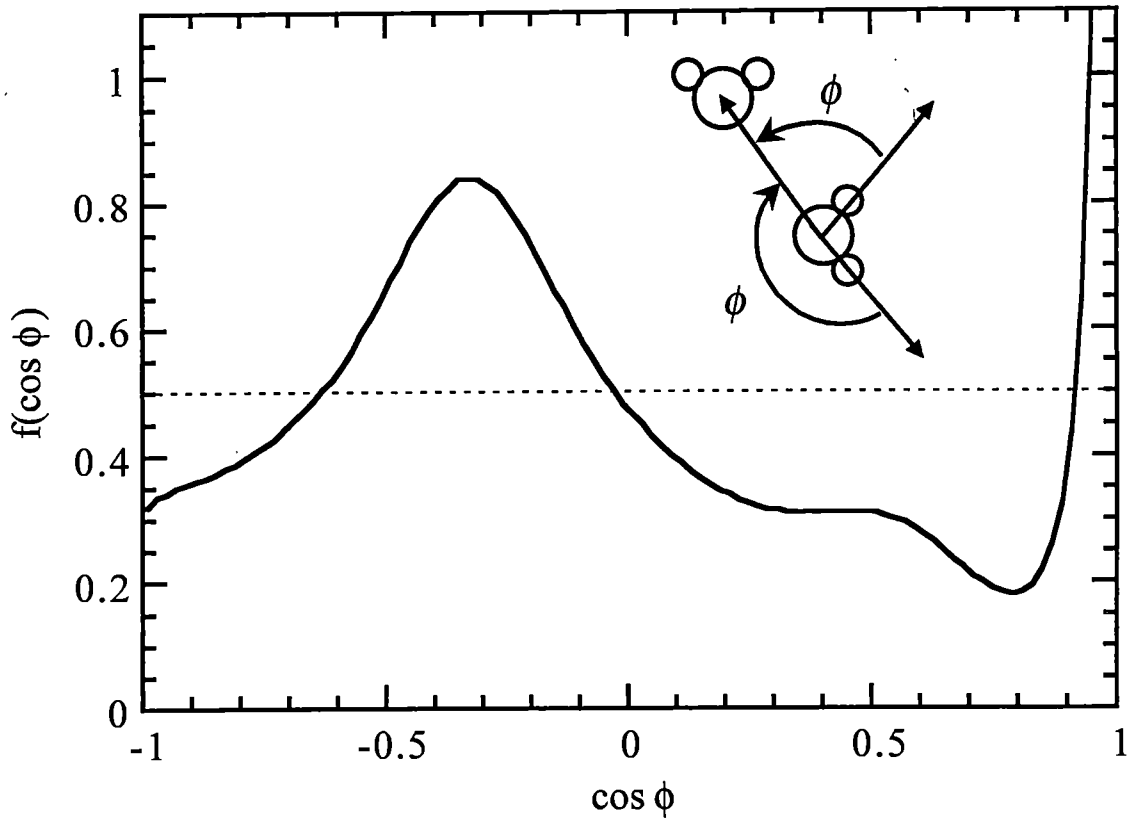


Figure 5.31: Interparticle-bond vector angle angular distribution function (adf) for water molecules within the bulk-like region of the aqueous core.

5.7 Effect of tail chemistry

An important requirement of any surfactant molecule that is intended for use in CO_2 is its CO_2-philic behavior i.e. its ability to dissolve in CO_2 in low concentrations. As shown earlier, for the dichain surfactant molecule used in this study, this behavior is imparted by the presence of a perfluoroalkane tail. Since the formation of RMs requires that the surfactant tails be bulkier than the head group [85] i.e. $v/a_o l_c$, where v is the volume of the tail groups, a_o is the optimal area of the head group, and l_c is the tail length, the function of the alkane tail is to provide the required architecture to the surfactant molecule thereby enabling the formation of RMs in non-polar solvents. However, it is not known as to what surfactant chemistry provides the optimum aggregation properties to the dichain surfactant. In other words, what should be the balance between the perfluoroalkane and the alkane tails for an effective surfactant molecule. This is important in determining the solubility characteristics of the surfactant molecule. To gain some insight into the role played by each of the two functionally distinct tails on surfactant self-aggregation and aggregate morphology, two independent simulations of the small system (aggregated starting configuration) were performed. Although the small system does not correspond to any experimental composition, it was chosen for the sake of computational ease because the simulations of the large system are computationally intensive and only a few such simulations can be performed. As shown earlier, the results of the small system give a reasonably good prediction of the aggregation dynamics, thus it is expected that these simulations can provide some useful qualitative insight. In one simulation, both the tails of the dichain surfactant were made perfluoroalkane tails (referred to as fully-fluorinated surfactant) while in the other case both the tails were made alkane tails (referred to fully-hydrogenated surfactant). Thus, the fully-fluorinated surfactant had both tails

CO_2-philic while the fully-hydrogenated surfactant molecule had none. Changing the chemical characteristics of the dichain surfactant from hybrid to fully-fluorinated (or fully-hydrogenated) not only changes the CO_2-philic behavior but also changes the molecular mass of the molecule quite significantly. Compared to the hybrid surfactant, the fully-fluorinated surfactant is quite heavier (M_w = 870 g/mol) while the fully-hydrogenated surfactant has much lower molecular weight (M_w = 330 g/mol). As shown earlier (Section 5.2) the aggregation dynamics observed in the surfactant system under investigation are diffusion-limited, so it is expected that the significant difference in the molecular mass of fully-fluorinated and fully-hydrogenated surfactants should have considerable influence in the rate of aggregation of these systems. Figure 5.32 shows the MSD curves for the two type of surfactant molecules during the first 100 ps of the aggregation process. As expected, the MSD curve for the fully-fluorinated surfactant molecules has a significantly lower slope (indicating slower diffusion) compared to fully-hydrogenated surfactant. This is consistent with the higher molecular weight of the fully-fluorinated surfactant.

Figure 5.33 shows the aggregation curves for the two surfactant molecules (fully-fluorinated and fully-hydrogenated) along with the aggregation curves for the hybrid surfactant and for the system with no surfactant molecules (water and carbon dioxide only). The aggregation curves for the fully-fluorinated and fully-hydrogenated surfactant molecules are quite similar and exhibit the diffusion-limited aggregation mechanism. The only difference is that the aggregation curve for the fully-fluorinated surfactant is displaced $\sim$ 1 $ln(t)$ units to the right. This implies that after starting from the same initial configuration, the fully-hydrogenated surfactants exhibit more rapid aggregation compared to fully-fluorinated surfactants. This is consistent with the fact that fully-fluorinated surfactant molecules have larger mass and thereby diffuse much slowly than fully-hydrogenated surfactants (Figure 5.32).

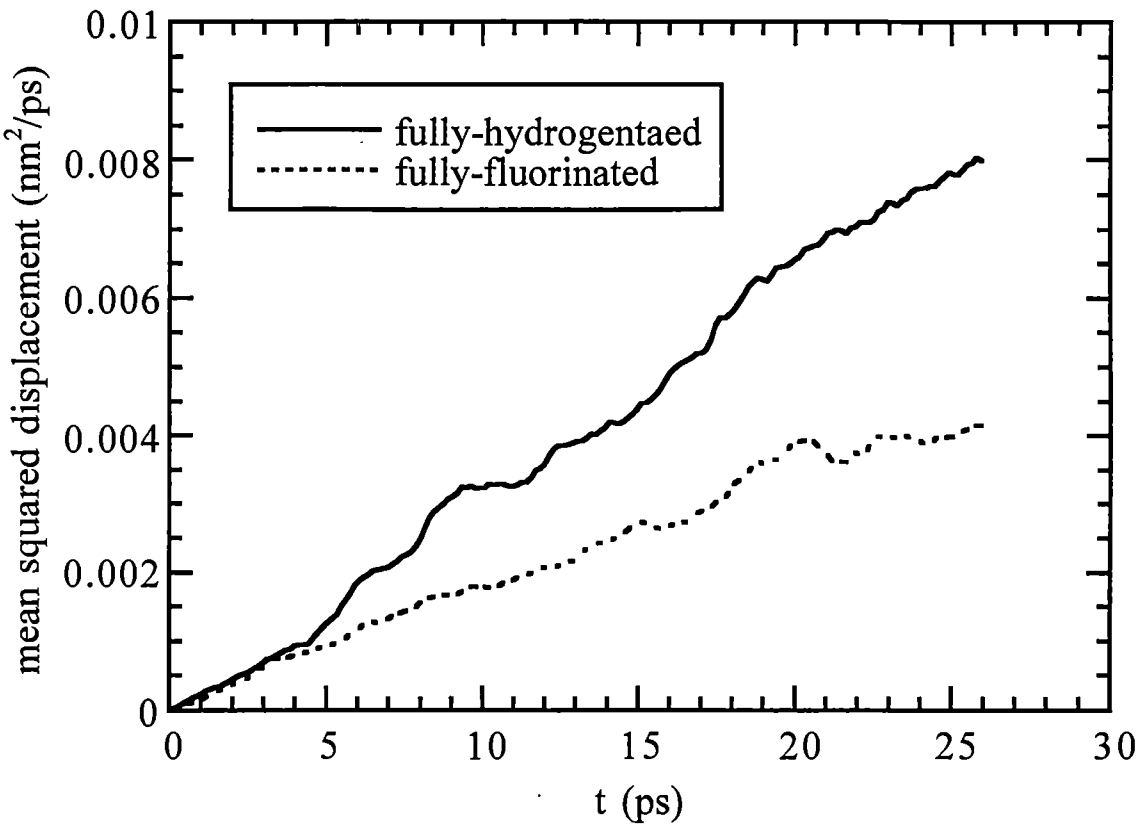


Figure 5.32: Mean-squared displacement (MSD) of the C_7-tailed fully-fluorinated and C_7-tailed fully-hydrogenated surfactants during the first 80 ps of the aggregation process.

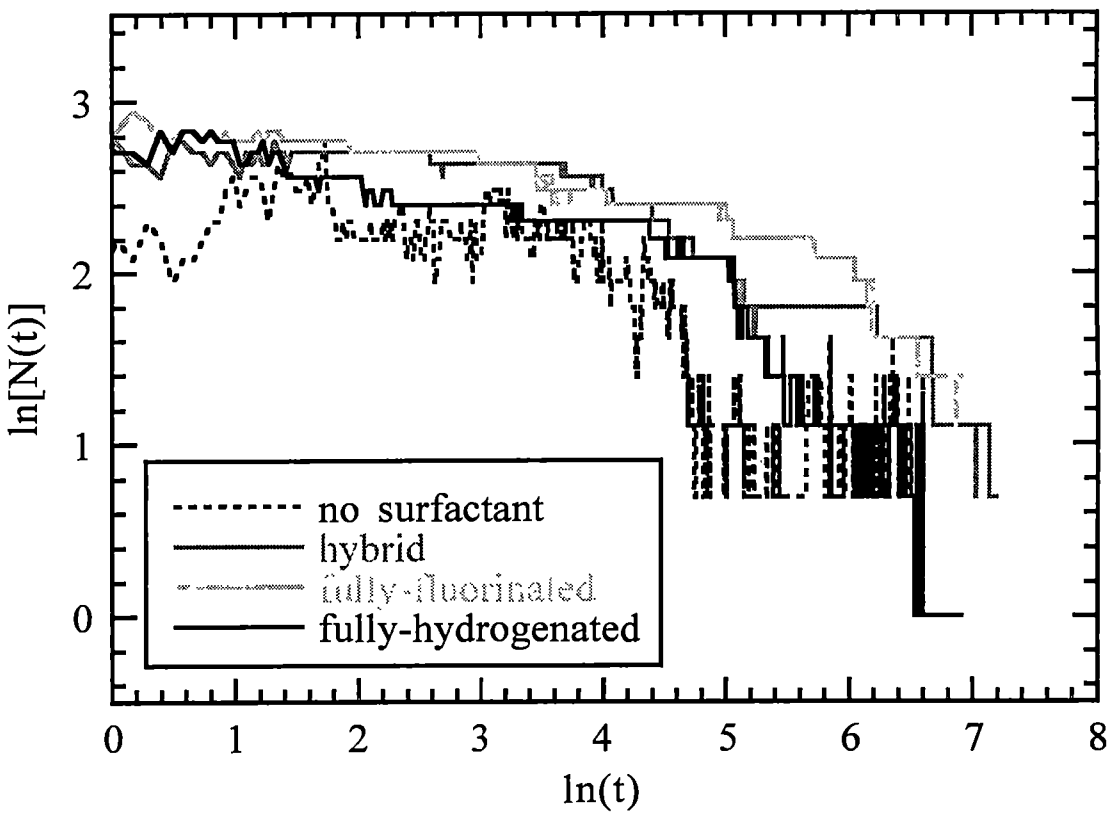


Figure 5.33: Time evolution of the number of aggregates during the simulation for the C_7-tailed fully-fluorinated and C_7-tailed fully-hydrogenated surfactant. The definition of an aggregate is based on the cluster counting algorithm of Sevick and co-workers [81].

The difference in surfactant chemistry of the two surfactants may also be responsible for different packing characteristics of these surfactant molecules within an aggregate. This is manifested as difference in the structural properties of aggregates formed in the two simulations. Figures 5.34(a)-(b) show the snapshots (at $\sim$ 1.2 ns) of the system configuration for the fully-fluorinated and the fully-hydrogenated surfactant molecules, respectively. It should be stressed that these configurations are only valid for the value of $W_o \sim 4$ in these two simulations. Within the simulation time of $\sim$ 1.2 ns, the fully-fluorinated surfactant molecules form five aggregates while the fully-hydrogenated surfactant molecules forms one aggregate. If formation of a single surfactant aggregate is assumed to be the expected final state, then clearly the system with fully-hydrogenated surfactants exhibits more rapid aggregation than fully-fluorinated surfactants. It may be also be argued that steric resistances may be more dominant in the fully-fluorinated surfactant molecules since the perfluoroalkane tails are not only bulkier but also more extended than alkane tails (Figures 5.20-5.21). Thus, fully-fluorinated surfactant molecules may experience stronger steric resistances to aggregation than their fully-hydrogenated counterparts. However, the feasibility of these two surfactant molecules as CO_2-philic surfactant molecules can be tested via GCMC simulation or experiments.

5.8 Effect of tail length

Besides the effect of surfactant chemistry on self-aggregation, another factor that significantly affects aggregation in non-polar solvents is the length of the surfactant tail groups. In fact, this has been a subject of numerous experimental studies [86, 87] on different surfactant molecules. The general conclusion of these studies has been that surfactant tails play a very important role (based on the type of surfactant molecule)

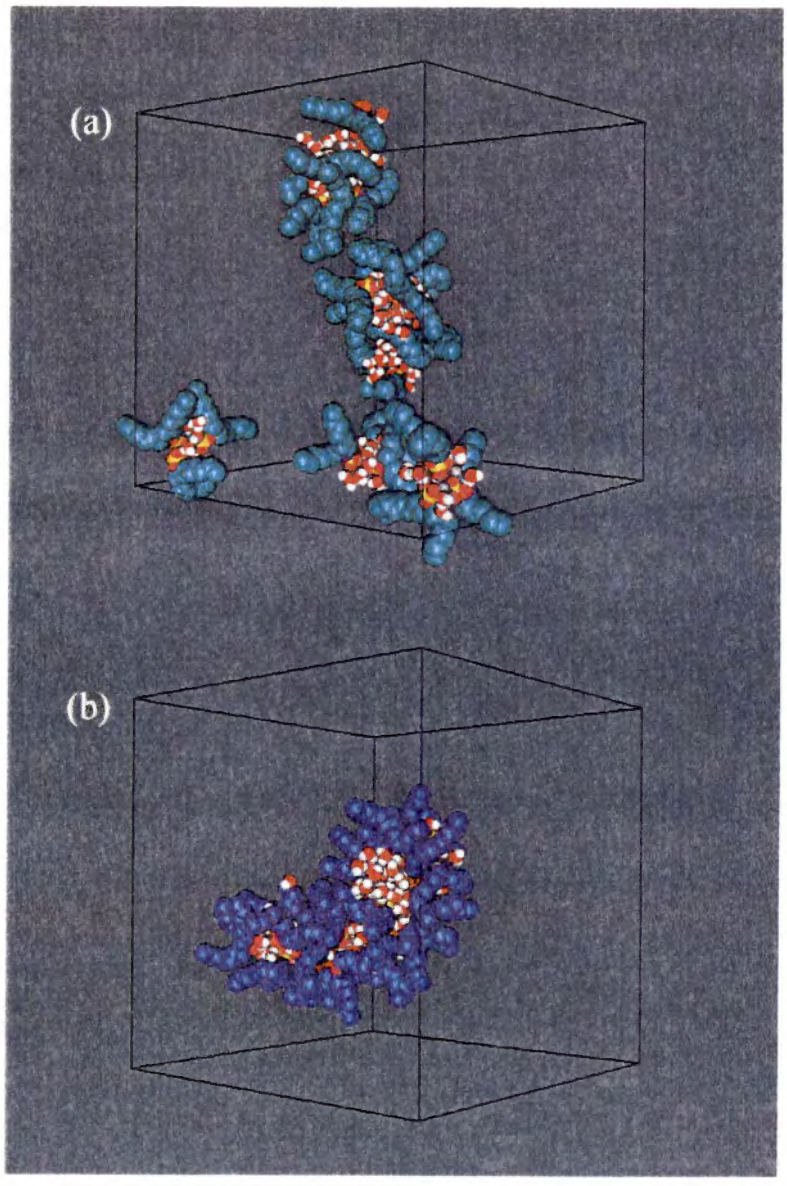


Figure 5.34: Snapshots of the system configuration for (a) C_7-tailed fully-fluorianted surfactant, and (b) C_7-tailed fully-hydrogenated surfactant. The snapshots are at $\sim$ 1.2 ns.

in determining the size and shape of reversed micellar aggregates. However, little is known regarding the effect of surfactant tail length on the dynamics of aggregation in non-polar solvents. In the effort to design new CO_2-philic surfactants, it is important to know as to what surfactant tail lengths provide optimum surfactant architecture. Thus, to gain some basic insight into this aspect, two independent simulations of the small system were performed. Again, the small systems were chosen because of their computational simplicity. In one of these simulations, the length of the each tail of the surfactant molecule was reduced by two functional groups i.e. a C_5-tailed hybrid surfactant was used, while in the other a two units longer tail i.e. C_9-tailed surfactant was used. Figure 5.35 shows the MSD of the surfactant molecules during the first 80 ps of the aggregation process during which most of the surfactant molecules are in the dispersed state. The figure shows that the MSD curves for the two different surfactant molecules differ but by less than that seen in Figure 5.32. This is not quite surprising, since the molecular weights of the two surfactants are relatively close (M_w = 472 g/mol for C_5-tailed surfactant compared to M_w = 728 g/mol for C_9-tailed surfactant) to each other. Thus, it is expected that the dynamics of aggregation in these two simulations should be quite similar. Figure 5.36 shows the aggregation curves for both the surfactant molecules. As expected, the aggregation curves for the two different surfactant molecules are quite similar. Both the surfactant molecules exhibit diffusion-limited aggregation behavior with similar slopes. Thus, changing the surfactant tail length appears to have little effect on the dynamics of aggregation for the surfactant system under consideration.

Figures 5.37(a)-(b) show the snapshots of the system of C_5-tailed surfactant and C_9-tailed surfactant respectively, at $\sim$ 1.1 ns. Both systems show the formation of a single surfactant aggregate within a nanosecond. The first observation of the two systems is that the aggregates formed in both cases are highly non-spherical. However,

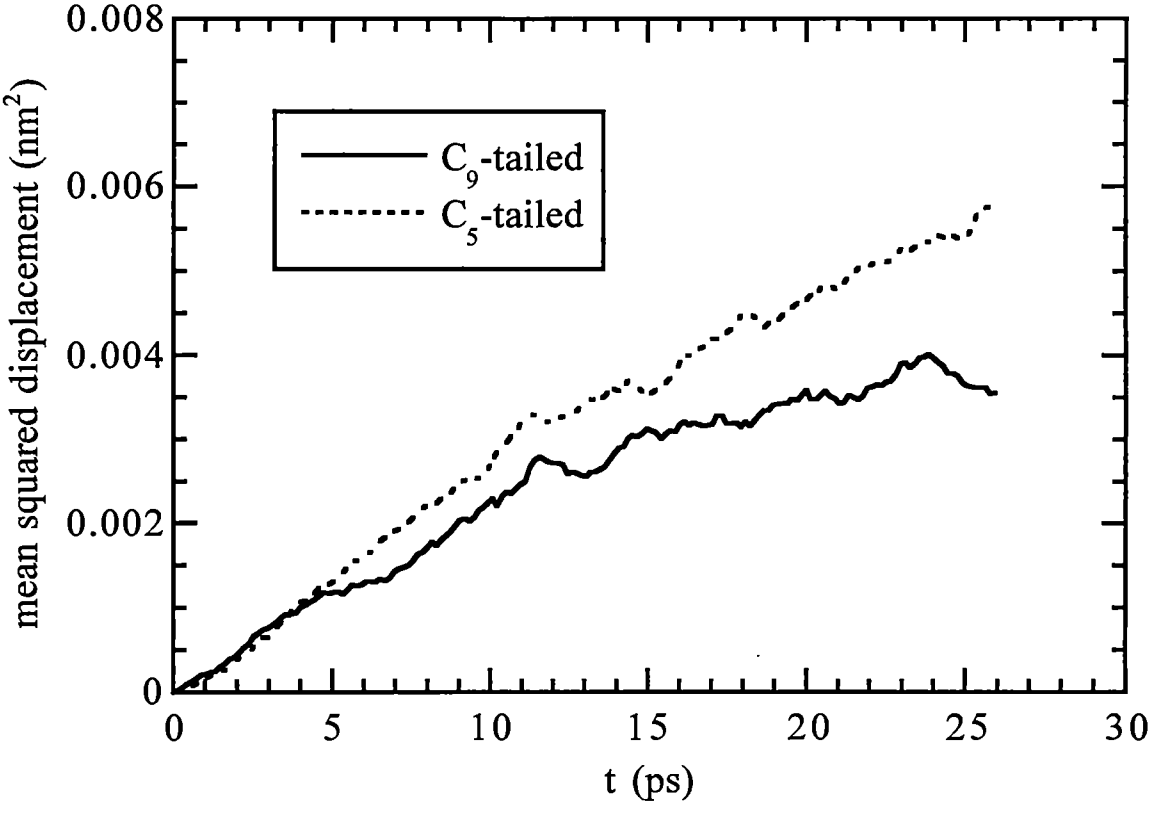


Figure 5.35: Mean squared displacement (MSD) of the C_5-tailed dichain surfactant and C_9-tailed dichain surfactant during the first 80 ps of the aggregation process.

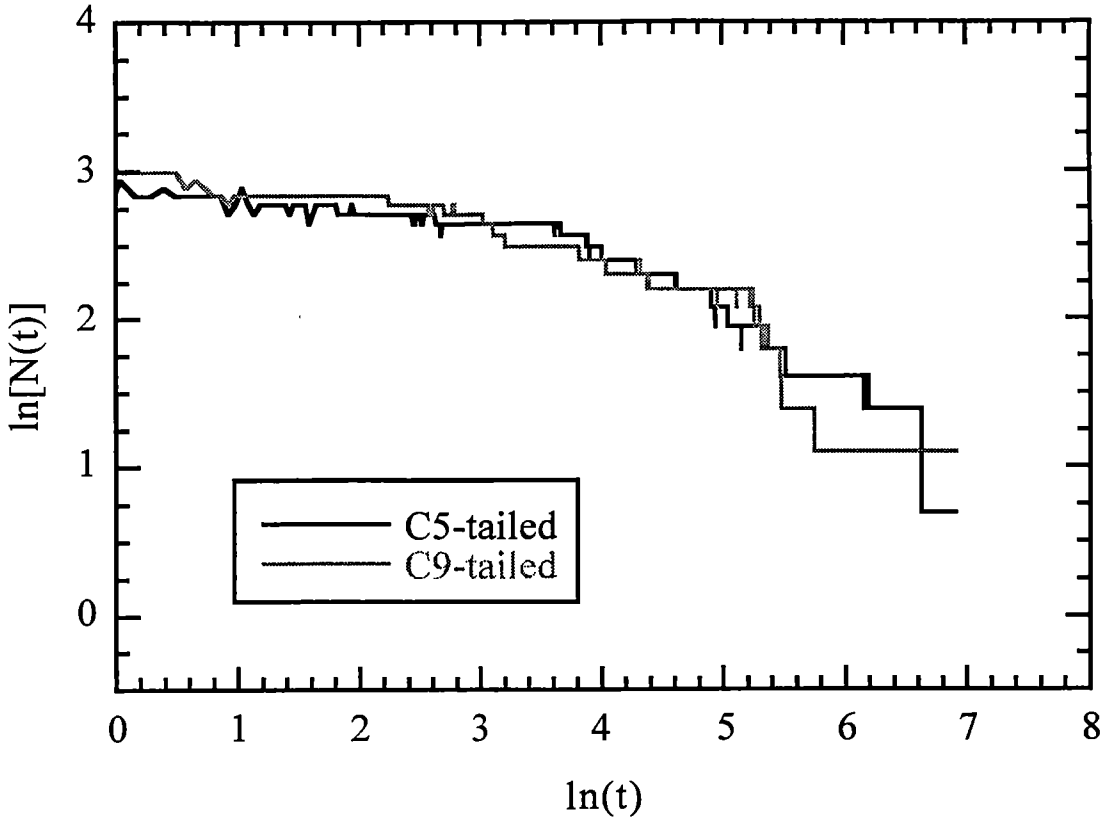


Figure 5.36: Time evolution of the number of aggregates during the simulation for the C_5-tailed dichain surfactant and C_9-tailed dichain surfactant. The definition of an aggregate is based on the cluster counting algorithm of Sevick and co-workers [81].

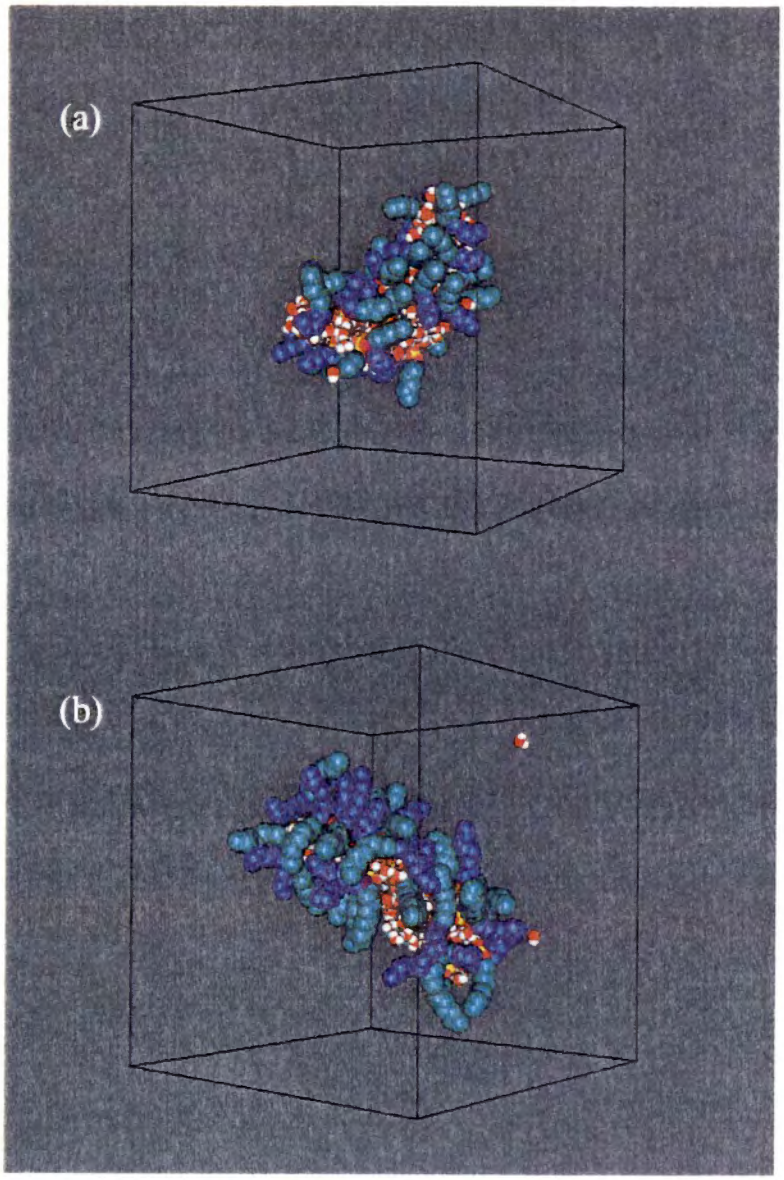


Figure 5.37: Snapshots of the system configuration for (a) C_5-tailed dichain surfactant, and (b) C_9-tailed hybrid surfactant. The snapshots are at $\sim$ 1.1 ns.

the extent of non-sphericity in the C_9-tailed surfactant appears to be much higher than that in the C_5-tailed surfactant. The aggregate formed from C_5-tailed surfactant has an eccentricity of 0.5 ± 0.1 compared to 0.9 ± 0.2 for the aggregate formed from C_9-tailed surfactant. Although the eccentricity of the aggregates in both cases may be due to the low water-to surfactant-ratio ($W_o \sim 4$), the exceptionally large non-sphericity of the aggregate of C_9-tailed surfactant could be due to the longer tails of this surfactant molecule. As mentioned earlier, steric effects (for a fixed W_o) play an important role in determining the structural properties of surfactant aggregates. Thus, the tails groups of the C_9-tailed surfactant experience stronger steric effects thereby resulting in a packing geometry that is highly non-spherical especially for the low W_o used in this system.

Chapter 6

Conclusions and Recommendations

6.1 Conclusions

The focus of this research work was to study the self-aggregation of dichain (or hybrid) surfactant molecules [$(C_7F_{15})(C_7H_{15})CHSO_4^-Na^+$] in carbon dioxide (solvent) via molecular dynamics simulation, with the objective of developing a molecular level understanding the physico-chemical properties of an effective CO_2-philic surfactant molecule. As mentioned earlier, the dichain surfactant molecule is one of the very few CO_2-philic surfactant molecules that have exhibited [51, 54] the propensity to form stable RMs capable of solubilizing polar and/or polymeric substances within their aqueous cores. The knowledge of the underlying principles responsible for surfactant aggregation is valuable to guide future efforts to design and develop new and/or improved surfactant molecules suitable for widespread industrial applications of CO_2.

The simulations reported in this work involve MD simulation of a dichain surfactant + water + carbon dioxide for two different system sizes (small system and large system). The composition of the small system was governed by computational simplicity, while the composition and the solvent condition in the large system mimicked the SANS study of Eastoe et al. [54], thereby enabling quantitative comparisons with the experimental results. Thus, to ensure that the simulation system is a real-

istic representation of an actual experimental system, detailed molecular models of all the three chemical species were used. The potential models for water and carbon dioxide were taken from literature, while the model for the surfactant molecule was generated by assembling existing potential models for the four distinct parts of the molecule (alkane tail, perfluoroalkane tail, sulfate head group, and sodium ion). Two different starting configurations (aggregated state and scattered state) were used as initial conditions for the simulations. The results focused on two aspects of surfactant self-assembly, viz. the dynamics of aggregation and the structural characteristics of surfactant aggregates. Specifically, the results presented in this study were related to the aggregation mechanism, size and shape of surfactant aggregates, microscopic details of the aqueous core, and effect of surfactant chemistry and architecture on aggregation.

The results of the simulation revealed a rapid and spontaneous self-aggregation of dichain surfactant and water molecules into aggregates that resemble RMs in appearance i.e. aggregates consisting of an aqueous core surrounded by surfactant molecules with their anionic head groups immersed in the core and the tails forming the corona. The aggregation process followed a two-step mechanism, similar to those observed experimentally for similar surfactants in other non-polar solvents [76]. The first step involved rapid ($\sim$ 150 - 300 ps) hydration of anionic head groups and Na^+ ions, while the (slower) second step involved gradual ($\sim$ 1 - 2 ns) aggregation of hydrated surfactant molecules into RM-like aggregates. For the small system, the two different starting configurations had no influence on the aggregation mechanism. However, for the large system, different aggregation mechanisms were observed for the two starting configurations. The scattered starting configuration of the large system (Figure 4.2(b)) followed the two-step mechanism similar to that observed for the small systems, although with somewhat larger time scales because of liquid-like solvent density,

while the evolution of aggregated starting configuration showed no evidence of the two-step mechanism. In general, the time scales of the aggregation steps observed in these simulations were a few orders of magnitude smaller than those normally observed in aqueous surfactant systems, and are attributed to the stronger and long-ranged electrostatic interactions (compared to hydrophobic interactions for aqueous systems) responsible for aggregation in the system under investigation.

An important aspect of the surfactant aggregates formed in these simulations was their tendency to scavenge almost all the water molecules from the solvent into the aqueous cores. This has also been observed experimentally for AOT surfactant [78], and is attributed to the presence of a driving force for transfer of water molecules because of the high ionic concentration within the aqueous cores.

A measure of the progress of surfactant aggregation in these simulations was estimated by the time evolution of the number of surfactant aggregates present in the system, $N(t)$. The results showed that when $ln[N(t)]$ is plotted versus $ln(t)$, an inverse linear dependence over a limited range of time was observed, indicating that the evolution of the number of aggregates over this time range is well-represented by a power-law function of the form $N(t) \sim t^{-z}$, where the magnitude of z is a measure of the rate of aggregation. This behavior of consistent with the Smolouchowski's aggregation theory, implying that the aggregation process is diffusion-limited. Thus, larger aggregates exhibited much slower aggregation compared to smaller aggregates. In fact, the simulations exhibited behavior consistent with the Stokes-Einstein relationship for diffusivity versus size of the aggregates formed. This explains why the time scales of aggregation in the large system were longer than the small system. The simulations also revealed that in addition to the diffusional characteristics, steric resistances also played an important role in determining the rate of aggregation. These resistances are due to the surfactant tails and come into play due to the typical

structure of the aggregates formed. The simulations showed that for successful aggregation, the aqueous cores of two colliding aggregates should come into contact with each other. Since, the aggregates had the aqueous cores surrounded by the corona formed from the surfactant tail, colliding aggregates had to overcome steric resistances to form larger aggregates. As a result, the frequency of successful collisions (collisions that lead to aggregation) is significantly reduced. This was evident in a simulation of water and CO_2 only (no surfactant present), which exhibited considerably higher aggregation rate compared to similar system with surfactants.

As mentioned earlier, the large system mimicked the experimental system of Eastoe et al. [54]. Thus, it was expected that the surfactant aggregates formed in this system should be quantitatively similar to those observed experimentally. The simulation showed that the large system aggregated starting configuration rapidly evolved into a state where most of the surfactant and water molecules formed an aggregate resembling an "average-sized" aggregate observed by Eastoe et al. [54]. In contrast, the aggregates in the large system with scattered starting configuration do not resemble those found experimentally, because the estimated simulation time ($\sim$ 200 ns) needed to reach that state is beyond the practically limits of this simulation study. The simulation results showed that size and shape of the aggregate formed in the large system with aggregated starting configuration was in a reasonable agreement with the properties of the "average-sized" aggregate observed experimentally. In contrast, the properties of the aggregates formed in the small system were strongly influenced by the low water-to-surfactant ratio ($W_o \sim 4$) in this system. The aggregates formed were much smaller than the aggregate formed in the large system, and also considerably non-spherical. This was attributed to steric resistances to packing due to small aqueous cores, and also due to ineffective dielectric screening. This is consistent with the simulation results of Brown and Clarke [58] for a model reversed micelle.

In the present study, advantage was taken of the MD simulation technique to explore the microstructure of the aggregates formed. The radial density distribution of the various molecules constituting the aggregate showed that the aqueous core essentially consisted of water molecules and Na^+ ions. The sulfate head groups were primarily situated at the surface of the aqueous core. The radial density distribution of the two tails indicated the presence of a corona surrounding the aqueous core and thereby effectively shielding it from the solvent. Negligible penetration of the solvent molecules into the aqueous core was observed. For the aggregate in the large system, the density of the water near the center of the core was $\sim$ 1.0 g/cc, indicating the presence of bulk-like water. A fairly broad (10 - 15 Å) interfacial region was observed where the water density reduced to zero, while the solvent density increased and finally reached bulk value outside the corona. The angular distribution functions (adfs) of the water molecules in the aqueous core revealed that the water molecules in the interfacial region were strongly oriented in response to the electric fields of the anionic head groups and Na^+ ions, while those near the center of core exhibited a hydrogen-bonded network. For the small system, the radial density distribution curve showed numerous peaks and troughs, manifesting the rigid structure of the aggregate because of low W_o. The tail conformations indicated that the perfluoroalkane tails were more extended than the alkane tails. Also, the tails in the surfactant system showed an opposite behavior than that in *vacuo*, indicating the different CO_2-philic behavior of the two tails. As expected, the perfluoroalkane tails were observed to be CO_2-philic while the alkane tails were observed to be CO_2-phobic.

To investiage the effect of surfactant chemistry and architecture additional simulations of the small system (small system was chosen for computational simplicity) were performed. To study the effect of surfactant chemistry, independent simulations were performed, one with C_7-tailed fully-fluorinated surfactants while the other with

C_7-tailed fully-hydrogenated surfactant molecules. The results showed that, because of significant difference in the molecular mass of the surfactant molecules, the fully-fluorinated surfactants exhibited slower aggregation dynamics compared to those observed to fully-hydrogenated surfactant molecules. The difference in tails chemistry also influenced the structural properties of the aggregates. During the same time scale, the fully-fluorinated surfactants formed smaller aggregates compared to fully-hydrogenated surfactants. This might be attributed to stronger steric resistances in the fully-fluorinated surfactants.

To study the effect of surfactant architecture also, two independent simulations of the small system were performed: one with C_5-tailed dichain surfactant, the other with C_9-tailed dichain surfactants. Since the molecular mass of these surfactants were not much different, the dynamics of aggregation observed in the two cases were quite similar. The only obervable difference was in the shape of the aggregates formed. The C_9-tailed dichain surfactant molecules formed a more non-spherical aggregate compared to the aggregate of C_5-tailed dichain surfactant molecules. This was directly attributed to higher steric resistances in the C_9-tailed dichain surfactants.

6.2 Recommendations for Future work

As mentioned earlier, the simulations presented in this study are a first step in an effort to use molecular simulation techniques as a tool to investigate surfactant aggregation in CO_2, and in non-polar solvents in general. Thus, many possible future directions are available following this work. An important question that arises from these simulations is whether the surfactant aggregates formed in these systems represent equilibrium structures or phase separation. This is particularly important for the small system used in this study. Thus, one future direction is to perform Grand

Canonical Monte Carlo (GCMC) simulation [70] on the RM-like structures formed in these simulations to verify their equilibrium structure. Also, because of the lack of experimental data on dichain surfactants and other CO_2-philic surfactants in general, it would be instructive to perform additional simulations to provide quantitative estimates of properties such as CMC, phase separation regime, aggregate size distribution etc., which could be the motivation for experimental studies.

It would be interesting to further examine the environment in the aqueous core of the large system. It would be particularly valuable to determine the chemical potential of water and various solutes as a function of position in the aqueous core relative to that in the bulk fluid. Determination of the suitability of the aqueous core to support polypeptides in their native conformations would be especially important.

BIBLIOGRAPHY

Bibliography

[1] M. J. Rosen, *Surfactants & Interfacial Phenomena* (John Wiley and Sons, New York, 1988), 2nd edition.

[2] D. Attwood and A. T. Florence, *Surfactant systems: Their Chemistry, Pharmacy and Biology* (Chapman Hall, 1983).

[3] D. Myers, *Surfactant Science and Technology* (VCH Publishers, New York, 1988).

[4] G. S. Hartley, *Aqueous Solution of Paraffin-Chain Salts* (Butterworth, London, 1936).

[5] K. A. Dill and P. J. Flory, Molecular Organization in micelles and vesicles, *Proc. Natl. Acad. Sci.*, **87**, 676-680 (1981).

[6] K. A. Dill, Molecular conformations in surfactant micelles, *Nature*, **313**, 603-604 (1985).

[7] P. Fromherz, Micelle Structure: A Surfactant-Block Model, *Chem. Phys. Lett.* **77**, 460-466 (1981).

[8] F. M. Menger and D. W. Doll, On the Structure of Micelles, *J. Am. Chem. Soc.*, **106**, 1109-1113 (1984).

[9] K. A. Dill, D. E. Koppel, R. S. Cantor, J. A. Dill, D. Bendedouch, and S. H. Chen, Molecular conformations in surfactant micelles, *Nature*, **309**, 42-45 (1984).

[10] J. B. Hayter and J. Penfold, Self-consistent Structural and Dynamic Study of Concentrated Micelle Solutions, *J. Chem. Soc. Faraday Trans.*, **77**, 1851-1863 (1981).

[11] J. B. Hayter and T. Zemb, Concentration-dependent structure of sodium octanoate micelles, *Chem. Phys. Lett.*, **93**, 91-94 (1982).

[12] D. Bendedouch, and S. H. Chen, and W. C. Koehler, Structure of Ionic Micelles from Small Angle Neutron Scattering, *J. Phys. Chem.*, **87**, 153-159 (1983).

[13] D. Bendedouch, and S. H. Chen, W. C. Koehler, and J. S. Lin, A method for determination of Intraparticle and Interparticle structure factors of Macroions in solution from Small-angle neutron- scattering, *J. Phys. Chem.*, **76**, 5022-5026 (1982).

[14] S. W. Haan and L. R. Pratt, Monte Carlo Study of a Simple Model for Micelle Structure, *Chem. Phys. Lett.*, **79**, 436-440 (1981).

[15] B. Owenson and L. R. Pratt, Molecular Statistical Thermodynamics of Model Micellar Aggregates, *J. Phys. Chem.*, **88**, 2905-2915 (1984).

[16] J. M. Haile and J. P. O'Connell, Internal Structure of a Model Micelle via Computer Simulation, *J. Phys. Chem.*, **88**, 6363-6366 (1984).

[17] M. C. Woods, J. M. Haile, and J. P. O'Connell, Internal Structure of a Model Micelle via Computer Simulation. 2. Spherically Confined Aggregates with Mobile Head Groups, *J. Phys. Chem.*, **90**, 1875-1885 (1985).

[18] S. Karaborni and J. P. O'Connell, Molecular Dynamic Simulations of Model Micelles. 3. Effects of Various Intermolecular Potentials, *Langmuir*, **6**, 905-911 (1990).

[19] S. Karaborni and J. P. O'Connell, Molecular Dynamic Simulations of Model Micelles. 4. Effects of Chain Length and Head Group Characteristics, *J. Phys. Chem.*, **94**, 2624-2631 (1990).

[20] S. Karaborni and J. P. O'Connell, Molecular Dynamics Simulations of Model Chain Molecules and Aggregates including Surfactants and Micelles, *Tenside Surf. Det.*, **30**, 235-242 (1993).

[21] B. Smit, P. A. J. Hilbers, K. Esselink, L. A. M. Rupert, N. M. van Os, and A. G. Schlijper, Computer simulations of a water/oil interface in the presence of micelles, *Nature*, **348**, 624-625 (1990).

[22] B. Smit, P. A. J. Hilbers, K. Esselink, L. A. M. Rupert, N. M. van Os, and A. G. Schlijper, Structure of a Water/Oil Interface in the Presence of Micelles: A Computer Simulation Study, *J. Phys. Chem.*, **95**, 6361-6368 (1991).

[23] B. Smit, K. Esselink, P. A. J. Hilbers, N. M. van Os, L. A. M. Rupert, and I. Szleifer, Computer Simulations of Surfactant Self-Assembly, *Langmuir*, **9**, 9-11 (1993).

[24] S. Karaborni, N. M. van Os, K. Esselink, and P. A. J. Hilbers, Molecular Dynamics Simulations of Oil Solubilization in Surfactant Solutions, *Langmuir*, **9**, 1175-1178 (1993).

[25] S. Karaborni, K. Esselink, P. A. J. Hilbers, B. Smit, J. Karthauser, N. M. van Os, and R. Zana, Simulating the Self-Assembly of Gemini (Dimeric) Surfactants, *Science*, **266**, 254-256 (1994).

[26] K. Watanabe, M. Ferrario, and M. L. Klein, Molecular Dynamics Study of a Sodium Octanoate Micelle in Aqueous Solution, *J. Phys. Chem.*, **92**, 819-821 (1988).

[27] B. Jonsson, O. Edholm, and O. Telleman, Molecular dynamics simulations of a sodium octanoate micelle in aqueous solution, *J. Chem. Phys.*, **85**, 2259-2271 (1986).

[28] J. C. Shelley, M. Sprik, and M. L. Klein, Molecular Dynamics Simulation of an Aqueous Sodium Octanoate Micelle using Polarizable Surfactant Molecules, *J. Phys. Chem.*, **9**, 916-926 (1993).

[29] A. D. Mackie, A. Z. Panagiotopoulos, I. Szleifer, Aggregation Behavior of a Lattice Model for Amphiphiles, *Langmuir*, **13**, 5022-5031 (1997).

[30] M. Antonio Floriano, E. Caponetti, and A. Panagiotopoulos, Micellization in Model Surfactant Systems, *Langmuir*, **15**, 3143-3151 (1999).

[31] H. F. Eicke, Surfactants in Nonpolar solvents: Aggregation and Micellization, *Topics in Curr. Chem.*, **87**, 85-145 (1980).

[32] H. F. Eicke and P. Kvita, *Reverse Micelles* (Plenum Press, New York, 1984).

[33] C. R. Singleterry, Micelle Formation and Solubilization in Nonaqueous Solvents, *J. Am. Chem. Soc.*, **32**, 446-452 (1955).

[34] K. Shinoda and S. Friberg, Microemulsions: Colloidal Aspects, *Adv. Colloid Int. Sc.*, **4**, 281-300 (1975).

[35] C. Tanford, *The Hydrophobic Effect: Formation of Micelles and Biological Membranes*, (Wiley Interscience, New York, 1973).

[36] B. Lindman and H. Wennerstrom, Micelles, Amphiphile Aggregation in Aqueous Solutions, *Topics in Curr. Chem.*, **87**, 1-83 (1980).

[37] K. L. Mittal and B. Lindman, *Surfactants in Solution* (Plenum Press, 1976), Vol I-III.

[38] R. W. Gale, J. L. Fulton, and R. D. Smith, Organized Molecular Assemblies in the Gas Phase: Reverse Micelles and Microemulsions in Supercritical Fluids, *J. Am. Chem. Soc.*, **109**, 920-921 (1987).

[39] J. L. Fulton, and R. D. Smith, Reverse Micelle and Microemulsion Phases in Supercritical Fluids, *J. Phys. Chem.*, **92**, 2903-2907 (1988).

[40] R. D. Smith, J. L. Fulton, J. P. Blitz, and J. M. Tingey, Reverse Micelle and Microemulsions in Near-Critical and Supercritical Fluids, *J. Phys. Chem.*, **94**, 781-787 (1990).

[41] J. M. Tingey, J. L. Fulton, and R. D. Smith, Interdroplet Attractive Forces in AOT Water-in-Oil Microemulsions formed in Subcritical abd Supercritical Solvents, *J. Phys. Chem.*, **94**, 1997-2004 (1990).

[42] M. A. McHugh and V. J. Krukonis, *Supercritical Fluid Extraction* (Butterworth, Heinemann, 1993).

[43] T. Clifford, *Fundamentals of Supercritical Fluids* (Oxford University Press, New York, 1999).

[44] K. A. Consani and R. D. Smith, Observations on the Solubility of Surfactants and Related Molecules in Carbon Dioxide at 50 ^oC, *J. Supercritical Fluids*, **3**, 51-65 (1990).

[45] T. Hoefling, R. M. Enick, and E. J. Beckman, Microemulsions in Near-Critical and Supercritical CO_2, *J. Phys. Chem.*, **95**, 7127-7129 (1991).

[46] T. A. Hoefling, R. R. Beitle, R. M. Enick, and E. J. Beckman, Design and Synthesis of Highly CO_2-Soluble Surfactants and Chelating Agents, *Fluid Phase Equilibria*, **83**, 203-212 (1993).

[47] G. J. McFann, K. P. Johnston, and S. M. Howdle, Solubilization in Nonionic Reverse Micelles in Carbon Dioxide, *AIChE J.*, **40**, 543-555 (1994).

[48] J. B. McClain, D. E. Betts, D. A. Canelas, E. T. Samulski, J. M. DeSimone, J. D. Londono, H. D. Cochran, G. D. Wignall, D. Chillura-Martino, and R. Triolo, Design of Nonionic Surfactants for Supercritical Carbon Dioxide, *Science*, **274**, 2049-2052 (1996).

[49] K. P. Johnston, K. L. Harrison, M. J. Clarke, S. M. Howdle, M. P. Heitz, F. V. Bright, C. Carlier, and T. W. Randolph, Water-in-Carbon Dioxide Microemulsions: An Environment for Hydrophiles Including Proteins, *Science*, **271**, 624-626 (1996).

[50] J. M. Desimone, Z. Guan, C. S. Elsbernd, Synthesis of Fluoropolymers in Supercritical Carbon Dioxide, *Science*, **257**, 945-947 (1992).

[51] K. L. Harrison, J. Goveas, K. P. Johnston, and E. A. O'Rear, Water-in-Carbon Dioxide Microemulsions with a Fluorocarbon-Hydrocarbon Hybrid Surfactant, *Langmuir*, **10**, 3536-3541 (1994).

[52] J. L. Fulton, D. M. Pfund, J. B. McClain, T. J. Romack, E. E. Maury, J. R. Combes, E. T. Samulski, J. M. DeSimone, and M. Capel, Aggregation of Amphiphilic Molecules in Supercritical Carbon Dioxide, A Small Angle X-ray Scattering Study, *Langmuir*, **11**, 4241-4249 (1995).

[53] M. P. Heitz, C. Carlier, J. deGrazia, K. L. Harrison, K. P. Johnston, T. W. Randolph, and F. V. Bright, Water Core within Perfluoropolyether-Based Microemulsions Formed in Supercritical Carbon Dioxide, *J. Phys. Chem.*, **101**, 6707-6714 (1997).

[54] J. Eastoe, Z. Bayazit, S. Martel, D. C. Steytler, and R. K. Heenan, Droplet Structure in a Water-in-CO_2 Microemulsion, *Langmuir*, **12**, 1423-1424 (1996).

[55] J. L. Fulton, J. P. Blitz, J. M. Tingey, and R. D. Smith, Reverse Micelle and Microemulsion Phase in Supercritical Xenon and Ethane: Light Scattering and Spectroscopic Probe Studies, *J. Phys. Chem.*, **93**, 4198-4204 (1989).

[56] H. J. C. Berendsen, J. P. M. Potsma, W. F. van Gunsteren, and J. Hermans, *Intermolecular Forces* (1981).

[57] H. J. C. Berendsen, J. R. Grigera, and T. P. Straatsma, The Missing Term in Effective Pair Potentails, *J. Chem. Phys.*, **91**, 6269-6271 (1987).

[58] D. Brown and J. H. R. Clarke, Molecular Dynamics Simulation of a Model Reverse Micelle, *J. Phys. Chem.*, **92**, 2881-2888 (1991).

[59] P. Linse, Molecular dynamics study of the aqueous core of a reversed ionic micelle, *J. Chem. Phys.*, **90**, 4992-5004 (1989).

[60] D. J. Tobias and M. L. Klein, Molecular Dynamics Simulations of a Calcium Carbonate/Calcium Sulfonate Reverse Micelle, *J. Phys. Chem.*, **100**, 6637-6648 (1996).

[61] J. I. Siepmann, S. Karaborni, and B. Smit, Simulating the critical behavior of complex fluids, *Nature*, **365**, 330-332 (1993).

[62] S. T. Cui, H. D. Cochran, and P. T. Cummings, Vapor-liquid coexistence of alkane carbon dioxide and perfluoroalkane carbon dioxide mixtures, *J. Phys. Chem.*, **103**, 4485-4491 (1999).

[63] P. van del Ploeg and H. J. C. Berendsen, Molecular dynamics simulation of a bilayer membrane, *J. Chem. Phys.*, **76**, 3271-3276 (1982).

[64] S. T. Cui, J. I. Siepmann, H. D. Cochran, and P. T. Cummings, Intermolecular potentials and vapor-liquid phase equilibria of perfluorinated alkanes, *Fluid Phase Equilibria*, **146**, 51-61 (1998).

[65] W. R. Cannon, B. M. Pettitt, and J. A. McCammon, Sulfate Anion in Water: Model Structural, Thermodynamic, and Dynamic Properties, *J. Phys. Chem.*, **98**, 6225-6230 (1994).

[66] J. G. Harris and K. H. Yung, Carbon Dioxide's Liquid-Vapor Coexistence Curve and Critical Properties as Predicted by a Simple Molecular Model, *J. Phys. Chem.*, **99**, 12021-12024 (1995).

[67] O. Steinhauser, Reaction field simulation of water, *Mol. Phys.*, **45**, 335-348 (1982).

[68] G. Hummer, D. M. Soumpasis, and M. Newmann, Pair correlations in an NaCl-SPC water model: Simulations versus extended RISM computations, *Mol. Phys.*, **77**, 769-785 (1992).

[69] S. Salaniwal, S. T. Cui, P. T. Cummings, and H. D. Cochran, Self-Assembly of Reverse Micelles in Water/Surfactant/Carbon Dioxide Systems by Molecular Simulation, *Langmuir*, **15**, 5188-5192 (1999).

[70] D. Frenkel and B. Smit, *Understanding Molecular Simulations* (Academic Press, San Diego, 1996).

[71] M. P. Allen, D. J. Tildesly, *Computer Simulation of Liquids* (Clarendon Press, Oxford, 1994).

[72] H. C. Andersen, Rattle: A velocity Verlet version of the Shake algorithm for molecular dynamics calculations, *J. Comput. Phys.*, **52**, 24-34 (1983).

[73] G. Ciccotti, M. Ferrario, and J. P. Ryckaert, Molecular dynamics of rigid systems in cartesian co-ordinates: A general formulation, *Mol. Phys.*, **47**, 1253-1264 (1982).

[74] S. Plimpton, Fast Parallel Algorithm for short-range molecular dynamics, *Comput. Phys.*, **117**, 1-19 (1995).

[75] P. G. DeGennes and C. Taupin, Microemulsions and the flexibility of oil/water interfaces, *J. Phys. Chem.*, **86**, 2294-2304 (1982).

[76] H. F. Eicke and H. Christen, Is Water critical to the formation of Micelles in Apolar Media, *Helv. Chim. Acta.*, **61**, 2258-2263 (1978).

[77] M. J. Kosita, C. Bohne, P. Alexandridis, T. A. Hatton, and J. F. Holzworth, Dynamics of micro- and macrophase separation of amphiphilic block-copolymers in aqueous solutions, *Macromolecules*, **32**, 5539-5551 (1999).

[78] S. Kaufmann and C. R. Singleterry, Effect of the Cation on Micelle formation by Sulfonates in Benzene, *J. Colloid Int. Sc.*, **12**, 465-479 (1957).

[79] M. B. Mathews and E. Hirschborn, Solubilization and Micelle Formation in a Hydrocarbon Medium, *J. Colloid Sci.*, **8**, 86-96 (1952).

[80] K. Jackson, L. E. Brown, and J. L. Fulton, Water Solubility Measurements in Supercritical Fluids and High-Pressure Liquids Using Near Infrared Spectroscopy, *Anal. Chem.*, **67**, 2368-2372 (1995).

[81] E. M. Sevick, P. A. Monson, and J. M. Ottino, Monte Carlo calculations of cluster statistics in continuum models of composite morphology, *J. Chem. Phys.*, **88**, 1198-1206 (1988).

[82] R. M. Ziff, E. D. McGrady, and P. Meakin, On the validity of Smoluchowski's equation for cluster-cluster aggregation kinetics, *J. Chem. Phys.*, **82**, 5269-5274 (1985).

[83] P. Meakin, T. Vicsek, and F. Family, Dynamic cluster-size distribution in cluster-cluster aggregation: Effect of cluster diffusivity, *Phys. Rev.*, **31**, 564-569 (1985).

[84] D. Chandler, *Introduction to Modern Statistical Mechanics*, (Oxford University Press, New York, 1987).

[85] J. N. Israelchvili, D. J. Mitchell, and B. W. Ninham, Theory of Self-Assembly of hydrocarbon amphiphiles into Micelles and Bilayers, *J. Chem. Soc. Faraday Trans.*, **72**, 1525-1568 (1976).

[86] J. B. Peri, The state of solution of Aerosol OT in Nonaqueous Solvents, J. Colloid Int. Sc., **29**, 6-15 (1969).

[87] E. J. Fendler, J. H. Fendler, R. T. Medary, and O. A. El Seoud, Proton Magnetic Resonance Investigations of Alkylammonium Carboxylate Micelles in Nonaqueous Solvents. II. Effect of Carboxylate structure in Benzene and in Carbon Tetrachloride, *J. Phys. Chem.*, **77**, 1432-1436 (1973).

[88] G. D. Wignall, *Encyclopedia of Polymer Science and Engineering* (Wiley Interscience, New York, 1987).

APPENDIX

Appendix A

Site-site reaction field method

In the site-site reaction field technique [67, 68] applied to a system consisting of ionic or polar molecules, the electrostatic potential consists of two parts. The first is a short-range contribution from particles situated within a cut-off sphere or "cavity" of radius R_c centered on the reference particle, while the second arises from particle outside R_c that are considered polarized by the charge distribution within the cavity and in turn produces an additional electric field in the cavity, known as the reaction field E_R. The magnitude of the reaction field acting on the reference particle i is proportional to the moment of the spherical cavity surrounding it and is given by

$$E_{R_i} = \frac{2(\epsilon_R - 1)}{2\epsilon_R + 1} \frac{1}{R_c^3} \sum_{j \in R_c} \mu_j \tag{A.1}$$

where μ_j represents the dipole moment of particle j within the spherical cavity and ϵ_R is the (unknown) dielectric constant of the continuum. The summation in Equation A.1 extends over all particles in the cavity, including particle i. The contribution to the total electrostatic energy from the reaction field of particle i is given by

$$\begin{aligned} U_R &= -\frac{1}{2}\mu_i . E_{R_i} \\ &= -\left(\frac{\epsilon_R - 1}{2\epsilon_R + 1}\right) \frac{1}{R_c^3} \sum_{j \in R_c} \mu_i . \mu_j \end{aligned} \tag{A.2}$$

where the factor $\frac{1}{2}$ is used for polarization effects and accounts for the polarization energy of the continuum. Thus the total contribution of reaction field electrostatic energy (U_R) of the given by

$$U_R = -\left(\frac{\epsilon_R - 1}{2\epsilon_R + 1}\right) \sum_{i=1}^{N} \sum_{j=1}^{N} \frac{\mu_i . \mu_j}{R_c^3} \tag{A.3}$$

$$U_R = \left(\frac{\epsilon_R - 1}{2\epsilon_R + 1}\right) \sum_{i=1}^{N} \sum_{j=1}^{N} \frac{q_i q_j}{R_c^3} (\mathbf{r}_i - \mathbf{r}_j)^2 - \frac{N}{2} \frac{\mu^2}{R_c^3} \tag{A.4}$$

where the double sum extends over all pairs of particles in the system which are separated by a distance R_{ij} smaller than R_c. The term $i = j$ is not omitted, but contributes a constant to the total potential energy. Thus the total electrostatic energy (U_E) is given by

$$U_E = U_D + U_R \tag{A.5}$$

where U_D is the direct contribution to the electrostatic energy, and is given by the equation

$$U_D = \sum_{i<j}^{N} \sum^{N} \frac{q_i q_j}{|\mathbf{r}_i - \mathbf{r}_j|} \tag{A.6}$$

Appendix B

Iterative procedure for Rattle algorithm

The Rattle algorithm [72] is a technique to perform constrained MD simulation on a molecular system with certain selected degrees of freedom constrained. Since the Rattle algorithm is based on the velocity version of the Verlet algorithm, the equations of motion for the system are of the form

$$\begin{aligned}\mathbf{r}_i(t+h) &= \mathbf{r}_i(t) + h\dot{\mathbf{r}}_i(t) + \left(\frac{h^2}{2m_i}\right)[\mathbf{F}_i(t) + \mathbf{G}_i(t)] \\ &= \mathbf{r}_i(t) + h\dot{\mathbf{r}}_i(t) + \left(\frac{h^2}{2m_i}\right)\left[\mathbf{F}_i(t) - 2\sum_j \lambda_{RR_{ij}}(t)\mathbf{r}_i(t)\right] \qquad \text{(B.1)}\end{aligned}$$

and

$$\begin{aligned}\dot{\mathbf{r}}_i(t+h) = \dot{\mathbf{r}}_i(t) + \left(\frac{h^2}{2m_i}\right)\Bigg[&\mathbf{F}_i(t) - 2\sum_j \lambda_{RR_{ij}}(t)\mathbf{r}_{ij}(t) \\ &+ \mathbf{F}_i(t+h) - 2\sum_j \lambda_{RV_{ij}}(t+h)\mathbf{r}_{ij}(t+h)\Bigg] \qquad \text{(B.2)}\end{aligned}$$

where $\mathbf{r}_i(t)$ and $\mathbf{r}_j(t)$ are the positions of atoms i and j, respectively, and $\mathbf{r}_{ij}(t) = \mathbf{r}_i(t) - \mathbf{r}_j(t)$. The quantities $\lambda_{RR_{ij}}(t)$ and $\lambda_{RV_{ij}}(t+h)$ are chosen to satisfy the following constraint equations, respectively

$$\sigma_{ij}\left(\{\mathbf{r}(t)\}\right) = |\mathbf{r}_i(t) - \mathbf{r}_j(t)|^2 - {d_{ij}}^2 = 0 \qquad \text{(B.3)}$$

and

$$|\dot{\mathbf{r}}_i(t) - \dot{\mathbf{r}}_j(t)| \,.\, |\mathbf{r}_i(t) - \mathbf{r}_j(t)| = 0 \tag{B.4}$$

where d_{ij} is the fixed distance between atoms i and j. With positions, velocities, and forces known at time t, the corresponding quantities at time $t + h$ are calculated by an iterative procedure given below [73]. Let

$$g_{ij} = h\lambda_{RR_{ij}}(t)$$

$$k_{ij} = h\lambda_{RV_{ij}}(t + h)$$

$$\mathbf{q}_i = \dot{\mathbf{r}}_j(t) + \left(\frac{h}{2m_i}\right)\mathbf{F}_i(t) - \left(\frac{1}{m_i}\right)\sum_j g_{ij}\mathbf{r}_{ij}(t)$$

Then Equations B.1 and B.2 can be expressed as

$$\mathbf{r}_i(t + h) = \mathbf{r}_i(t) + h\mathbf{q}_i \tag{B.5}$$

$$\dot{\mathbf{r}}_i(t + h) = \mathbf{q}_i + \left(\frac{h}{2m_i}\right)\mathbf{F}_i(t + h) - \left(\frac{1}{m_i}\right)\sum_j k_{ij}\mathbf{r}_{ij}(t + h) \tag{B.6}$$

First $\mathbf{q}_i$ is solved by iteration. To start the iteration, let

$$\mathbf{q}_i = \dot{\mathbf{r}}_i(t) + \left(\frac{h}{2m_i}\right)\mathbf{F}_i(t) \tag{B.7}$$

for $i = 1, 2, \ldots, N$. To begin the iterative loop, a constraint is picked. Suppose it involves atoms i and j. Let

$$\mathbf{s} = \dot{\mathbf{r}}_i(t) + h\mathbf{q}_i(t) - \mathbf{r}_j(t) - h\mathbf{q}_j(t)$$

The quantity $\mathbf{s}$ represents the current approximation for the vector displacement of atoms i and j. If $|\mathbf{s}|^2 - d_{ij}^2$ differs by an amount less than the acceptable tolerance, the present constraint is satisfied. The control then goes back to the beginning of the

iterative loop and a new constraint is picked. If not, then corrections for $\mathbf{q}_i$ and $\mathbf{q}_j$ are made to satisfy the constraints within the acceptable limit. For this, let

$$\mathbf{r}_i^T = \mathbf{r}_i(t) + h\left[\mathbf{q}_i - \frac{g\mathbf{r}_{ij}(t)}{m_i}\right] \tag{B.8}$$

and

$$\mathbf{r}_j^T = \mathbf{r}_j(t) + h\left[\mathbf{q}_j + \frac{g\mathbf{r}_{ij}(t)}{m_j}\right] \tag{B.9}$$

Equations B.7 and B.8 represent the new values $\mathbf{r}_i(t+h)$ and $\mathbf{r}_j(t+h)$, when corrections proportional to g are made to $\mathbf{q}_i$ and $\mathbf{q}_j$. The value of g is to be chosen such that

$$\left|\mathbf{r}_i^T - \mathbf{r}_j^T\right|^2 = d_{ij}^2 \tag{B.10}$$

Solving for g yields

$$g = \left(s^2 - d_{ij}^2\right)/2h\left[\mathbf{s}.\mathbf{r}_{ij}(t)\right]\left(\frac{1}{m_i} + \frac{1}{m_j}\right) \tag{B.11}$$

where quantities of order g^2 are neglected. Thus, the corrected values of $\mathbf{q}_i$ and $\mathbf{q}_j$ are given by the following expressions

$$\mathbf{q}_i = \dot{\mathbf{r}}_i(t) + \left(\frac{h}{2m_i}\right)\mathbf{F}_i(t) - \frac{gr_{ij}(t)}{m_i} \tag{B.12}$$

$$\mathbf{q}_j = \dot{\mathbf{r}}_j(t) + \left(\frac{h}{2m_j}\right)\mathbf{F}_j(t) + \frac{gr_{ij}(t)}{m_j} \tag{B.13}$$

The procedure described above is continued till all the constraints are satisfied to within the acceptable tolerance. The next step involves solving for $\dot{\mathbf{r}}_i(t+h)$ by an iterative procedure. to start, let

$$\dot{\mathbf{r}}_i(t+h) = \mathbf{q}_i + \left(\frac{h}{2m_i}\right)\mathbf{F}_i(t+h) \tag{B.14}$$

for $i = 1, 2, \ldots, N$. For a constraint, the Equation B.4 is tested. If the result differs by less than an acceptable tolerance, the constraint is satisfied and the control goes

to the next constraint. However, if the constraint is not satisfied, then the velocities of two atoms involved with the constraint need to be satisfied. For this, let

$$\dot{\mathbf{r}}_i^T = \dot{\mathbf{r}}_i(t+h) - \frac{k\mathbf{r}_{ij}(t+h)}{m_i} \tag{B.15}$$

$$\dot{\mathbf{r}}_j^T = \dot{\mathbf{r}}_j(t+h) + \frac{k\mathbf{r}_{ij}(t+h)}{m_j} \tag{B.16}$$

Equations B.15 and B.16 then represents the new values of $\dot{\mathbf{r}}_i(t+h)$ and $\dot{\mathbf{r}}_j(t+h)$ when corrections proportional to k are made. The value of k is chosen such that $\dot{\mathbf{r}}_i^T - \dot{\mathbf{r}}_j^T$ is perpendicular to $\mathbf{r}_{ij}(t+h)$. Thus, the value of k is given by

$$k = \mathbf{r}_{ij}(t+h).\left|\dot{\mathbf{r}}_i(t+h) - \dot{\mathbf{r}}_j(t+h)\right| / d_{ij}^2 \left(\frac{1}{m_i} + \frac{1}{m_j}\right) \tag{B.17}$$

Then Equation B.14 for atoms i and j is replaced by Equation B.15 and B.16, respectively, using the value of k given by Equation B.17. The control then goes to next constraint. This iterative procedure is continued till all constraints are satisfied.

Appendix C

SANS studies on polymers in supercritical carbon dioxide

Small-angle neutron scattering (SANS) is an important experimental tools to investigate the thermodynamic and/or dynamic behavior of polymers and surfactants in a solvent medium. This technique can also elucidate information regarding the size and shape of single polymer chains or supramolecular structure with a resolution of $\sim$ 5 - 2000 Å [88]. This studies were performed on the W. C. Koehler 30m SANS facility at Oak Ridge National Laboratory (ORNL). The systems studied included poly(dimethylsiloxane) (PDMS) and poly(styrene)(PS). The details of these experiments and the results are provided in the following four publications that resulted from this work.

Paper 1

SANS Studies of Polymers in Organic Solvents and Supercritical Fluids in the Poor, Theta and Good Solvent Domains

Y. B. Melnichenko[1], E. Kiran[2], K. Heath[1], S. Salaniwal[1], H. D. Cochran[1], M. Stamm[3], W. A. Van Hook[4] and G. D. Wignall[1]

[1]Solid State Division, Oak Ridge National Laboratory*, Oak Ridge, TN 37831
[2]Department of Chemical Engineering, University of Maine, Orono, ME 04468
[3]Max Planck Institut für Polymerforschung, 55021 Mainz, Germany
[4]Chemistry Department, University of Tennessee, Knoxville TN 37996

We demonstrate that semidilute polymer solutions in supercritical fluids (SCFs) reproduce all main features of the polymer behavior in organic solvents which is indicative of the intrinsic similarity between the thermodynamic properties of polymers in SCFs and in the far sub-critical liquids. Using small-angle neutron scattering, we studied the effect of temperature and pressure on the phase behavior of polystyrene (PS) in organic solvents as well as of poly(dimethylsiloxane) (PDMS) in supercritical carbon dioxide (SC CO_2). The radius of gyration R_g of polymer chains in both organic solvents and in SC CO_2 is invariant during both temperature and pressure quenches down to the critical point of demixing. The limit of infinite polymer miscibility (the Θ condition) of PDMS - SC CO_2 solutions may be reached by varying the pressure (P_Θ=52±4 MPa at the density of SC CO_2 ρ_{CO2} = 0.95 g/cm^3) and or the temperature (T_Θ = 65±5 ^oC). A sharp crossover between the critical and mean field behavior in PDMS – SC CO_2 is similar to that in solutions of PS in cyclohexane, and at $T > T_\Theta$, $P > P_\Theta$ the solutions reach the good solvent domain where R_g expands beyond the unperturbed dimensions $R_g(\Theta)$ at the Θ condition.

* Managed by Lockheed Martin Energy Research Corporation under contract DE-AC05-96OR-22464 for the U. S. Department of Energy.

Introduction

In organic solvents, it is well known that the radius of gyration, R_g (i.e. the r.m.s. distance of scattering elements from the center of gravity) of polymer molecules depends on the sign and magnitude of the interactions between the chain segments and the molecules of the surrounding liquid. In "good" solvents, the dominating repulsive forces between the segments (excluded volume effects) work to expand the R_g, and the second virial coefficient (A_2) is positive. In less favorable solvents, the pairwise attractive and repulsive segment interactions may compensate at the "Flory" or "theta temperature" (T_Θ), where $A_2=0$, and R_g corresponds to the dimension of a volume-less polymer coils, "unperturbed" by the excluded volume effects. By definition, T_Θ is the critical solution temperature (T_C) for a polymer with the molecular weight $M_W = \infty$ and thus corresponds to the threshold of unlimited polymer – solvent miscibility. One of the first significant applications of SANS was to confirm Flory's prediction that polymer chains would adopt such random-walk configurations in the condensed (amorphous) state [1].

In the poor solvent regime ($T<T_\Theta$, $A_2<0$), dominating attractive interactions between the segments work to collapse polymer chains into compact polymer globules. This phenomenon is well understood for dilute solutions of separated polymers which collapse as the temperature approaches T_C [2]. SANS has recently been used to extend the experimental observations to "semidilute" solutions of strongly interacting macromolecules. In accord with the de Gennes' concept [3], in the critical region $T \sim T_C$ of the solutions polymer chains do not interpenetrate significantly and thus should be collapsed [i.e. $R_g(T_C) < R_g(T_\Theta)$] as in dilute concentration regime. However, experiments on PS in cyclohexane (CH) [4,5] and acetone (AC) [6] have demonstrated that the predicted decrease in R_g is not observed as $T \Rightarrow T_C$. Instead, diverging concentration fluctuations near T_C lead to the formation of distinct microdomains of strongly interpenetrating molecules, which prevent the expected collapse [4-6]. Measurements have also been made in supercritical fluids to contrast such systems with organic solvents and to test the prediction [7] that the molecules will adopt the unperturbed dimensions at a critical "theta pressure"(P_Θ) as they do in polymer solutions at the theta temperature. A direct comparison of the phase behavior of PDMS in SC CO_2 with that of PS in CH and in AC is indicative of the intrinsic similarity between the structure and thermodynamic properties of polymers in SCFs and in sub-critical organic liquids.

Experimental

The SANS data were collected on the W. C. Koehler 30m SANS facility [8] at Oak Ridge National Laboratory (ORNL). The neutron wavelength was $\lambda = 4.75$ A ($\Delta\lambda/\lambda \sim 5\%$) and the 64 x 64 cm^2 area detector with cell size ~ 1 cm^2 was placed at various sample-detector distances to give an overall range of momentum transfer of $0.005 < Q = 4\pi\lambda^{-1} \sin\theta < 0.1$ A^{-1}, where 2θ is the angle of scattering. The data were

corrected for instrumental backgrounds and detector efficiency on a cell-by-cell basis, prior to radial (azimuthal) averaging and the net intensities were converted to an absolute (± 3%) differential cross section per unit solid angle, per unit sample volume [$d\Sigma(Q)/d\Omega$ in units of cm^{-1}] by comparison with pre-calibrated secondary standards [9]. The experiments in supercritical CO_2 were conducted in a high-pressure cell similar to the one used previously for polymer synthesis [10] and the SANS studies of block copolymer amphiphiles in supercritical CO_2 [11]. The cell's stainless body was fitted with sapphire windows with virtually no attenuation (cell transmission ~ 93%) or parasitic scattering. The sample cross sections were obtained after subtracting the intensities of the cell, and the signal from the CO_2 amounted to a virtually flat background (~ 0.04 cm^{-1}), which formed only a minor correction to the scattering from the homopolymer solutions.

To obtain R_g and the correlation length (ξ) of the concentration fluctuations we make use of the SANS high concentration isotope labeling method [12-14], which allows the determination of both parameters for semidilute polymer solutions. The coherent scattering cross section ($d\Sigma/d\Omega$ in units of cm^{-1}) of an incompressible mixture of identical protonated and deuterated polymer chains dissolved in a solvent is given by [4,5,14]:

$$I(Q,x) = I_s(Q,x) + I_t(Q,x) \quad , \tag{1}$$

$$I_s(Q,x) = KnN^2 S_s(Q) \quad , \tag{2}$$

$$I_t(Q,x) = LnN^2 S_t(Q) \quad . \tag{3}$$

The subscripts "s" and "t" correspond to scattering from a single chain and total scattering, respectively and thus $S_s(Q)$ is the single-chain structure factor, containing information on the intramolecular correlations (and hence R_g). Similarly, the total scattering structure factor, $S_t(Q)$ embodies information on the total (both intra- and intermolecular) correlations between monomer units and is related to the correlation length of the concentration fluctuations, ξ. The structure factors are normalized so that $S_s = 1$ at ($Q = 0$) and $S_t = S_s$ at infinite dilution. Also, x is the mole fraction of protonated chains in the solvent, and n and N are the number density of the polymer molecules and the degree of polymerization, respectively. The prefactors K and L are:

$$K = (b_H - b_D)^2 x(1 - x); \qquad L = [b_H x + (1 - x)b_D - b_S']^2 \quad , \tag{4}$$

where b_H and b_D are the scattering lengths of the protonated and deuterated monomers and b_S' is the scattering length of a solvent molecule, normalized to the ratio of specific volumes of the monomer and the solvent molecule.

The prefactor, L, in equation (4) controls the "total" scattering contribution and it has been shown [4] that for isotopic PS mixtures dissolved in fully deuterated acetone (AC-d), $L = 0$ at $x = 0.214$. Similarly for PDMS in CO_2, an isotopic ratio of $x = 0.512$ gives $L = 0$ at the density of the solvent ρ_{CO2}=0.95 g/cm^3. Thus, the

intramolecular scattering function may be obtained directly from the measured cross section at all temperatures and equation (1) gives the R_g directly [6]. For PS in CH-d, however, there is no isotopic ratio, $0 < x < 1$, which satisfies the condition $L(x) = 0$, and $d\Sigma/d\Omega(Q,x)$ always contains a minor ($\leq$ 10%) contribution from the total (intermolecular) scattering, which must be subtracted to extract R_g [6].

If all chains are all protonated (x=1), the prefactor, $K = 0$, and $d\Sigma/d\Omega \sim S_t(Q)$. Thus, the size of the concentration fluctuations may be measured via the Ornstein-Zernike (O-Z) formalism [9]: $d\Sigma/d\Omega(Q) = d\Sigma/d\Omega(0)/(1+Q^2\xi^2)$, where ξ is the composition fluctuation correlation length, which may be obtained from the slope of an O-Z plot of $[d\Sigma/d\Omega(0)]^{-1}$ vs. Q^2.

Samples of PS-h, defined by their weight (w) and number (n) averaged molecular weights (M_w = 10,200, 11,600 and 533,000 Dalton) and PS-d (M_w = 10,500, 11,200, and 520,000 Dalton) of polydispersity $M_w/M_n \leq 1.06$ were purchased from Polymer Laboratories. Deuterated solvents AC-d and CH-d (D/(H+D)=0.995) were purchased from Sigma Chemical and were dried over a molecular sieve prior to preparing solutions near the critical concentration C(PS/CH-d)=4.4 wt% [4] and C(PS/AC-d)=20.3wt% [15]. Solutions of (h+d) PS in AC-d and CH-d were prepared at x=0.214 and x=0.20, respectively. The latter condition provides a reasonably high signal-to-noise ratio, which minimizes the contribution from the intermolecular "total scattering" term in Eq.1.

Samples of protonated PDMS-h with M_w = 22,500 47,700, and 79,900 and polydispersity $M_w/M_n \leq 1.03$ were synthesized and characterized at Max Planck Institut für Polymerforschung, Germany, and PDMS-d (M_w = 27600 and 75600, $M_w/M_n \leq 1.11$) was purchased from Polymer Standards Service GmbH, Mainz, Germany. All solutions were prepared at the volume fraction of the polymer equal to the concentration of polymer coil overlap (ϕ^* = 0.1372, 0.0941, and 0.0727 for M_w = 22,500 47,700, and 79,900, respectively) which is practically indistinguishable from the critical concentration of phase demixing [3].

Samples were either run at atmospheric pressure in quartz cells as a function of temperature (e.g. PS-h in CH-d [4,5] or in AC-d [6]) or were loaded into the pressure cell with the appropriate isotopic ratio to eliminate (x = 0.512 for PDMS in CO_2) or minimize (e.g. x = 0.2 for PS-h in CH-d) the contribution of the total scattering term [Eq.(1)]. The maximum area accessible to the neutron beam is ~ 2 cm^2 and the path lengths of the quartz or pressure cells may be adjusted over the range, 0.1 to 2.0 cm. to optimize the transmission. The temperature was controlled by circulating fluids (± 0.1°K) and pressure was applied and measured using a screw-type pressure generator and a precision digital pressure indicator, respectively.

Results and Discussion

Fig.1 shows the temperature variation of the correlation length ξ for PS-h in CH-d at the critical concentration of the polymer and it may be seen that the chains do not collapse as $T \Rightarrow T_C$ as observed in dilute solutions [2]. Instead, they maintain their

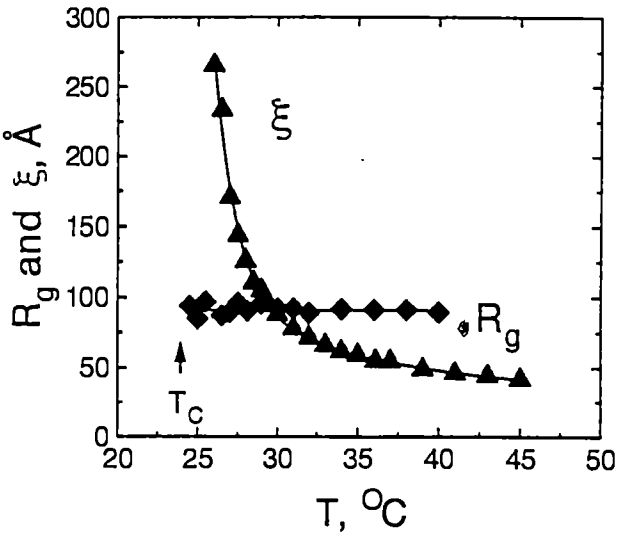


Figure 1. $R_g(T)$ and $\xi(T)$ for the solution of PS with M_W =115,000 in CH-d between T_Θ = 40 °C and the critical temperature of phase demixing (T_C).

unperturbed dimensions in accordance with the theoretical predictions of Muthukumar [16] and Raos and Alegra [17]. The size of the concentration fluctuations is very small in the Θ region, but increases dramatically near the critical point where it exceeds the chain dimensions [$\xi >> R_g(T_\Theta)$]. These findings indicate that critical polymer solutions can no longer be considered as an ensemble of collapsed, non-interpenetrating chains. Instead, the diverging thermodynamic fluctuations in the critical region lead to the formation of distinct microdomains, representing unperturbed, strongly interpenetrating macromolecules.

Fig. 2 shows values of ξ and R_g over a wide range of pressure and temperature extending from the Θ domain to the poor solvent condition near T_C. It may be seen that all isobars for $\xi(T)$ merge at the theta temperature, Θ=40 °C, where the average correlation length $\xi(\Theta) = 109 \pm 5$ Å. According to Fujita [18] and Des Cloizeaux and Jannink [19], $\xi(\Theta)=R_g(\Theta)/3^{1/2}$ at the theta condition, so $\xi(\Theta)$ = 114 Å for M_W = 533000 which agrees well with the experimental value.

Unlike the PS-CH system, which may undergo the transition from the poor solvent to the theta solvent by adjusting the temperature, the solvent quality is much poorer for PS - AC. Fig.3 shows the effect of pressure on the thermodynamic state of PS/AC-d solutions and the chain dimensions [$R_g \equiv 29$ Å] are independent of pressure and temperature and remain close to the unperturbed dimensions for Gaussian chains with M_W = 11,600 [i.e. $R_g = 0.27\ M_W^{1/2} \sim 29$ Å]. Conversely, the concentration fluctuations as monitored by the correlation length, ξ, diverge near the critical point and fall when $P >> P_C$. However, they do not decay sufficiently to reach $\xi(\Theta)$ =

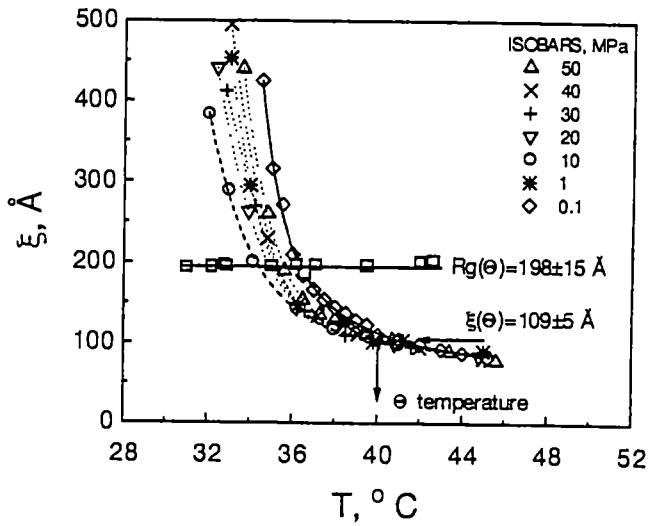


Figure 2. ξ(T) for PS-h (M_W = 533000) in CH-d at different pressures shown in the inset. R_g(P,T) of PS-h chains in the solution (h+d) PS in CH-d is also shown (open squares).

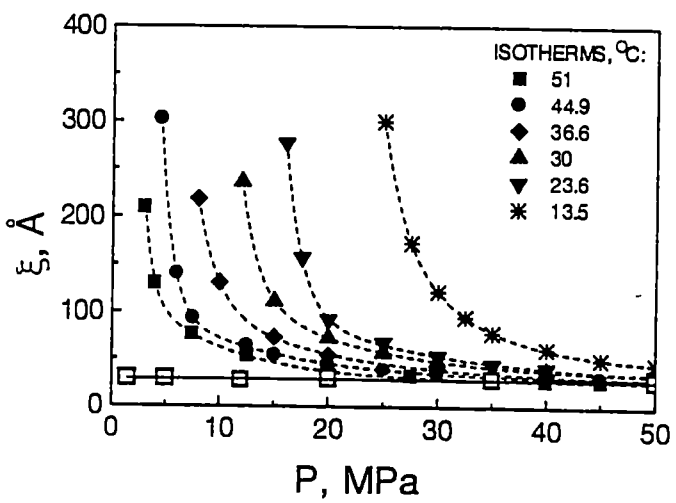


Figure 3. ξ(P) of PS-h (M_W = 11,600) in AC-d at the different temperatures shown in the inset. R_g(P,T) of labeled PS-h chains in the solution of (h+d) PS in AC-d is also plotted (open squares).

$R_g(\Theta)/3^{1/2} \cong 17$ Å, and thus, the system never leaves the poor solvent domain. Despite this, the macromolecules always exhibit their unperturbed (theta) dimensions, even though they never reach the theta domain. It is remarkable that the diverging concentration fluctuations which prevent chain collapse in PS-CH, also operate in PS-AC. So effective is this mechanism, that even for solutions which never leave the poor solvent domain, the macromolecules are always "stabilized" to exhibit the theta dimensions over wide ranges of pressure and temperature (Fig. (3).

The SANS experiments on PDMS in CO_2 were designed to compare the chain dimensions with those in organic solvents and to test the prediction [7] that they will adopt "ideal" configurations, unperturbed by excluded volume effects, at a critical "theta pressure"(P_Θ) as they do in polymer solutions at the theta temperature. The effect of temperature on the thermodynamic state of PDMS – CO_2 solution is illustrated in Fig. 4. The concentration fluctuations diverge as the temperature approaches the phase boundaries, which are themselves a function of pressure. When the correlation length decreases to the theoretical value $\xi(\Theta) = R_g(\Theta)/3^{1/2} \cong 41$ Å, the Θ condition is reached and this demonstrates that, unlike PS-AC, the solvent quality may be changed from the "poor" to theta solvent by varying the temperature, as in PS-

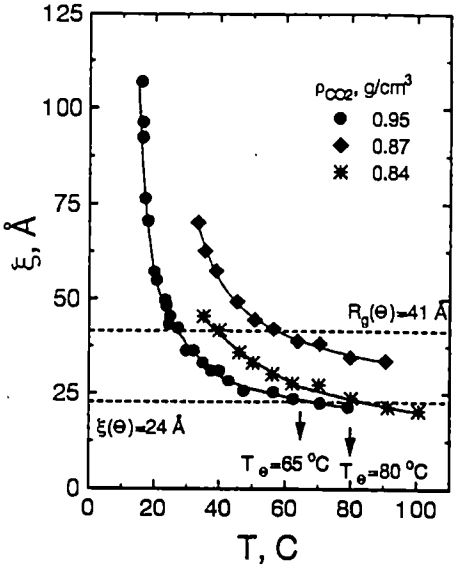


Figure 4. $\xi(T)$ of PDMS in SC CO_2 at different density of the supercritical solvent shown in the inset. The value of the Θ temperature depends crucially on the density of SC CO_2, e.g. $T_\Theta = 65 \pm 5\ ^oC$ at $\rho_{CO2} = 0.95$ g/cm^3, however $T_\Theta = 80 \pm 5\ ^oC$ at $\rho_{CO2} = 0.87$ g/cm^3. The Θ temperature may hardly be reached at $\rho_{CO2} \leq 0.84$ g/cm^3.

CH solutions. A typical variation of ξ vs. $(T - T_C)$ in PDMS-SC CO_2 solutions is shown in Fig.5. As is seen, the critical index ν in a scaling law for the correlation length $\xi \sim (T - T_C)^{-\nu}$ exhibits a sharp crossover from the mean-field value (ν=0.5) in the Θ region to the Ising model value (ν=1.24) in the critical region around T_C. The crossover takes place when the correlation length becomes equal to the radius of gyration of the polymer and thus reproduces the main features of the crossover of ξ observed in solutions of PS in CH-d (see the inset in Fig.5) [4,5]. These observations delineate an intrinsic analogy between the temperature behavior of polymers in SCFs and in organic solvents [20] and show that polymer solutions in SCFs belong to the universality class of Ising model.

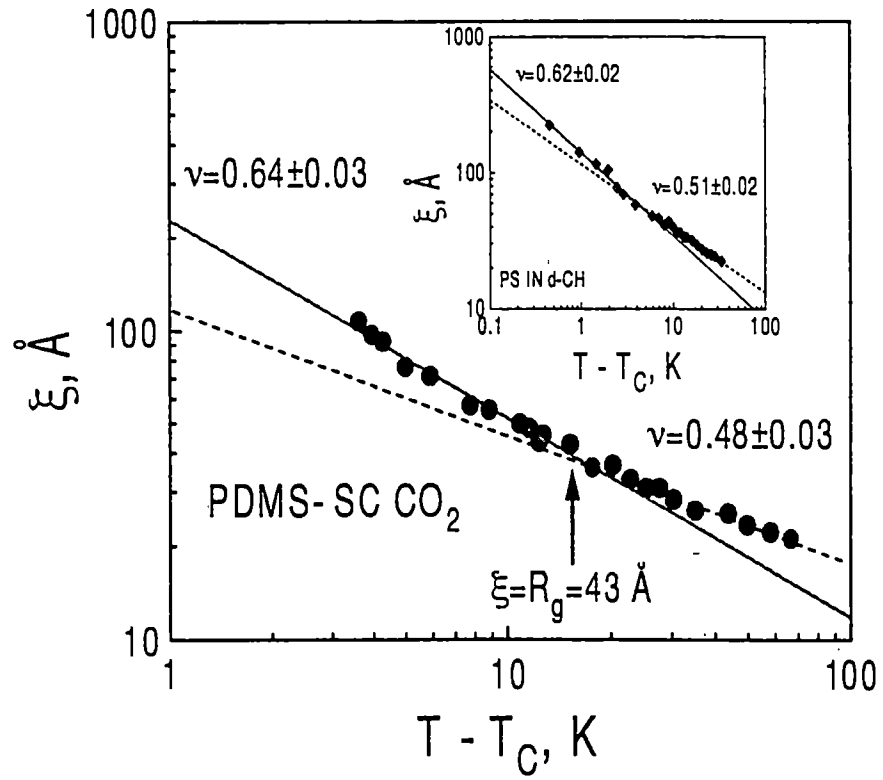


Figure 5. Variation of ξ as a function of $(T-T_C)$ for solution of PDMS (M_W =22500) in SC CO_2. The slope gives the value of the critical index ν. The inset shows ξ vs. $(T-T_C)$ for a solution of PS with M_W =28000 in CH-d [4,5].

Fig.6 shows that PDMS may also enter the "good solvent" domain at a "theta" temperature T_Θ = 65 ±5 °C, as observed in PS-CH solutions [21]. However, unlike organic solvents, this transition can also be made to occur at a critical "theta pressure" (P_Θ = 52 ± 4 MPa) in CO_2, as illustrated in the inset in Fig.6. To our knowledge, this is the first time that the existence of a "theta pressure" has been demonstrated experimentally and a more detailed description of this phenomenon is given in reference [22].

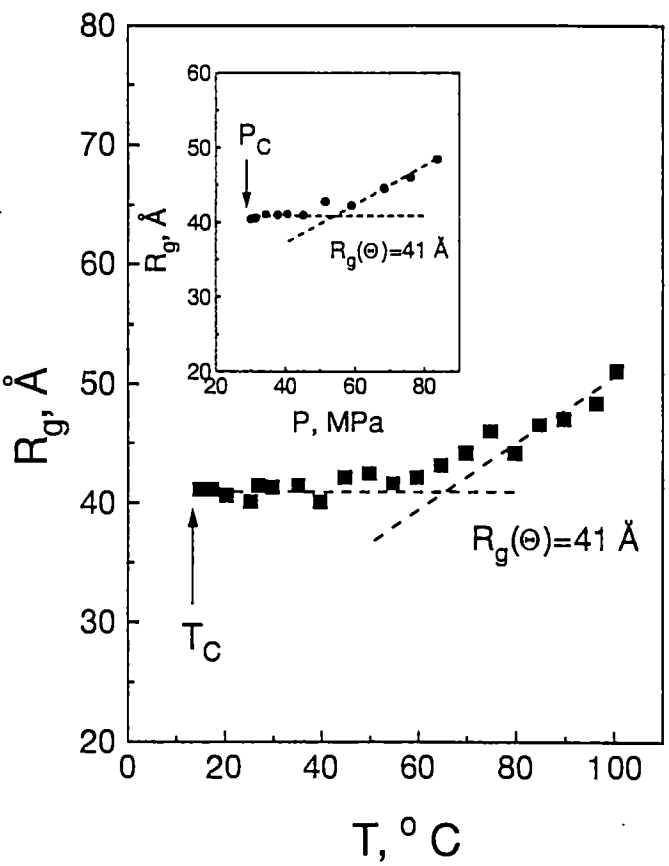


Figure 6. Expansion of PDMS chains in SC CO_2 above the Θ temperature T_Θ ~ 65 °C. Below T_Θ, diverging concentration fluctuations prevent the coil collapsing as observed in organic solvents. The inset illustrates first observation of a Θ pressure in solutions of PDMS in SC CO_2. As observed in organic solvents, the polymer chains do not collapse below P_Θ.

For $P > P_\Theta$ and $T > T_\Theta$, the system exhibits a "good solvent" domain, where the polymer molecules expand beyond the unperturbed R_g, in a good agreement with results of computer simulations [23]. However, for $T < T_\Theta$, and $P < P_\Theta$, the chains do not collapse and maintain their unperturbed dimensions, as observed in organic solvents [4-6], where the size of the concentration fluctuations, ξ diverges as $T \Rightarrow T_C$. Thus, the deterioration of the solvent quality again leads to the formation of microdomains, consisting of interpenetrating polymer coils, as in organic solvents. Near the critical point, the growth of the polymer concentration fluctuations brings together the initially non-overlapping chains, and the macromolecules adopt the unperturbed dimensions, as in highly concentrated systems and in the condensed state. Thus, the stabilization of the molecular dimensions in the poor solvent domain by diverging concentration fluctuations is a universal phenomenon, observed not only in "classical" polymer solutions in organic solvents (e.g. PS in CH), but also in supercritical fluids (e.g. PDMS in CO_2).

A unique attribute of SCFs is that the solvent strength is easily tunable with changes in the system density, offering exceptional control over the solubility. Thus, for PDMS, CO_2 becomes a "theta" solvent at P_Θ ~52 MPa and T_Θ ~65°C, whereas it behaves as a "good" solvent for $P > P_\Theta$ and $T > T_\Theta$. Below this transition, the chain dimensions never fall below the "theta" R_g, as observed in organic solvents, though for supercritical CO_2, the system may be driven through this transition as a function of pressure in addition to temperature. Understanding the solubility mechanisms is a necessary condition for the development of CO_2-based technologies and SANS promises to give the same level of insight into polymers in supercritical media that it has provided in the condensed state, organic solvents and in aqueous systems.

Acknowledgments

YBM and GDW wish to acknowledge stimulating discussions with M. Muthukumar. The research was supported the Divisions of Advanced Energy Projects and Materials Sciences, U. S. Department of Energy under contract No. DE-AC05-96OR-22464 (with Lockheed Martin Energy Research Corporation) and Grant No. DE-FG05-88ER-45374 (with the University of Tennessee).

References

1. Wignall, G. D. in: *Encyclopedia of Polymer Science and Engineering;* John Wiley & Sons, Inc.: New York, 1987; Vol. 10, p. 112.
2. Chu, B; Ying, Q; Grosberg, A. *Macromolecules* **1995**, 28, 180, and references therein
3. De Gennes, P. G. *Scaling Concepts in Polymer Physics*; Cornell University Press: Ithaca, 1979.
4. Melnichenko, Y. B.; Wignall, G. D. *Phys. Rev. Lett.* **1977**, *78*, 686.

5. Melnichenko, Y. B.; Anisimov, M. A.; Povodyrev, A. A.; Wignall, G. D.; Sengers, J. V.; Van Hook, W. A. *Phys. Rev. Lett.* **1997**, *79*, 5266.
6. Melnichenko, Y. B.; Wignall, G. D.; Van Hook, W. A.; Szydlowski, J.; Rebello, L. P.; Wilczura, H. *Macromolecules* **1998**, *31*, 8436.
7. Kiran, E.; Sen, Y. L. in: *Supercritical Fluid and Engineering Science*; ACS Symposium Series 1993.
8. Koehler, W. C., *Physica* **1986**, *137B*, 320.
9. Wignall, G. D.; Bates, F. S. *J. Appl. Cryst.* **1986**, *20*, 28.
10. DeSimone, J. M.; Guan, Z.; Elsbernd, C. S. *Science*, **1992**, *257*, 945.
11. McClain, J. B.; Betts, D. E.; Canelas, D. A.; Samulski, E. T.; DeSimone, J. M.; Londono, J. D.; Cochran, H. D.; Wignall, G. D.; Chillura-Martino, D.; Triolo, R. *Science* **1996**, 274, 2049.
12. Williams, C. E.; Nierlich, M.; Cotton, J. P.; Jannink, G.; Boue, F.; Daoud, M; Farnoux, B., Picot, C.; de Gennes, P.-G.; Rinaudo, M.; Moan, M.; Wolf, C. *J. Polym. Sci., Polym. Lett. Ed.* **1979**, *17*, 379.
13. Akasu, A. Z.; Summerfield, G. C.; Jahansan, S. N.; Han C. C.; Kim, C. Y.; Yu, H. J.: *Polym. Sci., Polym. Phys. Ed.* **1980**, *18*, 863.
14. King, J. S.; Boyer, W.; Wignall, G. D.; Ullman, R. *Macromolecules* **1985**, *18*, 709.
15. Szydlowski, J.; Van Hook, W. A. *Macromolecules* **1991**, *24*, 4883.
16. Muthukumar, M. *J. Chem. Phys.* **1986**, *85*, 4722.
17. Raos, G.; Allegra, G. *J. Chem. Phys.* **1996**, *104*, 1626.
18. Fujita, H. *Polymer Solutions*; Elsevier: Amsterdam, Oxford, NY, Tokyo; 1990, p. 192.
19. Des Cloizeaux, J.; Jannink, G. *Polymers in Solution. Their Modeling and Structure*; Claredon Press: Oxford; 1990, page 815.
20. This conclusion is strongly supported by recent theoretical calculations which demonstrated a close similarity between the scaling behavior of grafted polymer chains in supercritical and in liquid solvents [Meredith, J. C. and Johnston, K. P., *Macromolecules* **1998**, *31*, 5518].
21. Cotton, J. P.; Nierlich, M.; Boue, F.; Daoud, M.; Farnoux, B.; Jannink, G.; Duplessix, R.; Picot, C. *J. Chem. Phys.* **1976**, *65*, 1101.
22. Melnichenko, Y. B.; Kiran, E.; Wignall, G. D.; Heath, K.; Salaniwal, S.; Cochran, H. D.; Stamm, M., submitted to *Phys.Rev.Lett.*
23. Luna-Barcenas, G.; Meredith, J. C.; Sanchez, I. C.; Johnson, K. P.; Gromov, D. G.; de Pablo, J. J., *J. Chem. Phys.* **1997**, *107*, 10782; Gromov, D. G.; de Pablo, J. J.; Luna-Barcenas, G.; Sanchez, I. C.; Johnson, K. P., *J. Chem. Phys.* **1998**, *108*, 4647.

Paper 2

PRESSURE AND TEMPERATURE-INDUCED TRANSITIONS IN SOLUTIONS OF POLY(DIMETHYL SILOXANE) IN SUPERCRITICAL CARBON DIOXIDE

Y. B. Melnichenko[1], E. Kiran[2], G. D. Wignall[1], K. D. Heath[3], S. Salaniwal[3], H. D. Cochran[3], M. Stamm[4]

[1]*Oak Ridge National Laboratory*, Oak Ridge, TN 37831, USA*

[2]*Department of Chemical Engineering, University of Maine, Orono, ME 04469*

[3]*Chemical Technology Division, Oak Ridge National Laboratory and Department of Chemical Engineering, University of Tennessee, Knoxville, TN 37996*

[4]*Max Planck-Institut fur Polymerforschung, 55021 Mainz, Germany*

Supercritical fluids (SCFs) have great technological potential for minimizing the organic wastes associated with polymer manufacturing and processing. However, significant challenges remain for developing the same level of understanding of the behavior of polymers in SCFs as has been reached for polymers in traditional organic solvents. Small-angle neutron scattering was used to study the effect of pressure and temperature on the phase behavior of poly(dimethylsiloxane) (PDMS) in supercritical carbon dioxide (SC CO_2). It

was demonstrated that PDMS-SC CO_2 solutions reproduce all main features of the temperature-concentration phase diagram for polymers in organic solvents. Moreover, because of their continuously adjustable solubility, SCFs exhibit novel effects, such as a pressure-induced transition to the Θ point and to the good solvent domain, in addition to a polymer-solvent demixing at a lower critical solution pressure.

* Managed by Lockheed Martin Energy Research Corporation under contract DE-AC05-96OR-22464 for the U. S. Department of Energy.

A supercritical fluid (SCF) is a substance at a pressure and temperature above the liquid-vapor critical point where the coexisting liquid and vapor phases become indistinguishable. The physical properties of SCFs are similar to those of dense gases, although when highly compressed, their density may be comparable to that of the sub-critical liquids. SCFs in general and supercritical carbon dioxide (SC CO_2) in particular have emerged as an attractive alternative to the organic solvents used for polymer manufacturing and processing. One key advantage of SCFs is the possibility of continuously tuning the solvent quality by varying the pressure (P) in

addition to the temperature (T), which offers an unparalleled means for controlling polymer solubility. Despite recent progress in many specific areas of SCF science and technology (see e.g. [1,2] and references therein), significant challenges remain for developing the same level of understanding of the behavior of polymers in SCFs as has been reached for polymers in traditional organic solvents. Here we address the effect of temperature and pressure on the phase behavior of poly(dimethyl siloxane) (PDMS) in SC CO_2. We apply small-angle neutron scattering (SANS) to extract information on the concentration fluctuations and the dimensions of polymer chains at different conditions and find that the supercritical solutions reproduce all salient features of the temperature-concentration phase diagram for polymers in liquid solvents [3]. Moreover, because of their continuously adjustable properties, SCFs exhibit novel effects, such as a pressure-induced transition to the Θ point and to the good solvent domain, in addition to a polymer-solvent demixing at a lower critical solution pressure.

At the phenomenological level, liquid solvents for polymers are divided into three classes, namely poor, theta (Θ), and good solvents. The solvent quality is directly related to the ability of the solvent molecules to mediate the attractive intrachain forces responsible for the polymer – solvent

demixing. Poor solvents can hardly impede the intrachain interactions and hence can dissolve only short chain (or low molecular weight M_W) polymers with a limited number of contacts between the segments. The pairwise attractive and repulsive interactions compensate at the Flory or the "Θ temperature" (T_Θ) which is defined as the upper critical solution temperature (UCST) for a polymer with infinite molecular weight $M_W = \infty$ [4,5]. At $T=T_\Theta$ the radius of gyration $R_g(T_\Theta)$ of polymer chains is unperturbed by excluded volume effects and is also independent of the long-range critical concentration fluctuations. In the good solvent domain $T > T_\Theta$ the repulsive forces between the segments work to expand R_g above the unperturbed dimensions at $T=T_\Theta$.

The dimension of polymer chains R_g and the correlation length of the concentration fluctuations ξ in polymer solutions may be determined at different (P,T) using SANS combined with a high concentration isotope labeling method [6]. The coherent scattering intensity, I, for a mixture of identical hydrogenated and deuterated polymer chains in a solvent is:

$$I(Q,x) = K * S_s(Q) + L * S_t(Q) \quad , \tag{1}$$

where $S_s(Q)$ is the single-chain structure factor which contains information on the dimensions (R_g) of the polymers. Similarly, $S_t(Q)$ is the total scattering structure factor which contains information on the correlation length of the concentration fluctuations, ξ. The scattering vector is given by $Q = 4\pi\lambda^{-1}\sin\theta$, where 2θ is the scattering angle and λ is the neutron wavelength. The prefactor $K^* \sim (b_H - b_D)^2\, x(1-x)$ in Eq.(1) is a function of the neutron scattering lengths of the hydrogenated (b_H) and deuterated (b_D) monomers as well as on the mole fraction (x) of hydrogenated polymers. If all chains are hydrogenated (x=1), K^*=0, and one can obtain ξ(T,P) directly from $I(Q,x=1) \sim S_t(Q)$ using the Ornstein-Zernike formula

$$S_t(Q) = S(0)/(1+Q^2\xi^2) \quad . \tag{2}$$

In addition to b_H and b_D, the prefactor $L^* \sim [b_H x + (1-x)b_D - b_S']^2$ in Eq.(1) depends on the scattering length b_S' of a solvent normalized via the ratio of the specific volumes of the monomer and the solvent molecule. For PDMS-CO_2 mixtures, b_H =0.086 10^{-12} cm, b_D = 6.33 10^{-12} cm, and b_S' =1.47 10^{-12} to 3.76 10^{-12} cm in the range between the critical (ρ_{CO2}=0.469 g/cm^3) and the liquid state densities (ρ_{CO2}=1.2 g/cm^3). For a given combination of the

neutron scattering lengths ($b_H < b_S' < b_D$), it is possible to make the pre-factor L^* zero at any density of SC CO_2 by choosing an appropriate concentration (x) of hydrogenated PDMS (e.g. L^*=0 at x=*0.512* and ρ_{CO2}=0.95 g/cm). In this case, Eq.(1) gives the single chain (intramolecular) scattering directly and the R_g may be obtained by fitting *I(Q)* with the Debye function [7,8]:

$$S_s^D = (2/y^2)(y-1+e^{-y}) \quad , \quad y = Q^2 R_g^2 \quad . \tag{3}$$

For solutions of non-overlapping polymer chains [9] under the Θ condition, Eq.(3) yields in the limit of small Q [7,8]:

$$S(Q) = \frac{S(0)}{1+Q^2\xi^2(\Theta)} \quad , \quad \xi(\Theta) = R_g(\Theta)/\sqrt{3} \quad . \tag{4}$$

Thus, the SANS measurements of ξ vs. T (or P) may be used to determine the Θ temperature (or the Θ pressure) using Eq.(4) [10].

The experiments were performed on the 30-m SANS spectrometer at the Oak Ridge National Laboratory over Q-range of 0.005<Q/Å^{-1}<0.05

(λ=4.75 Å). The data were radially averaged and converted to an absolute coherent cross section (in units of cm^{-1}) using procedures described elsewhere [11]. The structure factors $S_s(Q)$ and $S_i(Q)$ were obtained from Eq.(1) and used to calculate ξ and R_g at different thermodynamic conditions using Eqs. (2) and (3). Polymer samples of PDMS-h (M_W =22500, 47700, and 79900 of polydispersity $M_W/M_N \leq 1.03$) and PDMS-d (M_W =27600, $M_W/M_N \leq 1.11$) were synthesized and characterized at the Max Planck Institute for Polymer Research, Germany. PDMS-d (75600, $M_W/M_N \leq 1.3$) was purchased from Polymer Standards Service GmbH, Mainz, Germany. All solutions were prepared at the overlap concentration [9] (C*=0.1397, 0.0959, and 0.0741 g/ml for M_W 22500, 47700, and 79900, respectively). H-PDMS or isotopic mixtures of (h+d) PDMS at x=0.512 were loaded into a stainless steel cylindrical cell which was fitted with optically polished sapphire windows virtually transparent to neutron radiation. The samples were pressurized at T=50 ^{o}C to 45.7 MPa (i.e. at ρ_{CO2}=0.95 g/cm^3) with CO_2 (SFC purity 99.99%, Matheson Gas products, Inc., USA) and stirred thoroughly until a transparent homogeneous solution was obtained. After completing the temperature scans ξ(T,P) or R_g(T,P) at constant density (ρ_{CO2}=0.95 g/cm^3), the variation of ξ(P,T=const) or R_g(P,T=const) was measured with pressure at isothermal conditions.

The temperature variation of ξ in PDMS - SC CO_2 solutions at constant density ρ_{CO2}=0.95 g/cm^3 is shown in Fig.1. As monitored by the intermolecular correlation length, the concentration fluctuations diverge ($\xi \Rightarrow \infty$) as T approaches the critical temperature of phase demixing T_C. The intermolecular correlations decline rapidly with the temperature, become comparable to the dimension of polymer chains at ($T-T_C$) ~ 12 - 16 ^oC and reach the theoretical value $\xi(\Theta)$ for each M_W (Eq.4) at $T=T_\Theta$ = 65±5 ^oC. To our knowledge, this is the first experimental observation of the temperature-induced transition to the Θ point in polymer solutions in SCFs. In the inset in Fig.1 we compare the temperature variation of the concentration fluctuations in supercritical CO_2 and in organic solvents [i.e. polystyrene (PS) in the Θ solvent cyclohexane-d (CH-d)]. The reduced correlation lengths $\xi/\xi(T_\Theta)$ for both systems fall on the same master curve when plotted vs. the reduced temperature $\tau' = \frac{T_\Theta}{T_\Theta - T_C}\frac{T-T_C}{T}$ which accounts for the temperature distance from both T_Θ and T_C. A typical variation of ξ vs. ($T - T_C$) in PDMS-SC CO_2 solutions is shown in Fig.2. As is seen, the critical index ν in a scaling law for the correlation length $\xi \sim (T-T_C)^{-\nu}$ exhibits a sharp crossover from the mean-field value (ν=0.5) in the Θ region to the

Ising model value (ν=0.630±0.001 [12]) in the critical region around T_C. Accordingly, the critical index γ=1.23±0.02 for the susceptibility (i.e. the osmotic compressibility) in $\chi \sim (T - T_c)^{-\gamma}$ at T⇒T_C for all solutions studied agrees within experimental errors with the Ising model value (1.239±0.002 [12]). The crossover takes place when $\xi \sim R_g$ and thus reproduces the main features of the crossover observed in solutions of PS in CH-d (see the inset in Fig.2) [13,14]. These observations delineate an intrinsic analogy between the temperature behavior of polymers in SCFs and in liquid Θ solvents in the vicinity of the UCST and show that polymer solutions in SCFs belong to the universality class of the Ising model.

The effect of pressure on the thermodynamic condition of PDMS – SC CO_2 solutions is illustrated in Fig.3. The concentration fluctuations diverge as P approaches the upper critical solution pressure (UCSP) P_C where the system exhibits pressure-induced phase demixing. The solvent quality increases rapidly with P in the range $(P-P_C) \leq 7$ MPa and more gradually after ξ becomes comparable to the radius of gyration of polymer chains $R_g(\Theta)$=75 Å. At P_Θ = 52±4 MPa the correlation length becomes equal to the theoretical value $\xi(\Theta) \cong 41$ Å (Eq.4) which indicates that the Θ condition has been reached. This is the first experimental observation of the

pressure-induced transition to the Θ point in polymer solutions in SCFs, the existence of which was predicted earlier in [15]. It is interesting that the effect of pressure may be quite opposite at less favorable thermodynamic conditions. If the experiment is performed at a temperature close to a UCST, $\xi(P)$ goes through the minimum after which the lower critical solution pressure (LCSP) is approached (see the inset in Fig.3). The best solvent quality is reached close to the theta pressure P_Θ=52 MPa, though the correlation length $\xi(P_\Theta)\cong$74 Å is still much larger than the dimension of polymer chains in the solution $R_g(\Theta)$ =58 Å. This indicates that pressure alone may not always be capable of moving supercritical polymer solutions out of the poor solvent domain. The situation is similar to polymer solutions in poor organic solvents (e.g. PS in acetone) where the intermolecular correlations never decrease below the dimension of the constituent polymer [10]. We are not aware of previously published data on the pressure-induced demixing upon an increase in pressure in supercritical polymer solutions and believe this result to be the first experimental observation of the LCSP.

Fig.4 illustrates the behavior of the radius of gyration of PDMS in SC CO_2 with P and T. As is seen, R_g of the polymer remains invariant during both pressure and temperature quenches which extend to the immediate vicinity of the (T,P) polymer-SCF demixing locus and agrees well with the

dimension of unperturbed chains with ($R_g = 0.267\ M_w^{1/2} \cong 40$ Å [16]). This observation indicates the universality of the constancy of R_g in semidilute polymer solutions below T_Θ and P_Θ which was previously demonstrated for liquid solvents [10,17] and has now been shown to extend to supercritical fluids. At $P>P_\Theta$ and/ or $T>T_\Theta$ the dimensions of polymer chains increase due to the excluded volume effects, as was observed in PS- CH-d solutions at $T>T_\Theta$ [18], indicating that SC CO_2 is becoming a good solvent for PDMS in this range of the thermodynamic parameters.

In conclusion, the experiments demonstrate universality between the structure and thermodynamic properties of the liquid and supercritical polymer solutions. In the latter case, the threshold of unlimited miscibility (the Θ point) may be reached by varying either the pressure or the temperature. The experimental data agree with the results of Monte Carlo simulations which indicate that polymer chains may adopt unperturbed and expanded conformations at high densities [19]. This provides a foundation for a better understanding the underlying physics of SCF – polymer assemblies.

Stimulating discussions with M. Muthukumar and T. Wagner are greatly acknowledged. The research was supported by the Divisions of Advanced Energy Projects and Materials Sciences, U. S. Department of

Energy under contract No. DE-AC05-96OR-22464 (with Lockheed Martin Energy Research Corporation). KDH and HDC were supported by the Division of Chemical Sciences of the U. S. Department of Energy. The financial support of YBM by Alexander von Humboldt-Stiftung is greatfully acknowledged. SS was supported by the National Science Foundation under grant number CTS-9613555 at the University of Tennessee.

REFERENCES

1. Kiran, E.; Levelt Sengers, J. M. H. Eds. *Supercritical Fluids: Fundamentals for Application;* Kluwer Acad. Publ.: Dodrecht, Boston, London, 1993.
2. McHugh, M. A.; Krukonis, V. J. *Supercritical fluid extraction: principles and practice;* Butterworth-Heinemann: Boston, 1994.
3. Daoud, M.; Jannink, G.; *J. Phys. (Paris)* **1976,** *37*, 973.
4. Sanchez, I. C. *Encyclopedia of Physical Science and Technology;* Academic Press: New York, 1992, vol. 13, pp.153-170.
5. The Θ condition may be viewed as corresponding to the threshold of unlimited polymer – solvent miscibility in the sense that a polymer of an arbitrary M_W becomes miscible in any proportion with the given solvent.
6. Williams, C. E.; Nierlich, M.; Cotton, J. P.; Jannink, G.; Boue, F.; Daoud, M; Farnoux, B., Picot, C.; de Gennes, P.-G.; Rinaudo, M.; Moan, M.; Wolf, C. *J. Polym. Sci., Polym. Lett. Ed.* **1979**, *17*, 379; Akasu, A. Z.; Summerfield, G. C.; Jahansan, S. N.; Han C. C.; Kim, C. Y.; Yu, H. J. *Polym. Sci., Polym. Phys. Ed.* **1980**, *18*, 863; King, J. S.; Boyer, W.; Wignall, G. D.; Ullman, R. *Macromolecules* **1985**, *18*, 709.

7. Des Cloizeaux, J. Jannink, G. *Polymers in Solution. Their Modeling and Structure;* Claredon Press: Oxford, 1990.

8. Fujita, H. *Polymer Solutions;* Elsevier: Amsterdam, Oxford, NY, Tokyo, 1990.

9. The concentration C* at which polymer chains begin to overlap may be defined as $C^* = 3M_W / 4\pi R_g^3 N_A$, where N_A is the Avogadro number [7,8]. The C* thus defined provides the closest proximity to the critical concentration of polymer solutions in organic solvents in the range $M_W \leq 80000$ [Melnichenko, Wignall, to be published].

10. The validity of Eq.(4) was verified using SANS for solutions of polystyrene in deuterocyclohexane at the Θ condition over a wide range of pressures 0.1 – 50 MPa in [Melnichenko, Y. B.; Wignall., G. D.; Van Hook, W. A.; Szydlowsky, J.; Wilczura H.; Rebelo, L. P. *Macromolecules* **1998**, *31*, 8436].

11. Wignall G. D.; Bates, F. S. *J. Appl. Crystallogr.* **1986**, *20*, 28.

12. Le Guillou J. C.; Zinn-Justin, J. *Phys.Rev.* **1980**, *B 21*, 3976.

13. Melnichenko Y. B. et al. *Europhys.Lett.* **1992**, *19*, 355.

14. Melnichenko, Y. B.; Anisimov, M. A.; Povodyrev, A. A.; Wignall, G. D.; Sengers J. V.; Van Hook, W. A. *Phys. Rev. Lett.*, **1997**, *79*, 5266.

15. Kiran E.; Sen, Y. L. in: *Supercritical Fluid Engineering Science,* Kiran, E.; Brenneke, J. F. Eds., *ACS Symposium Series*, 1993, ch. 9.

16. Mark, J. E. Ed. *Physical Properties of Polymers Handbook;* AIP Press: Woodbury, NY 1996.

17. Melnichenko Y. B.; Wignall, G. D. *Phys. Rev. Lett.* **1997**, *78*, 686.

18. Cotton., J. P.; Nierlich, M.; Boue, F.; Daoud, M.; Farnoux, B.; Jannink, G.; Duplessix, R.; Picot, C. *J. Chem. Phys.*, **1976**, *65*, 1101.

19. Luna-Barcenas, G.; Meredith, J. C.; Sanchez, I. C.; Johnson, K. P.; Gromov, D. G.; de Pablo, J. J., *J. Chem. Phys.* **1997**, *107*, 10782; Gromov,; D. G.; de Pablo, J. J.; Luna-Barcenas, G.; Sanchez, I. C.; Johnson, K. P. *J. Chem. Phys.* **1998**, *108*, 4647.

LEGENDS:

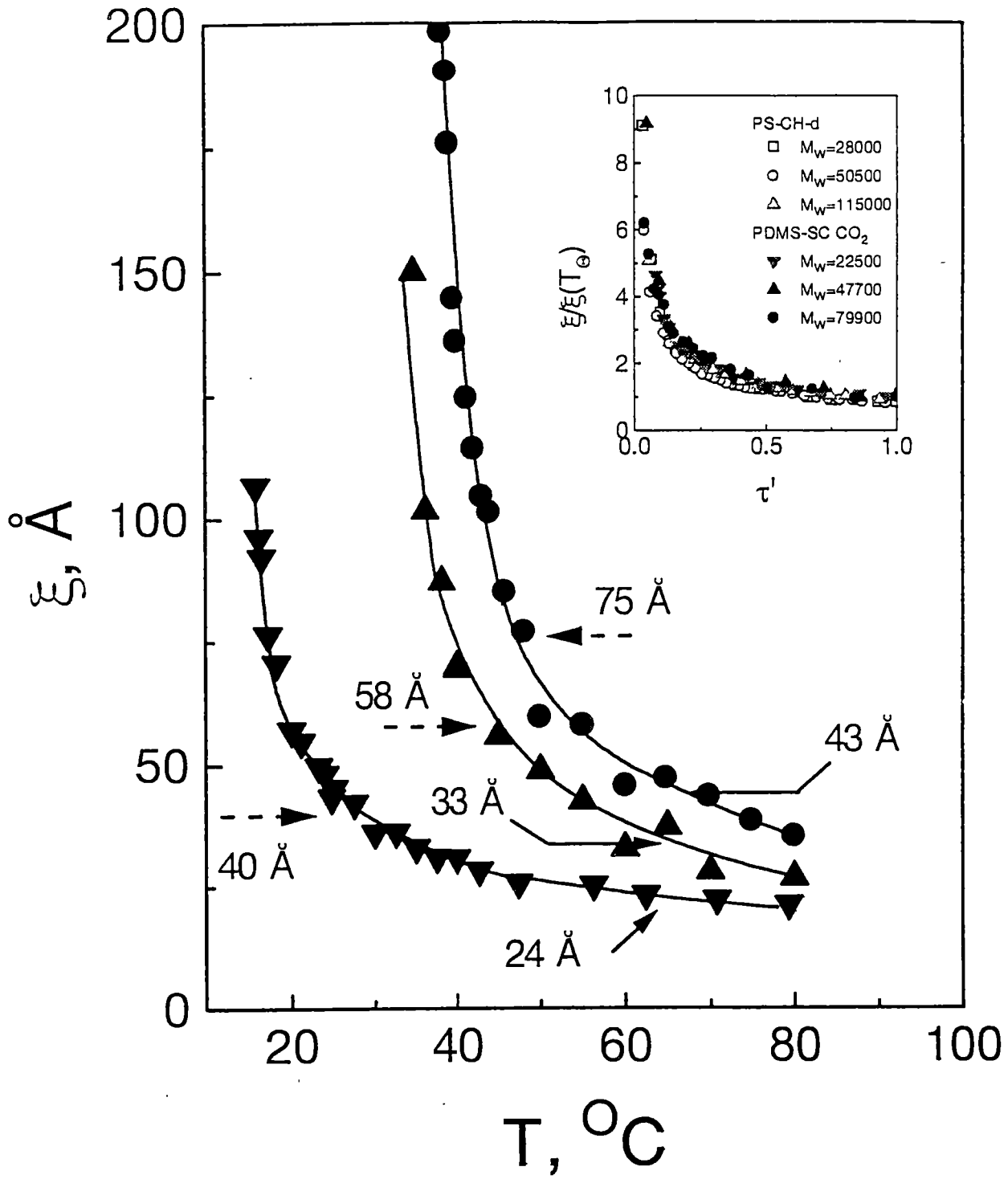
Fig.1. $\xi(T)$ for h-PDMS with M_W=22500 ($\blacktriangledown$), 47700 ($\blacktriangle$), and 79900 ($\bullet$). ρ_{CO2}=0.95 g/cm^3. Dashed and solid arrows show the value of $R_g(\Theta)=0.267\ M_w^{1/2}$ [16] and $\xi(\Theta)=R_g(\Theta)/\sqrt{3}$ (Eq.4), respectively. The inset shows the variation of the reduced correlation length vs. the reduced temperature $\tau'=\frac{T_\Theta}{T_\Theta - T_C}\frac{T-T_C}{T}$ for solutions of PS in CH-d [17] and PDMS in SC CO_2. In the latter case, the parameters used for calculations are: T_Θ=65 ^oC, T_C = 12.2 ^oC (M_W=22500), T_C = 31.8 ^oC (M_W=47700), and T_C = 36.1 ^oC (M_W=79900).

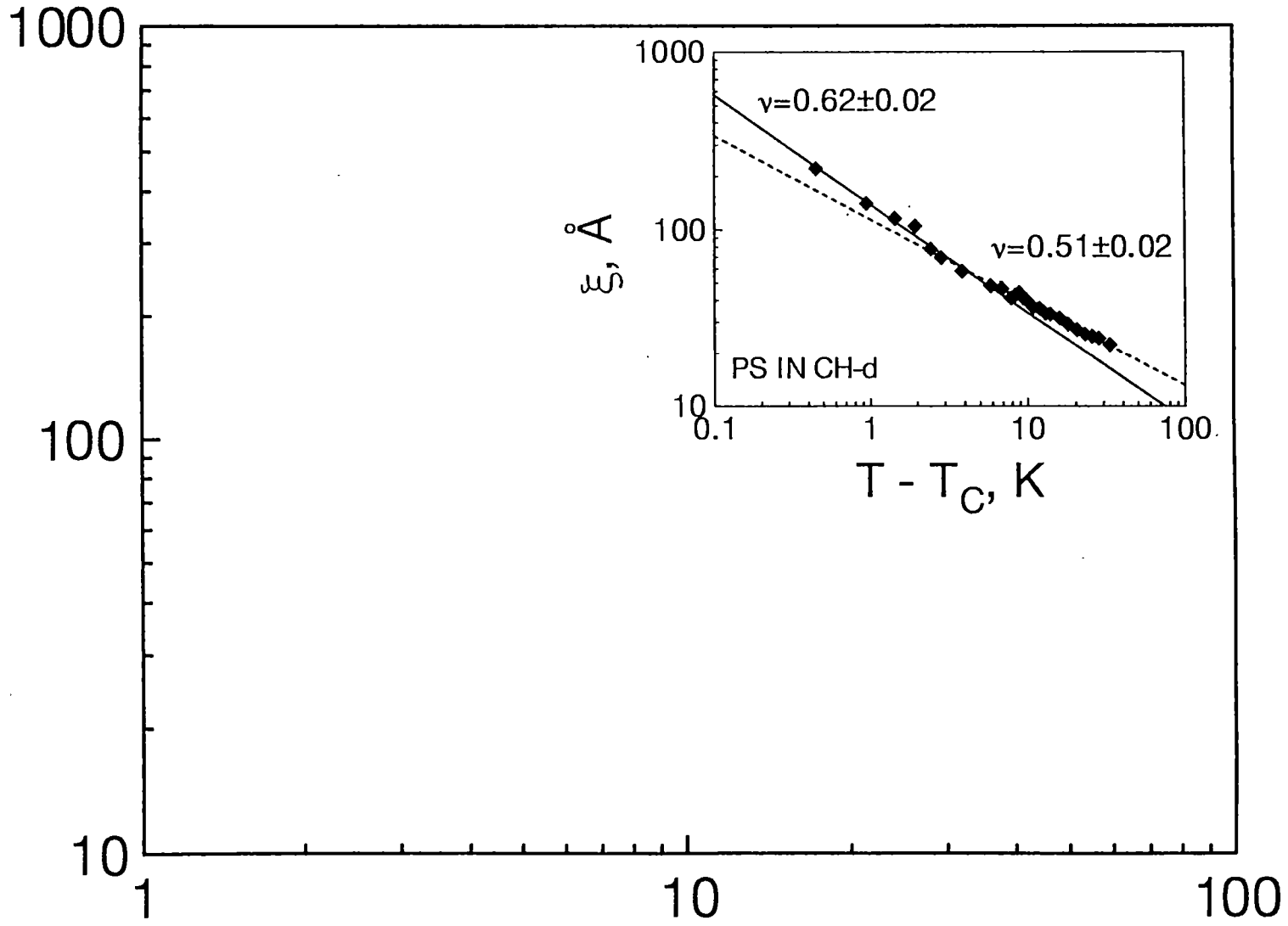
Fig.2. Variation of ξ as a function of ($T-T_C$) for solution of PDMS (M_W =22500) in SC CO_2. ρ_{CO2}=0.95 g/cm^3. The slope gives the value of the critical index ν. The inset shows ξ vs. ($T-T_C$) for PS – CH-d solution with a similar M_W =28000 of the polymer.

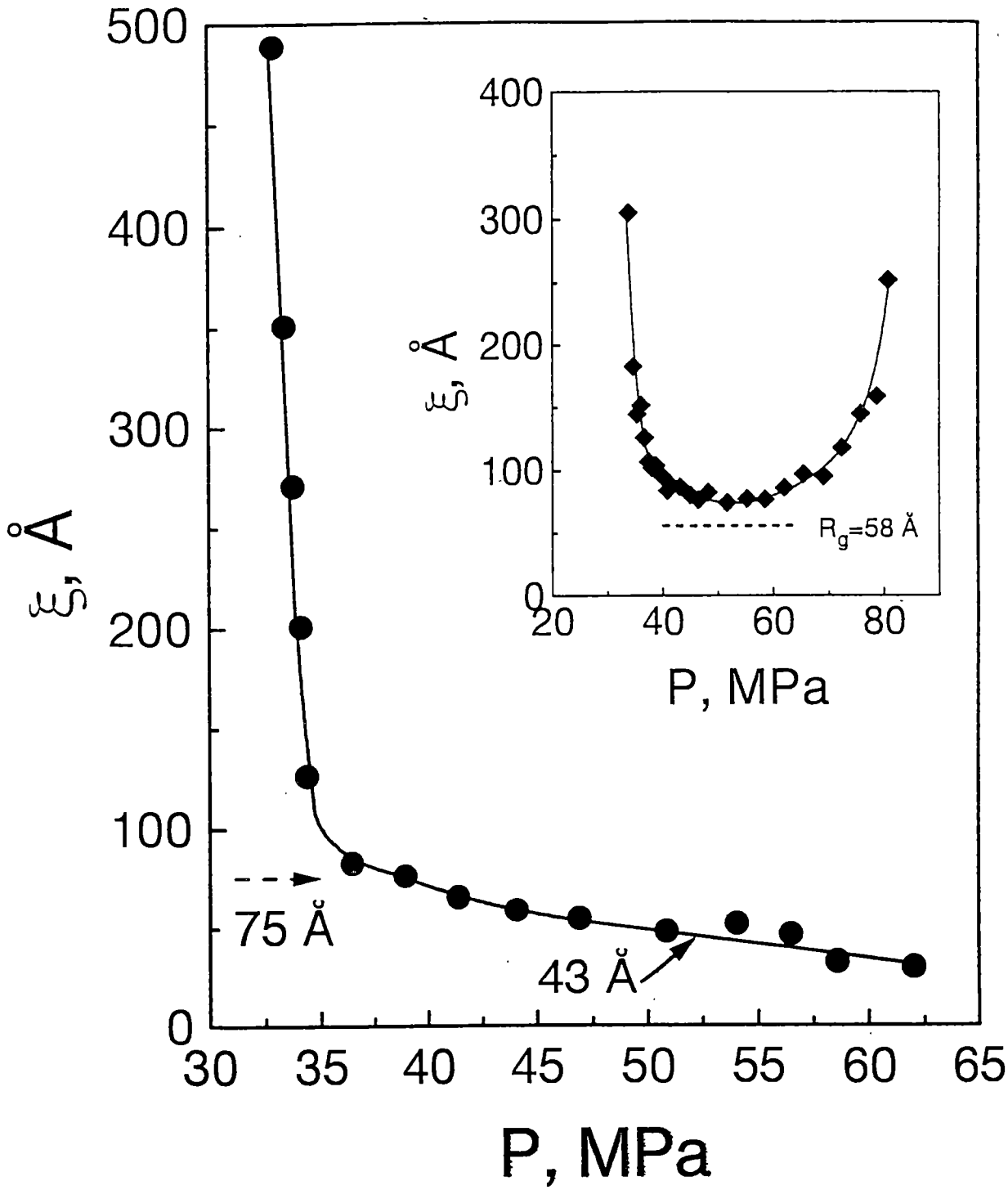
Fig.3. Variation of the correlation length ξ as a function of pressure for PDMS (M_W =79900) in SC CO_2 at T=50 ^oC. Dashed and solid arrows show the value of $R_g(\Theta)$ and $\xi(\Theta)$ (Eq.4), respectively. The inset shows $\xi(P)$ for solution of PDMS (M_W =47700) in SC CO_2 at T=32 ^oC close to the UCST for this solution (T_C =31.8 ^oC). The extrapolation of $\xi^{-1}(P)$ to zero

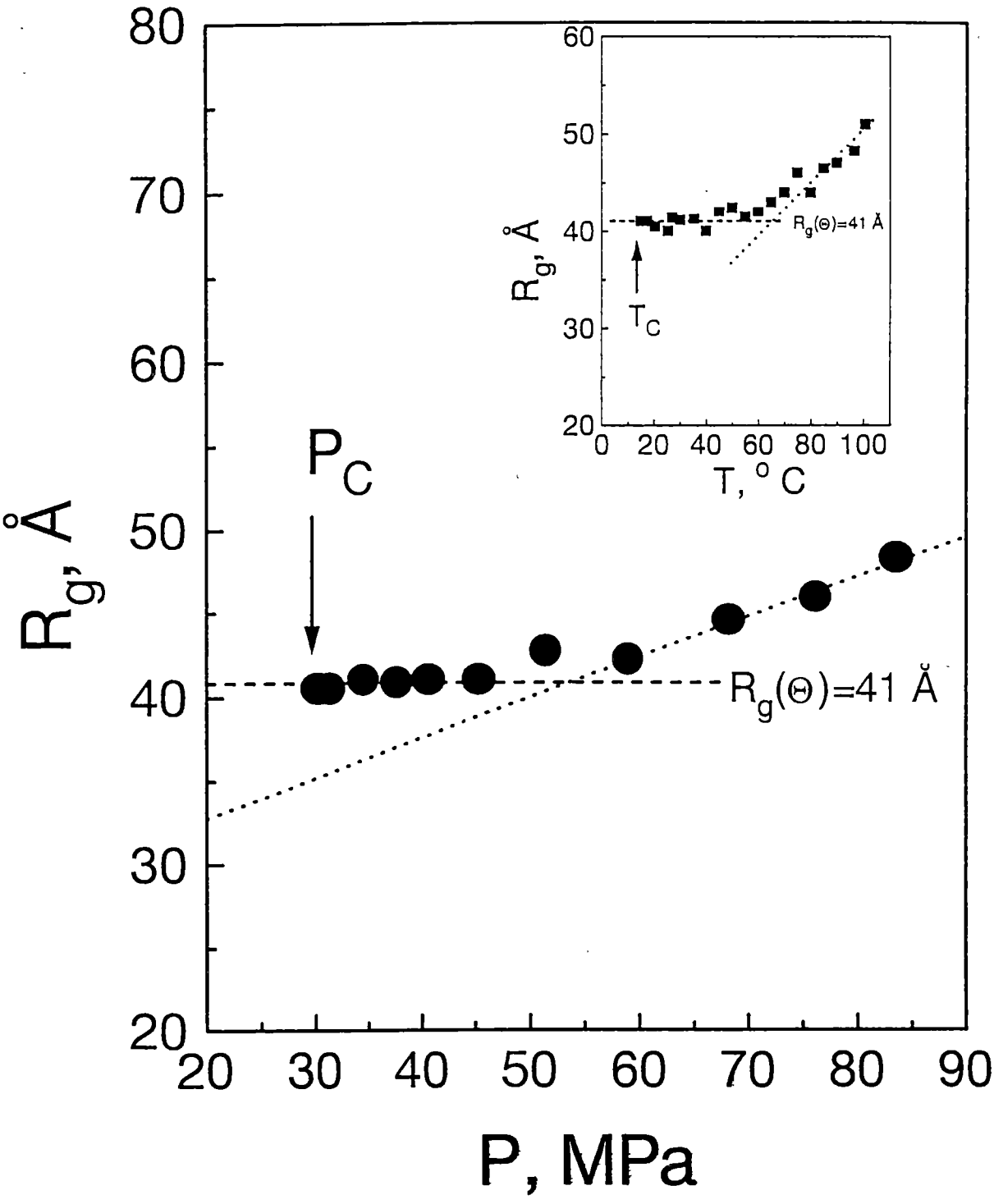
gives $P_C \cong 32$ MPa and $P_C \cong 90$ MPa for the UCSP and the LCSP, respectively.

Fig.4. Variation of the radius of gyration for PDMS with M_W=22500 in solution of (h+d) PDMS in SC CO_2 vs. pressure at T=70 ^oC. The inset shows R_g as a function of temperature at ρ_{CO2}=0.95 g/cm^3.


200
150
100
50
0
ξ, Å
20
40
60
80
100
T, °C
75 Å
58 Å
43 Å
33 Å
40 Å
24 Å
10
8
6
4
2
0
0.0
0.5
1.0
ξ/ξ(T_Θ)
τ'
PS-CH-d
M_W=28000
M_W=50500
M_W=115000
PDMS-SC CO_2
M_W=22500
M_W=47700
M_W=79900


1000
100
10
1
10
100
ξ, Å
1000
100
10
0.1
1
10
100
ν=0.62±0.02
ν=0.51±0.02
PS IN CH-d
T - T_C, K


500
400
300
200
100
0
ξ, Å
30
35
40
45
50
55
60
65
P, MPa
75 Å
43 Å
400
300
200
100
0
ξ, Å
20
40
60
80
P, MPa
R_g=58 Å


80
70
60
50
40
30
20
20 30 40 50 60 70 80 90
P, MPa
$R_{g'}$, Å
P_C
$R_g(\Theta)$=41 Å
60
50
40
30
20
0 20 40 60 80 100
T, ° C
$R_{g'}$, Å
T_C
$R_g(\Theta)$=41 Å

Paper 3

THERMODYNAMIC AND DYNAMIC PROPERTIES OF POLYMERS IN LIQUID AND SUPERCRITICAL SOLVENTS

Yuri B. Melnichenko[1], G. D. Wignall[1], W. Brown[2], E. Kiran[3], H. D. Cochran[4], S. Salaniwal[4], K. Heath[4], W. A. Van Hook[5], and M. Stamm[6]

[1]Oak Ridge National Laboratory*, Oak Ridge, TN 37831
[2]University of Uppsala, S-75121 Uppsala, Sweden
[3]University of Maine, Orono, ME 04469
[4]Oak Ridge National Laboratory and University of Tennessee, Knoxville, TN 37996
[5]University of Tennessee, Knoxville, TN 37996
[6]Max Planck-Institut für Polymerforschung, 55021 Mainz, Germany

INTRODUCTION

Critical phenomena are grouped into classes depending on the spatial dimension (D) and the dimension of the order parameter (N). In the vicinity of the critical temperature T_C, the properties of the systems with the same (D,N) scale with the reduced temperature $\tau=(T-T_C)/T_C$ with identical critical indices for each property. It has long been appreciated that solutions of polymers in liquid organic solvents belong to the same universality class as simple fluids and small molecule mixtures, and their behavior near T_C is described by the critical τ-indices of the three-dimensional Ising model ($N=1$) [1]. More recently it was found that the region where polymer solutions behave universally with temperature ($\xi>>R_g$) terminates at $T=T_X$ when the correlation length ξ of the concentration fluctuations becomes equal to the radius of gyration R_g of the polymer [2,3]. At $T>T_X$ ($\xi<R_g$) the solutions enter the Θ domain where their properties are described by the mean field τ-indices.

Recent experiments have demonstrated that the Θ condition may be also induced in polymer solutions in supercritical fluids (SCFs) by varying the temperature and/or pressure [4]. A SCF is a substance at a pressure and temperature above the liquid-vapor critical point where the coexisting liquid and vapor phases become indistinguishable. The physical properties of SCFs are similar to those of dense gases, although when highly compressed, their density may be comparable to sub-critical liquids. Despite recent

*Managed by Lockheed Martin Energy Research Corporation under contract DE-AC05-96OR-22464 for the U. S. Department of Energy.

progress in many areas of SCF science and technology (see e.g. [5] and references therein), significant challenges remain in developing the same level of understanding of polymer/SCF solutions as has been reached for solutions of polymers in traditional organic solvents. This article will focus on small angle neutron scattering (SANS) and dynamic light scattering (DLS) studies of mixtures of strongly interacting (overlapping) polymers in liquid and supercritical solvents. We have observed an unexpected universality in both thermodynamic and dynamic properties of these seemingly different physical systems.

INTER- AND INTRAMOLECULAR CORRELATIONS

At the phenomenological level, liquid solvents for polymers are divided into three classes, namely poor, theta (Θ), and good solvents. The solvent quality is directly related to the ability of the solvent molecules to mediate the attractive intrachain forces responsible for the polymer – solvent demixing. Poor solvents can scarcely impede the intrachain interactions and hence can dissolve only short chain (or low molecular weight M_W) polymers with a limited number of contacts between segments. The pairwise attractive and repulsive interactions compensate at the Flory (or Θ) temperature which is defined as the upper critical solution temperature (UCST) of a polymer with infinite molecular weight $M_W = \infty$ [1]. The Θ condition corresponds to the threshold of unlimited polymer – solvent miscibility in the sense that polymer of arbitrary M_W becomes miscible in any proportion with the solvent [4]. At $T=\Theta$ the radius of gyration $R_g(\Theta)$ of polymer chains is not perturbed by excluded volume effects and is also independent of the long-range critical concentration fluctuations. In the good solvent domain $T > \Theta$ repulsive forces between segments work to expand R_g above the unperturbed dimensions at Θ. The expansion of polymer coils in semidilute solutions, i.e. solutions in which the volume fraction, ϕ, of the polymer is equal to or larger than the concentration ϕ^* at which coils begin to overlap, is expected to be smaller than in the semidilute regime due to screening of the monomer – monomer interactions (Fig.1).

Semidilute polymer solutions are characterized by two distinct types of monomer – monomer correlations [6]. *Intramolecular* correlations between monomers which belong to the same coil are closely related to the conformation of the polymers in the solution and occur on length scales of the order of R_g. *Intermolecular* correlations are defined by fluctuations in the total concentration with a correlation length ξ. The dimension of polymer chains R_g and the correlation length ξ in polymer solutions may be determined at different thermodynamic conditions using SANS combined with the high concentration isotope labeling method (see [2] and references therein). The coherent scattering intensity, I, from an incompressible mixture of identical protonated and deuterated polymer chains dissolved in a solvent is:

$$I(Q,x) = I_s(Q,x) + I_t(Q,x) \quad , \tag{1}$$

$$I_s(Q,x) = KnN^2 S_s(Q) \quad , \tag{2}$$

$$I_t(Q,x) = LnN^2 S_t(Q) \quad . \tag{3}$$

Subscripts "s" and "t" correspond to scattering from a single chain and total scattering, respectively and thus $S_s(Q)$ is the single-chain structure factor which contains information on the intramolecular correlations. Similarly, the total scattering structure factor, $S_t(Q)$

progress in many areas of SCF science and technology (see e.g. [5] and references therein), significant challenges remain in developing the same level of understanding of polymer/SCF solutions as has been reached for solutions of polymers in traditional organic solvents. This article will focus on small angle neutron scattering (SANS) and dynamic light scattering (DLS) studies of mixtures of strongly interacting (overlapping) polymers in liquid and supercritical solvents. We have observed an unexpected universality in both thermodynamic and dynamic properties of these seemingly different physical systems.

INTER- AND INTRAMOLECULAR CORRELATIONS

At the phenomenological level, liquid solvents for polymers are divided into three classes, namely poor, theta (Θ), and good solvents. The solvent quality is directly related to the ability of the solvent molecules to mediate the attractive intrachain forces responsible for the polymer – solvent demixing. Poor solvents can scarcely impede the intrachain interactions and hence can dissolve only short chain (or low molecular weight M_W) polymers with a limited number of contacts between segments. The pairwise attractive and repulsive interactions compensate at the Flory (or Θ) temperature which is defined as the upper critical solution temperature (UCST) of a polymer with infinite molecular weight $M_W = \infty$ [1]. The Θ condition corresponds to the threshold of unlimited polymer – solvent miscibility in the sense that polymer of arbitrary M_W becomes miscible in any proportion with the solvent [4]. At $T=\Theta$ the radius of gyration $R_g(\Theta)$ of polymer chains is not perturbed by excluded volume effects and is also independent of the long-range critical concentration fluctuations. In the good solvent domain $T > \Theta$ repulsive forces between segments work to expand R_g above the unperturbed dimensions at Θ. The expansion of polymer coils in semidilute solutions, i.e. solutions in which the volume fraction, ϕ, of the polymer is equal to or larger than the concentration ϕ^* at which coils begin to overlap, is expected to be smaller than in the semidilute regime due to screening of the monomer – monomer interactions (Fig.1).

Semidilute polymer solutions are characterized by two distinct types of monomer – monomer correlations [6]. *Intramolecular* correlations between monomers which belong to the same coil are closely related to the conformation of the polymers in the solution and occur on length scales of the order of R_g. *Intermolecular* correlations are defined by fluctuations in the total concentration with a correlation length ξ. The dimension of polymer chains R_g and the correlation length ξ in polymer solutions may be determined at different thermodynamic conditions using SANS combined with the high concentration isotope labeling method (see [2] and references therein). The coherent scattering intensity, I, from an incompressible mixture of identical protonated and deuterated polymer chains dissolved in a solvent is:

$$I(Q,x) = I_s(Q,x) + I_t(Q,x) \quad , \tag{1}$$

$$I_s(Q,x) = KnN^2 S_s(Q) \quad , \tag{2}$$

$$I_t(Q,x) = LnN^2 S_t(Q) \quad . \tag{3}$$

Subscripts "s" and "t" correspond to scattering from a single chain and total scattering, respectively and thus $S_s(Q)$ is the single-chain structure factor which contains information on the intramolecular correlations. Similarly, the total scattering structure factor, $S_t(Q)$

Figure 1. Generic phase diagram of polymer solutions [7,8].

Figure 2. Variation of the parameter L in Eq.4 as a function of x, the mole fraction of PDMS-h in solutions of (PDMS-h+PDMS-d) in CO_2.

embodies information on the total (both intra- and intermolecular) correlations between monomer units, and is related to the correlation length of the concentration fluctuations, ξ. The structure factors are normalized so that $S_s(Q=0) = 1$ and $S_t = S_s$ at infinite dilution. The scattering vector $Q = 4\pi\lambda^{-1}\sin\theta$, where 2θ is the scattering angle and λ=4.75 Å is the neutron wavelength. Also, x is the mole fraction of protonated chains in the solvent, and n and N are the number density of the polymer molecules and the degree of polymerization, respectively. The prefactors K and L are:

$$K \equiv (b_H - b_D)^2\, x(1-x); \qquad L \equiv [b_H x + (1-x) b_D - b_S']^2 \quad , \tag{4}$$

where b_H and b_D are the scattering lengths of the protonated and deuterated monomers and b_S' is the scattering length of a solvent normalized via the ratio of the specific volumes of the monomer and the solvent molecule.

For isotopic mixtures of poly(dimethyl siloxane) (PDMS) in carbon dioxide (CO_2), b_H =0.086 10^{-12} cm, b_D = 6.33 10^{-12} cm, and b_S' =1.47 10^{-12} to 3.76 10^{-12} cm in the range between the critical (ρ_{CO2}=0.469 g/cm^3) and the liquid state densities (ρ_{CO2}=1.2 g/cm^3). For a given combination ($b_H < b_S' < b_D$), it is possible to set $L=0$ (Eq.4) at any density of SC CO_2 (Fig.2) by adjusting the concentration (x) of hydrogenated PDMS (e.g. L=0 at x=*0.512* and ρ_{CO2}=0.95 g/cm) [9]. Similarly, for isotopic mixtures of polystyrene (PS) in deutero acetone (AC-d) (b_H =2.33 10^{-12} cm, b_D = 10.66 10^{-12} cm, and b_S' =8.88 10^{-12} cm) or PDMS in deutero bromobenzene (BrBz-d) (b_S' =5.8 10^{-12} cm) the pre-factor L becomes zero at x=0.214 and 0.085, respectively. As follows from Eqs. (1-4), the condition L=0 completely eliminates the contribution of "total scattering" and Eq.1 gives the single chain (intramolecular) scattering directly. For some solutions (e.g. PS in deutero cyclohexane, CH-d), there is no isotopic ratio, $0<x<1$, which satisfies the condition $L(x)=0$, and $I(Q,x)$ always contains a contribution from the total (intermolecular) scattering which may be subtracted via [2]:

$$I(Q,x,\tau) - \frac{L(x)}{(b_H - b_S')^2} I_t(Q, x=1, \tau) = KnN^2 S_S(Q,\tau) \quad . \tag{5}$$

The value of the prefactor of the second term in Eq.(5) is on the order of several percent and thus the effect of this correction to $I(Q,x)$ is negligible for $T >> T_C$ [2]. However, the correction can become finite near T_C due to the divergence of $I_t(0) \sim \tau^{-1.24}$ [10]. As soon as deuteration of the part of the polymer leads to a shift of T_C of several degrees [11], the subtraction in Eq.5 should be performed at the same values of τ rather than at the same values of the absolute temperature.

The radius of gyration R_g may be obtained by fitting S_S with the Debye function :

$$S_s^D = (2/y^2)(y-1+e^{-y}) \quad , \quad y = Q^2 R_g^2 \quad . \tag{6}$$

For solutions of non-overlapping polymer chains under Θ conditions, Eq.(6) in the limit of small Q [12,13] yields:

$$S_s(Q) = \frac{S(0)}{1+Q^2\xi^2(\Theta)} \tag{7}$$

and the value of the correlation length (Θ conditions) is:

$$\xi(\Theta) = R_g(\Theta)/\sqrt{3} \quad . \tag{8}$$

Thus, SANS measurements of ξ vs. temperature or pressure may be used to determine the Θ temperature or the Θ pressure using Eq.(8) [4,9]. If all chains are protonated (x=1), the prefactor K=0, and one obtains ξ(T,P) directly from $I(Q,x=1) \sim S_t(Q)$ using the Ornstein-Zernike formula:

$$S_t(Q) = S(0)/(1+Q^2\xi^2) \quad . \tag{9}$$

EXPERIMENTAL

Materials and Sample Preparation

Polymer samples of PS-h standards (M_W = 5700, 8300, 10200, 11600, 13000, 28000, 51500, 115000, 200000, 257900, 515000, 533000) and and PS-d standards (M_W = 10500, 11200, 119000, 205000, and 520000 of polydispersity generally $M_W/M_N \leq 1.06$ were obtained from Polymer Laboratories, USA. PS-h (M_W = 22200, 73000) was obtained from Polymer Source, Canada. PDMS-h (M_W =22500, 47700, and 79900 of polydispersity $M_W/M_N \leq 1.03$) and PDMS-d (M_W =27600, $M_W/M_N \leq 1.11$ and 49600, $M_W/M_N \leq 1.03$) were synthesized and characterized at the Max Planck Institute for Polymer Research, Germany. PDMS-d (75600, $M_W/M_N \leq 1.3$) was purchased from Polymer Standards Service GmbH, Mainz, Germany. Protonated MCH-h and BrBz-h as well as deutero substituted solvents CH-d, AC-d, MCH-d, and BrBz-d with D/(H+D)=0.995 were obtained from Sigma Chemical and dried over molecular sieves prior to preparing solutions. CO_2 (SFC purity 99.99%) was obtained from Matheson Gas products, Inc., USA.

PS – MCH and PS – CH solutions were prepared at the critical volume fraction ϕ_C of the polymer which was assigned in accordance with the empirical power law $\phi_C=6.65(M_W)^{-0.379}$ [14] and $\phi_C=7.69(M_W)^{-0.385}$ [15], respectively. PS AC-d solutions were prepared at near critical concentration C=20.3 wt%. Solutions of PDMS in SC CO_2 and in BrBz were prepared at the overlap concentration $C^*=0.1397$ and 0.0959 g/ml for M_W 22500 and 47700, respectively calculated using $C^*=3M_W/4\pi(R_g)^3N_A$, where N_A is the Avogadro number. The overlap concentration is approximately the same as the critical concentration of a polymer solution [16]. The liquid solutions, PS-CH, PS–MCH, and PDMS-BrBz, were filtered through Millipore filters (0.22 μm) and thoroughly homogenized either in a 10 mm cylindrical optical cell (DLS) or in a 2 mm thick quartz cells (SANS) ~ 10 degrees above the Θ temperature of PS-CH (40 ^oC), PS-MCH (~ 78 ^oC) PDMS-BrBz (~ 68 ^oC) [17]. In PDMS – SC CO_2 experiments, the polymer was loaded into a stainless steel cylindrical cell having three optically polished sapphire windows one of which was located at the scattering angle $\theta=90^o$ and used for the DLS measurements. The samples were pressurized with CO_2 at T=50 ^oC, stirred thoroughly until a transparent homogeneous solutions was obtained after which the variation of the static correlation length (SANS) or the dynamic correlation length (DLS) were measured at various temperatures and/or pressures. The temperature of the samples was controlled to better than ±0.1 K. The range of T covered in the experiment was from the Θ temperature down to T_C of each solution. The critical temperature of phase demixing was identified as a sharp maximum in the integral neutron count rate as a function of T (SANS) or as the appearance of the meniscus (DLS). This allowed an estimate of T_C to better than ±0.2 K.

Small-Angle Neutron Scattering

Measurements were performed on the 30-m SANS spectrometer at the Oak Ridge National Laboratory. The neutron wavelength was $\lambda=4.75$ Å ($\Delta\lambda/\lambda=0.06$) and the range of scattering vectors was $0.005<Q=4\pi\lambda^{-1}\sin\theta<0.05$ Å^{-1}, where 2θ is the scattering angle. The data were corrected for scattering from the empty cells, detector sensitivity and beam-blocked background and placed on an absolute scale using pre-calibrated secondary standards after radial averaging to produce functions of the intensity *I vs. Q*. Procedures for subtracting the incoherent background have been described previously [18]. The functions $S_S(Q,T)$ were obtained using Eqs.1,2 (PS-AC-d, PDMS-BrBz-d, PDMS-SC CO_2) and Eq.5 (PS-CH-d) and used to extract the (z-averaged) $R_g(T)$ by fitting the Debye form factor Eq.6. The functions $S_I(Q,T)$ were obtained using Eqs.1,3 and used to extract the correlation length $\xi(T)$ using Eq.9.

Dynamic Light Scattering

DLS measurements were made in the self-beating (homodyne) mode using a setup the details of which were described previously [19]. The cylindrical scattering cells with liquid polymer solutions were sealed and immersed in a large-diameter thermostated bath containing decalin placed at the axis of the goniometer. Measurements were made at different angles in the range 30 to 135° as a function of temperature ($80 < T/^oC < 0$). Analysis of the data was performed by fitting the experimentally measured $g_2(t)$, the normalized intensity autocorrelation function, which is related to the electrical field correlation function, $g_1(t)$ by the Siegert relation [20]:

$$g_2(t)-1=\beta\,|\,g_1(t)\,|^2 \quad , \tag{10}$$

where β is a factor accounting for deviation from ideal correlation. For polydisperse samples, $g_1(t)$ can be written as the inverse Laplace transform (ILT) of the distribution of relaxation times, τA(τ):

$$g_1(t) = \int \tau A(\tau) \exp(-t/\tau) d \ln \tau \quad , \tag{11}$$

where t is the lag-time. The relaxation time distribution, τA(τ), is obtained by performing the inverse Laplace transform (ILT) with the aid of a constrained regularization algorithm (REPES). The mean diffusion coefficient (D) is calculated from the second moments of the peaks as $D_C = \Gamma/Q^2$, where $Q = (4\pi n_o/\lambda)\sin(\theta/2)$ is the magnitude of the scattering vector and $\Gamma = 1/\tau$ is the relaxation rate. Here Θ is the scattering angle, n_o the refractive index of pure solvent and λ the wavelength of the incident light.

The Stokes-Einstein equation relates the cooperative diffusion coefficient (D_c) to the "bare" dynamic correlation length (ξ_d^*) defined in terms of the temperature-dependent viscosity of the solvent (η_s) in Eq.12:

$$\xi_d^* = kT/(6\pi\eta_s D_c) \quad , \tag{12}$$

where $k_B T$ is the thermal energy factor. Another parameter of choice that may be used in the Stokes-Einstein Eq.12 is the macroscopic shear viscosity η_m. We define the "true" dynamic correlation length (ξ_d) as:

$$\xi_d = kT/(6\pi\eta_m D_c) \quad . \tag{13}$$

Viscometry

The viscosity of the blank solvents (MCH and BrBz) and polymer solutions was measured over the temperature range $0 \le T/^oC \le 80$ using a Ubbelohde-type viscometer which was sealed immediately after loading the liquids. The data for the blank solvents were fit using the second order polynomial function:

$$\eta_s = A + B(T_k) + C(T_k)^2 \tag{14}$$

where η_S is in centipoises and the temperature T_k in Kelvins. The parameters thus determined are: (A=9.3±0.9, B=-0.049±0.006, and C=(6.8±0.9)10^{-5} for MCH), and are: (A=13±0.8, B=-0.068±0.005, and C=(9.2±0.8)10^{-5} for BrBz). The viscosity of SC CO_2 was calculated using an empirical relation given by Sovova and Prochaska [22] ($200 < T/K < 1500$, $0 < P/MPa < 100$):

$$\eta_s = [(18.56 + 0.014T_k)(\rho^{-1} - 7.41\text{x}10^{-4} + 3.3\text{x}10^{-7}T_k)]^{-1}$$

where η_S is the viscosity of SC CO_2 in [Pa s] and ρ is the density of SC CO_2 in kg m^3. The viscosity of PS-MCH and PDMS-BrBz solutions was fit to a function obtained from mode coupling theory [23]:

$$\eta_m/\eta_b = B\tau^{-z\nu} \quad , \quad \eta_b = \eta_o \exp(A/T_k) \quad . \tag{15}$$

The product $z\nu$ is predicted to be 0.034 and B is a constant of the order of unity. The"background" viscosity η_b of PS-MCH solutions measured far from the critical demixing temperatures is well described with the values of the parameters η_O = (2.2 ± 0.3) 10^{-3} cP, and A = 2700 ± 400 over the range ($5700 \leq M_W \leq 115000$).

RESULTS AND DISCUSSION

Structure and Thermodynamic Properties at $\Theta \geq T \geq T_C$

The different theoretical approaches that have been applied to calculate R_g at the critical demixing point (T^c,ϕ^c) have led to conflicting conclusions. Starting from de Gennes' assumption that *at the critical point polymer chains just begin to overlap and do not interpenetrate significantly* [16] it was shown that the polymer chains should be partially collapsed at $T \equiv T_C$ and $\phi = \phi_C$ [24]. Conversely, the molecular theory [6,25] and computer simulations [26] show that conformation of individual chains below the Θ temperature should remain unperturbed and collapse to the globular state should occur only at $T<T_C$. The temperature variation of the dimension of polymer chains at $\Theta \geq T \geq T_C$ was first explored using SANS along with the high concentration isotope labeling in [2] for solutions of PS in the Θ solvent CH-d. As is seen from Fig.3, R_g of interacting PS coils does not decrease over the whole temperature range below the Θ temperature. At the same time, the correlation length of the concentration fluctuations ξ which is much smaller than R_g at $T \sim \Theta$ diverges in the vicinity of T_C. These findings indicate that the deterioration of the quality of Θ solvents leads to the formation of microdomains of the size ξ, representing clusters of unperturbed, strongly interpenetrating polymer coils.

The region $\xi > R_g$ is realized in the vicinity of the critical demixing temperature and is thus associated with the poor solvent domain. The solvent quality can be usually improved by increasing the temperature or pressure, to move the solution away from the phase boundary. In Θ solvents (e.g. PS – CH) the solution is capable of reaching the Θ condition at some T and P whereas in poor solvents, e.g. PS – AC the condition cannot be reached at any accessible T, P. The effect of pressure on the thermodynamic state of PS/AC-d solutions is illustrated in Fig.4. Within experimental error, R_g remains independent of pressure down to the critical demixing P_C. Although the Θ condition does not exist for PS-AC solutions, the values for R_g remain close to the unperturbed dimensions for Gaussian chains with M_W=11600 (i.e. $R_g \cong 0.27\ M_w^{1/2} \sim 29$ Å). The correlation length, ξ, diverges as P falls to $P \sim P_C$, where the system exhibits pressure-induced phase demixing, but for solutions of PS in AC, the magnitude of ξ remains generally $\geq R_g$ [9]. This delineates an important difference between the structure of the liquid Θ and poor solvents. The size ξ of the concentration fluctuations in polymer solutions in Θ solvents can decrease below the dimension of the constituent chains and reach the value of $\xi(\Theta)$ defined by Eq.8 (Figs.3, 5) whereas the value of ξ in poor solvents always remains > $\xi(\Theta)$ (Figs.4, 6) and levels off at some thermodynamic distance from the critical point.

Supercritical fluids in general and supercritical carbon dioxide in particular have emerged as an attractive alternative to the organic solvents used for polymer manufacturing and processing. One key advantage of SCFs is the possibility of continuously tuning the solvent quality by varying the pressure (or density) in addition to the temperature. Due to the high compressibility of SCF solvents the density may be conveniently varied with pressure over a much wider range (factors of 2 to 10) than is possible for organic liquid solvents where the range is at most a few percent. This

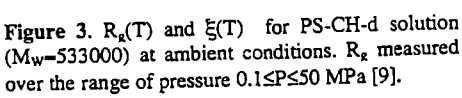


Figure 3. $R_g(T)$ and $\xi(T)$ for PS-CH-d solution (M_W=533000) at ambient conditions. R_g measured over the range of pressure 0.1≤P≤50 MPa [9].

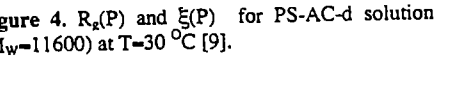


Figure 4. $R_g(P)$ and $\xi(P)$ for PS-AC-d solution (M_W=11600) at T=30 °C [9].

property of SCF solvents should offer an unparalleled means of controlling polymer solubility, but unfortunately, only two classes of polymeric materials, i.e. fluoropolymers and silicones have been shown to exhibit appreciable solubility in SC CO_2. The first SANS measurements of the second virial coefficient A_2 were performed in mixtures of hexafluoropropylene oxide (HFPPO) and poly(1,1-dihydroperfluoro-octylacrylane) (PFOA) with SC CO_2 at T=65 °C and P=34.5 MPa (see [27] and references therein). They have shown that $A_2 \cong 0$ for the former and $A_2 > 0$ for the latter systems and thus SC CO_2 is a Θ solvent and a good solvent for HFPPO and PFOA, respectively at these particular values of (T,P). In a recent work [4] SANS was applied to investigate the structure and thermodynamic properties of PDMS – SC CO_2 solutions as a function of pressure and temperature. Fig.7 illustrates the (T,P) dependence of the radius of gyration of PDMS in SC CO_2. R_g of the polymer remains invariant during both pressure and temperature quenches extending to the immediate vicinity of the (T,P) polymer-SCF demixing locus and agrees well with the dimension of unperturbed chains ($R_g = 0.267 M_w^{1/2} \cong 40$ Å). This observation indicates the universality of the constancy of R_g in semidilute polymer solutions below the Θ point previously demonstrated for liquid

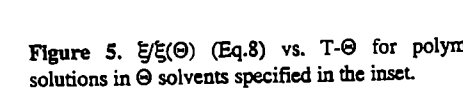


Figure 5. $\xi/\xi(\Theta)$ (Eq.8) vs. T-Θ for polymer solutions in Θ solvents specified in the inset.

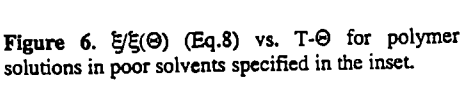


Figure 6. $\xi/\xi(\Theta)$ (Eq.8) vs. T-Θ for polymer solutions in poor solvents specified in the inset.

solvents (see Figs.3, 4) and now extended to supercritical fluids. The dimensions of polymer chains increase when T and/or P exceed the appropriate values of the Θ parameters ($\Theta = 65 \pm 5$ °C and $P_\Theta = 52 \pm 4$ MPa at ρ_{CO_2}=0.95 g/cm^3 [4]) due to excluded volume effects, indicating that SC CO_2 becomes a good solvent for PDMS. The experimental data agree with the results of Monte Carlo simulations which suggest that polymer chains may adopt unperturbed and expanded conformations at high densities [28].

A typical variation of ξ vs. τ in PDMS-SC CO_2 solutions is shown in Fig.8. As is seen, the critical index ν exhibits a sharp crossover from the mean-field value (ν=0.5) in the Θ region to the Ising model value (ν=0.630±0.001 [29]) in the region around T_C. Accordingly, the critical index γ=1.23±0.02 for the susceptibility (i.e. the osmotic compressibility) agrees within experimental errors with the Ising model value (1.239±0.002 [29]). The crossover takes place at $\xi \sim R_g$ and thus reproduces the main features of the crossover observed in solutions of PS in CH-d [3]. The dimension of the poor solvent domain may be made infinitely large (as in PS-AC) or small (as in PS-CH) depending on the density of SC CO_2. These observations certainly establish basic similarities of behavior in solutions of polymers in SCFs and in sub-critical solvents, and show that SCF/polymer solutions belong to the Ising model universality class.

Dynamic Properties at $\Theta \geq T \geq T_C$

Despite numerous efforts, the dynamic properties of semidilute polymer solutions in organic solvents at $T \leq \Theta$ are poorly understood. To our knowledge, only one DLS experiment has been performed so far in the poor solvent domain of supercritical polymer solutions [4]. The most important issue which is yet to be resolved is whether the viscosity of the solvent or that of the solution should be used to calculate the dynamic correlation length from the Stokes-Einstein Eq.12 [30].

In terms of a traditional description of critical phenomena, the temperature variation of the dynamic and static correlation lengths may be represented as [31]:

$$\xi_d^* = \xi_0^* |\tau|^{-\nu^*} \quad , \tag{16}$$

$$\xi = \xi_0 |\tau|^{-\nu} \quad . \tag{17}$$

Figure 7. R_g (P) of PDMS (M_w=22500) in SC CO_2 at T=70 °C. The inset shows R_g (T) at ρ_{CO_2}=0.95 g/cm^3.

Figure 8. $\xi(\tau)$ of PDMS (M_w=22500) in SC CO_2. ρ_{CO_2}=0.95 g/cm^3. The inset shows $\xi(\tau)$ for the same polymer in BrBz-d.

A master plot for ξ_d^* as a function of τ is shown in Fig.9. As is seen, the value of the critical exponent ν^* in Eq.16 for all solutions studied in the hydrodynamic regime $q\xi<<1$ around the Θ temperature is $\nu^*=0.8\pm0.1$ which value as yet has no theoretical justification. At smaller τ, generally at $\tau \sim 0.01$, the decay rate becomes independent of temperature characterizing entry to the critical non-diffusive regime [32]. There is a consequent observed "flattening-out" of the bare dynamic correlation length, defined via Eq.12, as a function of τ to a limiting value as T_C is approached. The variation of the dynamic correlation length with τ changes dramatically if Eq.(13) is used to define ξ_d due to significant difference in the temperature variation of η_s and η_m described by Eq. 14 and 15, respectively. In the vicinity of the Θ temperature the temperature variation of ξ_d and similarly that of the static correlation length, is described by the mean field critical index $\nu=0.5$ (Eq.17). At some "intermediate dynamic crossover temperature" T_X^* the index increases abruptly and the crossover to the critical non-diffusive regime is observed. We note that in the "intermediate" region of τ the critical index $\nu=0.77$ exceeds the theoretical value of $\nu=0.63$ probably due to a complex interference between the dynamic and static correlations of the order of $\xi(\Theta)$ and/or R_g (see Eqs.7 and 8). At the same time, the crossover to the critical non-diffusive regime occurs at about the same value of $\tau \sim 0.01$ for both ξ_d and ξ_d^*.

The description of the temperature variation of the correlation lengths (Eqs.16, 17) does not take into account the existence of the tricritical Θ point in the phase diagram of polymer solutions (Fig.1). A more general scaling description may be achieved by using the scaling variable [16]:

$$\tau' = (T - T_c)/(\Theta - T_c) \tag{18}$$

which accounts for the temperature distance from both the Θ temperature and T_c. In terms of τ', Eq.17 may be represented as [12]:

$$\xi = \xi(\Theta)(\tau')^{\nu} \quad , \tag{19}$$

where the amplitude $\xi(\Theta)$ is given by Eq.(8). In the case of the dynamic correlation length no theoretical interpretation for $\xi_d^*(\Theta)$ has yet been developed. However, one may suggest phenomenologically that ξ_d^* should follow the same scaling as Eq.19, writing

Figure 9. The bare dynamic correlation length (Eq.12) vs. τ. The symbols are spelled out in the insets.

Figure 10. ξ_d^* , ξ_d, and ξ_s for solution PS (M_W=5700) in CH-d. The solid and dashed arrows show the static and dynamic crossovers.

$$\xi_d^* = \xi_d^*(\Theta)(\tau')^{\nu^*} \quad , \tag{20}$$

where $\xi_d^*(\Theta)$ is the experimental value of the dynamic correlation length at T=Θ (Fig.11). As is seen in Fig.12, the reduced correlation lengths $\xi_d^*/\xi_d^*(\Theta)$ for various polymers in different solvents fall on the same master curve when plotted vs. the reduced temperature τ'. This is the first demonstration of the universality for the dynamic behavior of solutions of polymers in organic liquids and supercritical fluids.

Figure 11. $\xi_d^*(\Theta)$ for several polymer solutions. The symbols are spelled out in the insets.

Figure 12. Master plot for $\xi_d/\xi_d^*(\Theta)$ vs. de Gennes' scaling variable (Eq.18).

CONCLUDING REMARKS

Small angle x-ray scattering and static light scattering have been applied since the 1940s to obtain structural information on polymer solutions, though the limit of zero concentration was required to eliminate interchain interference. Thus, these methods could not be applied to the solutions of interacting macromolecules, due to the difficulties of separating the *inter-* and *intra*-chain contributions to the structure. However, SANS has removed this limitation and due to a fortuitous combination of several factors: high bulk penetrating power, the ability to manipulate local scattering amplitudes through isotopic labeling or an appropriate choice of solvent (contrast variation), the technique has developed into an extremely powerful tool for the study of polymers. By deuterating a fraction of the polymer, it is possible to measure the single-chain structure factor and thus the R_g of the individual polymer chains in strongly correlated systems. That approach provides exceptional means for investigating the structure of various complex fluids, e.g. solutions of synthetic and biological polyelectrolytes. Recent SANS and DLS measurements demonstrate a striking universality between structure, thermodynamic and dynamic properties of sub- and supercritical polymer solutions.

ACKNOWLEDGEMENTS

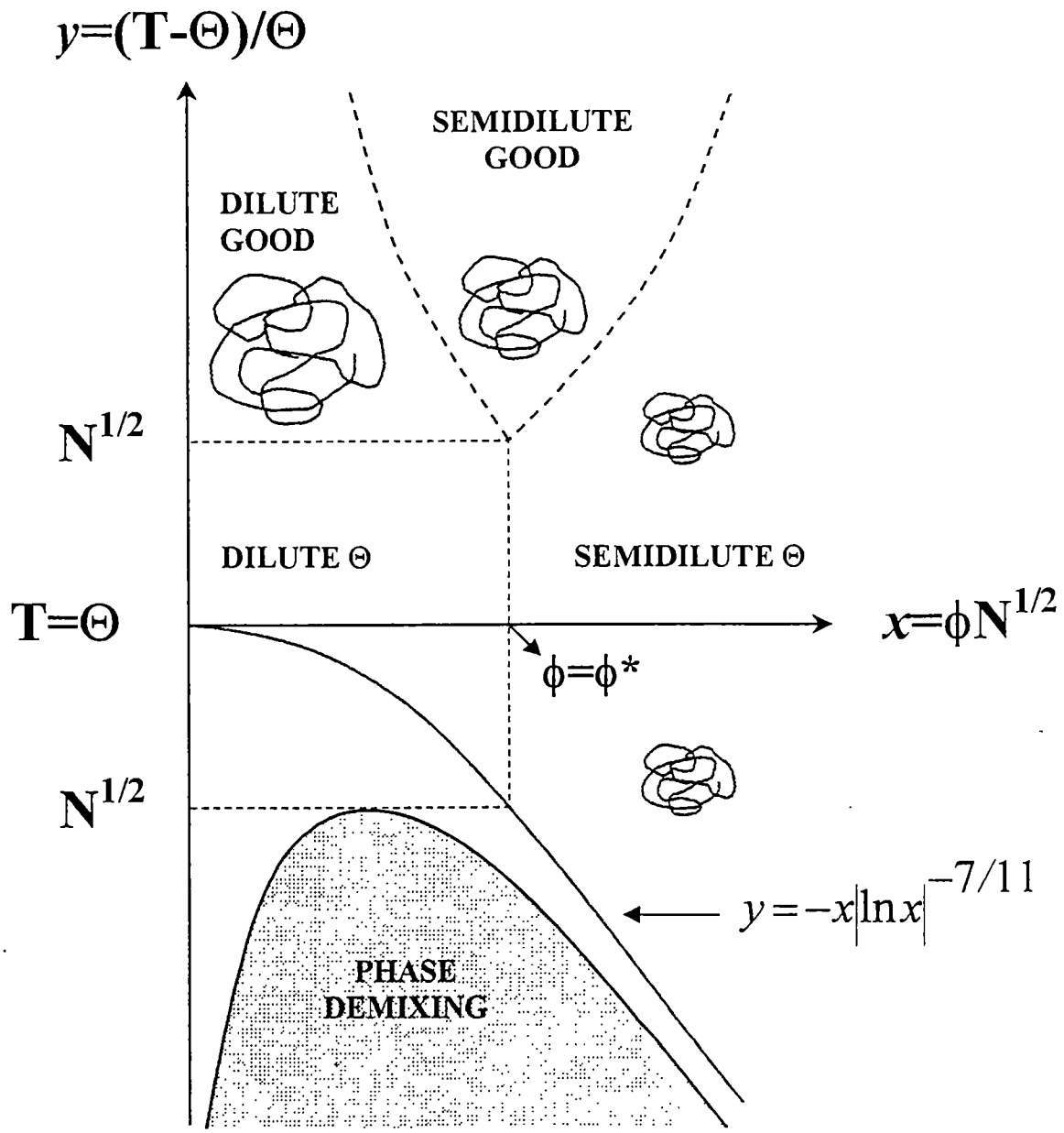
The research was supported the Divisions of Advanced Energy Projects, Materials Sciences, and Chemical Sciences, U. S. Department of Energy under contract No. DE-AC05-96OR-22464 (with Lockheed Martin Energy Research Corporation) and Grant No. DE-FG05-88ER-45374 (with the University of Tennessee) and by the National Science

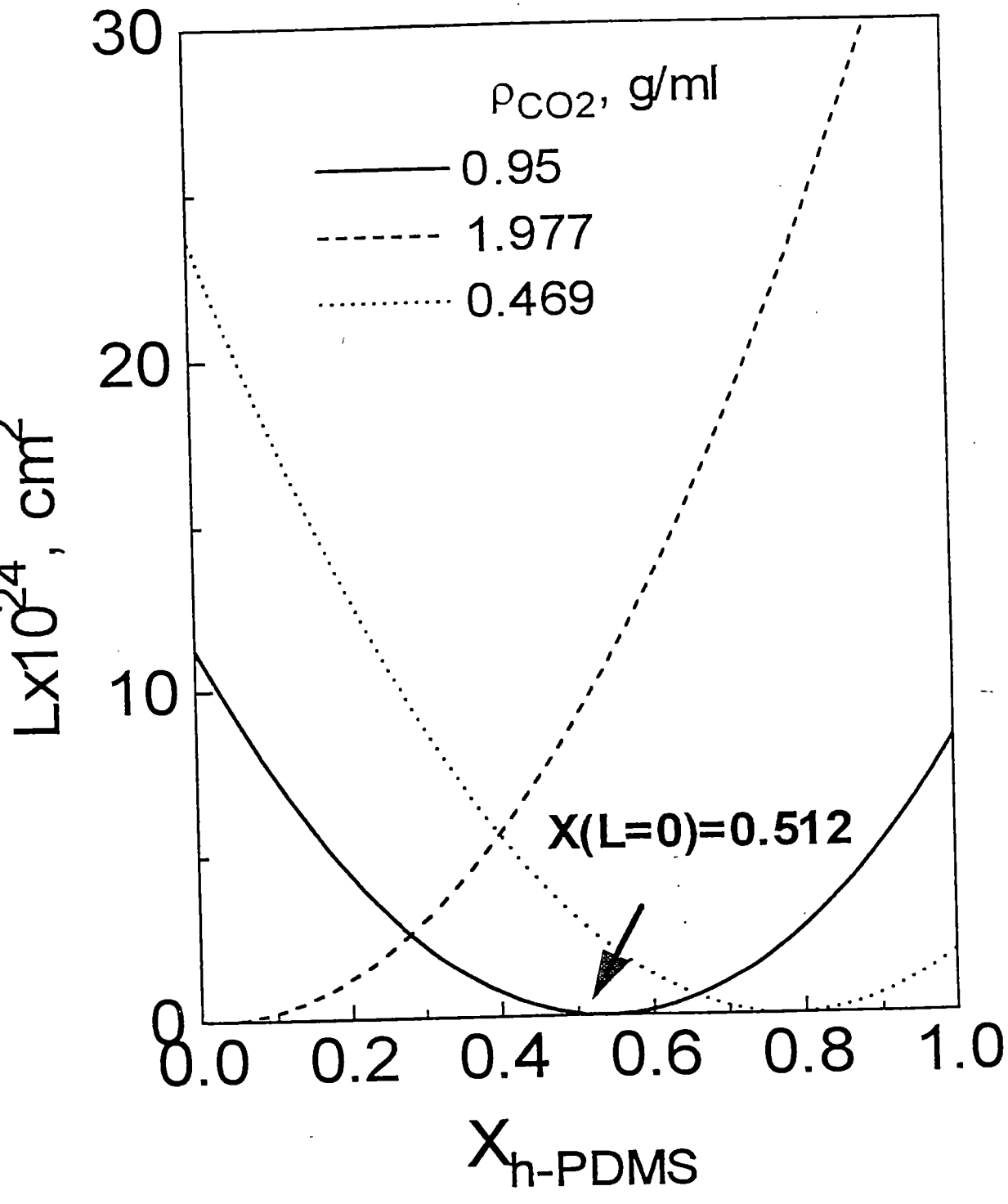
Foundation Grant No. CTS-9613555 (with the University of Tennessee). The financial support of YBM by Alexander von Humboldt-Stiftung is gratefully acknowledged.

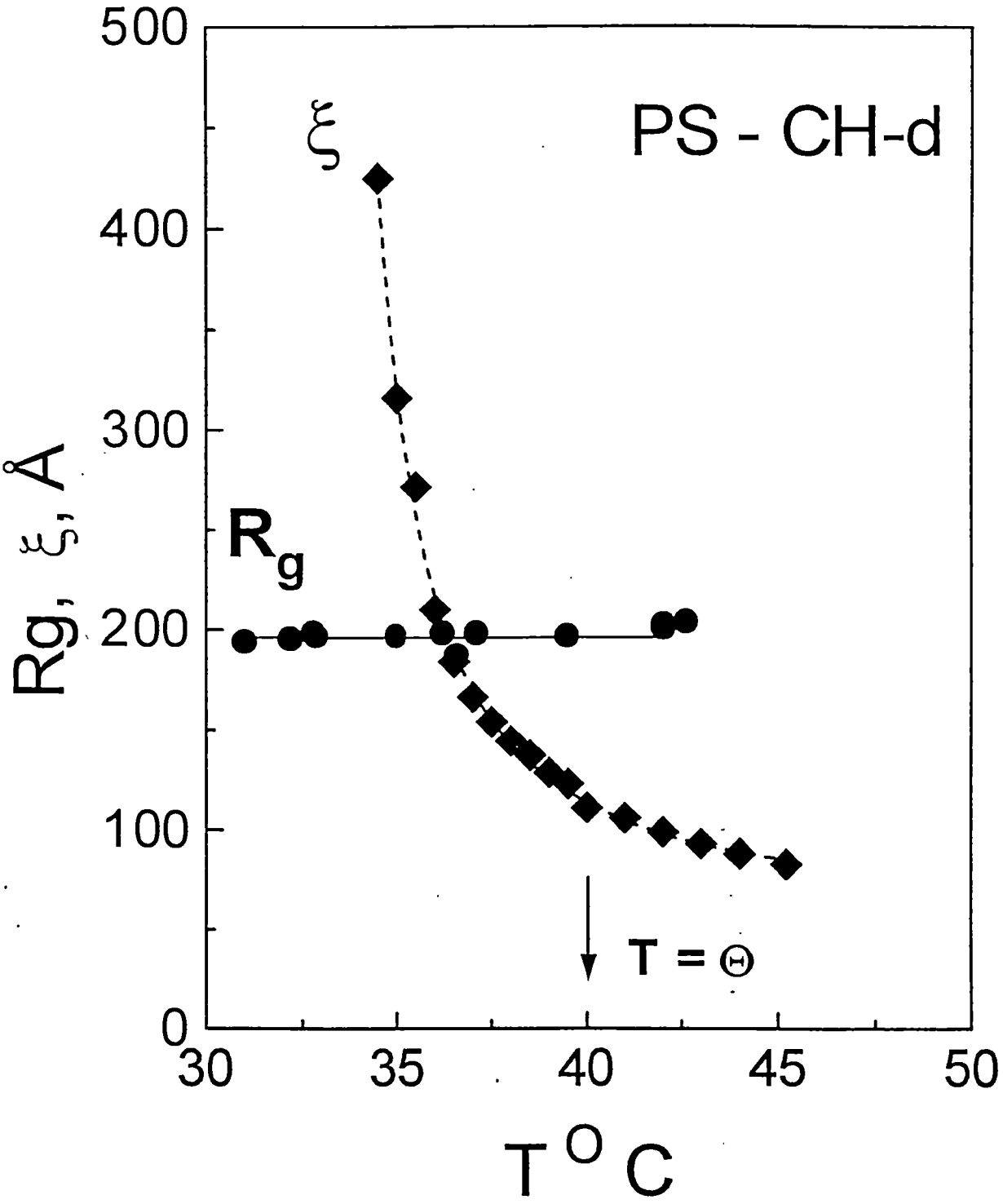
REFERENCES

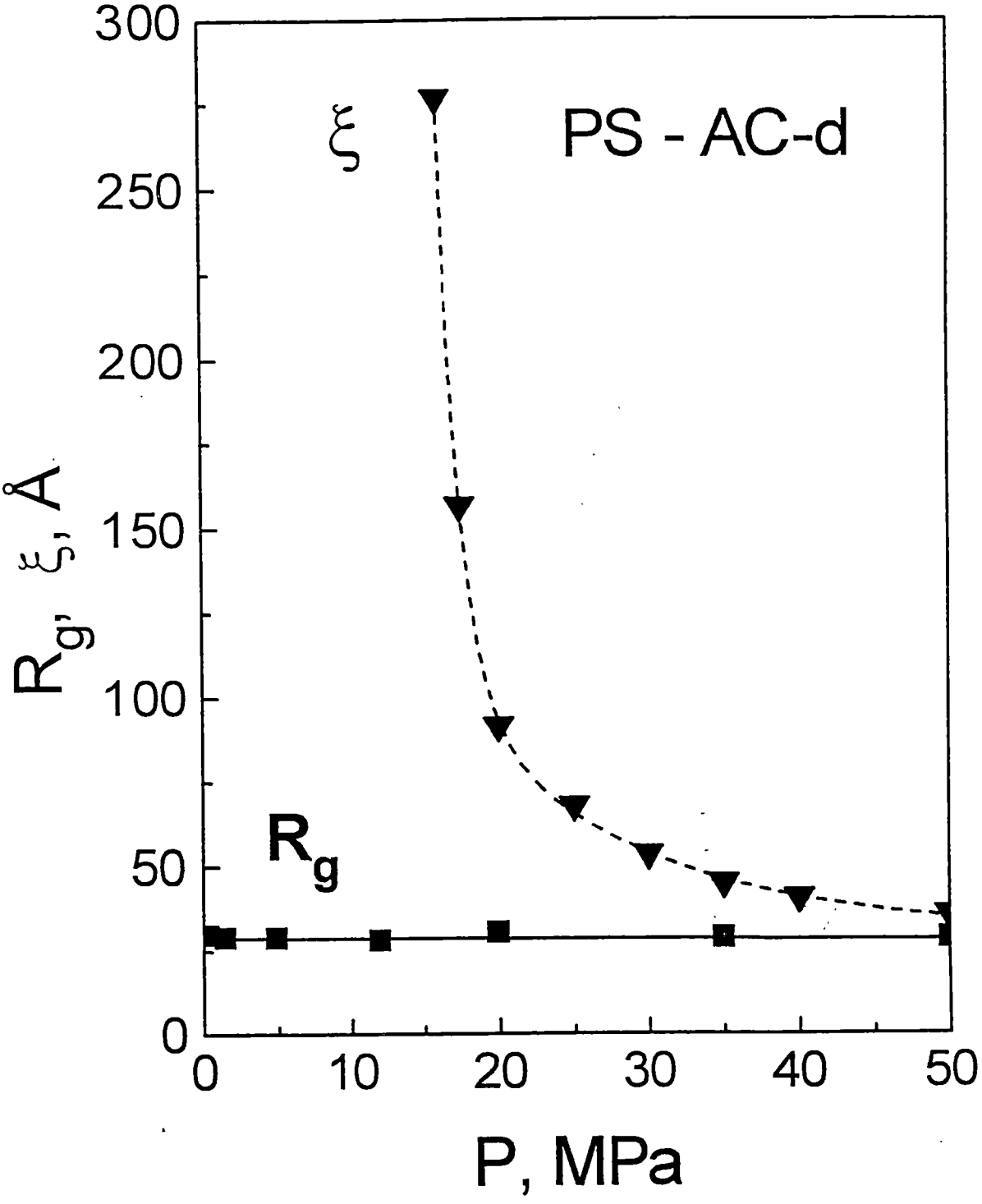
1. I. C. Sanchez. *Encyclopedia of Physical Science and Technology*, Academic Press, New York (1992).
2. Y. B. Melnichenko, G. D. Wignall, Dimension of polymer chains in critical semidilute solutions, *Phys. Rev. Lett.* 78: 686 (1997).
3. Y. B. Melnichenko, M. A. Anisimov, A. A. Povodyrev, G. D. Wignall, J. V. Sengers, and W. A. Van Hook, Sharp crossover of the susceptibility in polymer solutions near critical demixing point, *Phys. Rev. Lett.* 79: 5266 (1997).
4. Y. B. Melnichenko, E. Kiran, G. D. Wignall, K. D. Heath, S. Salaniwal, H. D. Cochran, and M. Stamm, Pressure- and temperature-induced transitions in solutions of poly(dimethyl siloxane) in supercritical carbon dioxide, *Macromolecules* 32: 5344 (1999).
5. M. A. McHugh and V. J. Krukonis. *Supercritical fluid extraction: principles and practice*, Butterworth-Heinemann, Boston (1994).
6. M. Muthukumar, Thermodynamics of polymer solutions, *J. Chem. Phys.* 85: 4722 (1986).
7. M. Daoud and G. Jannink, Temperature-concentration diagram of polymer solutions, *J. Phys. (Paris)* 37: 973 (1976).
8. B. Duplantier, Lagrangian tricritical theory of polymer chain solutions near the Θ-point, *J. Phys. (Paris)* 43: 991 (1982).
9. Y. B. Melnichenko,G. D. Wignall, W. A. Van Hook, J. Szydlowsky, H. Wilczura, L. P. Rebelo, Comparison of inter- and intramolecular correlations of polystyrene in poor and Θ solvents via small-angle neutron scattering, *Macromolecules* 31: 8436 (1998).
10. Y. Melnichenko, M. Agamalyan, V. Alexeev, V. Klepko and V. Shilov, Crossover between tricritical and critical demixing regimes of polymer solutions. Small-angle neutron scattering, *Europhys.Lett.* 19: 355 (1992).
11. C. Strazielle and H. Benoit, Some thermodynamic properties of polymer-solvent systems. Comparison between deuterated and undeuterated systems, *Macromolecules* 8: 203 (1975).
12. J. Des Cloizeaux and G. Jannink, *Polymers in Solution. Their Modeling and Structure*, Claredon Press, Oxford (1990).
13. H. Fujita, *Polymer Solutions*, Elsevier, Amsterdam, (1990).
14. T. Dobashi, M. Nakata, and M. Kaneko, Coexistence curve of polystyrene in methylcyclohexane, 1. Range of simple scaling and critical exponents, *J. Chem. Phys.* 72: 6685 (1980).
15. R. Perzynski, M. Delsanti, and M. Adam, Experimental study of polymer interactions in a bad solvent, *J. de Physique* 48: 115 (1987).
16. De Gennes P.-G., *Scaling Concepts in Polymer Physics*, 2nd ed., Cornell University Press, Ithaca (1979).
17. *Polymer Handbook*, J. Brandrup, E. H. Immergut, E. A. Grulke, eds, John Wiley, New York (1999).
18. G. D. Wignall, F. S. Bates, Absolute calibration of small-angle neutron scattering data, *J. Appl. Crystallogr.* 20: 28 (1987).
19. Y. B. Melnichenko, W. Brown, S. Rangelov, G. D. Wignall, M. Stamm, *Phys. Lett.*, submitted.
20. B. Chu, *Laser Light Scattering*, Academic Press, New York (1991).
21. W. Brown and T. Nicolai, Scattering from concentrated polymer solutions, in: *Dynamic Light Scattering*, W. Brown, ed., Clarendon Press, Oxford (1993).
22. H. Sovova and J. Prochaska, Calculations of compressed carbon dioxide viscosities, *Ind. Eng. Chem. Res.* 32: 3162 (1993).
23. H. C. Burstyn and J. V. Sengers, Decay-rate of critical concentration fluctuations in a binary liquid, *Phys. Rev.* A25: 448 (1982).
24. Y. Izumi and Y. Miyake, Universality of the coexistence curves in a polymer solutions, *J. Chem. Phys.* 81: 1501 (1984).
25. G. Raos and G. Allegra, Chain collapse and phase separation in poor-solvent polymer solutions: a unified molecular description, *J. Chem. Phys.* 104: 1626 (1996).
26. N. B. Wilding, M. Muller, and K. Binder, Chain length dependence of the polymer-solvent critical point parameters, *J.Chem.Phys.* 105: 802 (1996).
27. G. D. Wignall., Neutron scattering studies of polymers in supercritical carbon dioxide, *J. Phys.: Condens. Matter* 11: R157 (1999).
28. G. Luna-Barcenas, J. C. Meredith, I. C. Sanchez, K. P. Johnson, D. G. Gromov, and J. J. de Pablo, Relashionship between polymer chain conformation and phase boundaries in a supercritical fluid, *J. Chem. Phys.* 107: 10782 (1997).
29. J. C. Le Guillou and J. Zinn-Justin, Critical exponents from field theory, *Phys. Rev.* B21: 3976 (1980).

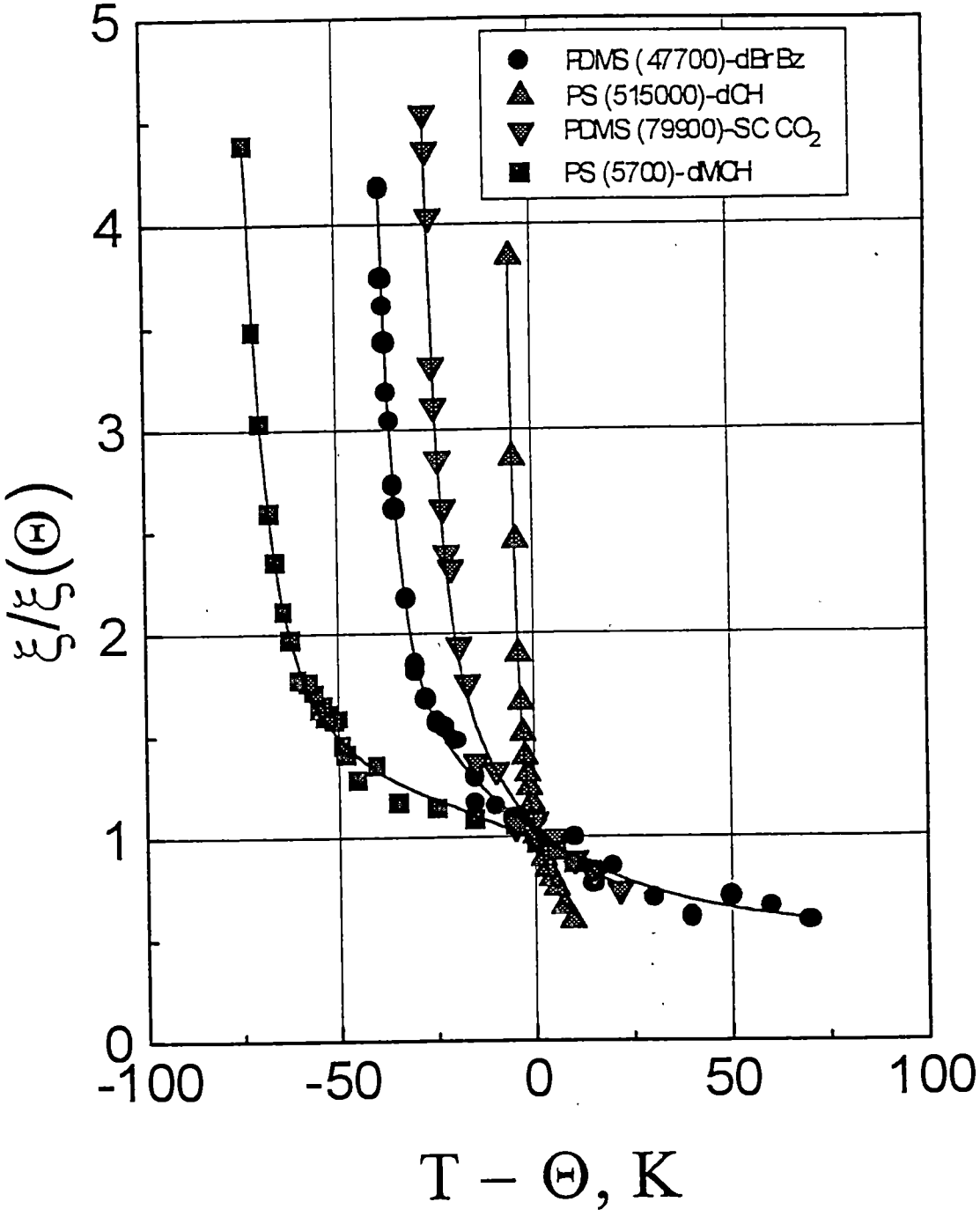
30. S. F. Edwards, private communication.
31. N. Kuwahara, D. V. Fenby, M. Tamsky, and B. Chu, Intensity and line width studies of the system polystyrene-cyclohexane in critical region, *J. Chem. Phys.* 55: 1140 (1971).
32. P. Stepanek, Critical dynamics of binary liquid mixtures and simple fluids studied using light scattering, in: *Dynamic Light Scattering*, W. Brown, ed., Clarendon Press, Oxford (1993).

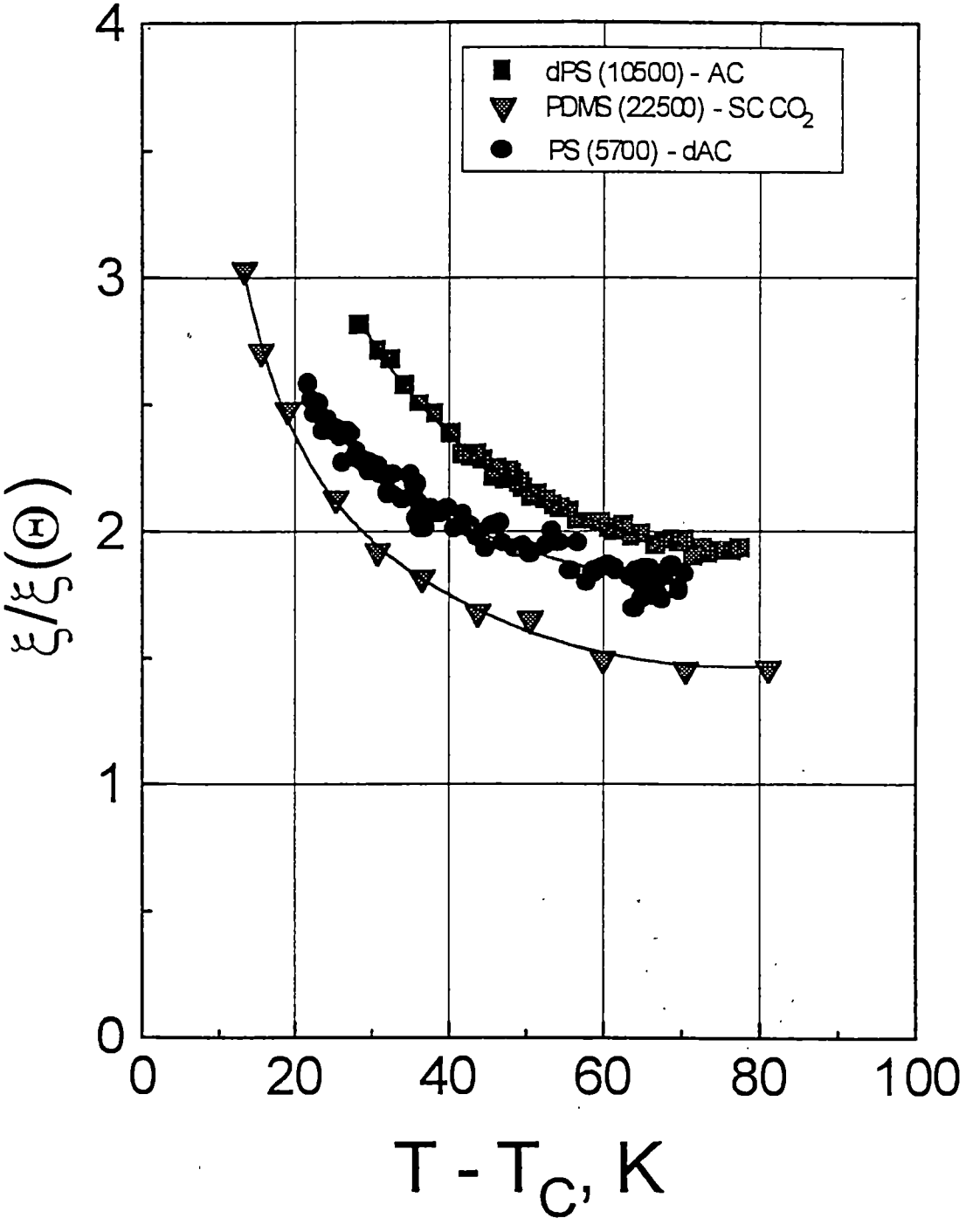

y=(T-Θ)/Θ
SEMIDILUTE
GOOD
DILUTE
GOOD
N^1/2
DILUTE Θ
SEMIDILUTE Θ
T=Θ
x=φN^1/2
φ=φ*
N^1/2
y=-x|lnx|^-7/11
PHASE
DEMIXING

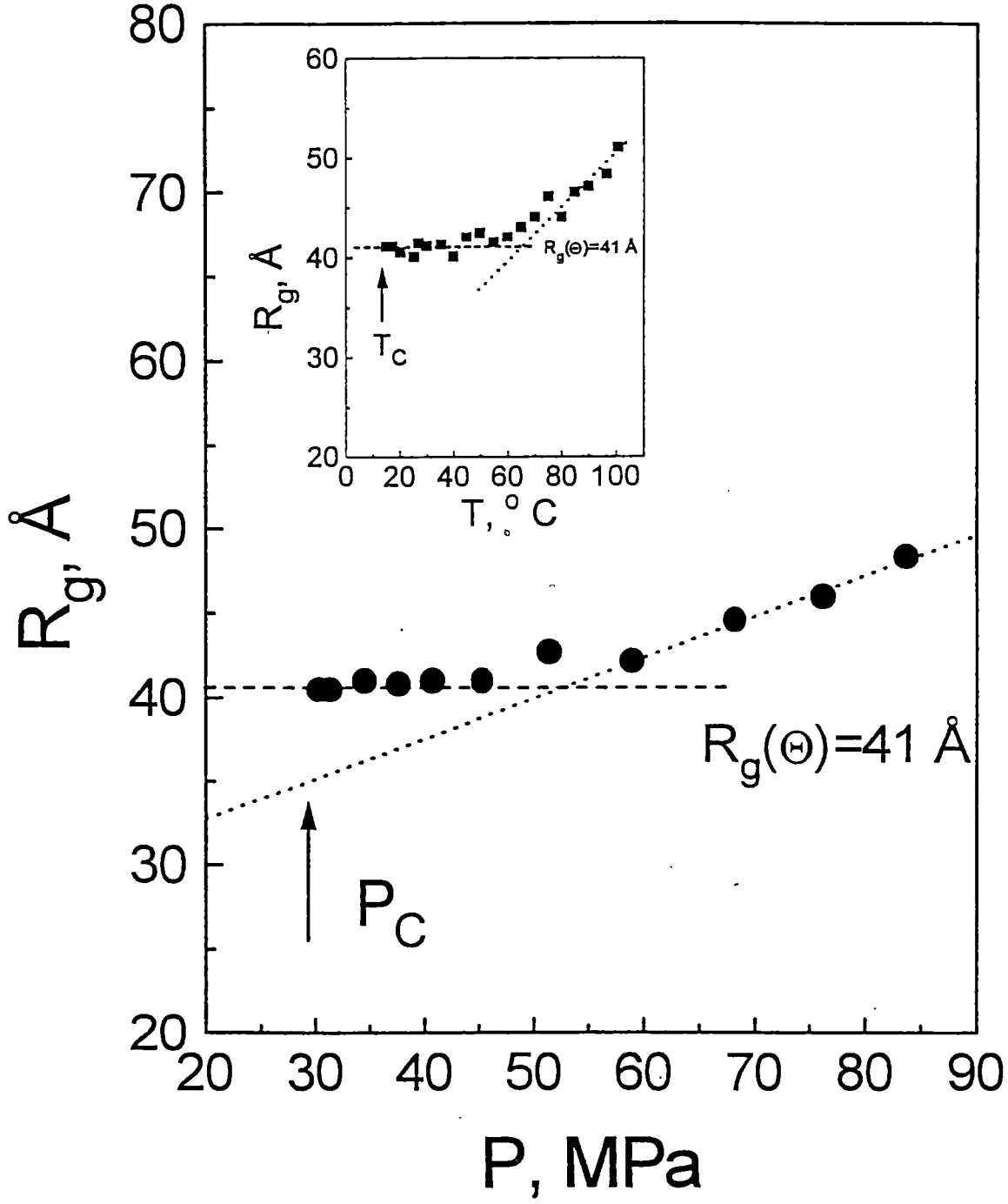

30
20
10
0
$L \times 10^{24}$, cm^2
ρ_{CO2}, g/ml
0.95
1.977
0.469
X(L=0)=0.512
0.0
0.2
0.4
0.6
0.8
1.0
$X_{h\text{-}PDMS}$

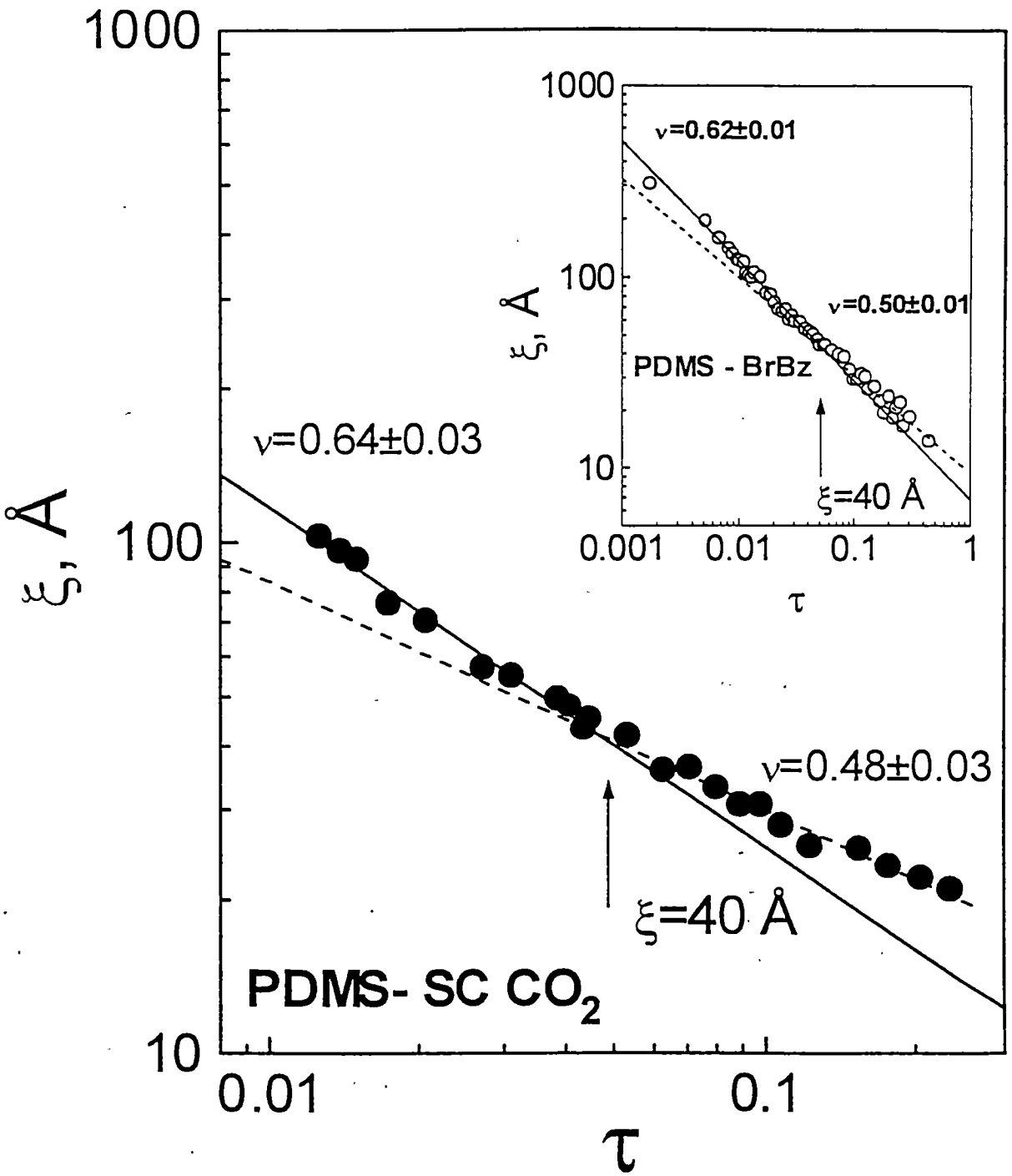

PS - CH-d
ξ
R_g
T = Θ
Rg, ξ, Å
T °C
500
400
300
200
100
0
30
35
40
45
50

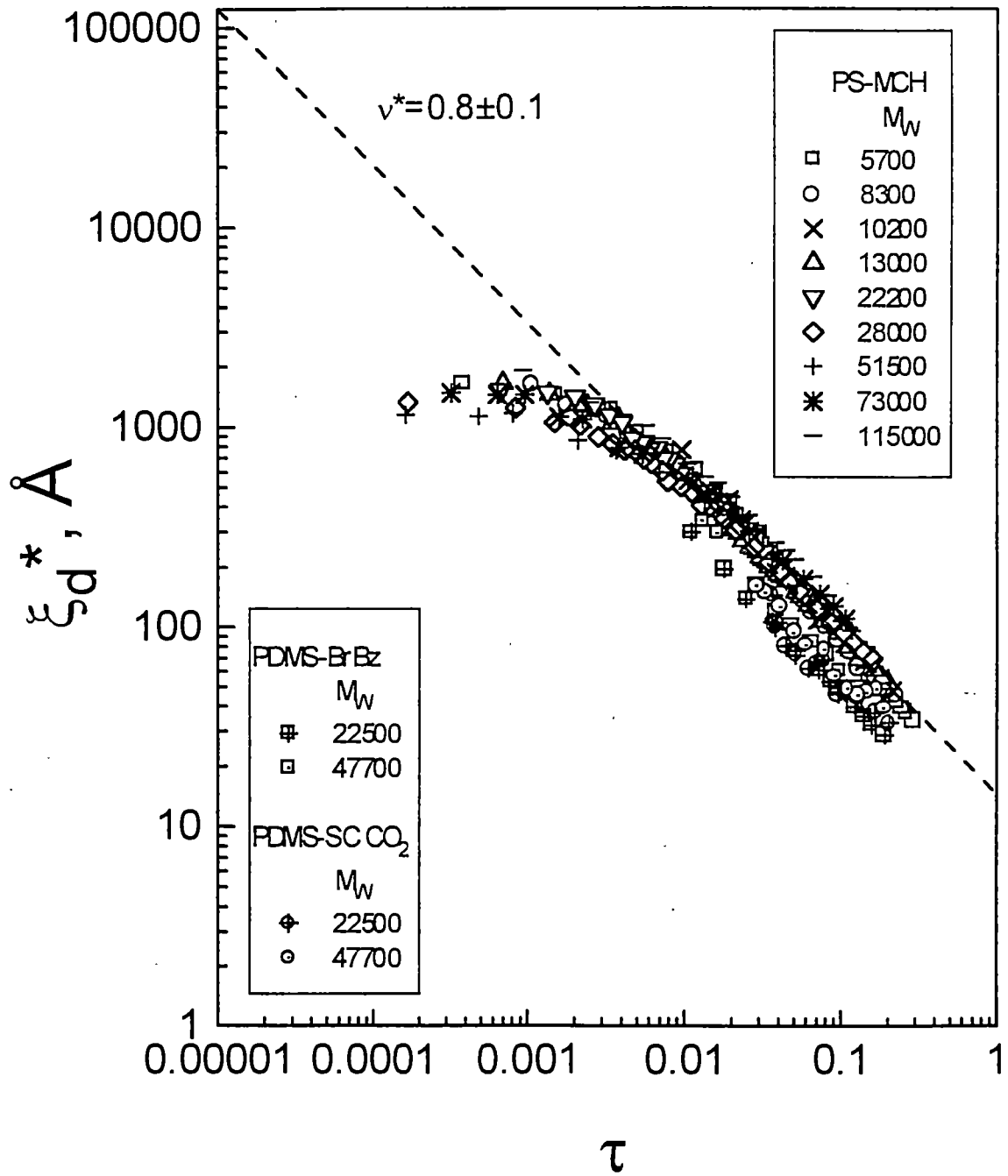

300
250
200
150
100
50
0
0
10
20
30
40
50
R_g, ξ, Å
P, MPa
ξ
PS - AC-d
R_g

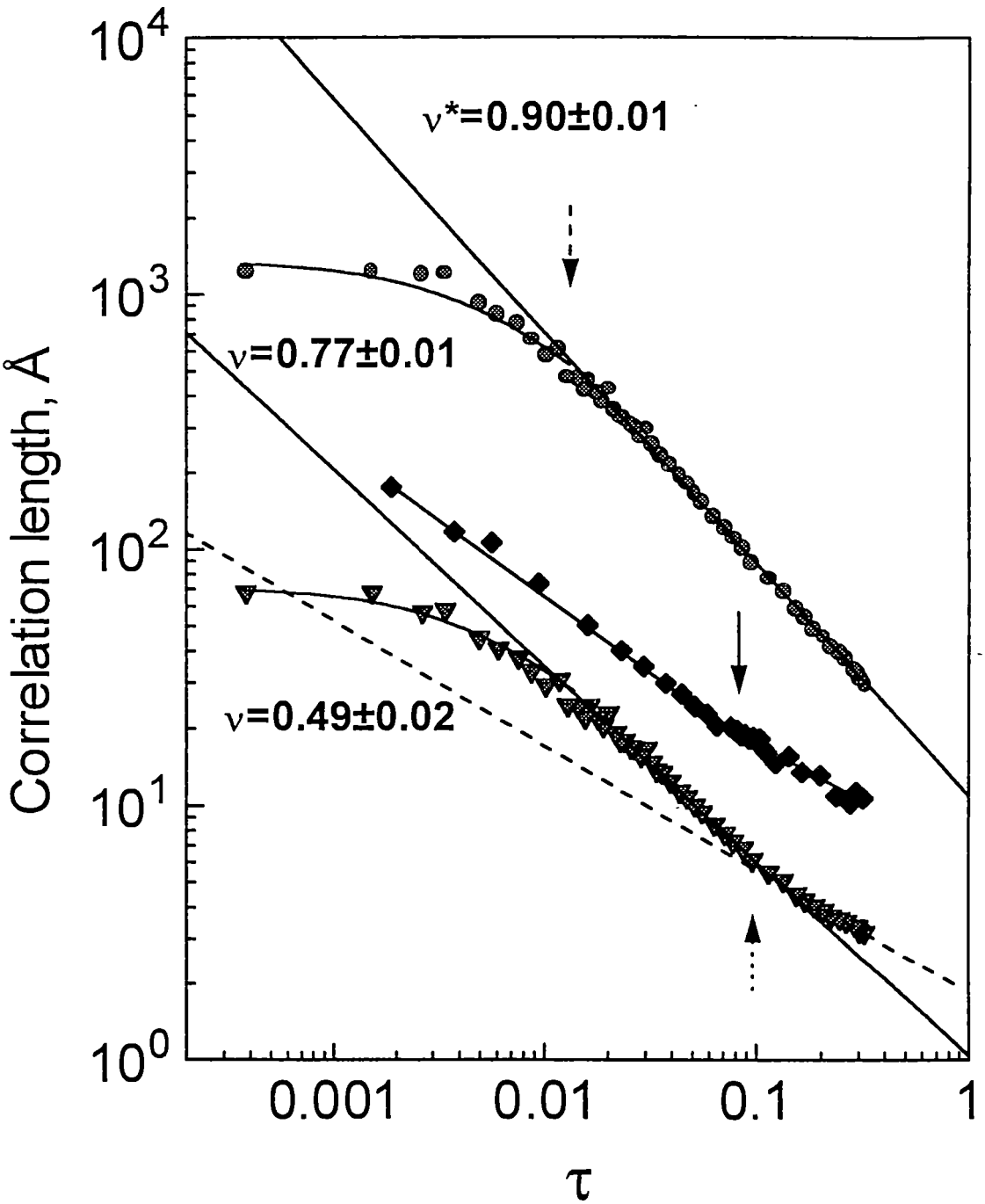

PDMS (47700)-dBrBz
PS (515000)-dCH
PDMS (79900)-SC CO2
PS (5700)-dMCH
5
4
3
2
1
0
-100
-50
0
50
100
ξ/ξ(Θ)
T – Θ, K

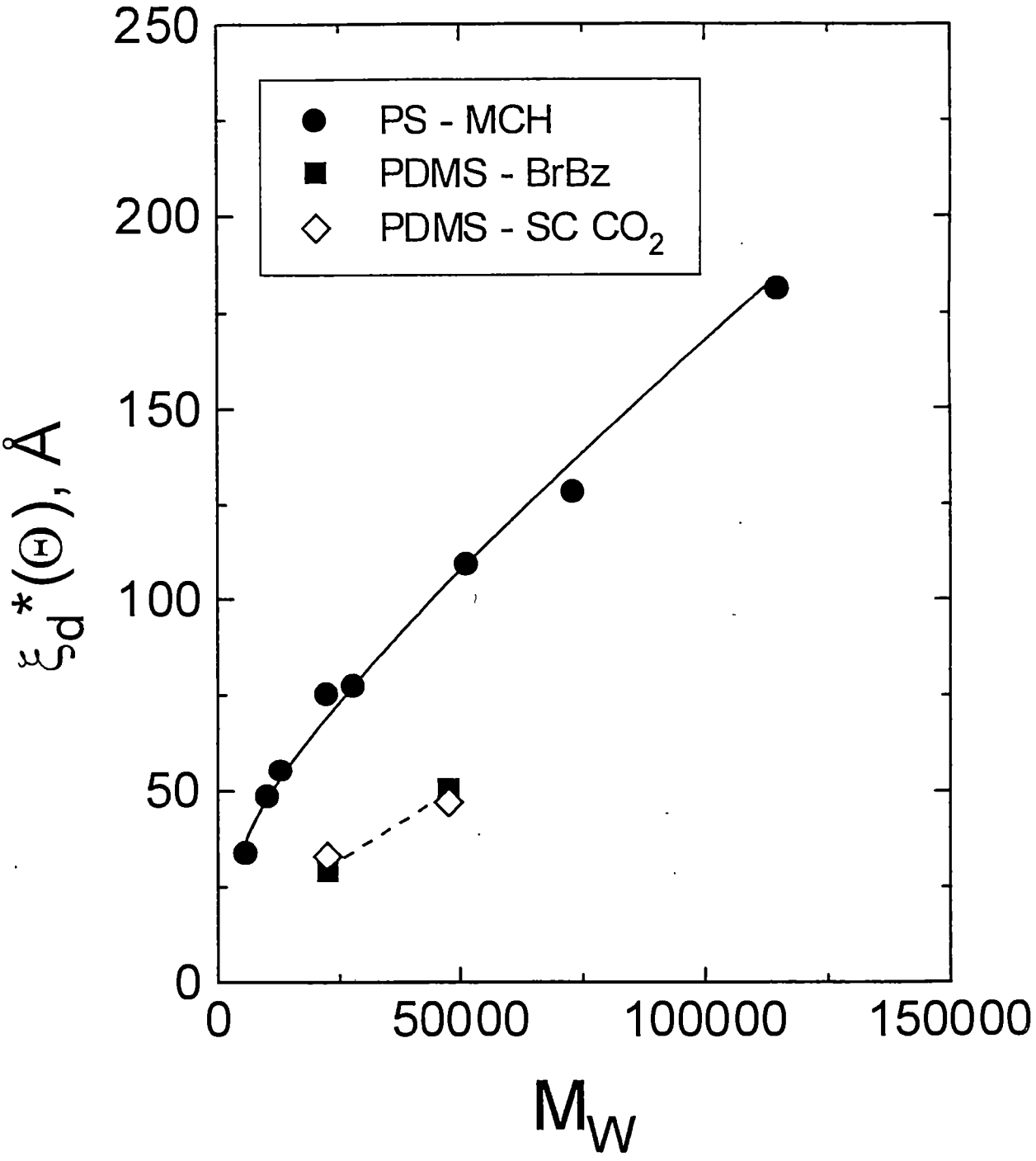

dPS (10500) - AC
PDMS (22500) - SC CO2
PS (5700) - dAC
ξ/ξ(I)
T - Tc, K
0
1
2
3
4
0
20
40
60
80
100

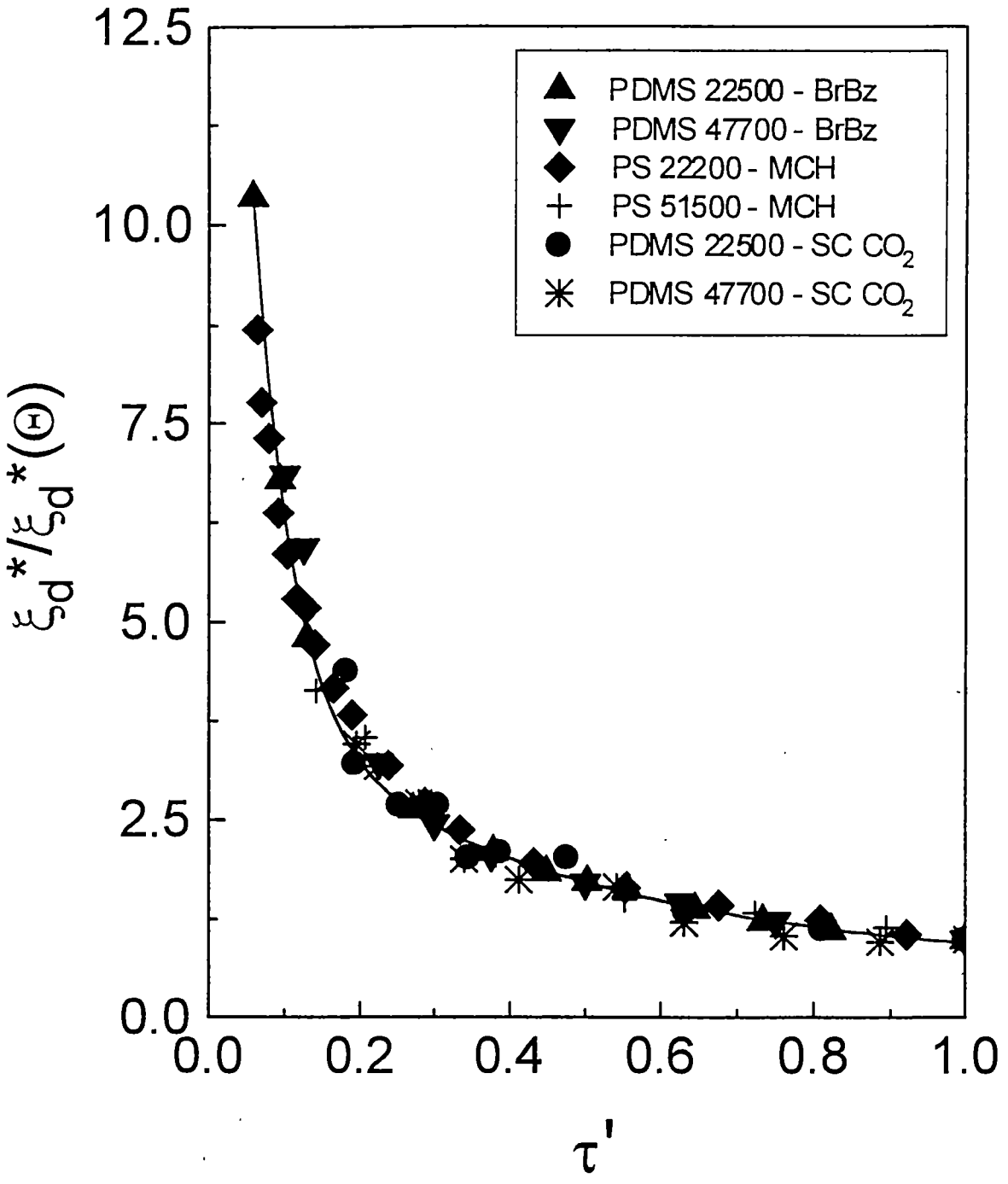

80
70
60
50
40
30
20
20 30 40 50 60 70 80 90
P, MPa
R_g, Å
$R_g(\Theta)$=41 Å
P_C
60
50
40
30
20
0 20 40 60 80 100
T, ° C
R_g, Å
$R_g(\Theta)$=41 Å
T_C


1000
100
10
0.01
0.1
ξ, Å
τ
ν=0.64±0.03
ν=0.48±0.03
ξ=40 Å
PDMS- SC CO2
1000
100
10
0.001
0.01
0.1
1
ν=0.62±0.01
ν=0.50±0.01
PDMS - BrBz
ξ=40 Å


100000
10000
1000
100
10
1
0.00001
0.0001
0.001
0.01
0.1
1
τ
ξd*, Å
ν*=0.8±0.1
PS-MCH
Mw
5700
8300
10200
13000
22200
28000
51500
73000
115000
PDMS-BrBz
Mw
22500
47700
PDMS-SC CO2
Mw
22500
47700


10^4
10^3
10^2
10^1
10^0
Correlation length, Å
ν^*=0.90±0.01
ν=0.77±0.01
ν=0.49±0.02
0.001
0.01
0.1
1
τ


250
200
150
100
50
0
0
50000
100000
150000
PS - MCH
PDMS - BrBz
PDMS - SC CO2
ξd*(Θ), Å
MW


12.5
10.0
7.5
5.0
2.5
0.0
0.0
0.2
0.4
0.6
0.8
1.0
τ'
ξd*/ξd*(Θ)
PDMS 22500 - BrBz
PDMS 47700 - BrBz
PS 22200 - MCH
PS 51500 - MCH
PDMS 22500 - SC CO2
PDMS 47700 - SC CO2

Paper 4

Comparison of the behaviour of polymers in supercritical fluids and organic solvents via small angle neutron scattering

Yuri B. Melnichenko ,[a*] E. Kiran ,[b] K. D. Heath ,[c] S. Salaniwal ,[c] H. D. Cochran ,[c] M. Stamm ,[d] W. A. Van Hook [e] and G. D. Wignall [a]

[a] *Solid State Division, Oak Ridge National Laboratory†, Oak Ridge, TN 37831, USA*
[b] *Department of Chemical Engineering, University of Maine, Orono, ME 04468, USA*
[c] *Chemical Technology Division, Oak Ridge National Laboratory and Department of Chemical Engineering, University of Tennessee, USA*
[d] *Institut für Polymerforschung, 55021 Mainz, Germany*
[e] *Chemistry Department, University of Tennessee, Knoxville TN 37996, USA*

Small-angle neutron scattering has been used to study the effect of temperature and pressure on the phase behaviour of semidilute solutions of polymers dissolved in organic and supercritical solvents. Above the theta temperature (T_Θ), these systems exhibit a "good solvent" domain, where the molecules expand beyond the unperturbed dimensions in both organic solvents and in CO_2. However, this transition can be made to occur at a critical "theta pressure" (P_Θ) in CO_2 and this represents a new concept in the physics of polymer-solvent systems. For $T < T_\Theta$, and $P < P_\Theta$, the system enters the "poor solvent" domain, where diverging concentration fluctuations prevent the chains from collapsing and allow them to maintain their unperturbed dimensions.

1. Introduction

In organic solvents, it is well known that the radius of gyration, R_g (i.e. the r.m.s. distance of scattering elements from the center of gravity) of polymer chains depends on the sign and magnitude of the interactions between the chain segments and the molecules of the surrounding liquid. In "good" solvents, the dominating repulsive forces between the segments (excluded volume effects) work to expand the R_g, and the second virial coefficient (A_2) is positive. In less favorable solvents, the pairwise attractive and repulsive segment interactions may compensate at the "theta temperature" (T_Θ), where $A_2 = 0$, and R_g corresponds to the dimension of a volume-less polymer coils, "unperturbed" by the excluded volume effects. One of the first applications of SANS was to confirm Flory's prediction that polymer chains would adopt such random-walk configurations in the amorphous state. By definition, T_Θ is the critical solution temperature (T_C) for a polymer with the molecular weight $M_W = \infty$ and thus corresponds to the threshold of unlimited polymer–solvent miscibility. In the poor solvent regime ($T < T_\Theta$, $A_2 < 0$), attractive interactions between the segments work to collapse polymer chains into compact polymer globules. This phenomenon is well understood for dilute solutions of widely separated polymer chains, which collapse as $T \Rightarrow T_C$ (Chu, Ying and Grosberg, 1995). SANS has recently been used to extend the experimental observations to semidilute solutions of strongly interacting macromolecules. According to the de Gennes' concept, in the critical region ($T \sim T_C$), the chains do not interpenetrate significantly and thus should be collapsed [i.e. $R_g(T_C) < R_g(T_\Theta)$] as in dilute concentration regime. However, experiments on PS in cyclohexane (CH) and acetone (AC) have demonstrated that the predicted decrease in R_g is not observed. Instead, diverging concentration fluctuations near T_C lead to the formation of distinct microdomains of strongly interpenetrating molecules, which prevents the expected collapse (Melnichenko et al., 1997, 1998). Measurements have also been made in supercritical fluids to test the prediction of Kiran and Sen (1993), that the molecules will adopt the unperturbed dimensions at a critical "theta pressure" (P_Θ) as they do in polymer solutions at the theta temperature and to explore the similarity and differences between the structure and thermodynamic properties of polymers in SCFs and in sub-critical organic liquids.

2. Experimental

The SANS data were collected on the 30m SANS facility (Koehler, 1986) at Oak Ridge National Laboratory. The wavelength was λ = 4.75 A ($\Delta\lambda/\lambda \sim 5\%$) and the 64 x 64 cm^2 area detector with cell size ~ 1 cm^2 was placed at sample-detector distances of 12m and 5m to give an overall range of momentum transfer of $0.005 < Q = 4\pi\lambda^{-1}\sin\theta < 0.1$ $Å^{-1}$, where 2θ is the angle of scattering. The data were corrected for instrumental backgrounds and detector efficiency on a cell-by-cell basis, prior to radial (azimuthal) averaging and the net intensities were converted to an absolute (± 3%) differential scattering cross section per unit solid angle, per unit sample volume [$d\Sigma(Q)/d\Omega$ in units of cm^{-1}] by comparison with precalibrated secondary standards (Wignall and Bates, 1986). The experiments in supercritical CO_2 were conducted in a cell similar to the one used previously for polymer synthesis and SANS studies of block copolymer amphiphiles in supercritical CO_2 (McClain et al., 1996). The cell was fitted with sapphire windows which caused virtually no attenuation of the neutron beam (cell transmission ~ 93%) or parasitic scattering. The signal from the CO_2 amounted to a virtually flat background (~ 0.04 cm^{-1}), which formed only a minor correction to the scattering from the homopolymer solutions.

High concentration isotope labeling methods [Williams (1979), Akcasu (1980), King (1985) and co-workers] were used to obtain the R_g of the polymer molecules and the correlation length (ξ) of the concentration fluctuations. The coherent scattering cross section [$d\Sigma(Q)/d\Omega$] of an incompressible mixture of identical protonated and deuterated polymer chains dissolved in a solvent is given by:

$$d\Sigma(Q,T,x)/d\Omega = I_s(Q,T,x) + I_t(Q,T,x) \quad , \tag{1}$$

$$I_s(Q,T,x) = KnN^2 S_s(Q,T) \quad , \tag{2}$$

$$I_t(Q,T,x) = LnN^2 S_t(Q,T) \quad , \tag{3}$$

where the subscripts "s" and "t" correspond to scattering from a single chain and total scattering, x is the mole fraction of protonated chains and n and N are the number density and degrees of polymerization. $S_s(Q)$ is the single-chain structure factor, containing information on the intramolecular R_g, and the total scattering structure factor, $S_t(Q)$ embodies both intra- and intermolecular correlations between segments. The structure factors are normalized

† Managed by Lockheed Martin Energy Research Corporation under contract DE-AC05-96OR-22464 for the U. S. Department of Energy.

so that $S_t = 1$ at ($Q = 0$) and $S_t = S_s$ at infinite dilution. The prefactors K and L are:

$$K = (b_H - b_D)^2 x(1 - x); \qquad L = [b_H x + (1 - x) b_D - b_S']^2 \quad , \quad (4)$$

where b_H and b_D are the scattering lengths of the H^1- and D^2-labeled segments and b_S' is the scattering length of a solvent molecule, normalized to the same specific volume.

The prefactor, L, in equation (4) controls the "total" scattering contribution and it has been shown (Melnichenko et al., 1997) that for isotopic polystyrene (PS) mixtures dissolved in deuterated acetone (AC-d), $L = 0$ at $x = 0.214$. Similarly for PDMS in CO_2, an isotopic ratio of $x = 0.512$ gives $L = 0$ at a solvent density of ρ_{CO2}=0.95 g/cm^3. Thus, the intramolecular scattering function may be obtained directly from the measured cross section at all temperatures using the Debye formfactor for Gaussian chains:

$$S_s^D(Q) = (2/y^2)(y - 1 + e^{-y}) \quad , \quad y = Q^2 R_g^2 \quad . \qquad (5)$$

For PS in CH-d, however, there is no isotopic ratio, $0 < x < 1$, which satisfies the condition $L(x) = 0$, and $d\Sigma/d\Omega$ always contains a minor (~10%) contribution from the total (intermolecular) scattering, which must be subtracted to extract R_g. If all chains are all protonated (x=1), the prefactor, K = 0, and $d\Sigma/d\Omega \sim S_t(Q)$. Thus, the size of the concentration fluctuations may be measured via the Ornstein-Zernike (O-Z) formalism:

$$S_t(Q,T) = S(Q = 0)/(1 + Q^2 \xi^2) \quad , \qquad (6)$$

where ξ may be obtained from the slope of an O-Z plot of $[d\Sigma(Q)/d\Omega]^{-1}$ vs. Q^2.

Polymer samples of PS-h standards (M_W=5700, 533000) and PS-d standards (M_W=10500, 520,000) of polydispersity generally $M_W/M_N \leq 1{,}06$ were obtained from Polymer Laboratories, USA and used to prepare solutions at the critical concentration of the polymer. Samples of protonated polydimethylsiloxane (PDMS-h) with M_W = 22,500 ($M_W/M_n \leq 1.03$) and PDMS-d (M_w = 27,600, $M_w/M_n \leq 1.11$) were synthesized and characterized at the Max Planck Institut für Polymer Forschung, Germany. The PDMS – SC CO_2 solutions were prepared at the overlap concentration which is close to the critical concentration of phase demixing (de Gennes, 1979). The deuterosubstituted solvents (CH-d, AC-d with D/(H+D)=0.0995 were obtained from Sigma Chemical and dried over a molecular sieve prior to preparing solutions. The CO_2 (SFC purity 99.99 %) was obtained from Matheson Gas Products, Inc. Samples were either run at atmospheric pressure in quartz cells as a function of temperature (e.g. PS-h in CH-d or in AC-d) or were loaded into the pressure cell with the appropriate isotopic ratio to eliminate ($x = 0.512$ for PDMS in CO_2) or minimize (e.g. $x = 0.2$ for PS-h in CH-d) the contribution of the total scattering term in equation (1). The temperature was controlled by circulating fluids (± 0.1 K) and pressure was applied using a screw-type pressure generator.

3. Results and discussion

Fig. 1 shows the temperature variation of R_g for PS in CH-d at the critical concentration and it may be seen that the chains do not collapse as $T \Rightarrow T_C$, as observed in dilute solutions. Instead, they maintain their unperturbed dimensions in accordance with the theoretical predictions of Muthukumar (1986) and Raos and Alegra (1996). The size of the concentration fluctuations is small in the Θ-region, but increases dramatically near the critical point where it exceeds the chain dimensions [$\xi >> R_g(T_\Theta)$]. These findings indicate that critical polymer solutions can not be considered as an ensemble of collapsed, non-interpenetrating chains, as was suggested by de Gennes, 1979. Instead, the diverging thermodynamic fluctuations in the critical region lead to the formation of distinct microdomains, representing unperturbed, strongly interpenetrating macromolecules. It is notable that at the theta temperature, $T_\Theta \cong 313$ K, the average correlation length $\xi(T_\Theta) = 109 \pm 5$ Å. According to Fujita (1990) and Des Cloizeaux and Jannink (1990)],

$$\xi(T_\Theta) = R_g(\Theta)/3^{1/2} \qquad (7)$$

at the theta condition, so $\xi(T_\Theta) = 114$ Å for M_W = 533,000 which agrees well with the experimental value.

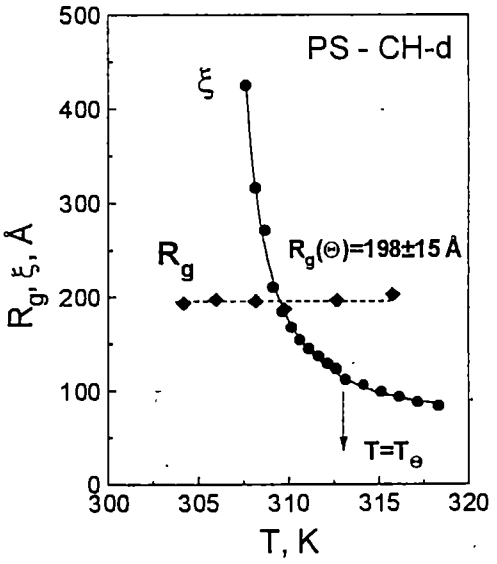


Figure 1
$R_g(T)$ and $\xi(T)$ for the solution of PS (M_W=533,000) in the Θ solvent CH-d. Rg measured over the pressure range $0.1 \leq P \leq 50$ MPa.

Unlike the PS-CH system, which may undergo the transition from the poor solvent to the theta solvent by adjusting the temperature, the solvent quality is much poorer for PS - AC. Nevertheless, the chain dimensions of PS in this solvent remain close to the unperturbed dimensions for appropriate $M_W = R_g \cong 0.27\ M_W^{1/2}$ and are

independent of pressure and temperature and (Melnichenko et al., 1998). Fig. 2 shows the effect of temperature on the thermodynamic state of PS/AC-d. Away from the critical point ($T >> T_C$), the concentration fluctuations fall, though they do not decay sufficiently to reach $\xi(T_\Theta) = R_g(\Theta)/3^{1/2}$, so the system never leaves the poor solvent domain. The same effect is observed for solutions of PDMS in SC CO_2 at moderate densities of the supercritical solvent. As is seen in Fig. 2, the temperature variation of ξ for PDMS-SC CO_2 levels out at some temperature distance from T_C which means SC CO_2 remains a poor solvent for PDMS at density $\rho_{CO2} < 0.85$ g cm^{-3}.

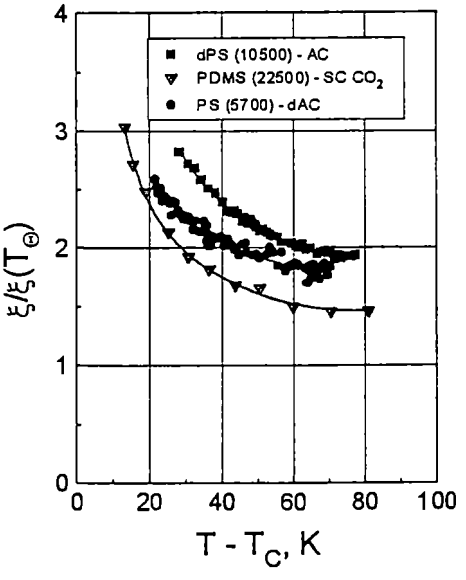


Figure 2
The correlation length ξ normalized to $\xi/(T_\Theta)$ (Eq.7) vs. $T - T_C$ for solutions of PS-AC and PDMS-SC CO_2 (ρ_{CO2} = 0.84 g/ml).

SANS has also been used (Melnichenko et al., 1999) to test the prediction of Kiran and Sen (1993) that the polymer coils may adopt "ideal" configurations, unperturbed by excluded volume effects, at a critical "theta pressure" (P_Θ) as they do in polymer solutions at the theta temperature. Experiments on PDMS in CO_2 (Figs. 3 and 4) confirm that the Θ condition may be reached at a theta pressure, P_Θ ~52±4 MPa at T=343 K and a theta temperature T_Θ ~ 338 K at the density of the supercritical solvent ρ_{CO2} = 0.95 g/ml. It is notable that the Θ temperature of PDMS depends crucially on the density of SC CO_2, e.g. it becomes 353 K at ρ_{CO2} = 0.87 g/ml and can hardly be reached for $\rho_{CO2} < 0.85$ g/ml when SC CO_2 remains poor solvent at all accessible temperatures (see Fig. 2). To the authors' knowledge, this is the first time that the existence of both a "theta pressure" and a "theta temperature" has been demonstrated and this effect constitutes a new concept in the physics of polymer-

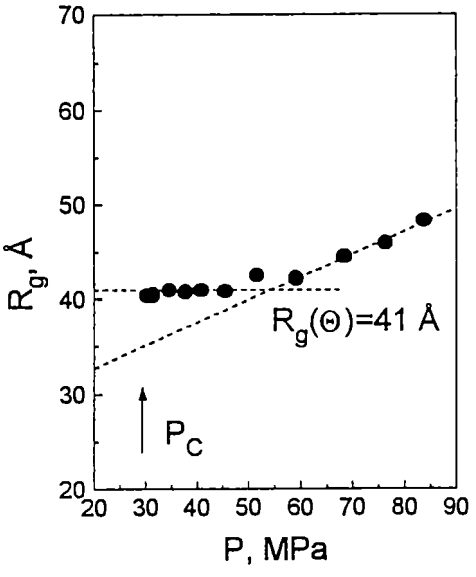


Figure 3
Variation of the radius of gyration for PDMS (M_w=22,500) in solution (h+d) PDMS in SC CO_2 vs. pressure at T=343 K.

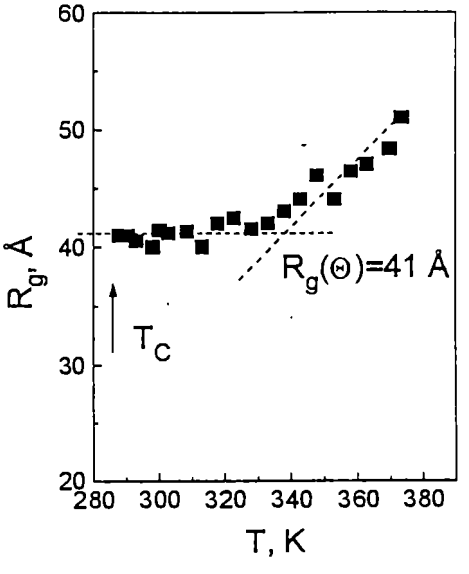


Figure 4
Variation of the radius of gyration for PDMS (M_w=22,500) in solution (h+d) PDMS in SC CO_2 vs. temperature at ρ_{CO2} = 0.95 g/ml.

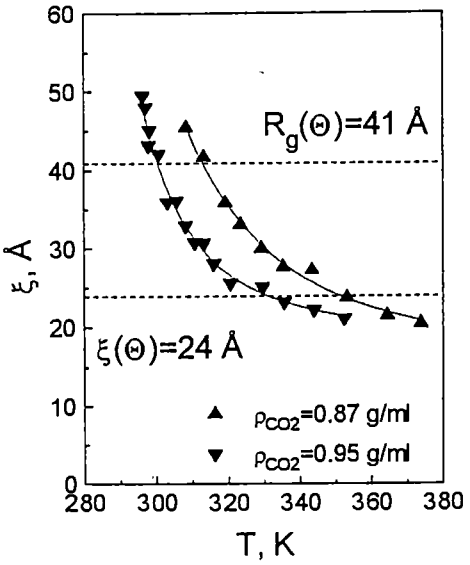


Figure 5
Variation of the correlation length for PDMS (M_w=22,500) in SC CO_2 vs. temperature at two different densities of CO_2 shown in the inset.

solvent systems. For $P > P_\Theta$ and $T > T_\Theta$, the system enters a "good solvent" domain, where the polymer molecules expand beyond the unperturbed R_g, the same way as they do in polymer solutions in organic liquids (Cotton et al., 1976). However, for $T < T_\Theta$, and $P < P_\Theta$, the chains do not collapse (Figs. 3 and 4), as is observed in organic solvents. Near T_c, the growth of the polymer concentration fluctuations brings together the initially diluted chains, which retain the unperturbed dimensions, as in highly concentrated systems and in the condensed state. Thus, the stabilization of the molecular dimensions in the poor solvent domain by diverging concentration fluctuations is a universal phenomenon, observed not only in "classical" polymer solutions in organic liquids, but also in supercritical fluids. This reveals a close similarity between the behavior of polymer molecules in organic solvents and in CO_2.

A unique attribute of SCFs is that the solvent strength is easily tunable with changes in the system density, offering exceptional control over the solubility. As it follows from Figs. 3 and 4, supercritical polymer solutions may be driven through the Θ condition as a function of pressure in addition to temperature. Understanding the solubility mechanisms is a necessary condition for the development of CO_2-based technologies and SANS promises to give the same level of insight into polymers and in supercritical media that it has provided in the condensed state and organic solvents.

YBM and GDW wish to acknowledge stimulating discussions with M. Muthukumar. The research was supported the Divisions of Advanced Energy Projects, Materials Sciences, and Chemical Sciences, U. S. Department of Energy under contract No. DE-AC05-96OR-22464 (with Lockheed Martin Energy Research Corporation) and Grant No. DE-FG05-88ER-45374 (with the University of Tennessee) and by the National Science Foundation Grant No. CTS-9613555 (with the University of Tennessee). The financial support of YBM by Alexander von Humboldt-Stiftung is gratefully acknowledged.

4. References

Akcasu, A. Z., Summerfield, G. C., Jashan, S. N., Han C. C., Kim, C. Y. & Yu, H. J. (1980). *Polym. Sci., Polym. Phys. Ed.*, **18**, 863-869.

Chu, B., Ying, Q. & Grosberg, A. (1995). *Macromolecules*, **28**, 180-185, and references therein.

Cotton, J. P., Nierlich, M. Boue, F. Daoud, M. Farnoux, B. Jannink, G. Duplessix, R. & Picot, C. *J.* (1976). J. *Chem. Phys.* **65**, 1101-1108.

De Gennes, P. G. (1979). *Scaling Concepts in Polymer Physics*. New York: Cornell University Press.

Des Cloizeaux, J. & Jannink, G. (1990). *Polymers in Solution. Their Modeling and Structure*, p. 815. Oxford: Claredon Press.

Fujita, H. (1990). *Polymer Solutions*, p. 192. Amsterdam: Elsevier Publ.

King, J. S. Boyer, W. Wignall, G. D. & Ullman, R. (1985). *Macromolecules* **18**, 709-718.

Kiran, E. & Sen, Y. L. (1993). In: *Supercritical Fluid Engineering Science*, edited by E. Kiran & J. F. Brenneke, pp. 104-120. ACS Symposium
Series No. 514. Washington DC: ACS Publ.

Koehler, W. C. (1986). *Physica*, **137B**, 320-325.

Melnichenko, Y. B. & Wignall, G. D. (1997). *Phys. Rev. Lett.* **78**, 686-688.

Melnichenko, Y. B., Wignall, G. D., Van Hook, W. A., Szydlowski, J., Rebello, L. P. & Wilczura, H. (1998). *Macromolecules* **31**, 8436-8438.

Melnichenko, Y. B., Kiran, E., Wignall, G. D., Heath, K., Salaniwal, S., Cochran, H. D. & Stamm, M. (1998). *Macromolecules*, **32**, 5344-5347.

McClain, J. B., Betts, D. E., Canelas, D. A., Samulski, E. T., DeSimone, J. M., Londono, J. D., Cochran, H. D., Wignall, G. D., Chillura-Martino, D. & Triolo, R. (1996). *Science* **274**, 2049-2053.

Muthukumar, M. (1986). *J. Chem. Phys.* **85**, 4722-4727.

Raos, G. & Allegra, G. (1996). *J. Chem. Phys.* **104**, 1626-1645.

Wignall, G. D. & Bates, F. S. (1986). *J. Appl. Cryst.* **20**, 28-34.

Williams, C. E., Nierlich, M., Cotton, J. P., Jannink, G., Boue, F., Daoud, M., Farnoux, B., Picot, C., de Gennes, P -G., Rinaudo, M., Moan, M., & Wolf, C. (1979). *J. Polym. Sci., Polym. Lett. Ed.* **17**, 379-384.

VITA

Sumeet Salaniwal was born in New Delhi, India on June 28, 1971. He finished his schooling from St. Xaviers School, New Delhi in April, 1989. He entered the Panjab University in August, 1989 and received a Bachelor of Engineering (Honors) degree majoring in Chemical Engineering in May, 1993. He then attended the Indian Institute of Technology at Kanpur (IIT-K) from where he earned a Master of Technology in Chemical Engineering in April, 1995. From July, 1995 till July, 1996 he then worked as a Process Engineer at Reliance Industries Limited, Hazira, India. In August, 1996 he entered the Ph.D. program in the Department of Chemical Engineering at the University of Tennessee, Knoxville. He received his doctorate in May 2000.